

**Department of Chemical Engineering  
National Tsing Hua University  
&  
Department of Chemistry  
The University of Liverpool**

**PhD Thesis**

**Optimising cell voltage and understanding charge storage  
mechanism of transition metal oxides and hydroxides for  
aqueous supercapacitors**

**水相超級電容器之操作電壓最適化與過渡金屬  
氧化物及氫氧化物的充放電機制探討**

**Student: Tzu-Ho Wu (吳子和)**

**Supervisors: Prof. Chi-Chang Hu (胡啟章 教授)**

**Dr. Laurence Hardwick**

**June 2016**

## Acknowledgements

First of all, I would like to thank my supervisors, Prof. Chi-Chang Hu and Dr. Laurence Hardwick, for organising a project in the dual PhD programme between NTHU (NTHU) and UoL (UoL). This project from my supervisors/universities supports me the financial support for my 2-year study in Liverpool. It is greatly appreciated that my supervisors always provide useful suggestions on experiments.

I would like to thank my parents for their supports to study postgraduate degree. I am grateful that Kang-Ju (Catherine) Chao is rooting for me all the time. It is greatly appreciated for her being with me during my 4-year PhD study, especially for my 2-year study in Liverpool.

I would like to thank my seniors, Dr. Ying-Hui Lee, Dr. Kuo-Hsin Chang, Dr. Jing-Mei Li, Dr. Chien-Hung Lien and Ms. Yi-Hsuan Chu for their valuable suggestions and strategies on experiments in the postgraduate programme when I just started my first year study in NTHU.

I would like to thank my classmate, Dr. Hsiao-Hsuan Shen, to deal with all the issues in NTHU when I studied in UoL. It is greatly appreciated that Mr. Chih-Hao Su provided RGO materials when I studied in Liverpool.

I would like to thank my labmates in Liverpool, Dr. Laura Cabo-Fernandez, Dr. Nick Drewett, Dr. Jianli Zou, Mr Christopher Sole, Mr. Iain Aldous, Mr. Tom Galloway, Mr. Petar Radjenovic and Mr. Scott Lewis for their help to deal with all the lab issues.

I would like to thank Dr. Nick Drewett and Mr Christopher Sole for their help on Swagelok electrochemical cells.

I would like to thank China Steel Chemical Corporation, Taiwan for their generosity to provide activated carbon sample (ACS-679).

I would like to thank Dr. Chris Collins (Department of Chemistry, UoL) and Mr. Ming-Guan Chen (Department of Chemical Engineering, NTHU) for their help on XRD measurements of  $\text{MnO}_x$ .

I would like to thank Dr. David Hesp, Mr. Thomas Whittles and Mr. Mohammed Althobaiti (Stephenson Institute for Renewable Energy, UoL) for XPS measurements of  $\text{MnO}_x$ . I would like to thank Prof. Alan Chadwick and Dr. David Pickup (School of Physical Sciences, University of Kent) for their help on XAS measurements and analyses of  $\text{MnO}_x$ .

I would like to thank Dr. Ming Liu (Department of Chemistry, UoL) for BET, Dr. Tobias Heil (Nano Investigation Centre at Liverpool) and Dr. Laura Cabo-Fernandez for TEM and Mr. Filipe Braga (Department of Chemistry, UoL) for SEM analyses of  $\text{MnO}_x$ .

I would like to thank Mr. Jia-Cing Chen (Department of Chemical Engineering, NTHU) for his preliminary EQCM studies of  $\text{Ni}(\text{OH})_2$ .

I would like to thank Dr. Ivan Scivetti and Dr. Gilberto Teobaldi (Department of Chemistry, UoL) for their efforts on computational simulation (DFT) of  $\text{Ni}(\text{OH})_2$ . I am grateful to have constructive suggestions and feedback from them.

I would like to thank my viva examiners, Prof. Chi-Chao Wan, Prof. Ten-Chin Wen, Prof. Hsisheng Teng, Dr. Alexander Cowan and Dr. Tzu-Chien Wei, for their valuable suggestions and comments about my thesis. The discussion in viva is also very useful for deploying further studies on various materials.

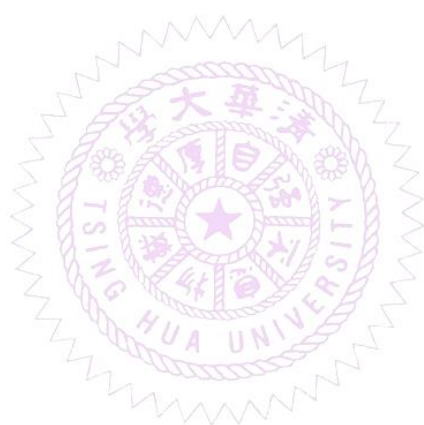
## 摘要

本論文針對水相超級電容器之操作電壓最適化與過渡金屬氧化物及氫氧化物的充放電機制進行探討。第一部分探討最適化水相對稱型及非對稱型電化學電容器的方法。第四章以商用活性炭為電極材料，探討電極材料的開路電壓對於對稱型電化學電容器操作電壓的影響，並且指出符合正負極電荷平衡的對稱型電化學電容器才能夠有效地運用電極材料的穩定電化學電容電位窗。此外，藉由諸多電化學分析方式，例如：循環伏安法、定電流充放電法、電化學阻抗頻譜，以及電感電容電阻表分析，本研究提出有效評估對稱型電化學電容器的最佳操作電位之方法。以此電荷平衡為基礎，無論其電化學活性物質與電解液，此一評估方法適用於所有對稱型電化學電容器。非電荷平衡的對稱型電化學電容器擁有較低的比能量，彰顯出正負極電荷平衡的重要性。第五章則是以電化學活化法得到的錳氧化物當正極搭配微波水熱法還原的石墨烯為負極的非對稱型電化學電容器，根據第四章的電化學分析方法，有效地制訂出非對稱型電化學電容器的最佳上限操作電壓之準則。藉由了解非對稱型電化學電容器的上限操作電壓，將對於其儲存能量與充放電壽命有相當大的幫助。此外，鈦氧化物與石墨烯的非對稱型電化學電容器也適用於此準則，為此準則提供了確效性。

本論文的第二部分則是針對水相電化學電容器常用的過渡金屬氧化物與氫氧化物，進行其充放電機制的探討。第六章針對硫酸鈉水溶液中進行電化學活化的錳氧化物進行深入探討，主要運用臨場拉曼來分析電化學活化過程中錳氧化物的結構改變，搭配粉體X光繞射、X光電子能譜儀與掃描式與穿透式電子顯微鏡，對於錳氧化物的物化性質於電化學活化前後有更完整的分析。由於電化學活化後的錳氧化物不具有規則排列的層狀結構，其充放電機制為氧化還原反應於錳氧化物的表面活性位置，與陽離子遷入結構無關。第七章則是探討氫氧化鎳於不同電解液中的電化學行為，運用電化學石英微天秤和臨場拉曼來探討氫氧化鎳的充放電機制，並且根據電化學的數據來進行密度泛函理論模擬，其結果提供氫氧化鎳



於充放電過程中成分變化的資訊，有助於全盤地了解氫氧化鎳在不同電解液中的充放電機制。在氫氧化鋰的溶液中進行充放電，鋰離子進出氫氧化鎳的結構並不會改變結構中水份含量。但若是在氫氧化鈉及氫氧化鉀中進行充電，陽離子進入氫氧化鎳的結構會導致結構中原有的水分子離開；而在放電過程中，水分子卻無法完全可逆地回到氫氧化鎳的結構中。氫氧化鎳結構中的水份含量是氫氧化鎳相轉換的關鍵，其行為受到電解液中的鹼金族元素所影響。



## Abstract

This study focuses on aqueous electrochemical capacitors (ECs) for optimising the cell voltage and understanding the charge storage mechanism of transition metal oxides and hydroxides. The first part discusses how to optimise cell voltage of symmetric and asymmetric ECs. In Chapter 4, a commercial activated carbon (ACS-679) was employed as an electroactive material to demonstrate the necessity of charge-balanced condition of aqueous symmetric ECs in order to improve the utilisation of electrochemically stable potential window of electroactive material. Besides, the effect of stable open-circuit potential on electroactive materials is also addressed here. The concept is on the basis of electrochemical charge-balance principle, therefore, it is believed to be applicable to all the symmetric ECs no matter what kind of material is used as electroactive material. The charge-balanced electric double-layer capacitors (EDLCs) was assembled to evaluate the acceptable cell voltage by means of electrochemical analyses, including cyclic voltammogram, constant current charge-discharge, electrochemical impedance spectroscopy and inductance-capacitance-resistance meter measurements. Moreover, charge-unbalanced EDLCs were used to demonstrate the necessity of charge balance in symmetric ECs since those exhibit lower cell voltage and specific energy compared with the charge-balanced case. Similarly, in Chapter 5, asymmetric ECs consisting of reduce graphene oxide and manganese oxide (RGO//MnO<sub>x</sub>) were employed as an example to establish criteria for determining the highest acceptable cell voltage of asymmetric ECs with excellent reversibility and capacitor-like behaviour. It is very useful to evaluate the practical specific energy of asymmetric ECs by understanding the highest acceptable cell voltage. Besides, RGO//RuO<sub>2</sub> was also demonstrated to verify the validity of the proposed criteria.

The second part probes the charge storage mechanism of transition metal oxides and hydroxides in aqueous ECs. In Chapter 6, a wide-ranging study on electrochemical activation from  $\text{Mn}_3\text{O}_4$  to  $\text{MnO}_2$  in 0.5 M  $\text{Na}_2\text{SO}_4$  medium were presented, which includes *in operando* monitoring of the structural evolution during the activation process via *in situ* Raman microscopy. Other advanced material characterisation techniques, such as powder X-ray diffraction, X-ray photoelectron spectroscopy, scanning electron and transmission electron microscopy, were also applied to analyse the as-prepared and activated  $\text{MnO}_x$ . Due to the structural disordering of electrochemically activated birnessite- $\text{MnO}_2$  and residual  $\text{Mn}_3\text{O}_4$ , the charge storage is attributable to the redox reaction between Mn(III) and Mn(IV) at outer surface active sites, rather than cations and/or protons intercalation into layer structures. In Chapter 7, the redox behaviours of  $\gamma\text{-NiOOH}/\alpha\text{-Ni(OH)}_2$  in various electrolytes (LiOH, NaOH, KOH, CsOH and  $\text{NH}_4\text{OH}$ ) are discussed. The charge storage mechanism of  $\gamma\text{-NiOOH}/\alpha\text{-Ni(OH)}_2$  was studied by means of EQCM and *in situ* Raman microscopy. Moreover, the computational simulation (DFT+U) based on EQCM results gives a better idea on the compositional changes in the first few potential cycles. The insertion/removal of  $\text{Li}^+$  does not alter the content of water inside the structure, while the insertion of  $\text{Na}^+$  and  $\text{K}^+$  leads to a significant removal of water. The removed water molecules cannot be reversibly re-inserted back into the nickel structure, leading to the loss of water molecules in  $\text{Ni(OH)}_2$  structure during charge-discharge process. The capability to retain water molecules inside the  $\text{Ni(OH)}_2$  is crucial for the stability of  $\gamma\text{-NiOOH}/\alpha\text{-Ni(OH)}_2$  redox reaction.

# Table of Contents

<b>Chapter 1</b> .....	1
<b>Introduction and Objective</b> .....	1
<b>Chapter 2</b> .....	7
<b>Literature Review</b> .....	7
2.1 Aqueous Electric Double–Layer Capacitors (EDLCs) .....	7
2.2 Manganese Oxide Pseudocapacitors.....	14
2.3 Carbon//Manganese Oxide Aqueous Asymmetric ECs.....	29
2.4 Charge Storage Mechanisms of Manganese Oxides.....	35
2.5 Raman Spectroscopic Applications .....	50
2.6 Electrochemically Activated Manganese Oxide.....	57
2.7 Redox Mechanism of NiOOH/Ni(OH) <sub>2</sub> .....	62
<b>Chapter 3</b> .....	69
<b>Experimental Methods</b> .....	69
3.1 Chemicals and Instruments .....	69
3.1.1 Chemicals.....	69
3.1.2 Instruments.....	71
3.2 Experimental .....	72
3.2.1 Preparation of Graphene Oxide .....	72
3.2.2 Preparation of Manganese Oxide.....	72
3.2.3 Microwave–Assisted Hydrothermal Reduction of Graphene Oxide ..	73

3.2.4 Graphite Substrate Pretreatment .....	73
3.2.5 Electrodeposition of Ni(OH) <sub>2</sub> .....	74
3.3 Electrochemical Analyses .....	74
3.3.1 Cyclic Voltammetry (CV).....	76
3.3.2 Chronopotentiometry (CP).....	78
3.3.3 Electrochemical Impedance Spectroscopy (EIS).....	80
3.3.4 Inductance–Capacitance–Resistance Meter (LCR) .....	82
3.3.5 Electrochemical Quartz Crystal Microbalance (EQCM) .....	83
3.4 Textural Analysis .....	84
3.4.1 X–ray Diffraction (XRD).....	84
3.4.2 Scanning Electron Microscopy (SEM) .....	85
3.4.3 Transmission Electron Microscopy (TEM) .....	85
3.4.4 Nitrogen Adsorption/desorption Isotherms.....	86
3.4.5 Raman Spectroscopy .....	87
3.4.6 X–ray Photoelectron Spectroscopy (XPS).....	91
3.4.7 X–ray Absorption Spectroscopy (XAS) .....	92
Chapter 4.....	93
Important Parameters Affecting the Cell Voltage of Aqueous Electric double–Layer Capacitors (EDLCs) .....	93
4.1 Motivation.....	93
4.2 Open–circuit Potential Effect on EDLCs.....	94
4.3 Establish Criteria for Aqueous EDLCs.....	98
4.4 Necessity of Charge Balance in EDLCs .....	109
4.5 Overall Capacitive Performances of Charge–balanced and –unbalanced EDLCs.....	118
4.6 Conclusion .....	122

Chapter 5.....	124
Criteria for Appointing the Highest Acceptable Cell Voltage of RGO//MnO <sub>x</sub> Asymmetric ECs.....	124
5.1 Motivation.....	124
5.2 Establish Criteria for RGO//MnO <sub>x</sub> Asymmetric ECs by Electrochemical Methods.....	125
5.3 Criteria Validation by RGO//RuO <sub>2</sub> Asymmetric ECs .....	134
5.4 Conclusions.....	137
Chapter 6.....	138
Charge Storage Mechanism of Electrochemically Activated Manganese Oxide Composites.....	138
6.1 Motivation.....	138
6.2 Chemical Synthesised As-prepared MnO <sub>x</sub> .....	139
6.3 Electrochemical Activation Process of MnO <sub>x</sub> .....	145
6.4 Charge Storage Mechanism of Electrochemically Activated MnO <sub>x</sub> .....	156
6.5 Conclusions.....	164
Chapter 7.....	165
A New Redox Mechanism of Ni(OH) <sub>2</sub> and Its Phase Transformation ..	165
7.1 Motivation.....	165

7.2 Electrochemical Behaviours of Ni(OH) <sub>2</sub> .....	166
7.3 <i>In situ</i> Raman Spectroscopic Studies of Ni(OH) <sub>2</sub> .....	177
7.4 The Proposed New Redox Mechanism of Ni(OH) <sub>2</sub> .....	183
7.5 Conclusions.....	187
Chapter 8.....	189
Summary and Future Works.....	189
References.....	193
Appendix.....	205
Acronyms.....	219
Curriculum Vitae.....	222



## List of Figures

- Figure 1–1** The Ragone plot for various electrochemical energy storage devices. ....2
- Figure 1–2** The open–circuit potential ( $E_{ocp}$ ) effect on the utilisation of electrochemically stable potential window of electroactive material under equal mass loading of positive and negative electrodes. ....3
- Figure 1–3** The operating cell voltage effect on the specific energy of RGO// $MnO_x$  asymmetric ECs. ....4
- Figure 1–4** The electrochemical activation of  $MnO_x$  in neutral  $Na_2SO_4$  aqueous electrolyte. Dash lines indicate the current responses obtained from the CV curve of activated  $MnO_x$  in order to avoid taking the oxidative current responses of  $Mn_3O_4$  into account. ....5
- Figure 1–5** Phase transformation (ageing) from  $\gamma$ -NiOOH/ $\alpha$ -Ni(OH)<sub>2</sub> to  $\beta$ -NiOOH/ $\beta$ -Ni(OH)<sub>2</sub> in repeated CV cycling in KOH medium. ....6
- Figure 2–1** CV curves showing the potential window of chemical converted graphene in 6 M KOH, 1 M  $H_2SO_4$  and 1 M  $Li_2SO_4$  (the CV of the blank substrate in 1 M  $Li_2SO_4$  is also listed) at the scan rate of  $2\text{ mV s}^{-1}$  [58]. .... 12
- Figure 2–2** Schematic illustration of band theory [85]. .... 16
- Figure 2–3** Different  $MnO_2$  structures: (a) pyrolusite  $\beta$ - $MnO_2$  ( $1\times 1$ ), (b) ramsdellite  $R$ - $MnO_2$  ( $1\times 2$ ), (c) birnessite  $\delta$ - $MnO_2$  ( $1\times \infty$ ), (d) spinel  $\lambda$ - $MnO_2$  ( $1\times 1$ ) [97]. ....21



**Figure 2–4** Crystallographic structures of MnO<sub>2</sub> (a) birnessite, (b) spinel, (c–e) cryptomelane (2×2) and (f) OMS–5 (2×4) together with selected characteristic crystal planes and distances [96].....23

**Figure 2–5** (A to D) Electrochemical characteristics distinguish capacitor and battery materials. (A) Cyclic voltammograms distinguish a capacitor material where the response to a linear change in potential is a constant current, (B) as compared to a battery material, which exhibits faradaic redox peaks. (C) Galvanostatic discharge behaviour (where *Q* is charge) for a MnO<sub>2</sub> pseudocapacitor is linear for both bulk and nanoscale material, (D) but a LiCoO<sub>2</sub> nanoscale material exhibits a linear response while the bulk material shows a voltage plateau [1].....26

**Figure 2–6** Potential–pH diagram. Lines 5 and 6 represents the kinetic limits for O<sub>2</sub> evolution on MnO<sub>2</sub> and for H<sub>2</sub> evolution on activated carbon, respectively [16]....32

**Figure 2–7** (a) From left to right: AISI 304L stainless steel current collector, coated with conductive paint and co–laminated with the active material composite film, (b) 10–pack cells covered with a cellulosic paper separator and (c) large capacitance final device in the PVC casing prior to sealing [80].....33

**Figure 2–8** Cyclic voltammograms at 5 mV/s of an amorphous MnO<sub>2</sub>·nH<sub>2</sub>O electrode between –0.2 and +1.0 V vs. SCE in 2 M ACl (A=Li, Na, K) electrolyte with Pt–gauze counter electrode [62]. .....37

<b>Figure 2–9</b> Mn 3s core level spectra for reduced, as–prepared and oxidised thin film electrodes. The raw data are represented by the dots and the fitted data are represented by the lines [86].	39
<b>Figure 2–10</b> Na 1s and S 2p core level spectra for composite and thin film electrodes after cycling in 0.1M Na <sub>2</sub> SO <sub>4</sub> [86].	39
<b>Figure 2–11</b> <i>In situ</i> Synchrotron XRD patterns of MnO <sub>2</sub> ·nH <sub>2</sub> O electrodes during CV cycling in 1 M NaCl [143].	41
<b>Figure 2–12</b> (a) Mn K–edge XANES spectra of the electrodeposited manganese oxide at various applied potentials together with the reference manganese oxides. (b) Oxidation state determination of manganese oxide at applied potentials using the Mn K–edge energy shift of the reference Mn compounds [144].	43
<b>Figure 2–13</b> Dependences of the Mn oxidation state and the edge energy on the applied potential during the electrochemical redox cycle [145].	44
<b>Figure 2–14</b> (a) Transformation in Raman spectra of MnO <sub>2</sub> under anodic potential sweep; inset: frequency shift of the $\nu_1$ and $\nu_2$ stretching modes as a function of applied potential. (b) Schematic illustration showing the reversible hexagonal–monoclinic phase transition [146].	45
<b>Figure 2–15</b> Raman spectroscopic evolution of pseudocapacitive MnO <sub>2</sub> thin film when WE is cycled between 0.7, 0, and 0.7 V (vs Ag/AgCl) in 2 M (a) LiNO <sub>3</sub> , (b)	

NaNO<sub>3</sub>, and (c) KNO<sub>3</sub> aqueous electrolyte. The dash lines were applied to show the evolution of band positions ( $\nu_1 - \nu_4$ ) as a function of WE potential approximately. A colour bar was used to depict the WE potential. The schematic sketches of cation-incorporated MnO<sub>2</sub> and water-incorporated MnO<sub>2</sub> corresponding to high-potential state and low-potential state, respectively, are also shown [147]...47

**Figure 2–16** Key spectroscopic features of pseudocapacitive MnO<sub>2</sub> model electrode as functions of WE potential when LiNO<sub>3</sub>, NaNO<sub>3</sub>, and KNO<sub>3</sub> were used as electrolyte. The state of discharge (SOD) is also plotted in each subplot to correlate with spectroscopic features. (a) The  $\nu_2$  band positions as a function of WE potential. (b) The FWHM of  $\nu_2$  as a function of WE potential [147].....48

**Figure 2–17** (a) Cyclic voltammograms and (b)  $\Delta m-E$  curves of a-MnO<sub>x</sub> measured between -0.2 and 1.2 V at 25 mV s<sup>-1</sup> for 5 cycles in 10 mM Na<sub>2</sub>SO<sub>4</sub>. The solid lines stand for the positive scans and the dash lines represent the negative scans [129].....49

**Figure 2–18** Schemes for Rayleigh (elastic) scattering, Stokes (inelastic) scattering, anti-Stokes (inelastic) scattering and fluorescence. ....51

**Figure 2–19** SEM photos of the milled Mn<sub>3</sub>O<sub>4</sub> electrode surface (a) before and after electrochemical cycle test; after (b) 10, (c) 50 and (d) 200 cycles in 0.1 M Na<sub>2</sub>SO<sub>4</sub> aqueous solution [20].....61

<b>Figure 2–20</b> XRD patterns of the ball–milled $Mn_3O_4$ at different cycling stages. Cycle numbers are indicated in the figure [20].	61
<b>Figure 2–21</b> Bode diagram of $Ni(OH)_2$ and $NiOOH$ [183].	63
<b>Figure 2–22</b> Plot of frequency shift versus atomic number of alkali metal for $\alpha$ - $Ni(OH)_2$ film [191].	66
<b>Figure 2–23</b> $E/i$ and $E/\Delta m$ potentiodynamic profiles recorded with $\alpha$ - $Ni(OH)_2$ film in 1M KOH (left) and LiOH (right) solution, $v= 0.01\text{ V s}^{-1}$ [192].	67
<b>Figure 2–24</b> Calculated topotactic voltage curve of $\gamma$ - $NiOOH$ within the generalised gradient approximation (GGA) approximation [188].	68
<b>Figure 3–1</b> Schematic diagram of $Mn_3O_4$ synthetic process.	73
<b>Figure 3–2</b> (a) Cyclic voltammetric sweep and (b) the corresponding ideal capacitive performance.	77
<b>Figure 3–3</b> (a) Constant current charge–discharge function and (b) the corresponding ideal capacitive performance.	78
<b>Figure 3–4</b> Scheme for electrochemical impedance spectroscopy.	80
<b>Figure 3–5</b> The equivalent–circuit models used for (a) EDLCs, (b) pseudocapacitors and (c) $RGO//MnO_x$ (or $RGO//RuO_2$ ) asymmetric ECs.	82
<b>Figure 3–6</b> Schematic diagram of electrochemical quartz crystal microbalance apparatus.	84

**Figure 3–7** (a) schematic diagram of *in situ* electrochemical Raman instrument and

(b) the configuration of *in situ* Raman cell. ....88

**Figure 3–8** CV of MnO<sub>x</sub> measured at a sweep rate of 25 mV s<sup>-1</sup> in 0.5M Na<sub>2</sub>SO<sub>4</sub>

against Ag/AgCl (blue) and quasi–reference electrode (red). The dash curve is measured against quasi–reference electrode after shifting by +0.1 V. ....90

**Figure 4–1** (a) Cyclic voltammograms of AC (in three–electrode mode) measured at

25 mV s<sup>-1</sup> in 0.5 M Na<sub>2</sub>SO<sub>4</sub> and (b) available working potential window for E<sub>OCP</sub> of the electrode material at the middle and one–third points (located at P) of the potential window under equal mass loading of positive and negative electrodes and

(c) mass ratio (positive/negative) dependence of cell voltage and specific retention for E<sub>OCP</sub> at middle (circle) and one–third points (triangular) cases. Inset in (a) shows corresponding E<sub>OCP</sub> of AC. ....95

**Figure 4–2** (a,b) Cyclic voltammograms of charge–balanced cell A at 25 mV s<sup>-1</sup> and

(c) constant–current charge–discharge curves of charge–balanced cell A at 2 A g<sup>-1</sup> with different cell voltages for (a,1) negative and (a,2) correspondingly charge–balanced positive electrode and (b,c) the activated carbon symmetric EC with cell voltage of (1) 1.4, (2) 1.6, (3) 1.8, (4) 2.0, (5) 2.2, (6) 2.5 V in 0.5 M Na<sub>2</sub>SO<sub>4</sub>. ....99

**Figure 4–3** (a,1) columbic efficiency (CE) and (a,2) energy efficiency (EE) of

charge–balanced cell A measured at 2 A g<sup>-1</sup> with different cell voltages and (1)

columbic efficiency (CE) and (2) energy efficiency (EE) of charge–balanced cell A measured at (b) 2.0 and (c) 2.5 V with different current density in 0.5 M Na <sub>2</sub> SO <sub>4</sub> . .....	100
<b>Figure 4–4</b> constant–current charge–discharge curves of cell A measured at (a) 2.0, (b) 2.2 and (c) 2.5 V. Charge–discharge curves of (1) a full cell and the corresponding (2) positive and (3) negative electrode.....	102
<b>Figure 4–5</b> (a) EIS spectra and (b) frequency dependence of specific capacitance for charge–balanced cell A at 25 °C in 0.5 M Na <sub>2</sub> SO <sub>4</sub> at different cell voltages. Inset in (a) shows the corresponding equivalent circuit model, inset in (b) enlarges the lower frequency region. Bode plots measured by EIS and LCR at (c) 2.0 and (d) 2.2 V.....	104
<b>Figure 4–6</b> Cell capacitance retention (dash) and energy efficiency retention (solid line) measured at 2.0 (diamond) and 2.2 V (circle) of charge–balanced cell A. Inset shows the constant–current charge–discharge curves of (1) the first and (2) the 600 <sup>th</sup> cycle at 2.0 V and (3) the first and (4) the 600 <sup>th</sup> cycle at 2.2 V.....	108
<b>Figure 4–7</b> (a,b) Cyclic voltammograms of cell B at 25 mV s <sup>-1</sup> and (c) constant–current charge–discharge curves at 2 A g <sup>-1</sup> with different cell voltages for (a,1) negative and (a,2) corresponding positive electrode of cell B with cell voltage of (1) 1.0, (2) 1.2, (3) 1.4, (4) 1.6, (5) 1.7 V in 0.5 M Na <sub>2</sub> SO <sub>4</sub> .....	110

<b>Figure 4–8</b> (1) columbic efficiency (CE) and (2) energy efficiency (EE) measured at (a) 2 A g <sup>-1</sup> with different cell voltages and at (b) 1.4 and (c) 1.6 V with different current density of cell B in 0.5 M Na <sub>2</sub> SO <sub>4</sub> .....	111
<b>Figure 4–9</b> Constant–current charge–discharge curves of cell B measured at (a) 1.4 and (b) 1.6 V. Charge–discharge curves of (1) a full cell and the corresponding (2) positive and (3) negative electrode. ....	112
<b>Figure 4–10</b> (a) EIS spectra and (b) frequency dependence of specific capacitance for cell B at 25 °C in 0.5 M Na <sub>2</sub> SO <sub>4</sub> at different cell voltages. Insets in (b) enlarge the lower frequency region. ....	113
<b>Figure 4–11</b> (a,b) Cyclic voltammograms of cell C at 25 mV s <sup>-1</sup> and (c) constant–current charge–discharge curves at 2 A g <sup>-1</sup> with different cell voltages for (a,1) negative and (a,2) corresponding positive electrode of cell C with cell voltage of (1) 1.0, (2) 1.2, (3) 1.4, (4) 1.6, (5) 1.7 V in 0.5 M Na <sub>2</sub> SO <sub>4</sub> .....	114
<b>Figure 4–12</b> (1) columbic efficiency (CE) and (2) energy efficiency (EE) measured at (a) 2 A g <sup>-1</sup> with different cell voltages and at (b) 1.2 and (c) 1.6 V with different current density of cell C in 0.5 M Na <sub>2</sub> SO <sub>4</sub> .....	116
<b>Figure 4–13</b> Constant–current charge–discharge curves of cell C measured at (a) 1.2 and (b) 1.6 V. Charge–discharge curves of (1) a full cell and the corresponding (2) positive and (3) negative electrode. ....	116



**Figure 4–14** (a) EIS spectra and (b) frequency dependence of specific capacitance for cell C at 25 °C in 0.5 M Na<sub>2</sub>SO<sub>4</sub> at different cell voltages. Insets in (b) enlarge the lower frequency region. .... 117

**Figure 4–15** Cell capacitance retention (dash) and energy efficiency retention (solid line) measured at (a) 1.6 V of cell B and (b) 1.4 V of cell C. Inset shows the 600–cycle potential stability at full–charge state of positive (blue) and negative (red) electrodes with the starting potential (black) for each cycle..... 120

**Figure 4–16** The specific energy and power of (1) charge–balanced cell A (circle), (2) cell B (star) and (3) cell C (triangular) based on the total mass of active material. The estimated specific energy and power of (4) cell A (dot) and (5) cells B and C on the basis of the device mass [2]. .... 122

**Figure 5–1** CVs measured under three–electrode mode at 25 mV s<sup>–1</sup> for (1) RGO and (2) activated MnO<sub>x</sub> in 0.5 M Na<sub>2</sub>SO<sub>4</sub>..... 126

**Figure 5–2** (a) CVs at 25 mV s<sup>–1</sup> and (b) constant–current charge–discharge curves at 3 A g<sup>–1</sup> of an asymmetric EC consisting of RGO and activated MnO<sub>x</sub>. .... 126

**Figure 5–3** (a) the cell voltage dependence of energy efficiency (EE) and current efficiency (CE) of RGO//MnO<sub>x</sub> at 3 A g<sup>–1</sup>. And the current density dependence of EE and CE with cell voltage of (b) 2.0, (c) 2.2 and (d) 2.4 V. .... 128



**Figure 5–4** Constant–current charge–discharge curves for an asymmetric EC (black) with the cell voltage of (a) 1.0, (b) 1.5, (c) 2.0, (d) 2.2, (e) 2.4 V and the corresponding charge–discharge curves of individual activated MnO<sub>x</sub> (blue) and RGO (red) electrodes. .... 129

**Figure 5–5** EIS spectra measured at 25 °C in 0.5 M Na<sub>2</sub>SO<sub>4</sub> for individual (a) RGO at –0.1 V, (b) activated MnO<sub>x</sub> at 0.2 V. Insets in (a) and (b) show the corresponding equivalent circuits and fitted values of elements. .... 131

**Figure 5–6** (a) EIS spectra measured at 25 °C in 0.5 M Na<sub>2</sub>SO<sub>4</sub> with RGO//MnO<sub>x</sub> at (1) 1.0, (2) 1.5, (3) 2.0, (4) 2.2 and (5) 2.4 V. (b) the corresponding full–cell equivalent circuit. Insets in (a) shows the enlarged high frequency region. .... 133

**Figure 5–7** The specific energy and power of asymmetric supercapacitor consisting of RGO and activated MnO<sub>x</sub> operating at 2.0 V. .... 134

**Figure 5–8** The constant–current charge–discharge curves with the cell voltage equal to (a,1) 1.2, (a,2) 1.8, (a,3) 2.2 V and (b) 2.3 V for a RGO//RuO<sub>2</sub> asymmetric EC. .... 135

**Figure 5–9** EIS spectra measured at 25 °C in the frequency range between 0.1 and 100 kHz in 0.5 M Na<sub>2</sub>SO<sub>4</sub> for a RGO//RuO<sub>2</sub> asymmetric EC at (1) 1.2, (2) 1.8, (3) 2.2, (4) 2.3V. .... 136

<b>Figure 6–1</b> (a) X–ray diffraction pattern, (b) SAED pattern and (c,d) TEM images of as–prepared MnO <sub>x</sub> .	140
<b>Figure 6–2</b> XPS (a) Mn 3s and (b) O 1s spectra of as–prepared MnO <sub>x</sub> .	143
<b>Figure 6–3</b> Lorentz fitting of <i>ex situ</i> Raman spectrum of as–prepared MnO <sub>x</sub> . Green line = envelope of total of the fitted peaks.	144
<b>Figure 6–4</b> CVs measured at a sweep rate of 25 mV s <sup>-1</sup> between 0 and 1.2 V (vs. Ag/AgCl) in 0.5 M Na <sub>2</sub> SO <sub>4</sub> for 5, 10, 50, 100, 150, 200 and 500 cycles.	146
<b>Figure 6–5</b> <i>In situ</i> Raman spectra series of (a) the 1 <sup>st</sup> and (b) the 2 <sup>nd</sup> cycle. Each cycle started from 0.1 V (PS 0.1V) and ended at –0.1 V (NS –0.1V).	146
<b>Figure 6–6</b> Lorentz fitting of <i>in situ</i> Raman spectra (a) 1st cycle PS 0.1V, (b) 1st cycle PS 0.5V, (c) 1st cycle PS 0.9V and (d) 2nd cycle PS 0.1V. Green line = envelope of total of the fitted peaks.	150
<b>Figure 6–7</b> Cycle number dependence of specific capacitance calculated by CV at 25 mV s <sup>-1</sup> and intensity ratio (I <sub>MnO<sub>2</sub></sub> of 575 cm <sup>-1</sup> /I <sub>Mn<sub>3</sub>O<sub>4</sub></sub> of 658 cm <sup>-1</sup> ) of MnO <sub>x</sub> .	152
<b>Figure 6–8</b> Lorentz fitting of <i>ex situ</i> Raman spectra recorded after (a) 5 <sup>th</sup> , (b) 10 <sup>th</sup> , (c) 50 <sup>th</sup> , (d) 100 <sup>th</sup> , (e) 150 <sup>th</sup> , (f) 200 <sup>th</sup> and (g) 500 <sup>th</sup> CV cycle. Green line = envelope of total of the fitted peaks.	153
<b>Figure 6–9</b> SEM images of (a) as–prepared MnO <sub>x</sub> and after (b) 100 (c,d) after 500 CV cycles in 0.5 M Na <sub>2</sub> SO <sub>4</sub> .	154

<b>Figure 6–10</b> (a) PXRD (MoK $\alpha$ 1 source), (b) SAED pattern and (c,d) TEM images of activated MnO $_x$ . JCPDS CARD 18–0802 is standard birnessite MnO $_2$ from database.....	158
<b>Figure 6–11</b> XPS (a) Mn 3s, (b) O 1s spectra of activated MnO $_x$ . .....	158
<b>Figure 6–12</b> Mn K–edge XAS spectra of as–prepared MnO $_x$ , after 100 and 500 CV cycles in 0.5 M Na $_2$ SO $_4$ . .....	159
<b>Figure 6–13</b> XPS Na 1s of (blue) as–prepared, (red) activated MnO $_x$ and (black) Na $_{0.33}$ MnO $_2$ sample. The denoted values are the fitted peak position (eV) and Full Width at Half Maximum (FWHM, eV in parenthesis) .....	160
<b>Figure 6–14</b> Schematic diagrams of (a) activation process of as–prepared MnO $_x$ under potential cycling and (b) the proposed charge storage mechanism of activated MnO $_x$ .....	162
<b>Figure 7–1</b> CV curves of $\alpha$ -Ni(OH) $_2$ deposited on EQCM gold electrodes at 5 mV s $^{-1}$ in 1M (1) LiOH, (2) NaOH, (3) KOH, (4) CsOH, and (5) NH $_4$ OH. ....	167
<b>Figure 7–2</b> mass change profiles of Ni(OH) $_2$ deposited on EQCM gold electrodes at 5mV s $^{-1}$ in 1 M (1) LiOH, (2) NaOH (3) KOH (4) CsOH and (5) NH $_4$ OH. ....	171
<b>Figure 7–3</b> (a–d) CV curves and (e–h) mass change curves of Ni(OH) $_2$ deposited on EQCM gold electrodes in 1 M (a, e) LiOH, (b, f) NaOH (c, g) KOH and (d, h)	

CsOH for 10 cycles at 10 mV s <sup>-1</sup> after 10 proceeding cycles in the same potential window at 5 mV s <sup>-1</sup> . .....	173
<b>Figure 7–4</b> Massograms of Ni(OH) <sub>2</sub> on EQCM gold electrodes in 1 M (a) LiOH, (b) NaOH, (c) KOH and (d) CsOH for 10 cycles at 10 mV s <sup>-1</sup> after 10 proceeding cycles in the same potential window at 5 mV s <sup>-1</sup> . .....	175
<b>Figure 7–5</b> Raman spectra at (a) 300–600 and (b) 3400–3800 cm <sup>-1</sup> of as–prepared α-Ni(OH) <sub>2</sub> on Ni electrode surface recorded in 1M LiOH. ....	178
<b>Figure 7–6</b> Raman spectra of bare gold electrode surface in 1M LiOH. ....	179
<b>Figure 7–7</b> <i>In situ</i> Raman spectra of Ni(OH) <sub>2</sub> recorded after (a) 10, (b) 30, (c) 150, and (d) 200 CV cycles at 10 mV s <sup>-1</sup> in 1 M LiOH, NaOH, KOH and CsOH. ....	180
<b>Figure 7–8</b> CV curves of Ni(OH) <sub>2</sub> deposited on gold electrodes measured at 10 mV s <sup>-1</sup> in 1M (a) LiOH, (b) NaOH, (c) KOH, (d) CsOH.....	181
<b>Figure 7–9</b> The corresponding <i>in situ</i> Raman spectra recorded after specific CV cycles at 10 mV s <sup>-1</sup> in 1M (a) LiOH, (b) NaOH, (c) KOH and (d) CsOH. ....	182
<b>Figure 7–10</b> The proposed new redox mechanism of nickel hydroxide.....	187
<b>Figure 8–1</b> CV curves of (a) Co <sub>3</sub> O <sub>4</sub> and (b) Co(OH) <sub>2</sub> in 1 M LiOH, NaOH and KOH. ....	192

## List of Tables

<b>Table 2–1</b> The reported crystal structures and Raman vibrational modes of $\text{MnO}_x$ in literature. ....	53
<b>Table 2–2</b> Reported material characterisation analyses on electrochemical activation from $\text{Mn}_3\text{O}_4$ to $\text{MnO}_2$ .....	59
<b>Table 4–1</b> Fitted values of all elements in the equivalent–circuit model shown in the inset of Figure 4–5a from the impedance spectra in Figure 4–5a for charge–balanced cell A.....	105
<b>Table 4–2</b> Fitted values of all elements in the equivalent–circuit model shown in the inset of Figure 5a from the impedance spectra in Figure 4–10a for cell B.....	113
<b>Table 4–3</b> Fitted values of all elements in the equivalent–circuit model shown in the inset of Figure 4–5a from the impedance spectra in Figure 4–14a for cell C.....	118
<b>Table 5–1</b> The potential limits (vs. Ag/AgCl) of RGO and activated $\text{MnO}_x$ .....	130
<b>Table 5–2</b> Values of the equivalent–circuit element model in Figure 2d from the fitted impedance data shown in Figure 2c.....	133
<b>Table 5–3</b> Values of the equivalent–circuit element model in Figure 5–6b for a RGO// $\text{RuO}_2$ asymmetric EC. ....	136
<b>Table 6–1</b> Comparisons of diffraction peaks and d–spacing calculated from the SAED pattern of as–prepared and activated $\text{MnO}_x$ with standards (hausmannite	

Mn <sub>3</sub> O <sub>4</sub> , JCPDS CARD 24–0734 and birnessite MnO <sub>2</sub> , JCPDS CARD 18–0802)	
from database.....	141
<b>Table 6–2</b> Peak position and area percentage of O 1s spectrum of as–prepared and activated MnO <sub>x</sub> .....	143
<b>Table 6–3</b> Peak position (cm <sup>-1</sup> ) and Full Width at Half Maximum (FWHM, cm <sup>-1</sup> in parenthesis) of the Mn <sub>3</sub> O <sub>4</sub> and MnO <sub>2</sub> peaks by Lorentz fitting.....	148
<b>Table 6–4</b> Peak position (cm <sup>-1</sup> ) and Full Width at Half Maximum (FWHM, cm <sup>-1</sup> in parenthesis) of the Mn <sub>3</sub> O <sub>4</sub> and MnO <sub>2</sub> peaks by Lorentz fitting of <i>ex situ</i> Raman spectra.....	148
<b>Table 6–5</b> Normalised area (by atomic sensitivity factor) and area ratio calculated from XPS spectra.....	155
<b>Table 6–6</b> Capacitive performance of electrochemically activated MnO <sub>x</sub> .....	163
<b>Table 7–1</b> Base dissociation constant (K <sub>b</sub> ), the onset potentials of hydrogen evolution on a Pt electrode (E <sub>HER</sub> ) and the potential difference of γ–NiOOH/α–Ni(OH) <sub>2</sub> (ΔE) in 1 M CsOH, KOH, NaOH, LiOH and NH <sub>4</sub> OH.....	168

# Chapter 1

## Introduction and Objective

As addressed by the United Nations, 'energy' is one of the top 10 issues that need to be dealt with in the 21<sup>st</sup> century. Studies on improving energy storage and efficiency in 'electrochemical energy storage and conversion' devices are becoming urgently important. Electrochemical capacitors (ECs), also known as supercapacitors or ultracapacitors, show a wide range of specific energy and power in the Ragone plot for energy storage (shown in Figure 1-1) [1-4]. In comparison with other electrochemical energy storage devices, such as rechargeable batteries and fuel cells, ECs exhibit relatively lower specific energy. However, ECs have been widely investigated for decades in many aspects of applications due to the rapid charge-discharge rates and excellent cyclic stability characteristics. As such ECs have found application within hybrid electric vehicles, starting assistance of fuel cells, energy management/conservation applications, day-night storage, power sources of electronics/tools and power sources of public transportation [3-6]. ECs, especially for aqueous ECs, also possess features of lower cost, better safety, more environmentally friendly and easy to manufacture, which is advantageous in comparison with other energy storage devices [7].

According to the charge storage mechanism, ECs can be categorised into three types. First, the electric double-layer capacitors (EDLCs) utilise the arrangement of ions/polar molecules for charge storage at the electrode/electrolyte interfaces under an electric field [3, 4]. In principle, the electrostatic double-layer charge-discharge process is infinitely reversible [4, 8]. Second, the pseudocapacitance comes from the electrochemical faradaic redox reactions of electroactive species at the electrode/electrolyte interfaces or within the bulk active materials [8, 9].



Pseudocapacitors utilise fast faradaic redox reactions of electroactive material, leading to good electrochemical reversibility. Third, in order to increase cell voltage of ECs, asymmetric type ECs consisting of two different electroactive materials with complementary working potential windows are designed to promote the specific energy and power in comparison with symmetric supercapacitors [10–14]. Due to the large reserved capacity of pseudocapacitive material and the high power characteristics of double-layer material, electroactive material hybridisation of the above devices is also investigated to reach high specific energy/power, low cost and long life-time benefits [15].

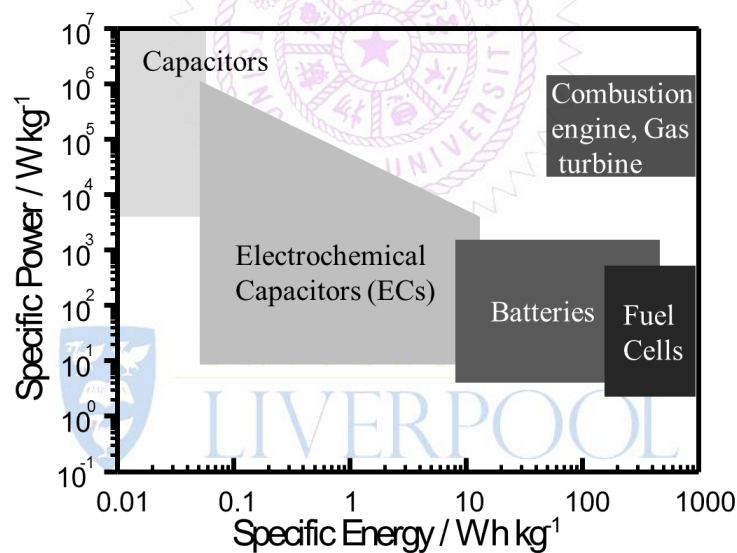


**Figure 1–1** The Ragone plot for various electrochemical energy storage devices.

According to the equation for estimating the specific energy of ECs,

$$E = \frac{1}{2} C_s V^2 \quad \text{Eq 1-1}$$

there are two ways to promote energy storage of ECs, i.e., increase the specific capacitance ( $C_s$ ) and enlarge the cell voltage ( $V$ ) of ECs. Due to the square term of cell voltage, enlarging the cell voltage is an effective way to improve energy storage of ECs. Although organic electrolytes have been widely investigated with the



decomposition potential windows varying from 3 to 5 V, organic electrolytes generally show the shortcomings such as high equivalent series resistance (ESR), high costs in both materials and production, flammable and environmentally unfriendly properties and the safety issue [3, 16]. On the other hand, the cell voltage is limited by the potential window of water decomposition (i.e., 1.229 V at 25 °C) for aqueous ECs. Accordingly, how to increase energy storage without compromising power capability of ECs is still a big challenge in developing advanced ECs.

From an engineering viewpoint, it is important to optimise cell voltage (and hence improve energy storage) of ECs by tuning the cell parameters without changing electroactive materials and electrolytes. Therefore, the first part of this thesis discusses how to optimise the cell voltage of symmetric (Chapter 4) and asymmetric ECs (Chapter 5) through comparisons of cyclic voltammogram (CV), charge–discharge curves and electrochemical impedance spectroscopy (EIS).

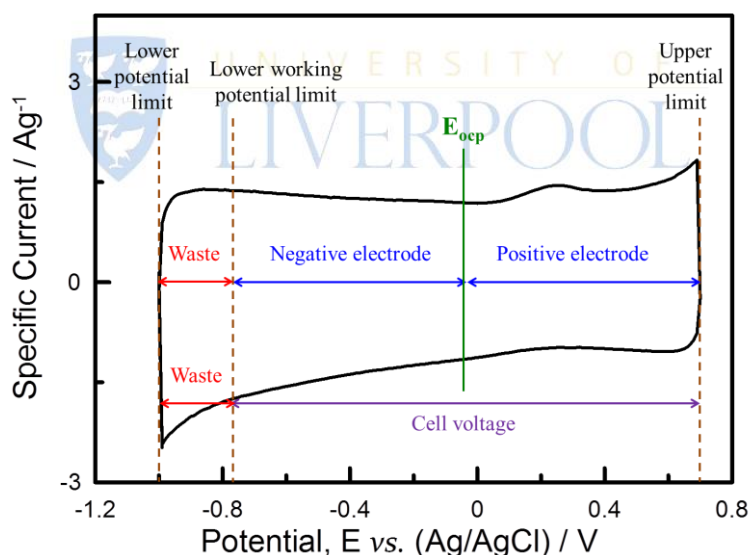


**Figure 1–2** The open–circuit potential ( $E_{ocp}$ ) effect on the utilisation of electrochemically stable potential window of electroactive material under equal mass loading of positive and negative electrodes.

In Chapter 4, EDLCs consisting of two activated carbon electrodes in neutral aqueous medium (i.e., 0.5 M Na<sub>2</sub>SO<sub>4</sub>) were employed as the model system for identifying key parameters (such as open-circuit potential and charges stored in the working potential window on positive and negative electrodes), which could affect the operating cell voltage and the energy stored in aqueous EDLCs. Besides, the necessity of charge-balance (but not capacitance-balance) for positive and negative electrodes is substantiated from the lower acceptable cell voltage of charge-unbalanced EDLCs.

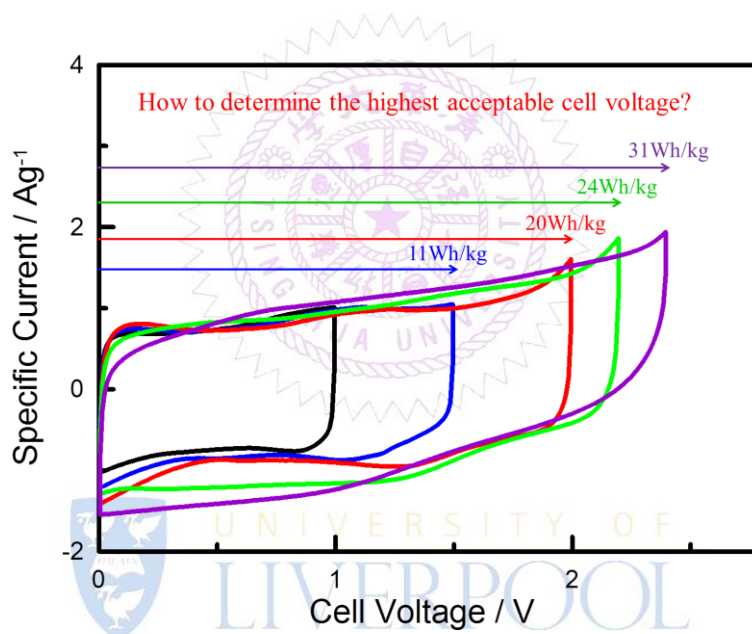


**Figure 1-3** The operating cell voltage effect on the specific energy of RGO//MnO<sub>x</sub> asymmetric ECs.

Chapter 5 demonstrates another approach to enlarge the cell voltage of aqueous ECs by using asymmetric design, by which reduce graphene oxide (RGO) with high hydrogen-evolving overpotential and manganese oxide (MnO<sub>x</sub>) with high oxygen-evolving overpotential were used as electroactive materials of the negative and positive electrodes, respectively. RGO//MnO<sub>x</sub> asymmetric EC was used to establish criteria for determining the highest acceptable cell voltage of asymmetric ECs with excellent reversibility and capacitor-like behaviour. It is very useful to evaluate the

practical specific energy of asymmetric ECs by understanding the highest acceptable cell voltage. Besides, the criteria were also found to be applicable to the RGO//RuO<sub>2</sub> asymmetric EC, indicating the reliability of the criteria.

From a scientific viewpoint, it is necessary to fully understand the charge storage mechanism of transition metal oxides and hydroxides in order to further improve their electrochemical performance in various electrochemical applications. Therefore, the second part of this thesis probes the charge storage mechanism of electrochemically activated MnO<sub>x</sub> (Chapter 6) and nickel hydroxide (Ni(OH)<sub>2</sub>, Chapter 7) in aqueous ECs.

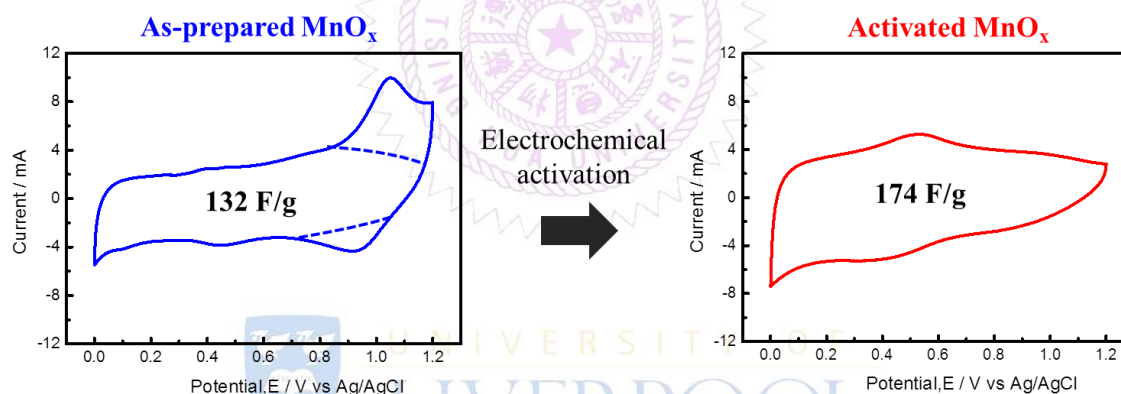


**Figure 1-4** The electrochemical activation of MnO<sub>x</sub> in neutral Na<sub>2</sub>SO<sub>4</sub> aqueous electrolyte. Dash lines indicate the current responses obtained from the CV curve of activated MnO<sub>x</sub> in order to avoid taking the oxidative current responses of Mn<sub>3</sub>O<sub>4</sub> into account.

MnO<sub>x</sub> can undergo an electrochemical activation step that leads to greater capacitances [17–23], of which the structural change and mechanism remains poorly understood. Our previous work [24] demonstrated that the one-pot synthesised manganese oxide (‘Mn<sub>3</sub>O<sub>4</sub>’) is a practical and scalable process. This material needs approximately 100 potential cycles to activate to ‘MnO<sub>2</sub>’. However, the charge storage mechanism remains poorly understood. Thus, in Chapter 6, we used advanced

material characterisation techniques, such as *in operando* monitoring of the structural evolution during the activation process via *in situ* Raman microscopy, accompanied with other material characterisation techniques (such as powder X-ray diffraction, X-ray photoelectron spectroscopy, scanning electron microscopy, transmission electron microscopy) to explain both the activation process and the charge storage mechanism of electrochemically activated  $\text{MnO}_x$  composites.

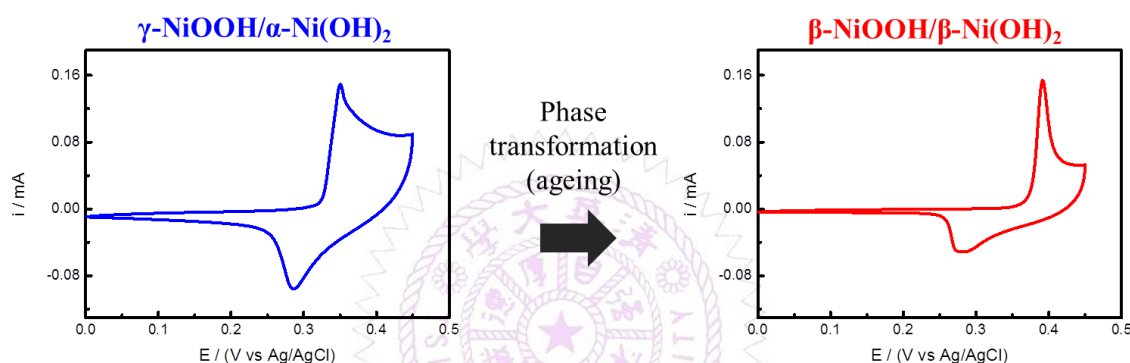


**Figure 1-5** Phase transformation (ageing) from  $\gamma\text{-NiOOH}/\alpha\text{-Ni(OH)}_2$  to  $\beta\text{-NiOOH}/\beta\text{-Ni(OH)}_2$  in repeated CV cycling in KOH medium.

On the other hand, nickel hydroxide has been widely applied in electrochemical energy storage and conversion devices [25–30]. Our previous study [31] demonstrated the importance of cation species on cycling retention of  $\gamma\text{-NiOOH}/\alpha\text{-Ni(OH)}_2$  in various electrolytes. While most of the published works focused on the relationship between the composition or microstructure of synthesised  $\text{Ni(OH)}_2$  and the performance retention, only a few studies probed the ageing process of  $\alpha\text{-Ni(OH)}_2$  into  $\beta\text{-Ni(OH)}_2$ . Accordingly, the effects of alkali metal cation species (LiOH, NaOH, KOH and CsOH) on the phase transformation is investigated by means of EQCM and *in situ* Raman microscopy in Chapter 7. Moreover, the computational simulation (DFT+U) based on EQCM results gives a better idea on the compositional changes in the first few potential cycles.

# Chapter 2

## Literature Review

### 2.1 Aqueous Electric Double-Layer Capacitors (EDLCs)

Electric double-layer capacitors (EDLCs) utilise the arrangement of ions/polar molecules for charge storage in an electric double-layer (Helmholtz layer), in which positive/negative ions accumulate at the surface of negative/positive electrodes and compensate the electronic charge at the electrode surface under an electric field [3, 4, 32]. Generally, the thickness of the double-layer is in the order of 5–10 Å, depending on the concentration of the electrolyte and on the size of the ions [3]. According to equation Eq 2-1,

$$\frac{C}{A} = \frac{\epsilon_0 \epsilon_r}{d} \quad \text{Eq 2-1}$$

$\epsilon_0$  is vacuum permittivity ( $8.85 \times 10^{-12}$  F m<sup>-1</sup>) and  $\epsilon_r$  is relative permittivity.  $d$  represents the double-layer thickness with surface area  $A$ . Accordingly, the double layer capacitance is about 10–20  $\mu\text{F cm}^{-2}$  for a smooth electrode in concentrated electrolyte solution [3]. Assuming the surface area of carbon material is 1000 m<sup>2</sup> g<sup>-1</sup> with double-layer capacitance of 10  $\mu\text{F cm}^{-2}$ , it leads to 100 F g<sup>-1</sup> for a single electrode. In order to improve double-layer capacitance, extremely high surface area carbon materials are usually applied in EDLCs. Besides, the pore size and structure of carbon materials can be controllable by different synthetic routes.

Carbon materials used in EDLCs can be generally categorised as sp<sup>2</sup>-bonded carbon and disordered/porous carbon. The former includes 2D graphene-based material and 1D carbon nanotubes (CNT), which possess good electrical conductivity. The latter includes activated carbon, templated carbon, carbon aerogels and carbide derived carbon, which generally possess relatively lower electrical conductivity

comparing with  $sp^2$ -bonded carbon. Nevertheless, it is advantageous that disordered/porous carbon has 3D hierarchical structure with high porosity (high specific surface area).

Reduced graphene oxide (RGO) is normally achieved from reduction of graphene oxide (GO), which can be prepared from graphite precursor via modified Hummer's method. Various reduction processes have reported to effectively reduce GO, such as chemical reduction (hydrazine [33], sodium borohydride [34], vitamin C [35] etc.), thermal annealing [36] and microwave-assisted hydrothermal method [37]. Stoller *et al.* [38] suggested RGO with high electrical conductivity ( $\sim 2 \times 10^2 \text{ S m}^{-1}$ ) can be possibly designed to increase the electrode thickness without using conductive fillers (such as carbon black with lower surface area). Increasing the electrode thickness and eliminating additives leads to an improved electrode material to current collector/separator ratio, resulting in the improvement of the energy stored in graphene-based ECs. Typically, the graphene-based ECs (full cell) give  $130\text{--}200 \text{ F g}^{-1}$  in concentrated KOH aqueous electrolyte [38, 39]. Besides, the ultra-high-power performance of graphene-based ECs has been reported as the RC time-constants less than  $200 \mu\text{s}$  by Miller *et al.* [40], indicating the key to ultra-high-power performance is vertically oriented graphene nanosheets grown directly on metal current collectors. This design not only minimises both electronic and ionic resistance but also effectively utilises the preponderance of exposed edge planes of graphene nanosheets. However, the graphene-based materials suffer from restacking of graphene layers, which significantly reduces the realistic specific surface area ( $320\text{--}700 \text{ m}^2 \text{ g}^{-1}$ ) from the theoretical surface area of a single layer graphene ( $2630 \text{ m}^2 \text{ g}^{-1}$ ) [38, 39]. Although the restacking of graphene during electrode preparation is inevitably serious, the concept of inserting spacer between graphene layers has been proposed as an effective way to prevent graphene layers aggregating. For example, Yang *et al.* [41]



successfully introduced 1D multiwall CNT into graphene layers, which CNT can act as pillars to effectively separate graphene layers, leading to an excellent capacitive performance (i.e., 330 F g<sup>-1</sup> in 0.5M H<sub>2</sub>SO<sub>4</sub>). On the other hand, Zhu *et al.* [42] demonstrated that chemical activation of exfoliated graphite oxide by KOH forms a continuous 3D network with sp<sup>2</sup>-bonded carbon, which possesses not only high electrical conductivity (~5×10<sup>2</sup> S m<sup>-1</sup>) but also high specific surface area (3100 m<sup>2</sup> g<sup>-1</sup>). However, the cost of sp<sup>2</sup>-bonded carbon is relatively high, which is one of the biggest concerns in a manufacturing point of view.

With regard to disordered/porous carbon materials, the most commonly used in commercial products is activated carbon. The activation processes can be categorised as physical (steam activation) and chemical activation. The former is primarily used for coconut shell and coal under high temperature (600–1200 °C) activation. H<sub>2</sub>, CO and CO<sub>2</sub> are generally the bi-products during steam activation [43]. The latter is typically applied for activating wood, which utilises activating agents with relatively low temperature (450–900 °C), such as acidic solvents (H<sub>3</sub>PO<sub>4</sub>, H<sub>2</sub>SO<sub>4</sub>, HCl, HNO<sub>3</sub> etc.), basic solvents (KOH, NaOH etc.) and chloride salts (CaCl<sub>2</sub>, ZnCl<sub>2</sub> etc.). This process generally gives an even higher internal surface area comparing with steam activation. Also, it is sometimes preferred because it requires less heat and time. Fic *et al.* [44] reported the specific capacitance of activated carbon in Li<sub>2</sub>SO<sub>4</sub> is 150 F g<sup>-1</sup> at 10 mV s<sup>-1</sup> without significant capacitance fade after 15,000 cycles. Most importantly, the use of neutral aqueous electrolyte is cheap, non-corrosive and applicable to use diverse current collectors. Wu *et al.* [45] demonstrated the steam activated carbon can perform in various aqueous electrolytes (NaNO<sub>3</sub>, HNO<sub>3</sub> and H<sub>2</sub>SO<sub>4</sub>). After tuning the pore structure by activation time, the specific capacitance can reach 120–140 F g<sup>-1</sup> at 25 mV s<sup>-1</sup> in aqueous electrolytes. Generally, the pore size of activated carbon can be tuned by carbon precursor and activation method. And the porosity of activated

carbon can be controllable by the parameters of the activation process such as temperature, time and activating agent [46]. The resultant product ('activated' carbon) has an incredibly high specific surface area and adapted pore structure, which are crucial for EDLCs performance. Hence, activated carbons are still the most often used electrode material [3, 8, 46, 47].

Lee *et al.* [48] had a detail review on templated porous carbon materials. Templated porous carbon materials usually possess 3D hierarchical network and ordered pore structure, which the pore size can be tuned to be mesoporous and macroporous. Silica materials such as MCM-48, HMS, SBA-15, MCF and MSU-X are commonly used as templates to synthesise hierarchically ordered mesoporous carbons with various pore structures. The ordered mesoporous carbons can be synthesised to have graphitic ( $sp^2$ -bonded) pore walls by annealing soft-carbon sources at high temperature. Ordered macroporous carbon materials can be synthesised using colloidal crystals as templates. Jurewicz *et al.* [49] reported highly ordered mesoporous carbon materials with interconnected mesopores and secondary micropores can be obtained by using MCM-48 or SBA-15 as template, which demonstrate up to  $140\text{--}170\text{ F g}^{-1}$  at  $10\text{ mV s}^{-1}$  in  $1\text{ M H}_2\text{SO}_4$  and  $150\text{--}160\text{ F g}^{-1}$  at  $10\text{ mV s}^{-1}$  in  $6\text{ M KOH}$ . Fuertes *et al.* [50] used SBA-16 as template to synthesis mesoporous carbon materials with mainly 3 and 8 nm pores. The specific capacitance is about  $130\text{--}200\text{ F g}^{-1}$  at  $10\text{ mV s}^{-1}$  in  $1\text{ M H}_2\text{SO}_4$ , while it varies significantly about  $50\text{--}200\text{ F g}^{-1}$  at the same scan rate in  $6\text{ M KOH}$ . Although the templated carbons possess 3D hierarchically ordered porous structure, the high cost of template carbons are perfect for fundamental research but cannot practically replace activated carbons in commercial products [50].

Carbon aerogels usually have high porosity (80–98%), controllable pore structure and high surface area. Li *et al.* [51] reported carbon aerogels synthesised



from resorcinol and formaldehyde via a classical RF synthesis route demonstrate ca. 70 F/g at 10 mV s<sup>-1</sup> in 6M KOH. Li *et al.* [52] also reported a modified RF route by adding cresol to partially replace resorcinol during the synthetic process. After tuning cresol and resorcinol ratio, the surface area can reach 400–700 m<sup>2</sup> g<sup>-1</sup> with specific capacitance of ca. 100 F g<sup>-1</sup> at 5 mV s<sup>-1</sup> in 1M H<sub>2</sub>SO<sub>4</sub>.

Gogotsi *et al.* [53–55] reported carbide-derived carbon (CDC) possesses tunable pore structure at atomic level and a narrow pore-size distribution. Usually, CDC can be produced from metal carbide materials (such as SiC, TiC, Ti<sub>3</sub>SiC<sub>2</sub> etc.) via a chlorination process at a wide temperature range (200–1200 °C). CDC pore structure can be templated by the rigid metal carbide lattice with a 50 to 80% open pore volume. However, CDC can be reasonably presumed to be hydrophobic character due to the high temperature annealing in chlorine atmosphere. As a result, CDC is usually used in organic electrolytes (TEABF<sub>4</sub>/acetonitrile) and ionic liquids (BMI–PF<sub>6</sub>).

Aqueous carbon EDLCs can be generally considered to be low cost, environmental-friendly, high specific surface area, good electrical conductivity, high-rate capability and reliable cycle life. For the various forms of carbon materials, pore size distribution is one of the key factors that affect the capacitive performance of carbon EDLCs [46, 56]. The pore size has been proposed to fit the size of ions to optimise capacitive performance by avoiding over-screen effect in both of aqueous and non-aqueous media [46, 50, 55, 57]. It has been reported that micropores (ca. 0.7–0.9 nm) plays an essential role for hydrogen adsorption and charging the electric double-layer by solvated and non-solvated ions, which predominantly determines the capacitance of EDLCs. Mesopores (ca. 2–4 nm) interconnected with micropores is thought to facilitate ions propagation and adsorption on the carbon surface [46]. Macropores can act as reservoir to accommodate sufficient ions, which can significantly improve the high-rate capability of EDLCs. However, the increase of

mesopores and macropores volume leads to a lower density of carbon material, which further reduces volumetric energy of EDLCs. Therefore, well balanced micro, meso and macro porosity is crucial for a good capacitor operation.

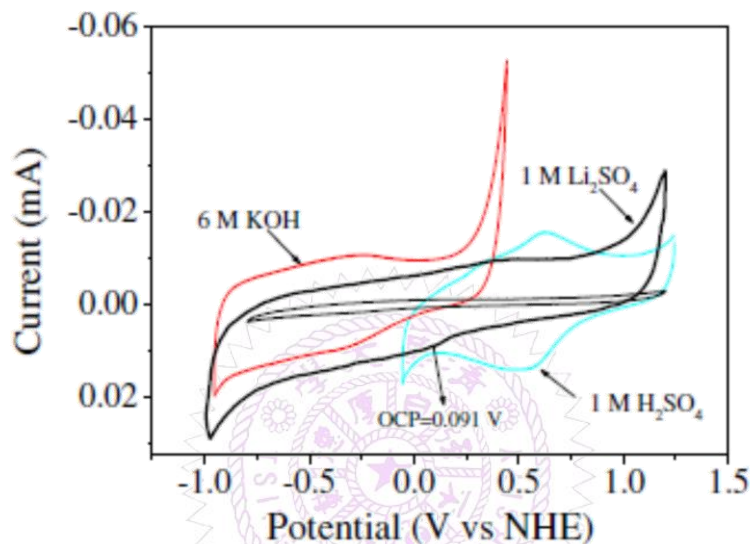


**Figure 2–1** CV curves showing the potential window of chemical converted graphene in 6 M KOH, 1 M H<sub>2</sub>SO<sub>4</sub> and 1 M Li<sub>2</sub>SO<sub>4</sub> (the CV of the blank substrate in 1 M Li<sub>2</sub>SO<sub>4</sub> is also listed) at the scan rate of 2 mV s<sup>-1</sup> [58].

As discussed in Chapter 1, the cell voltage of aqueous ECs might be limited by the decomposition potential window of solvent and the potential window of water decomposition (1.229 V at 25 °C). According to Nernst equation, oxygen and hydrogen evolving reactions occur at 0.82 and -0.41 V (vs. NHE) at pH = 7, respectively. Therefore, it is crucial to choose appropriate aqueous electrolytes to allow electroactive materials to have high overpotential on oxygen and/or hydrogen evolving reactions without compromising capacitive performance. Most commonly used aqueous electrolytes for carbon EDLCs are concentrated H<sub>2</sub>SO<sub>4</sub> and KOH due to their high conductivity, accompanied by good charge propagation and power rates of EDLCs [44]. Neutral aqueous electrolytes, such as alkali metal sulphate, have been examined to have wide stable potential window of carbon materials (i.e., at least 1.6

V), compared with 1.25 and 1.2 V for acidic and basic electrolytes (shown in Figure 2–1), respectively, which can significantly improve the energy storage of aqueous carbon EDLCs [44, 58].

On the other hand, the presence of surface functional groups (heteroatoms) on carbon materials has also been substantiated to enhance the capacitance by the contribution of pseudocapacitance [32, 46, 47]. For aqueous ECs, the presence of surface groups in the carbon electrodes not only improves wettability of the electrodes but also contributes pseudocapacitance to the apparent capacitance of the electrodes. Those surface functional groups, generally nitrogenated or oxygenated functionalities incorporated into the carbon framework, might be electrochemically reactive to perform quick faradaic redox reactions in certain potential ranges [46, 59]. Because pseudocapacitance comes from electrochemically faradaic redox reactions, cyclability of pseudocapacitance would not be as good as pure electric double-layer. Therefore, the introduction of surface functional groups (pseudocapacitance) would somehow reduce the cycle life of EDLCs. It is necessary to have more studies on improving the capacitance without compromising cyclability.

## 2.2 Manganese Oxide Pseudocapacitors

For pseudocapacitors, electroactive materials are generally transition metal oxides (such as  $\text{RuO}_2$  [9, 60, 61],  $\text{MnO}_x$  [61–63],  $\text{Ni}(\text{OH})_2$  [30, 64, 65],  $\text{Co}(\text{OH})_2$  [28, 66, 67], Ni–Co oxides [68–70],  $\text{VO}_x$  [71–73] and  $\text{Fe}_3\text{O}_4$  [74–76]) and conducting polymers (such as polyaniline [77] and polypyrrole [78]). Among these materials, conducting polymers generally suffer from poor cyclability due to intrinsically low conductivity. Nickel and cobalt oxides/hydroxides do not have excellent electrochemical reversibility comparing with  $\text{RuO}_2$  and  $\text{MnO}_x$ . Furthermore, Nickel and cobalt oxides/ hydroxides demonstrate higher capacity in high concentration of alkali metal hydroxide solutions, which is corrosive to most of the current collectors. Crystalline  $\text{RuO}_2$  in the hydrous form has been widely recognised as the best electrode materials for pseudocapacitors because of its high specific capacitance, good electronic conductivity and cycle stability [9, 60, 61]. However,  $\text{RuO}_2$  is too expensive to have widespread commercial use.  $\text{MnO}_x$  in both amorphous and crystalline forms are one of promising candidates due to improving cycle life (at least 10,000 cycles [79–81]), acceptable specific capacitance at moderate scan rates for  $\text{MnO}_2$  thin films (100–400 F/g [62, 82–84]), environmentally friendly and low cost [61, 62, 85, 86].

Manganese is low cost, abundant (the twelfth most abundant element on the earth) and environmental–friendly material with various oxidation states. Manganese

oxides have been widely used in electrochemical energy storage field since it's firstly used in Leclanché cell in the 1866. The most familiar example is electrolytic manganese dioxide (EMD) applied in alkaline batteries. For supercapacitor application, Lee and Goodenough [62] firstly provoked the interest of  $\text{MnO}_x$  pseudocapacitors in 1999, which demonstrated the capacitive behaviour of amorphous manganese oxide in neutral aqueous media (LiCl, NaCl and KCl). The specific capacitance of  $\text{MnO}_2$  composite electrode (with 25% acetylene black and 5% PTFE binder) is ca.  $200 \text{ F g}^{-1}$  at  $5 \text{ mV s}^{-1}$ , which was firstly reported as a cost-effective capacitor-type material comparing with pricy hydrous  $\text{RuO}_2$  in concentrated  $\text{H}_2\text{SO}_4$ .

$\text{MnO}_x$  can exhibit extremely rectangular shape in cyclic voltammogram, which is similar to electric double-layer charge-discharge behaviour rather than a pair of sharp redox peak at a fixed potential for electrochemically faradaic reaction. The thickness of  $\text{MnO}_x$  electrode has been proposed as a crucial factor that significantly influences the electrochemical characteristics of  $\text{MnO}_x$  [87]. Zhang and Chen [85] indicate the mass loading (thickness, in another word) of  $\text{MnO}_x$  in supercapacitor electrodes is much less than that used in a bulk quantity in batteries, leading to a smaller charge storage capacity but a greater overall charge transfer rate to perform high-power delivery. For bulky  $\text{MnO}_x$  used in batteries, the redox active sites are well separated, non-interactive to each other and only support localised electron transfer from the electrode substrate to each of the redox active sites and *vice versa*, but no electron conduction between any neighbouring sites, which is analogue to the electron energy states in isolated molecules and insulators. The energy states of localised redox active sites are fairly closed to each other, indicating the potential for donating or accepting electrons is similar for all the active sites. Therefore, a fixed potential for electron transfer for  $\text{MnO}_x$  in batteries can be observed. On the other hand, the redox active sites in  $\text{MnO}_x$  supercapacitors are located within a thinner electrode surface layer,

which the redox active sites are interactive to form a broad energy states. This is analogue to semiconductors, in which continuous excitation of electrons from the valance band to the conduction band can occur under an appropriate range of electric field (overcome the band gap of semiconductors). This process produces delocalised electrons in conduction band and mobile holes in valence band, leading to continuous charge accumulation (i.e., capacitive current) during potential sweeping. This concept is also comparable with electron delocalisation in conjugated chemical bonds of conducting polymers resulting from the overlapping electron orbits between neighbouring atoms. Accordingly,  $\text{MnO}_x$  pseudocapacitors can exhibit ideal capacitive behaviour (rectangular CV shape and triangular charge–discharge profile) in electrochemically stable potential window with no more than tens of  $\text{mg cm}^{-2}$  or  $\mu\text{m}$  in thickness. However, this explanation of  $\text{MnO}_x$  pseudocapacitance from the viewpoint of band theory (Figure 2–2) is still debatable.

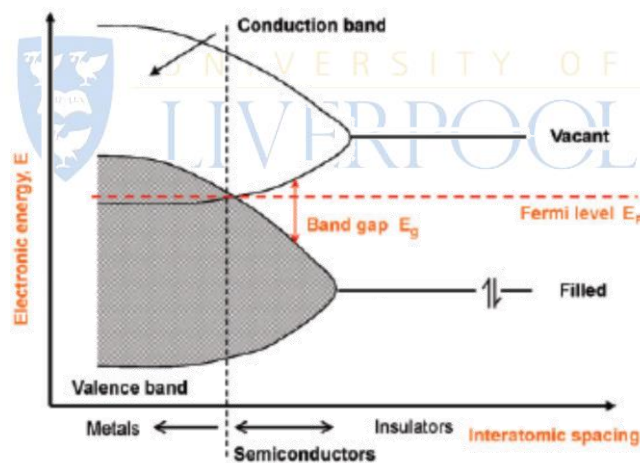
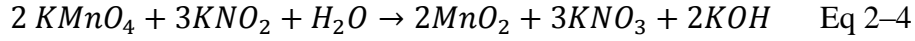
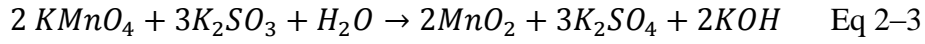
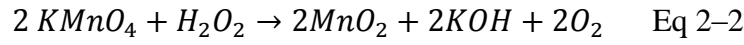


**Figure 2–2** Schematic illustration of band theory [85].

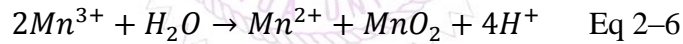
$\text{MnO}_x$  can be obtained via various chemical and electrochemical synthetic routes.  $\text{MnO}_x$  can be chemically synthesised by either reducing  $\text{Mn(VII)}$  or oxidising  $\text{Mn(II)}$ . An alternative way is mixing  $\text{Mn(VII)}$  with  $\text{Mn(II)}$  to form  $\text{Mn(IV)}$  with the molar ratio of 2 to 3. Narita and Okabe [88] reported hydrous  $\text{MnO}_2$  can be formed by



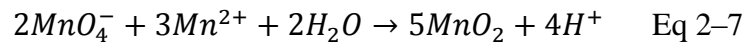
reduction of  $KMnO_4$  with various reducing agents ( $H_2O_2$ ,  $K_2SO_3$  and  $KNO_2$ ) in alkaline solutions.



The content of chemically bound water in the hydrous  $MnO_2$  decreases with a decrease in the pH of suspensions and predominant amorphous  $MnO_2$  can be formed at pH 8 or higher. Unuma *et al.* [89] reported the oxidation of manganese (II) chloride by  $NaBrO_3$  undergoes a two-step reaction, including the oxidation of  $Mn^{2+}$  to  $Mn^{3+}$  and disproportionation of  $Mn^{3+}$  to  $Mn^{2+}$  and  $MnO_2$ , leading to the formation of  $\gamma$ - $MnO_2$ .



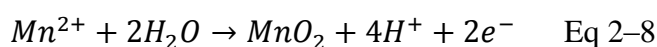
Ternary  $MnO_x$  composite (i.e.,  $Mn_3O_4$ ,  $\beta$ - $MnOOH$  and  $\gamma$ - $MnOOH$ ) can be formed by adding appropriate amount of  $CH_3COONa$  to raise pH to 7.5. On the other hand, an alternative way to form  $MnO_2$  is mixing  $KMnO_4$  with  $Mn(CH_3COO)_2$  [62] at a molar ratio of  $Mn(VII)/Mn(II) = 2/3$  via the following reaction



The amorphous hydrated  $MnO_2$  exhibits ca.  $200 \text{ F g}^{-1}$  at  $5 \text{ mV s}^{-1}$  (or at  $2 \text{ mA cm}^{-2}$  during constant charge-discharge process) in  $2M \text{ KCl}$  with specific surface area of  $300 \text{ m}^2 \text{ g}^{-1}$ . Besides, Stadnychuk *et al.* [90] reported amorphous  $MnO_2$  thin film can be achieved via sol-gel synthesis route, which fumaric acid salt ( $C_2H_2O_4Na_2$ ) was used to reduce  $NaMnO_4$  with a molar ratio of  $C_2H_2O_4Na_2/NaMnO_4 = 3/10$ . Since  $Mn(IV)$  precursors cannot be stably soluble in aqueous solution, manganese at other oxidation states were suggested to be suitable precursors that can produce  $Mn(IV)$  via oxidation or reduction reactions in either alkaline or acidic media. This amorphous

MnO<sub>2</sub> was examined as small particle size, high porosity, uniform pore size and structural integrity. Furthermore, Pang *et al.* [63] reported stable colloidal MnO<sub>2</sub> can be prepared by reducing Mn(VII) with Mn(II), i.e., KMnO<sub>4</sub> and Mn(ClO<sub>4</sub>)<sub>2</sub> in alkaline aqueous medium at ca. pH 10.5. Sol–gel–derived MnO<sub>2</sub> can be deposit either dip-coating or drop-coating colloidal MnO<sub>2</sub> directly onto Ni foils. The specific capacitance of the MnO<sub>2</sub> thin film (1.05 μg cm<sup>-2</sup>) is as high as 680 F g<sup>-1</sup> at 50 mV s<sup>-1</sup> in 0.1 M Na<sub>2</sub>SO<sub>4</sub> solution.

However, the mass loading of MnO<sub>x</sub> thin film (1–4 μg cm<sup>-2</sup>) prepared by sol–gel–derived method is extremely low although its specific capacitance is very high (up to 700 F g<sup>-1</sup>) [61]. And amorphous MnO<sub>x</sub> prepared by a chemical coprecipitation method was found to possess poor capacitive characteristics due to the high resistance of bulk MnO<sub>x</sub> [91]. An alternative way to prepare MnO<sub>x</sub> is via electrochemical deposition, which nanostructured hydrous MnO<sub>x</sub> with different mass (thickness) and morphology can be prepared by simply adjusting the applied electrodeposition method, deposition bath chemistry and temperature [92]. Also, electrodeposited MnO<sub>x</sub> can be controllable to form uniform thin films onto current collectors without using any polymer binder in the electrode. Wu [92] reported MnO<sub>2</sub> can be prepared by anodic deposition with Mn(II) precursor.



The MnO<sub>x</sub> thin film (0.11 mg cm<sup>-2</sup>) exhibits 350 F g<sup>-1</sup> at 50 mV s<sup>-1</sup> in 0.1 M Na<sub>2</sub>SO<sub>4</sub> solution. Hu and Tsou [93] reported anodic deposited amorphous MnO<sub>x</sub> can be optimised through experimental strategies, including fractional factorial design (FFD), the path of steepest ascent and the central composite design coupled with the response surface methodology (RSM). In this work, deposition current density, pH of deposition bath, Mn(II) precursor (MnSO<sub>4</sub>) concentration and temperature of plating bath were found to be key factors in anodic deposition (potentiostatic mode) process



affecting the capacitive performance of deposited  $\text{MnO}_x$ . The results demonstrate that the optimal condition ( $220 \text{ F g}^{-1}$ ) can be obtained at  $3.7 \text{ mA cm}^{-1}$  with a passed charge of  $0.3 \text{ C cm}^{-2}$ ,  $\text{pH} = 5.6$ ,  $0.16 \text{ M MnSO}_4$  and  $24 \text{ }^\circ\text{C}$  of plating bath according to the developed regression model [93]. Followed this work, Hu and Wang [61] reported nanostructured amorphous  $\text{MnO}_x$  can be electrochemically deposited onto graphite substrates from  $0.16 \text{ M MnSO}_4$  with  $\text{pH} = 5.6$  by various plating mode, such as potentiostatic, galvanostatic and potentiodynamic modes. Those  $\text{MnO}_x$  prepared from different plating modes all exhibit ideal capacitive performance (i.e., large specific capacitance, highly electrochemical reversibility and high power property). However, the specific capacitance strongly depends on the nanostructure of  $\text{MnO}_x$ . The  $\text{MnO}_x$  prepared from galvanostatic mode exhibits the highest capacitance of ca.  $230 \text{ F g}^{-1}$  at  $25 \text{ mV s}^{-1}$  in  $0.1 \text{ M Na}_2\text{SO}_4$ , resulting from a 3D network morphology with interconnected  $\text{MnO}_x$  nanowires (ca.  $30 \text{ nm}$  in diameter) and larger mesopores comparing with other cases. Besides, Chen *et al.* [87] used various Mn(II) precursors ( $\text{Mn}(\text{CH}_3\text{COO})_2$ ,  $\text{MnSO}_4$ ,  $\text{MnCl}_2$  and  $\text{Mn}(\text{NO}_3)_2$ ) to prepare hydrous  $\text{MnO}_x$  thin film via anodic deposition under potentiostatic mode. This work indicates  $\text{Mn}(\text{CH}_3\text{COO})_2$  is a promising precursor due to its high deposition rate at much lower potentials comparing with other Mn(II) precursors. However, the capacitive performance of the  $\text{MnO}_x$  thin films are suggested to be independent of precursors, probably due to the fact that the mean oxidation state of Mn is not significantly affected by anions during the deposition mode. The interfacial capacitance (capacitance based on the geometric area of substrate) for  $\text{MnO}_x$  thin films (ca.  $1 \text{ mg cm}^{-2}$ ) can be optimised at the applied charge density equal to  $3.5 \text{ C cm}^{-2}$ , which is ca.  $300 \text{ mF cm}^{-2}$  at  $25 \text{ mV s}^{-1}$  in  $0.1 \text{ M Na}_2\text{SO}_4$  regardless of Mn(II) precursors. Furthermore, other electrochemical deposition methods (such as pulse deposition [94] and electrostatic spray deposition [18]) have also been reported to be potential routes to prepare  $\text{MnO}_x$  electrodes. Hu *et*

*al.* [94] successfully utilised pulse–rest deposition method to prepare variable aspect ratios of MnO<sub>x</sub> nanowires from 0.1 M Mn(CH<sub>3</sub>COO)<sub>2</sub> by applying different on/off time (i.e., pulse/rest) onto various substrates (such as ITO, Si wafer, stainless steel and graphite block). The 1D nanowires consisting of β–MnOOH core and Mn<sub>3</sub>O<sub>4</sub> shell has also been suggested as a good material for field emission (FE) array cathodes. Porous Mn<sub>3</sub>O<sub>4</sub> thin film electrode prepared by electrostatic spray method has been reported by Nam and Kim [18], which can be electrochemically oxidised to pseudocapacitive amorphous MnO<sub>2</sub> by potential cycling. The resultant capacitance is ca. 330 F g<sup>-1</sup> at 50 mV s<sup>-1</sup> in 0.1 M Na<sub>2</sub>SO<sub>4</sub>. However, this value would significantly drop to 150 F g<sup>-1</sup> as the mass increase from 18 to 116 μg cm<sup>-2</sup>.

MnO<sub>x</sub> pseudocapacitors have been widely studied for decades, in summary, its electrochemical behaviour has been reported to be determined by many factors, such as crystalline structure, surface area/pore structure, surface morphology and mass loading (thickness), MnO<sub>x</sub> particle size and hydrous content of MnO<sub>x</sub>, which are generally determined by the conditions of synthetic methods (e.g., chemical synthesis, sol–gel hydrothermal, electrodeposition and sputter deposition) and post–treatment conditions (annealing conditions).

Amorphous hydrous MnO<sub>x</sub> with predominant Mn(IV) is thought to be a good pseudocapacitive material, which has been successfully fabricated via various routes [62, 87, 93, 95]. However, crystalline birnessite MnO<sub>2</sub> (δ–MnO<sub>2</sub>) with well–defined layer structure has been suggested as one of the possible alternatives to amorphous MnO<sub>x</sub> for pseudocapacitors [96, 97]. Brousse *et al.* [97] compared the electrochemical performance of different crystalline MnO<sub>2</sub> polymorph (α–MnO<sub>2</sub>, β–MnO<sub>2</sub>, R–MnO<sub>2</sub>, δ–MnO<sub>2</sub> and λ–MnO<sub>2</sub> as shown in Figure 2–3) in K<sub>2</sub>SO<sub>4</sub> solution.

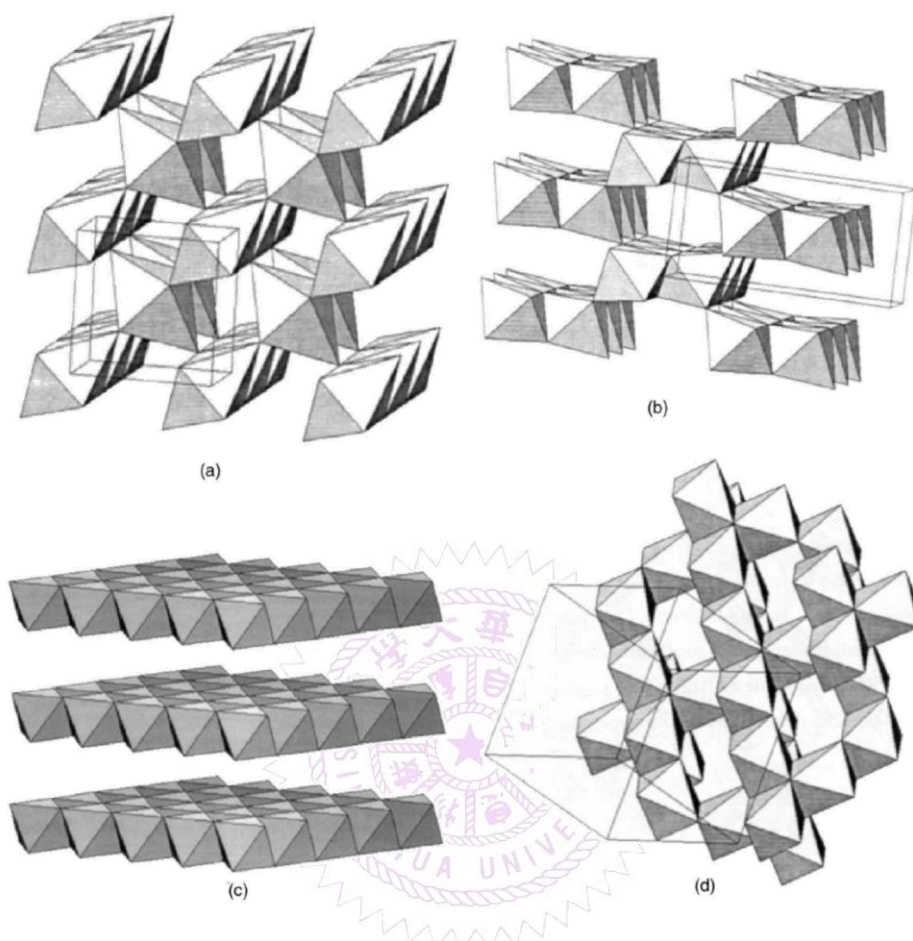


**Figure 2–3** Different MnO<sub>2</sub> structures: (a) pyrolusite  $\beta$ -MnO<sub>2</sub> (1×1), (b) ramsdellite R-MnO<sub>2</sub> (1×2), (c) birnessite  $\delta$ -MnO<sub>2</sub> (1×∞), (d) spinel  $\lambda$ -MnO<sub>2</sub> (1×1) [97].

The results show the specific capacitance of amorphous MnO<sub>2</sub> (a-MnO<sub>2</sub>) is ca. 150 F g<sup>-1</sup>, which is saturated with the surface area equal to ca. 200 m<sup>2</sup> g<sup>-1</sup> (i.e., the specific capacitance cannot be improved with further increasing the surface area). For crystalline MnO<sub>2</sub>, the capacitance strongly depends on the crystalline structure and the size of open tunnels to provide cation intercalation. 1D tunnel structures, such as pyrolusite  $\beta$ -MnO<sub>2</sub> (1×1) and ramsdellite R-MnO<sub>2</sub> (1×2), were found to possess low capacitance (only pseudofaradaic surface capacitance) that is strongly relied on surface area of materials. 2D birnessite  $\delta$ -MnO<sub>2</sub> (1×∞) doped with potassium demonstrates 110 F g<sup>-1</sup> with surface area of merely 17 m<sup>2</sup> g<sup>-1</sup>, indicating the presence of potassium in the 2D layer space allows the participation of a larger fraction of

MnO<sub>2</sub> during charge–discharge storage process. The specific capacitance of 3D spinel  $\lambda$ -MnO<sub>2</sub> (1×1) shows intermediate between 1D and 2D MnO<sub>2</sub>. On the other hand, Ghodbane *et al.* [96] used *in situ* synchrotron X–ray diffraction to investigate alkali metal cation (Li<sup>+</sup> and K<sup>+</sup>) insertion/removal for MnO<sub>2</sub> allotropes (cryptomelane (2×2), OMS–5 (2×4), birnessite and spinel MnO<sub>2</sub> as shown in Figure 2–4) during charge–discharge process. The results also indicate the open pore structure and pore size of MnO<sub>2</sub> polymorph are important for (partially hydrated) cations insertion (or intercalation). For birnessite MnO<sub>2</sub>, the structural breathing along c–axis direction by ca. 0.2 Å comes from the electrostatic interaction between charged framework layers and hydrated electrolyte cations. The contraction/swelling of (111) crystalline planes of 3D spinel–MnO<sub>2</sub> can also be observed by ca. 0.05 Å. Besides, Boisset *et al.* [98] demonstrated up to 1.4 V potential window of birnessite and cryptomelane MnO<sub>2</sub> in specific lithium salts (i.e., Li<sub>2</sub>SO<sub>4</sub>, LiNO<sub>3</sub> and LiClO<sub>4</sub>) aqueous electrolytes, which significantly enhance the overpotential of MnO<sub>2</sub>. Accordingly, how to improve the electrolyte ions accessible to active sites by tuning the open pore structure of crystalline MnO<sub>2</sub> is crucial for improving the specific capacitance of this type of pseudocapacitors. In fact, Reddy and Reddy [99] synthesised xerogel and ambigel forms of MnO<sub>2</sub> with different solvents washing treatments. These two materials have been suggested as nearly amorphous (broadening of X–ray diffraction peaks) MnO<sub>2</sub> structure with similar surface area of 63 and 72 m<sup>2</sup> g<sup>-1</sup>, respectively. However, the specific capacitance of ambigel MnO<sub>2</sub> (130 F g<sup>-1</sup>) was much higher than xerogel MnO<sub>2</sub> (73 F g<sup>-1</sup>), indicating ambigel MnO<sub>2</sub> with larger portion of mesopores is crucial for pseudocapacitive performance. The pore size distribution of MnO<sub>x</sub> has been suggested to be a key factor affecting the capacitive performance of MnO<sub>x</sub> pseudocapacitors, especially for high–rate application [99–101]. It is believed that the effectively opened surface area coupled with appropriate pore structures can facilitate

the electrolyte accessibility to electrochemically active sites, in which mesopores are suggested to be an ideal pore size of  $\text{MnO}_x$  due to its lower pore resistance and better accessibility of ions [101].

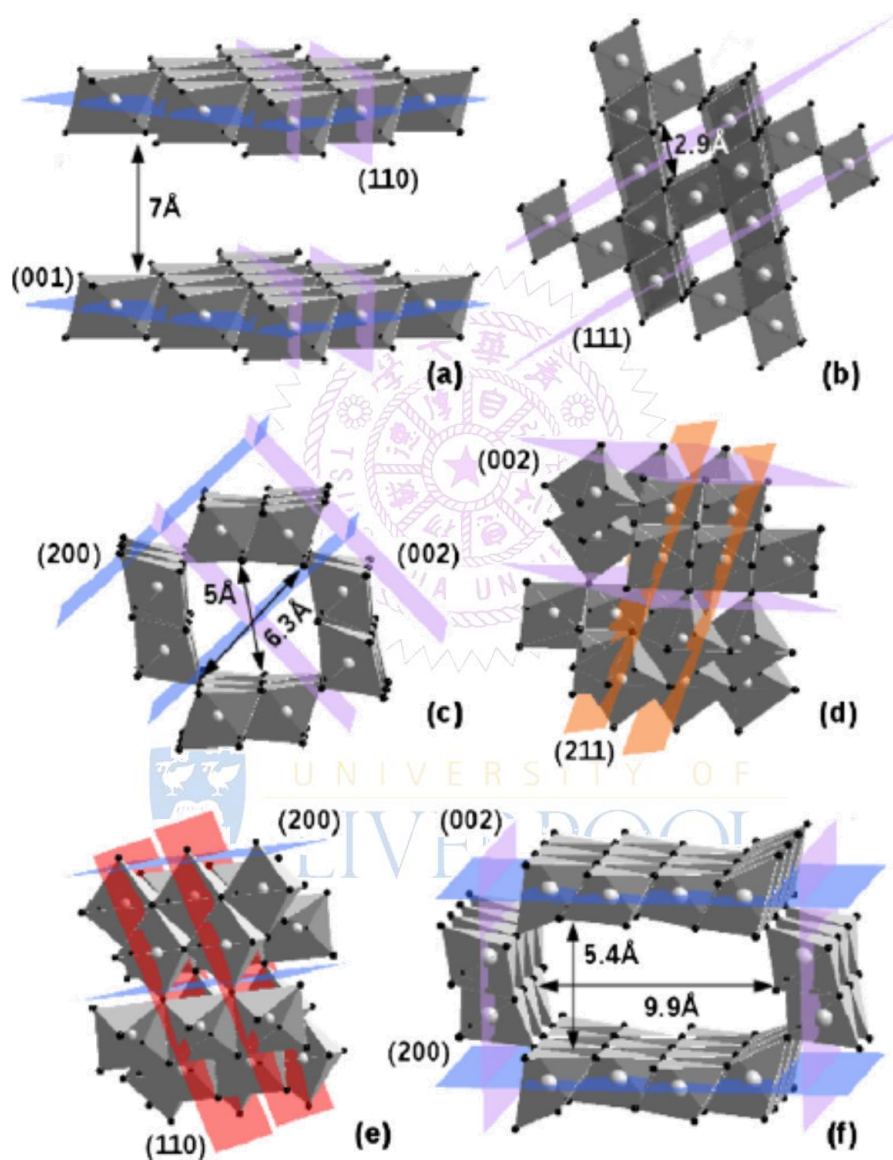


**Figure 2–4** Crystallographic structures of  $\text{MnO}_2$  (a) birnessite, (b) spinel, (c–e) cryptomelane ( $2 \times 2$ ) and (f) OMS–5 ( $2 \times 4$ ) together with selected characteristic crystal planes and distances [96].

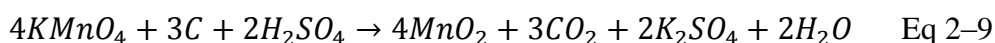
Toupin *et al.* [86] used X–ray photoelectron spectroscopy to analyse the Mn mean oxidation state of  $\text{MnO}_2$  thin film ( $< 5 \mu\text{m}$ ) and thicker composite (ca.  $100 \mu\text{m}$ )



electrode. The results exhibited the manganese oxidation state of thin film electrode was varying from Mn(III) to Mn(IV) for the reduced and oxidised forms. Unlike thin film electrode, no change of the Mn oxidation state (at 3.5 for both reduced and oxidised conditions) was detected for thicker composite electrode. The authors pointed out only a very thin layer of MnO<sub>x</sub> electrode can be involved during charge–discharge process. And the reason for remaining the same Mn oxidation state for thicker composite electrode is attributed to the internal redox interconversion, resulting in the Mn oxidation state lied between Mn(III) to Mn(IV) at both reduced and oxidised conditions. From this finding, it is reasonable to claim the extremely high specific capacitance of MnO<sub>x</sub> thin films with exceedingly low mass loading of MnO<sub>x</sub> cannot be practical application in energy storage since the capacitance in terms interfacial capacitance (mF cm<sup>-2</sup>) would be < 35 mF cm<sup>-2</sup> [18, 63, 86, 102]. The essential reason for drastically decrease of capacitance upon increasing the thickness (or mass loading) of MnO<sub>x</sub> is the poor electrical conductivity (10<sup>-5</sup>–10<sup>-6</sup> S cm<sup>-1</sup>) and the long proton diffusion path of MnO<sub>x</sub> [82, 87], resulting in much lower specific capacitance values comparing with the theoretical capacitance value of MnO<sub>2</sub> (ca. 1233 F g<sup>-1</sup>) on the basis of one electron transfer of redox between Mn (IV)/Mn(III) [103].

In order to improve the electrical conductivity of MnO<sub>x</sub> pseudocapacitors, the most commonly used method is adding conductive material (generally highly electrical conductive carbon material) with MnO<sub>x</sub> in electrode preparation. Enhancing the electrical conductivity by adding carbon materials leads to reduce the equivalent series resistance (ESR) of MnO<sub>x</sub> composite electrodes. Besides, using high surface area and porous carbons can also provide a porous network to support MnO<sub>x</sub> particles, which facilitates the access and rapid transport of electrolyte ions to the surface of active sites. Plenty of carbon materials (carbon black [104], activated carbon [105],

templated mesoporous carbon [106], RGO [107], CNTs [108], RGO/CNTs [109] and carbon aerogels [110]) through various synthetic routes have been reported to improve the capacitive performance of MnO<sub>x</sub> pseudocapacitors. An interesting way to prepare these MnO<sub>x</sub>/carbon composite materials is using carbon to reduce Mn(VII) to Mn(IV) through a one-step reaction in acidic solution [111].



Exfoliated graphite plates [112], activated carbon [113] and CNTs [108] have been reported as effective reducing agents to produce MnO<sub>2</sub>/carbon composites in this method.

On the other hand, nanostructured MnO<sub>x</sub> has been suggested to be an alternative way to improve the pseudocapacitive performance of MnO<sub>x</sub> by reducing the distances for the solid-state transport of insertion cations [1, 114, 115]. Simon and Gogotsi [114] suggested the increase capacitance (improve the usage of active materials) can be obtained by reducing the particle size of pseudocapacitive materials since the pseudocapacitors store charge in the first few nanometers from the surface. Simon *et al.* [1] addressed the battery-like materials with nanoscale at the size < 10 nm would demonstrate capacitor-like properties (Figure 2-5D). The kinetic information can be always obtained from the sweep voltammetry based on the semi-infinite diffusion (i.e.  $i = av^b$ ), which the slope (b) reveals the charge storage mechanism. The double-layer behaviour gives b close to 1, while faradaic charge transfer process would show b close to 0.5. Interestingly, the nanostructured battery-like materials exhibit capacitor-like kinetics (with b ~ 1), which is different from the bulk material (with b ~ 0.5). This is the so-called 'extrinsic pseudocapacitive material', where battery-like materials can possess pseudocapacitive performance by reducing the crystalline size to a certain level.



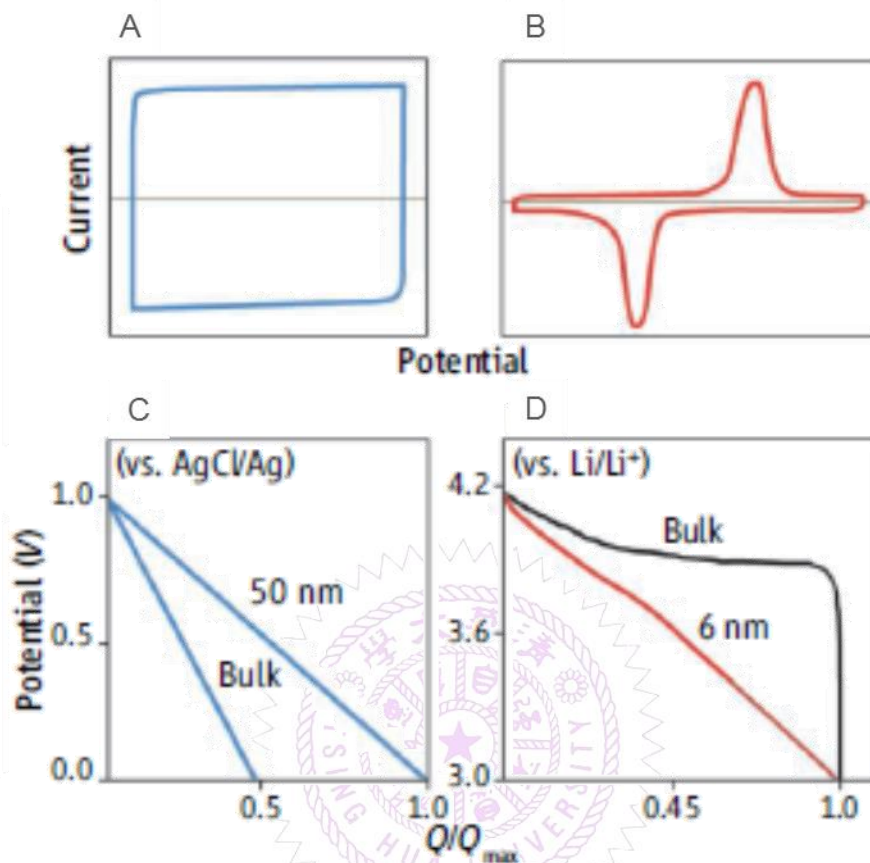


**Figure 2–5** (A to D) Electrochemical characteristics distinguish capacitor and battery materials. (A) Cyclic voltammograms distinguish a capacitor material where the response to a linear change in potential is a constant current, (B) as compared to a battery material, which exhibits faradaic redox peaks. (C) Galvanostatic discharge behaviour (where  $Q$  is charge) for a  $\text{MnO}_2$  pseudocapacitor is linear for both bulk and nanoscale material, (D) but a  $\text{LiCoO}_2$  nanoscale material exhibits a linear response while the bulk material shows a voltage plateau [1].

Annealing post-treatment has also been proposed to affect the  $\text{MnO}_x$  capacitive performance by losing hydrous water content, decrease in surface area and changes in oxidation states and crystalline structures. Hydrous water content has been proposed to affect the electrochemical reactivity of  $\text{MnO}_x$  due to the variation in protonic and electrical conductivity and surface area [8, 83, 95, 116, 117]. Generally, the hydrous information of  $\text{MnO}_x$  can be obtained from XPS O 1s, which the peak position at 529.8, 531.3 and 532.5 eV are attributed to Mn–O–Mn (for anhydrous oxide), Mn–OH (hydroxide) and H–O–H bonds (crystalline water), respectively [86, 95, 116, 118].

Djurfors *et al.* [119] analysed the annealed  $\text{MnO}_x$  with only Mn–O–Mn and H–O–H bonds, indicating the lack of hydrous content (Mn–OH) is likely to be the reason for poor capacitive performance. Moreover, it has been reported high annealing temperature ( $> 300\text{ }^\circ\text{C}$ ) is detrimental to pseudocapacitive performance, which is believed to be drastic decrease of usable surface area [83, 117, 119]. The structural change of  $\text{MnO}_x$  after heat treatments has been widely reported [83, 120, 121]. Generally, the hydrous and amorphous  $\text{MnO}_x$  (mainly Mn(IV)) would be reduced to  $\text{Mn}_2\text{O}_3$  or  $\text{Mn}_3\text{O}_4$  at a higher temperature [20, 117, 122, 123]. The formation of crystalline  $\text{Mn}_2\text{O}_3$  and  $\text{Mn}_3\text{O}_4$  has been reported to exhibit relatively poor pseudocapacitive performance. Devaraj *et al.* [117] reported the specific surface area of as-prepared  $\text{MnO}_2$  powder is about  $190\text{ m}^2\text{ g}^{-1}$ . The surface area of  $\text{MnO}_x$  continuously decreases when the annealing temperature increases. Meanwhile,  $\text{Mn}_2\text{O}_3$  and  $\text{Mn}_3\text{O}_4$  were formed when the temperature reached 500 and 900  $^\circ\text{C}$ , respectively. The surface area of  $\text{Mn}_2\text{O}_3$  and  $\text{Mn}_3\text{O}_4$  drastically decreased to ca. 16 and  $1\text{ m}^2\text{ g}^{-1}$ , respectively, which is attributed to the aggregate of  $\text{MnO}_x$  particles. Note that the formation of  $\text{Mn}_3\text{O}_4$  (with intermediate  $\gamma\text{-Mn}_2\text{O}_3$ ) triggered by an increase in lattice temperature due to local heating by laser has also been reported [124–126], which is similar to the annealing effect on  $\text{MnO}_2$  sample.

According to Potential–pH diagram [127] (the replotted diagram is shown in Figure 2–6), the thermodynamic equilibrium of  $\text{MnO}_x$  at various oxidation states are dependent on the potential and pH of the system. It has been proposed the redox transitions of hydrous  $\text{MnO}_x$  include the redox transitions between Mn(III)/Mn(II), Mn(IV)/Mn(III) and Mn(VI)/Mn(IV) within the potential window of water decomposition [82]. From the thermodynamic point of view, the performance limitation of  $\text{MnO}_2$ -based electrochemical capacitors is the relatively narrow stable potential window for  $\text{MnO}_2$ . In aqueous neutral media, the upper cut-off potential for

MnO<sub>2</sub> is limited by the oxygen evolution reaction (ca. 0.63 V vs. Ag/AgCl) and dissolution of Mn(VII) into electrolyte (ca. 0.9 V vs. Ag/AgCl). On the other hand, the lower cut-off potential is determined by the onset of the Mn<sup>4+</sup> irreversible reduction and subsequent Mn(II) dissolution (ca. 0.1 V vs. Ag/AgCl). Note that the Pourbaix diagram of MnO<sub>x</sub> is based on pyrolusite MnO<sub>2</sub> (β-MnO<sub>2</sub>) from the thermodynamic viewpoint. However, in kinetics, MnO<sub>x</sub> with different crystalline structures and microstructures would lead to different cut-off potentials. For examples, birnessite and cryptomelane MnO<sub>2</sub> has been reported as the potential window up to 1.4 V in specific lithium salts (i.e., Li<sub>2</sub>SO<sub>4</sub>, LiNO<sub>3</sub> and LiClO<sub>4</sub>) aqueous solutions [98].

The other limitation is capacitance fade with increasing cycling numbers though cycling in a safe potential window for both amorphous and crystalline manganese oxides. Until now, two mechanisms have been proposed to explain the capacitance fading behaviour. The first mechanism involves partial dissolution of manganese into the electrolyte during cycling. It leads to gradually loss of active electrode material during cycling, which has been confirmed by chemical analysis of Mn content in the electrolytes [63, 128]. Besides, a careful examination of MnO<sub>x</sub> in electrochemical quartz crystal microbalance (EQCM) demonstrated the dissolution of manganese at higher potential (ca. 0.8–1.2 V) and re-deposition of dissolved manganese on to MnO<sub>x</sub> surface at ca. 0.8–0.2 V in the negative sweep [129]. A second mechanism proposed the accelerated fading might be mainly attributed to mechanical failure of the electrode materials caused by cyclic volumetric variations of the oxide particles upon cycling. The failure leads to increasingly deteriorating electrical contact among the constituent particles within the electrode, which has been confirmed by an increase in impedance for the cycled electrode [130]. Both proposed mechanisms imply that the electrochemical cyclability is closely related to physicochemical

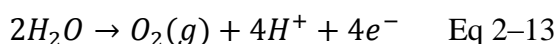
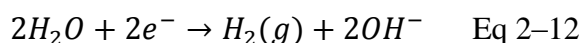
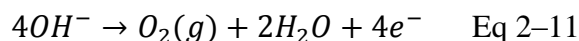
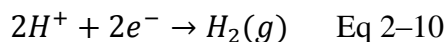
change in MnO<sub>2</sub> electrodes during charge–discharge cycles, such as morphological, chemical and structural changes. Therefore, it is crucial to stabilise MnO<sub>x</sub> and maintain its performance during charge–discharge process. For example, Kobama, *et al.* [131] proposed that adding small amounts (ca. 3%) of Na<sub>2</sub>HPO<sub>4</sub> or NaHCO<sub>3</sub> into the electrolyte not only enhances the capacitance but also suppresses manganese dissolution into electrolyte. The author proposed that HPO<sub>4</sub><sup>2-</sup> and the HCO<sub>3</sub><sup>-</sup> can form insoluble salts on the surface of manganese oxide and inhibit the dissolution of manganese. Therefore, the cycle stability of amorphous MnO<sub>x</sub> was found to be significantly improved by introducing HPO<sub>4</sub><sup>2-</sup> or HCO<sub>3</sub><sup>-</sup> into the electrolyte. Another example is using MnO<sub>x</sub> composite material consisting of MnO<sub>2</sub> and Mn<sub>3</sub>O<sub>4</sub>, the synergistic effect has been proposed not only improve the specific capacitance (enhanced by ca. 25%) but also prolong the cycle life of MnO<sub>x</sub> [21].

### 2.3 Carbon//Manganese Oxide Aqueous Asymmetric ECs

As described in Chapter 1, asymmetric type ECs consisting of two different electrode materials with comprehensive working potential windows were designed to enlarge the cell voltage of aqueous ECs. Asymmetric ECs consisting of MnO<sub>2</sub> as positive electrode and activated carbon as negative electrode was firstly proposed to exhibit up to 2 V operating cell voltage in neutral aqueous medium in 2002 [132]. Since then, carbon//MnO<sub>x</sub> asymmetric ECs has been widely investigated due to the low cost of electrode materials and the mild electrolyte environment. Besides, carbons with high hydrogen–evolving overpotential and MnO<sub>x</sub> with high oxygen–evolving overpotential have been proposed to extend the cell voltage of asymmetric ECs to promote the device energy and power densities [16, 103].

Hong *et al.* [132] compared the electrochemically stable potential window of

HCl, KOH and KCl by linear sweep voltammograms with a Pt metal plate. The gas evolution reactions are related to water decomposition,  $H^+$  reduction and  $OH^-$  oxidation.



The pH of electrolyte influences the gas evolution reactions. For 1 M HCl, it gives about 1.2 V of electrochemically stable potential window in 1 M HCl since  $H^+$  reduction (Eq 2-10) limits the lower cut-off potential at  $-0.2$  V(vs Ag/AgCl). Beyond the stable potential window, the large anodic or cathodic current responses corresponding to the oxygen and hydrogen evolution reactions (OER and HER) occur at ca. 1.0 and  $-0.2$  V (vs Ag/AgCl). Similarly,  $OH^-$  oxidation limits the potential at 0.7 V for 1 M KOH (Eq 2-11), resulting in a 1.8 V electrochemically stable potential window. With regard to 1M KCl, instead of  $H^+$  reduction and  $OH^-$  oxidation, water decomposition reactions (Eq 2-12 and 2-13) can be observed at  $-0.9$  and 1.1 V. Although the electrochemically stable potential window is subjected to the overpotential of the above reactions on Pt metal, the electrochemically stable potential window for neutral KCl electrolytes was assigned as 2.0 V in this work. The enlarged cell voltage of neutral KCl medium leads to a significant improvement on the specific energy stored in carbon// $MnO_x$  aqueous asymmetric ECs. Even though the cell capacitance of carbon// $MnO_x$  asymmetric EC ( $52 \text{ F g}^{-1}$ ) is much lower than  $RuO_2$  symmetric EC ( $190 \text{ F g}^{-1}$ ), the specific energy of carbon// $MnO_x$  ( $28.8 \text{ Wh kg}^{-1}$ ) were found to be comparable to  $RuO_2//RuO_2$  ( $26.7 \text{ Wh kg}^{-1}$ ). Brousse *et al.* [81] also pointed out the occurrence of OER and HER on the  $MnO_2$  and activated carbon (AC) surfaces upon charging the AC// $MnO_2$  asymmetric ECs limits the cell voltage of the

devices in mild aqueous electrolyte (0.65 M K<sub>2</sub>SO<sub>4</sub>). Although high specific energy (19 Wh kg<sup>-1</sup> at a power density of 200 W kg<sup>-1</sup>) can be reached with the cell voltage of 2.2 V for AC//MnO<sub>2</sub> asymmetric ECs, the cell performance was limited by the gas evolution occurring at the electrodes upon cycling. Hydrogen evolution was proposed to be the main hindrance of AC//MnO<sub>2</sub> asymmetric ECs because the volume of hydrogen exceeds by 1000 times of oxygen. The hydrogen evolution is much too high for a large-scale system and can cause serious safety problems during long-term cycle life. An alternatively and feasibility way is using a lower working cell voltage at 1.5 V, which was characterised by negligible gas evolution over a long cycling period (23,000 cycles).

Khomenko *et al.* [16] reported the electrochemically stable potential window for MnO<sub>x</sub> and AC in neutral aqueous electrolyte (2 M KNO<sub>3</sub> with pH=6.4) from both thermodynamic and kinetic viewpoints. As Figure 2-6 shows, the kinetics limits for OER on MnO<sub>x</sub> and HER on AC are higher than thermodynamic values, indicating a reasonable 2 V cell voltage can be reached with a careful charge balance on positive and negative electrodes. With a further increase working cell voltage to 2.2 V, the coulombic efficiency significantly drops although a small increase of capacitance can be obtained.



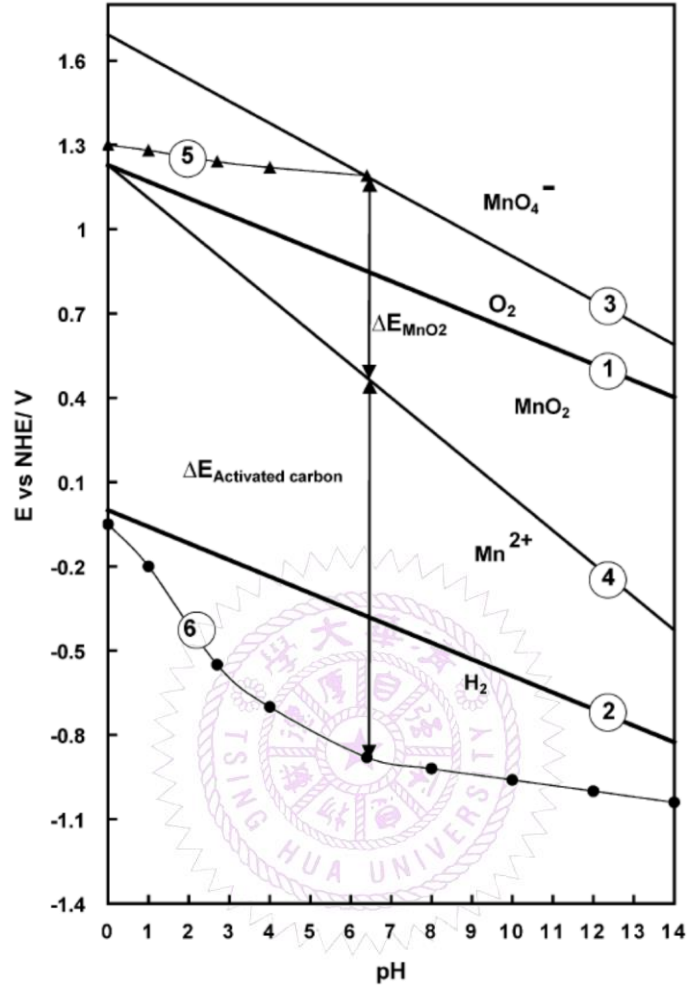


**Figure 2–6** Potential–pH diagram. Lines 5 and 6 represents the kinetic limits for O<sub>2</sub> evolution on MnO<sub>2</sub> and for H<sub>2</sub> evolution on activated carbon, respectively [16].

Brousse *et al.* [80] also reported long–term stable cyclability (195,000 cycles) of AC//MnO<sub>2</sub> asymmetric ECs with 2 V operating cell voltage can be achieved by removal of dissolved oxygen from the electrolyte (0.1 M K<sub>2</sub>SO<sub>4</sub>). And the individual potentials at full–charge state at 2 V are 0.8 ~ 0.9 and –1.1 ~ –1.2 V for MnO<sub>x</sub> and AC, respectively. The authors pointed out the presence of oxygen in electrolyte leads to corrosion of stainless steel current collectors. For AC//MnO<sub>2</sub> asymmetric EC in deaerated electrolyte, 87% capacitance retention and 27% increase of internal resistance was found over 195,000 cycles, which demonstrated considerable improvements in comparison with AC//MnO<sub>2</sub> asymmetric EC without degassing with



N<sub>2</sub> flow (53% capacitance retention and 167% increase of internal resistance over 50,000 cycles). Besides, the authors also demonstrated the practical use of AC//MnO<sub>2</sub> asymmetric ECs by a large capacitance stacks with 20 units (20 positive and 20 negative electrodes). As Figure 2–7a shows, the carbon conductive painting was applied to lower the interface resistance between current collector and MnO<sub>x</sub> active material. The electrodes were assembled by stack of 10 units (Figure 2–7b) with cellulosic paper separators (50 μm thickness) and installed in the PVC casing (Figure 2–7c). The feasibility of manufacturing large packs (2 V–380 F) was demonstrated over 600 cycles without significant capacitance decrease and internal resistance increase of the device.

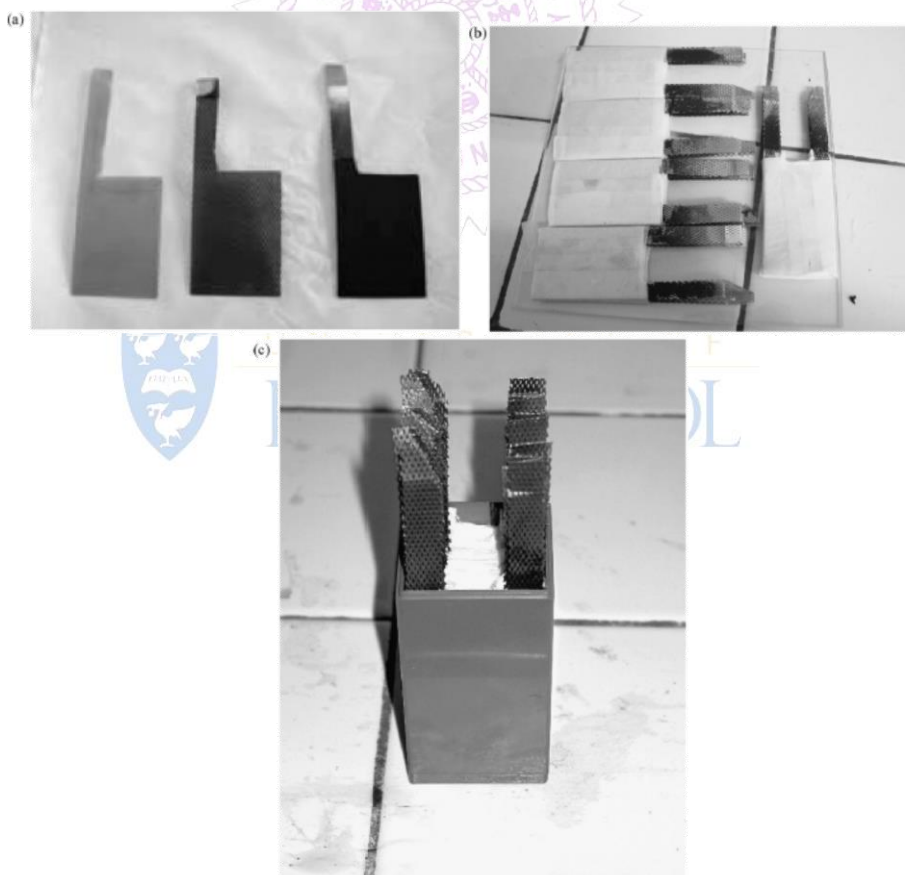


**Figure 2–7** (a) From left to right: AISI 304L stainless steel current collector, coated with conductive paint and co-laminated with the active material composite film, (b) 10-pack cells covered with a cellulosic paper separator and (c) large capacitance final device in the PVC casing prior to sealing [80].

Since then, the studies related to Carbon//MnO<sub>x</sub> asymmetric ECs generally focused on the electrochemical behaviour of asymmetric design and its cell voltage limits. Usually, activated carbon and amorphous MnO<sub>x</sub> were applied in the asymmetric ECs, where 2 V operating cell voltage gives a comparable specific energy to organic-based EDLCs. The strength of carbon//MnO<sub>x</sub> asymmetric ECs includes low cost of materials (MnO<sub>x</sub>, carbon and neutral aqueous salts) and non-toxic/safer components. Recently, more studies focus on enhancing carbon//MnO<sub>x</sub> asymmetric ECs performance (energy storage, power capability and cyclability) by improving active electrode materials. For example, nanostructured MnO<sub>2</sub> [133, 134], alkali-metal doped MnO<sub>2</sub> [135, 136] and MnO<sub>2</sub>/graphene composites [10, 137] have been used as positive electrode material to improve the capacitance retention and power capability. Qu *et al.* [133] reported asymmetric ECs consisting of activated carbon as negative electrode and MnO<sub>2</sub> nanorod as positive electrode demonstrates 1.8 V working cell voltage with 94% capacitance retention and specific energy = 17 Wh kg<sup>-1</sup> at 2 kW kg<sup>-1</sup> after 23,000 cycles in 0.5 M K<sub>2</sub>SO<sub>4</sub>. Qu *et al.* [135, 136] reported doping alkali-metal cations (Na<sup>+</sup> or K<sup>+</sup>) in the MnO<sub>2</sub> lattice (Na<sub>x</sub>MnO<sub>2</sub> or K<sub>x</sub>MnO<sub>2</sub>) can form lamellar structure, which can improve the capacitive performance and no need to remove oxygen from electrolyte. The fairly simple synthesis of this doped MnO<sub>2</sub> was achieved by a solid-state method. For example, K<sub>x</sub>MnO<sub>2</sub> was prepared by ball-milling the mixture of K<sub>2</sub>CO<sub>3</sub> and MnO<sub>2</sub> (with molar ratio of 1:2) for 12 hr and followed by calcination at 550 °C for 8 hr. AC//K<sub>0.27</sub>MnO<sub>2</sub> asymmetric EC exhibits 25.3 and 17.6 Wh kg<sup>-1</sup> at 0.14 and 2 kW kg<sup>-1</sup> in 0.5 M K<sub>2</sub>SO<sub>4</sub>, respectively, which meets the requirements for supercapacitors as power sources for EVs (15 Wh kg<sup>-1</sup>). Fan *et al.* [10] reported the composite MnO<sub>2</sub> and graphene synthesised from self-limiting reaction of aqueous permanganate with graphene (Eq 2–9). The advantage of this process is that MnO<sub>2</sub> coating can be deposited closely on

carbon surface, which can separate the adjacent graphene sheets efficiently. Assembled MnO<sub>2</sub>/graphene composite material with activated carbon nanofibers as asymmetric EC demonstrates high-rate capability, i.e. ca. 11 Wh kg<sup>-1</sup> at 10 kW kg<sup>-1</sup> in 1 M K<sub>2</sub>SO<sub>4</sub>.

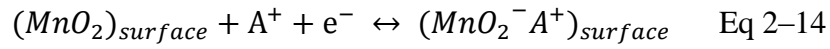
Apart from the improvements of active materials, the studies on electrolytes have also been investigated. Xu *et al.* [138] reported ideal capacitive behaviour, high specific capacitance, good coulombic efficiency and high-rate capability of MnO<sub>2</sub> in aqueous electrolytes containing bivalent cations (i.e., Mg(NO<sub>3</sub>)<sub>2</sub>, Ca(NO<sub>3</sub>)<sub>2</sub>, or Ba(NO<sub>3</sub>)<sub>2</sub>) can be obtained, indicating alkaline-earth cations are possible alternatives for the state-of-the-art univalent alkaline cations. The specific energy of AC//MnO<sub>2</sub> with 2 V cell voltage reaches 21.1 Wh kg<sup>-1</sup> at a current density of 0.3 A g<sup>-1</sup>.

Flexible asymmetric ECs have also been achieved [139–141]. For example, Chen *et al.* [141] used single wall carbon nanotubes (SWNT) to improve the electrical conductivities of In<sub>2</sub>O<sub>3</sub> and MnO<sub>2</sub> thin films. Flexible In<sub>2</sub>O<sub>3</sub>/SWNT//MnO<sub>2</sub>/SWNT asymmetric EC can perform 2 V operating voltage with the specific energy reaching ca. 30 Wh kg<sup>-1</sup> at 25 kW kg<sup>-1</sup>.

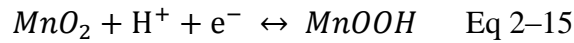
## 2.4 Charge Storage Mechanisms of Manganese Oxides

Two charge storage mechanisms of MnO<sub>2</sub> pseudocapacitors have been proposed in literature. The first was proposed by Lee and Goodenough in 1999 [62]. The results show cyclic voltammetric behaviour and the specific capacitance depend on the nature of cations (Li<sup>+</sup>, Na<sup>+</sup> and K<sup>+</sup>) in the electrolyte (as shown in Figure 2–8). MnO<sub>2</sub> in KCl shows the best capacitive performance comparing with LiCl and NaCl, indicating that the K<sup>+</sup> ions have a rapid chemisorption/desorption reaction rate. The hydration sphere of the cations and the chemisorption of cations on the oxide surface

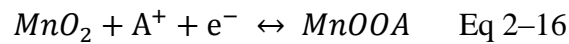
were considered to be important parameters. Therefore, a mechanism based on the surface adsorption of electrolyte cations ( $A^+$ ) on  $MnO_2$  can be described as:



where  $A^+ = Li^+, Na^+, K^+$ . On the other hand, the second mechanism was proposed by Pang *et al.* in 2000 [63], indicating charge storage process of  $MnO_2$  in neutral electrolytes can be presented as:



which is analogous to the double injection charge storage mechanism of  $RuO_2$  (i.e., protons and electrons are both incorporated). The authors suggested the high reversibility of  $H^+$  intercalation/de-intercalation into/from  $MnO_2$  lattice during charge-discharge process can be maintained in an appropriate potential window. Moreover, Chin *et al.* [142] reported the higher charge capacity can be achieved in  $LiClO_4$  electrolyte comparing with ( $NaClO_4$  and  $KClO_4$  salts), which was proposed to be attributed to the enhanced ionic mobility of the smaller  $Li^+$  ions within the oxide matrices during intercalation/deintercalation. Therefore, a modified mechanism was proposed that alkali metal cations can also intercalate/de-intercalate within the oxide lattice during the redox process.



Therefore, the second charge storage mechanism implies the intercalation of protons ( $H^+$ ) and/or alkali metal cations ( $A^+$ ) in the bulk of the material upon reduction followed by a de-intercalation process upon oxidation.

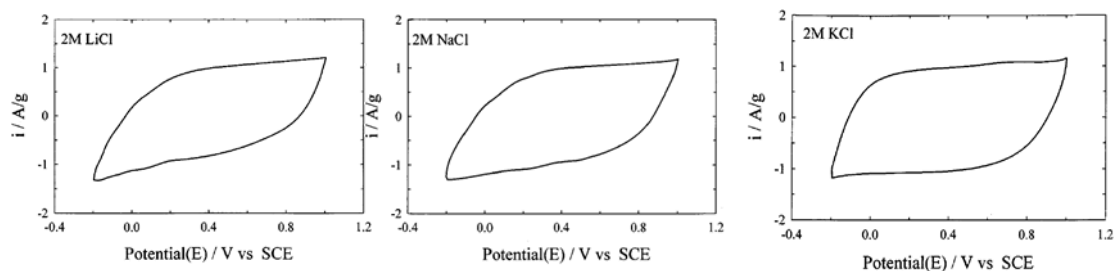


**Figure 2–8** Cyclic voltammograms at 5 mV/s of an amorphous  $\text{MnO}_2 \cdot n\text{H}_2\text{O}$  electrode between  $-0.2$  and  $+1.0$  V vs. SCE in 2 M  $\text{ACl}$  ( $\text{A}=\text{Li}, \text{Na}, \text{K}$ ) electrolyte with Pt–gauze counter electrode [62].

Although the previous investigations showed that redox cycling of the  $\text{MnO}_2$  in mild aqueous electrolytes was responsible for the observed pseudocapacitance, this fact was not conclusively demonstrated until spectroscopic tools were applied to such systems [115]. In order to have more understanding on the charge storage mechanism of amorphous–like  $\text{MnO}_2$ , X–ray photoelectron spectroscopy (XPS) has been used to determine the mean Mn oxidation states at oxidised and reduced polarisations of  $\text{MnO}_2$  thin film ( $< 2 \mu\text{m}$ ) and composite electrodes ( $\sim 100 \mu\text{m}$ ) by Toupin *et al.* in 2004 [86]. The mean Mn oxidation state of  $\text{MnO}_x$  can be determined by the energy separation between the two peaks of Mn 3s core level spectrum ( $\Delta E_b$ ) [86, 95, 116, 118]. It has been reported that more interaction can occur upon photoelectron ejection since a lower valence state implies more electrons in the 3d orbital. Consequently, the energy separation between the two components of the Mn 3s multiplet will increase. The energy separation between these two peaks of Mn 3s spectra is 5.79, 5.50, 5.41 and 4.78 eV for reference sample of  $\text{MnO}$ ,  $\text{Mn}_3\text{O}_4$ ,  $\text{Mn}_2\text{O}_3$  and  $\text{MnO}_2$ , respectively [95, 107, 118]. This quasi–linear relationship between Mn 3s peak energy separation and the mean Mn oxidation state provides a way to estimate the mean oxidation state of  $\text{MnO}_x$ . The results exhibited the Mn oxidation state of thin film electrode was varying from Mn(III) to Mn(IV) for the reduced and oxidised forms (as shown in Figure 2–9). Unlike thin film electrode, no change of the Mn oxidation state (at 3.5

for both reduced and oxidised conditions) was detected for thicker composite electrode. The authors pointed out only a very thin layer of  $\text{MnO}_x$  electrode can be involved during charge–discharge process. And the reason for remaining the same Mn oxidation state for thicker composite electrode is attributed to the internal redox interconversion, resulting in the Mn oxidation state lied between Mn(III) to Mn(IV) at both reduced and oxidised conditions. Furthermore, the Na 1s and S 2p were also applied to probe the charge storage mechanism of  $\text{MnO}_2$  (as shown in Figure 2–10). When the composite electrode was switched from 0 to 0.9 V, the Na 1s signal decreased, whereas the S 2p signal increased. The oxidised composite electrode contains an excess of  $\text{SO}_4^{2-}$  (ratio S/Mn = 0.081), whereas the reduced electrode has an excess of  $\text{Na}^+$  (ratio Na/Mn = 0.141). Besides, the featureless S 2p spectra can be observed for both oxidised and reduced thin films. The excess of  $\text{Na}^+$  and  $\text{SO}_4^{2-}$  for the reduced and oxidised electrodes, respectively, were proposed to be related to classic double–layer ions adsorption/desorption onto/from carbon (used to enhance electrical conductivity of composite electrodes) surface in the composite electrodes. However, the Na/Mn ratio for the reduced thin film electrode was much lower than that was anticipated for charge compensation by  $\text{Na}^+$  (ratio Na/Mn = 0.09), thus suggesting the involvement of protons in the charge storage mechanism.



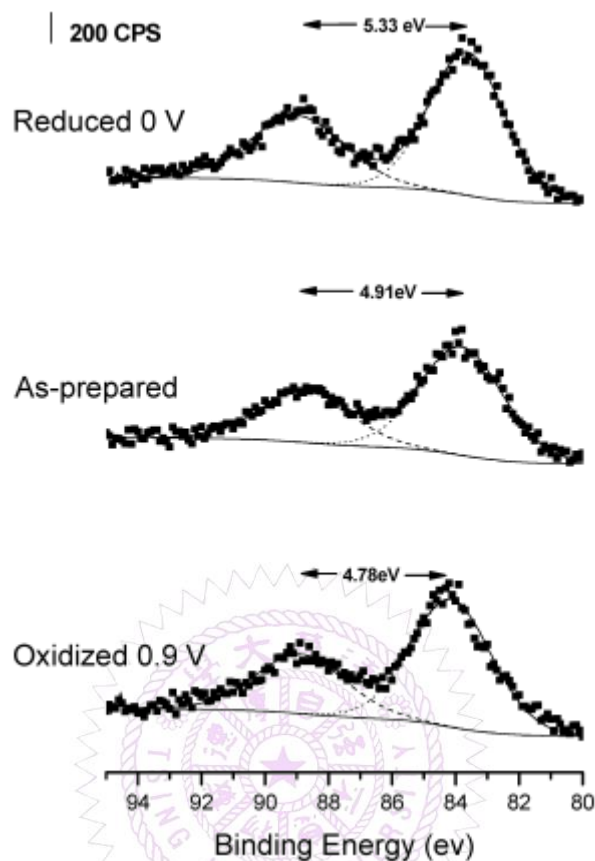


**Figure 2–9** Mn 3s core level spectra for reduced, as–prepared and oxidised thin film electrodes. The raw data are represented by the dots and the fitted data are represented by the lines [86].

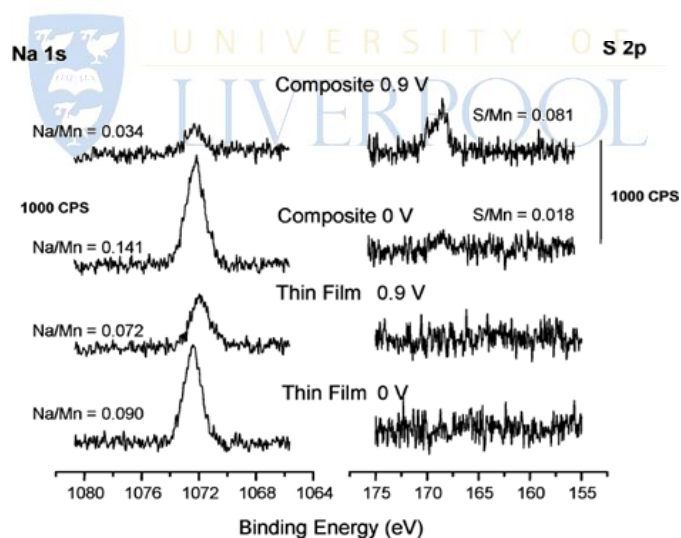


**Figure 2–10** Na 1s and S 2p core level spectra for composite and thin film electrodes after cycling in 0.1M Na<sub>2</sub>SO<sub>4</sub> [86].



Direct evidence for the variance of the manganese valence for a crystallised form of MnO<sub>2</sub> was analysed by *in situ* X-ray absorption near-edge structure (XANES) and *in situ* synchrotron X-ray diffraction reported by Kuo and Wu in 2006 [143]. It was found that the main absorption edge, which is associated with the transition from Mn 1s to p-like states, progressively shifted to lower energies upon electrochemical reduction of the MnO<sub>2</sub> electrode, in agreement with a decrease of the manganese valence. In the same study, the authors also discovered a reversible expansion and shrinkage in lattice spacing of MnO<sub>2</sub> (100) during reduction/oxidation process by using *in-situ* synchrotron X-ray diffraction (as shown in Figure 2-11). The lattice expansion indicates that cations intercalate/de-intercalate into/from the bulk MnO<sub>2</sub> structure and is not limited to only the surface in contact with the electrolyte. The results reveal that charge transfer at the Mn sites upon reduction/oxidation is balanced by insertion/removal of the solution cations into/from the oxide structure. Besides, it was found that H<sub>3</sub>O<sup>+</sup> plays the predominant (60%) role based on the EQCM results. Athouël *et al.* [79] also reported a similar finding on Mg-doped Na-birnessite MnO<sub>2</sub>. An increase of the interlayer spacing of an Mg-doped Na-birnessite MnO<sub>2</sub> from 0.710 to 0.720 nm upon electrochemical oxidation in the presence of Na<sup>+</sup> cations in Na<sub>2</sub>SO<sub>4</sub> electrolyte is associated with the de-intercalation of Na<sup>+</sup> and the intercalation of H<sub>2</sub>O between the layers.

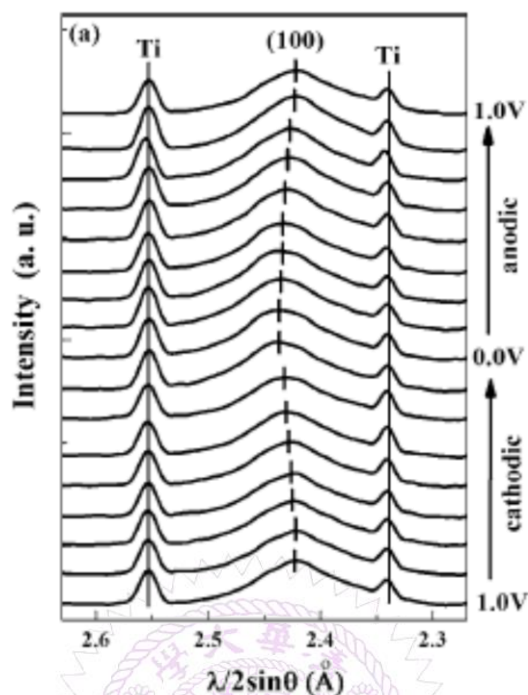


**Figure 2–11** *In situ* Synchrotron XRD patterns of  $\text{MnO}_2 \cdot n\text{H}_2\text{O}$  electrodes during CV cycling in 1 M NaCl [143].

Moreover, Nam *et al.* [144] and Chang *et al.* [145] both reported that the reversible surface redox reaction between Mn(III) and Mn(IV) can be found in the  $\text{MnO}_2$  film during charge–discharge cycles within the electrochemically stable potential window in 2M KCl based on the *in situ* X–ray absorption near–edge structure results (Figure 2–12 and 2–13). The mean valence state of manganese can be specifically identified by the absorption threshold energy, which can be determined by the first inflection point on the main absorption edge. The results revealed the quasi–linear relationship between the manganese oxidation state and the absorption threshold energy. This edge shift is related to the increase in binding energy of the core–level electron with increasing oxidation state, which is attributed to the reduced screening of the core level by valence electrons [145]. The continuous and reversible change of Mn oxidation state with respect to the applied potential was found to be attributed to pseudocapacitive performance of  $\text{MnO}_2$ . It was also reported the Mn–O and Mn–Mn (edge) bond length increase during reduction process, which indicates an

increase in the local structural disorder related to the existence of the Jahn–Teller distortion of Mn(III) [144]. Interestingly, the mean oxidation states were +3.71 and +3.98 at 0.1 and 0.8 V vs. SCE, respectively [144]. This suggests that most of the Mn ions in the electrode did not participate in the redox reaction and remained in the Mn(IV) even though the electrode film was polarised to 0.1 V. Note that the analytical signals were generally collected from a sub–micrometer depth beneath the electrode surface under a fluorescence mode used in XANES, which would not be restricted at near–surface region but also involve the bulk of manganese oxide electrode. The similar phenomenon was also found as the hysteresis of Mn oxidation state with respect to the applied potential in Figure 2–13 [145]. This indicates the electrochemical redox reaction might be restricted to a thin surface layer of the manganese oxide electrode due to the poor conductivity of manganese oxide.



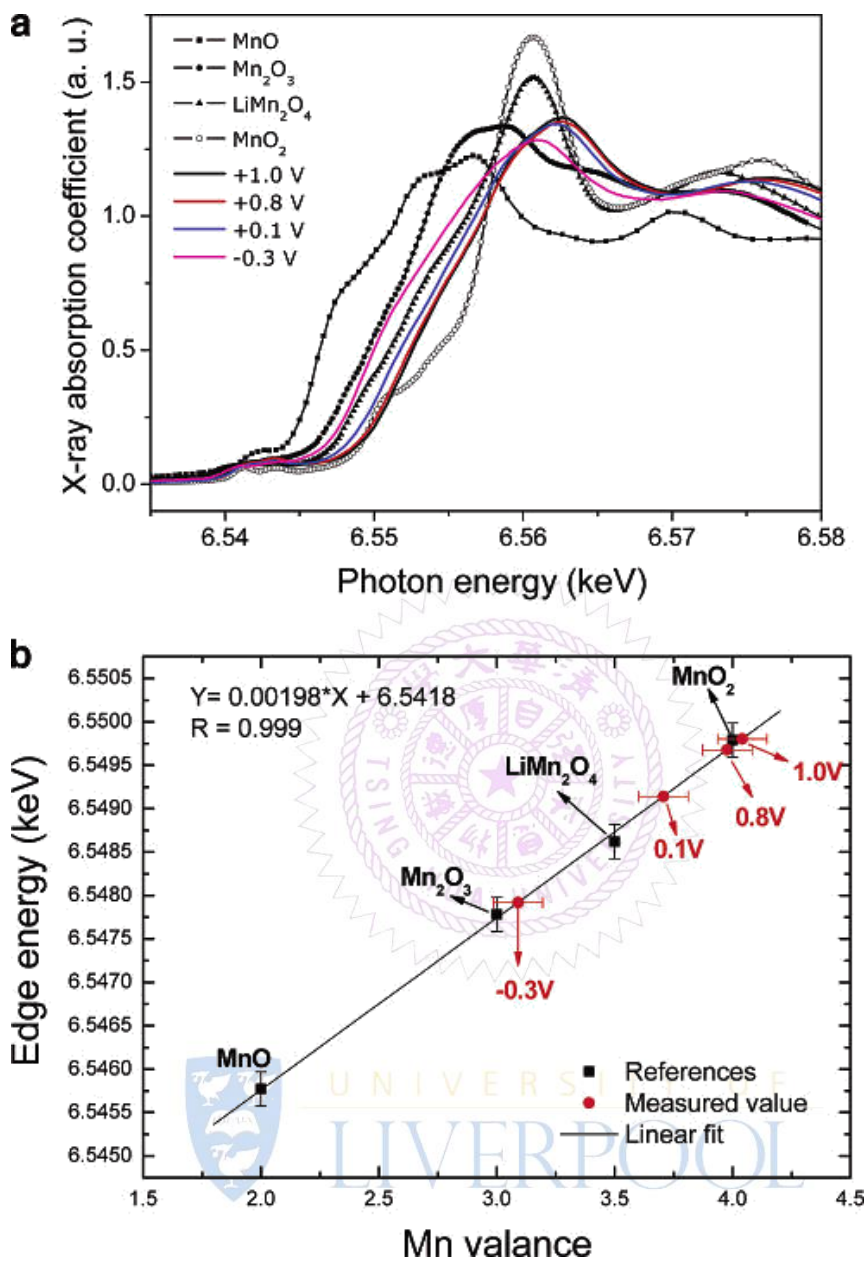


**Figure 2-12** (a) Mn K-edge XANES spectra of the electrodeposited manganese oxide at various applied potentials together with the reference manganese oxides. (b) Oxidation state determination of manganese oxide at applied potentials using the Mn K-edge energy shift of the reference Mn compounds [144].

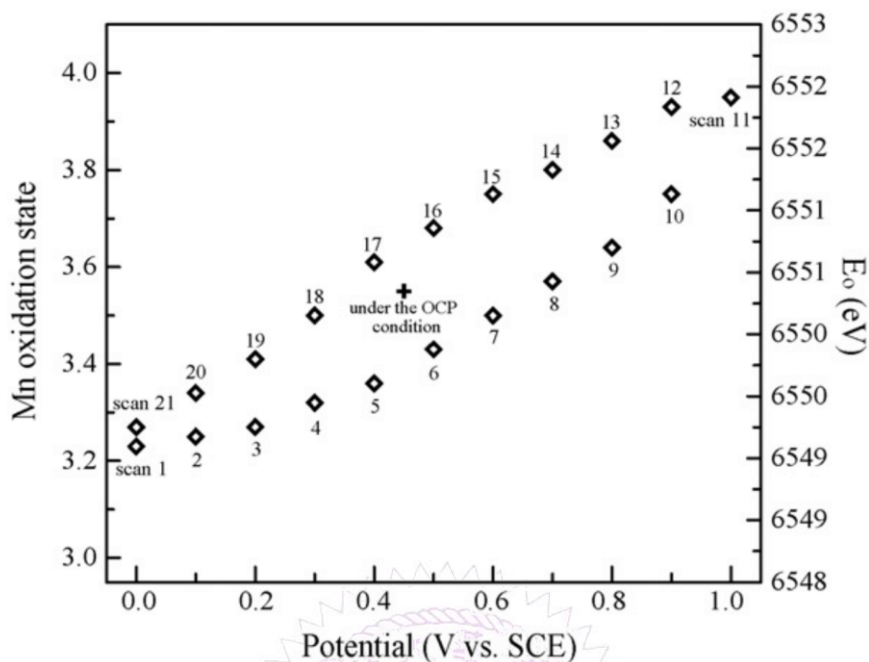


**Figure 2–13** Dependences of the Mn oxidation state and the edge energy on the applied potential during the electrochemical redox cycle [145].

In 2011, Hsu *et al.* [146] used *in situ* Raman microscopy to investigate the alkali–metal cation ( $\text{Na}^+$ ) intercalation/de–intercalation process. The reversible phase transformation was reported from hexagonal to monoclinic structure corresponding to the intercalation of  $\text{Na}^+$  ions into  $\text{MnO}_2$  nanosheets upon reduction process. As shown in Figure 2–14, a stepped frequency shift of  $\nu_1$  mode and the coexistence of two bands at 0.5 V (vs. Ag/AgCl) indicates that two different structural phases appeared at different sides of the potential and coexisted in the potential range of 0.4–0.6 V. And this step increase of the  $\nu_1$  stretching mode resulted from the increase of distance between two successive layers of birnessite  $\text{MnO}_2$  due to the replacement of  $\text{Na}^+$  ions by water molecules from the interlayer during positive sweep. With regard to the peak shift of  $\nu_2$  mode toward lower wavenumber,  $\text{Na}^+$  ion incorporation during the negative sweep leads to the partial reduction of  $\text{Mn}^{4+}$  and shorter Mn–O chemical bonds of the  $\text{MnO}_6$  layer, resulting in the local lattice distortion by a shift of the distance of one  $\text{MnO}_6$  layer with regard to the next. Besides, preferential orientation corresponding to

the alignment of  $\text{MnO}_6$  layers parallel to the  $ab$  plane (i.e., a well-ordered hexagonal phase) would have a stronger Raman intensity. And the enhanced intensity of the vibration mode can be observed for oxidised condition. Therefore, the authors suggested the shrinkage of interlayer spacing and local lattice distortion of the  $\text{MnO}_6$  layer upon  $\text{Na}^+$  ion intercalation leads to the structure transition from hexagonal phase to the monoclinic phase.

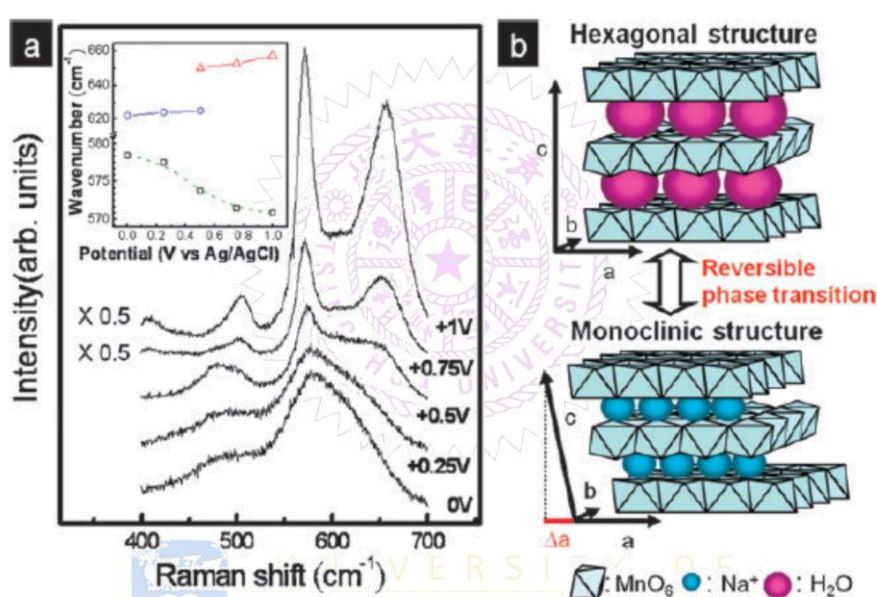


**Figure 2–14** (a) Transformation in Raman spectra of  $\text{MnO}_2$  under anodic potential sweep; inset: frequency shift of the  $\nu_1$  and  $\nu_2$  stretching modes as a function of applied potential. (b) Schematic illustration showing the reversible hexagonal–monoclinic phase transition [146].

Chen *et al.* [147] also used *in situ* Raman technique to study the cation effect on the redox behaviour of birnessite  $\text{MnO}_2$ . The authors indicate the structure change, especially for  $d_{001}$ , is very sensitive to the sizes, charges, and stoichiometry of the species incorporated into the structure. The size of the incorporated species may affect the  $d$ -spacing sterically due to steric hindrance and charge density. In Figure 2–15, the redshift of  $\nu_1$  and blueshift of  $\nu_2$  was observed in this work, which is similar to that



reported by Hsu *et al.* [146]. The authors also found the peak shift was most significant for  $\text{Li}^+$  and least significant for  $\text{K}^+$ , since a smaller cation can lead to more significant steric effects as mentioned in previous sections. Raman band intensities depend strongly on the charge of the interlayer species, which influences the distribution of the charge density within the  $\text{MnO}_2$  crystal structure. The insertion/removal of larger cations may lead to more significant change in polarisability of the vibrational modes. Finally, the evolution of bandwidth also exhibited significant cation-size effects (Figure 2-16); the significance of band broadening of  $\nu_2$  band is most obvious for  $\text{Li}^+$  and least obvious for  $\text{K}^+$ . Such experimental observation matches the fact that smaller-sized cations will lead to stronger Jahn-Teller distortion, which leads to a greater band broadening effect.

The authors also correlate the cation size to the capacitive performance of  $\text{MnO}_2$  pseudocapacitors. The use of smaller cations results in slightly larger specific capacitances. Moreover, the difference in specific capacitances become more significant at higher cycling rate because it is easier for smaller cations to be inserted into or extracted out of the layered structure. As a result, the obtainable capacitance of  $\text{MnO}_2$  is the highest in  $\text{LiNO}_3$  and the lowest in  $\text{KNO}_3$ . However, the capacitance retention of the  $\text{MnO}_2$  electrode during cycling is the worst in the  $\text{LiNO}_3$  electrolyte and the best in the  $\text{KNO}_3$  electrolyte. This is because the insertion and extraction of smaller cations induce greater structural changes (as inferred from the more drastic shifts of Raman band features), which are potentially detrimental to long-term reversible operation of the supercapacitor electrodes.



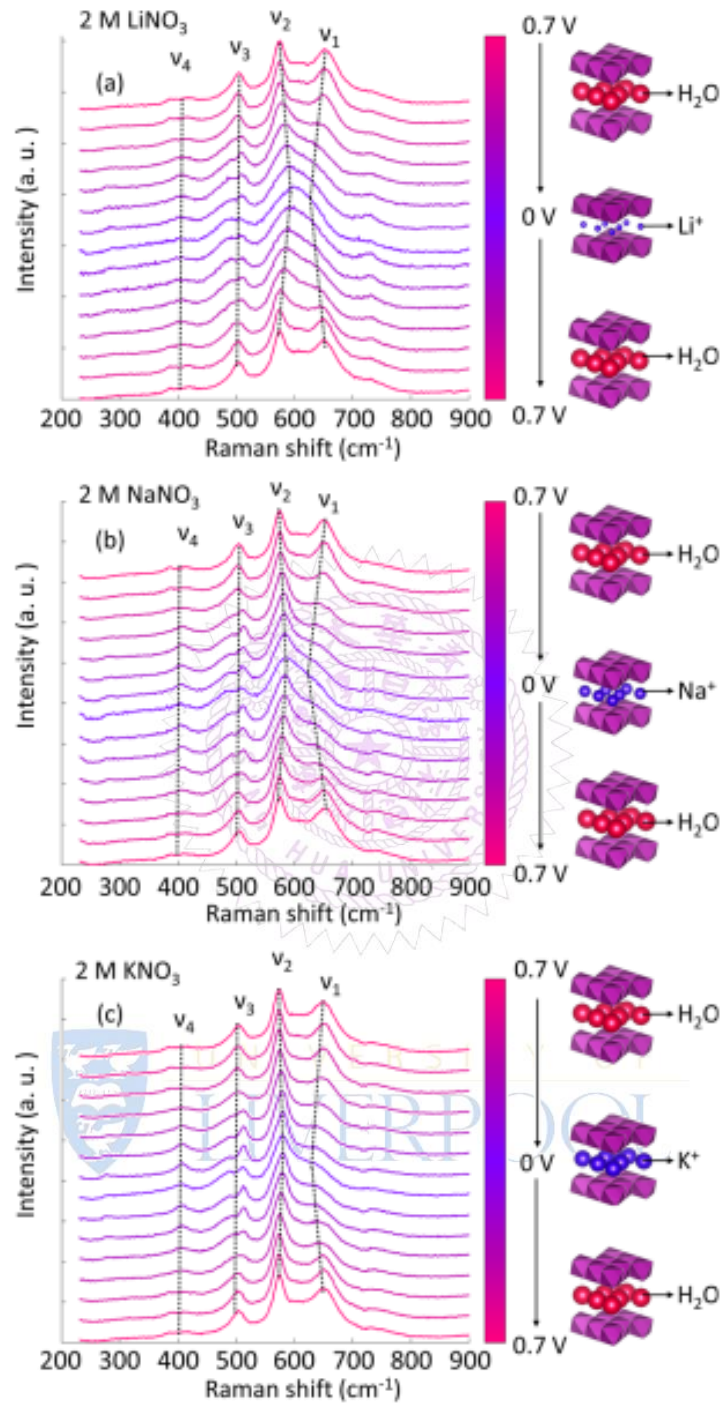


**Figure 2–15** Raman spectroscopic evolution of pseudocapacitive MnO<sub>2</sub> thin film when WE is cycled between 0.7, 0, and 0.7 V (vs Ag/AgCl) in 2 M (a) LiNO<sub>3</sub>, (b) NaNO<sub>3</sub>, and (c) KNO<sub>3</sub> aqueous electrolyte. The dash lines were applied to show the evolution of band positions ( $v_1 - v_4$ ) as a function of WE potential approximately. A colour bar was used to depict the WE potential. The schematic sketches of cation-incorporated MnO<sub>2</sub> and water-incorporated MnO<sub>2</sub> corresponding to high-potential state and low-potential state, respectively, are also shown [147].

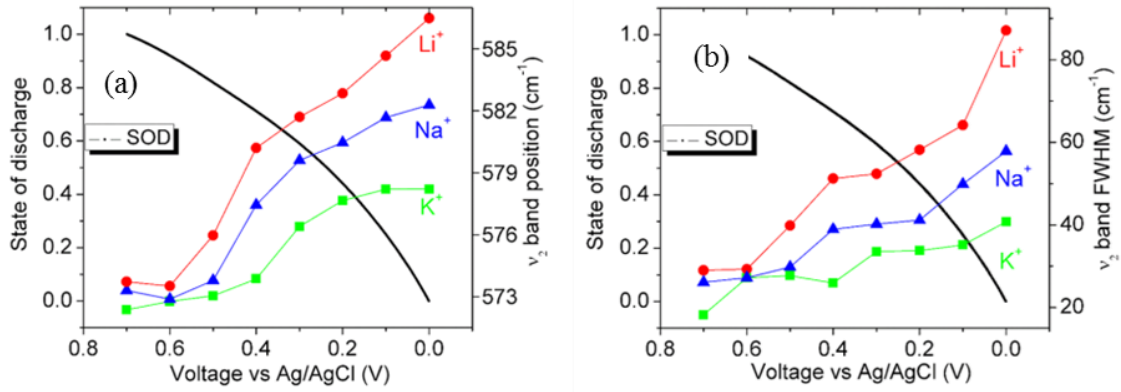
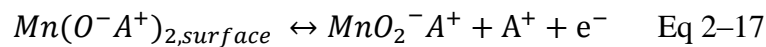
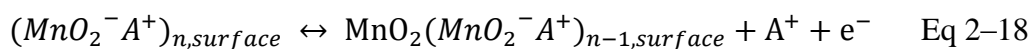


**Figure 2–16** Key spectroscopic features of pseudocapacitive MnO<sub>2</sub> model electrode as functions of WE potential when LiNO<sub>3</sub>, NaNO<sub>3</sub>, and KNO<sub>3</sub> were used as electrolyte. The state of discharge (SOD) is also plotted in each subplot to correlate with spectroscopic features. (a) The  $\nu_2$  band positions as a function of WE potential. (b) The FWHM of  $\nu_2$  as a function of WE potential [147].

Chu *et al.* [129] used EQCM analyses to have more understanding on the charge–discharge process of amorphous MnO<sub>2</sub> in Na<sub>2</sub>SO<sub>4</sub> electrolyte in 2012. The CVs and corresponding  $\Delta m$ –E curves of amorphous MnO<sub>2</sub> measured between –0.2 and 1.2 V at 25 mV s<sup>-1</sup> are shown in Figure 2–17. In the potential range of –0.2~0.2 V (vs. Ag/AgCl), the reversible redox transition between Mn(III)/Mn(II) can be found. Since the mass–charge ratio (MCR) is much lower than 19 and 23 for H<sub>3</sub>O<sup>+</sup> and Na<sup>+</sup>, respectively, the expelling/inserting from/into MnO<sub>x</sub> mainly contributes from H<sup>+</sup>.



where the major species of A<sup>+</sup> is H<sup>+</sup> with minor amount of H<sub>3</sub>O<sup>+</sup> and Na<sup>+</sup>. The ideal capacitive performance is between 0.2 and 0.8 V, which is attributed to the partial oxidation/reduction of MnO<sub>x</sub>. The expelling/inserting from/into the oxide can be expressed as:



On the other hand, mass loss can be observed not only in positive scan but also in the negative scan in the potential range of 0.8~1.2 V, indicating the dissolution of Mn

species in this potential window is severe. The re-deposition of  $\text{MnO}_x$  between 0.8 and 0.2 V on the followed negative sweep due to the mass increase in this potential window can be found. Therefore, the electrochemical reactions involve not only the redox transition of superficial Mn species but also the dissolution/re-deposition of  $\text{MnO}_x$  (including Eq 2-18 and 2-19).

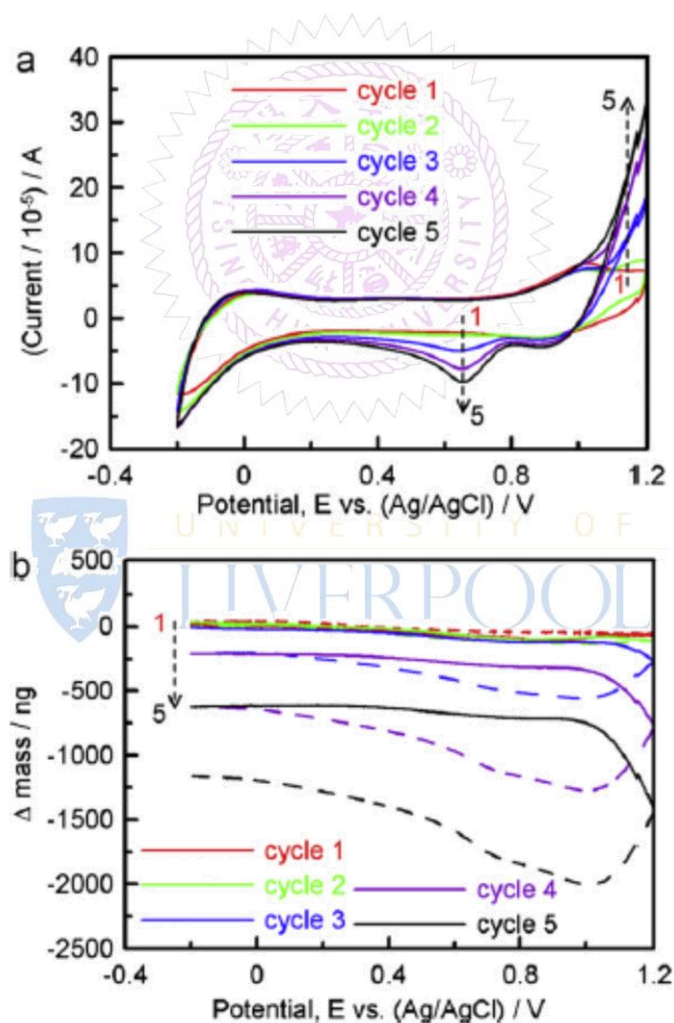
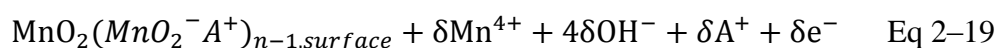
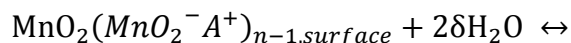


**Figure 2-17** (a) Cyclic voltammograms and (b)  $\Delta m$ -E curves of  $\alpha\text{-MnO}_x$  measured between  $-0.2$  and  $1.2$  V at  $25$   $\text{mV s}^{-1}$  for 5 cycles in  $10$  mM  $\text{Na}_2\text{SO}_4$ . The solid lines stand for the positive scans and the dash lines represent the negative scans [129].

## 2.5 Raman Spectroscopic Applications

Raman spectroscopy is a technique used to observe vibrational/rotational modes of molecules by inelastic scattering. The incident light (usually laser with the wavelength from near-infrared to near-ultraviolet range) is exposed to a sample, but the energy of laser beam is too low to excite to excited electronic states. Instead, the photons of laser beam produce an oscillating polarisation in the molecules, exciting to virtual state. If the polarisation in the molecule does not couple to other possible polarisations, the scattered photon will have the same energy as the incident photon. This elastic scattering is known as Rayleigh scattering. On the other hand, two types of inelastic scattering with much lower intensity comparing with Rayleigh scattering can be found as Stoke and anti-Stoke scattering. The emitted photon energy is lower than absorbed energy in the former. The latter is the opposite (shown in Figure 2-18). The spectrum of inelastic scattered photons is termed as Raman spectrum, which the intensity of the scattered light as a function of its frequency difference to the incident photons (also called Raman shift). Stokes and anti-Stokes lines only arise if the polarisability changes during the vibration (selection rule), which yields complementary information from infrared spectroscopy.

Raman spectroscopy can be used to analyse a wide range of materials, including gases, liquids and solids. It can also provide unique and valuable information on molecular and crystal structures, such as the force constant and bond length for molecules. Among the local probes, vibrational spectroscopies, i.e. Raman scattering and Fourier transform infrared (FTIR), are techniques sensitive to the short-range environment of oxygen coordination around the cations in oxide lattices. Since Raman scattering technique can solve the problem of phase determination when various environments are present. As a general rule, the frequencies and relative intensities of

the bands are sensitive to coordination geometry and oxidation states. Thus, the spectra are less affected by the grain size or the degree of long-range order of the lattice [126]. Besides, Raman scattering is sensitive to amorphous components and those with short-range order, it yields a more complete and reliable description of materials such as the manganese oxides, where crystalline disorder may be expected [148].

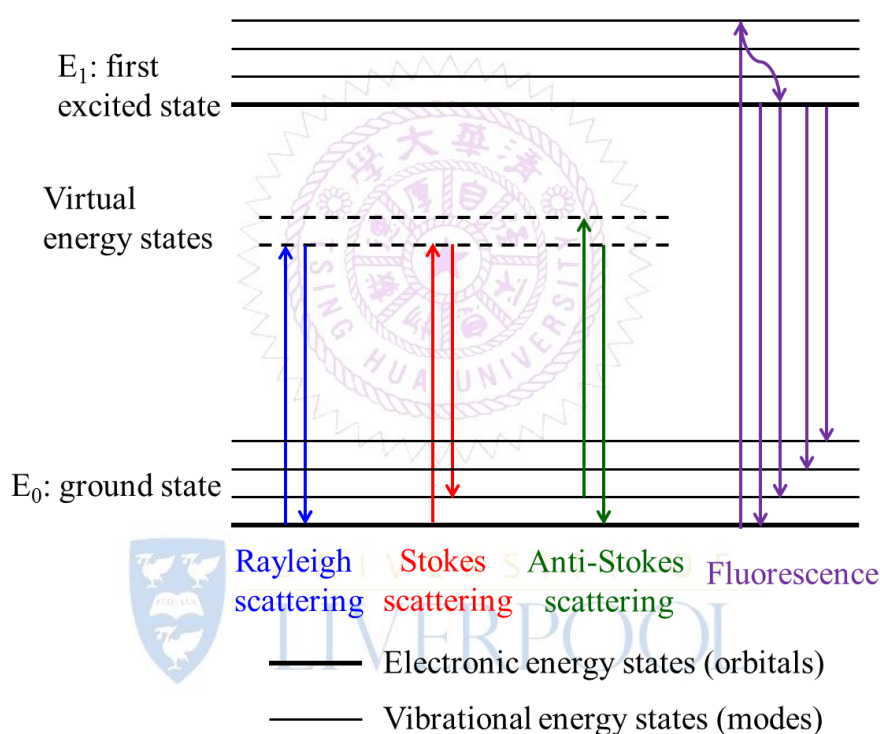
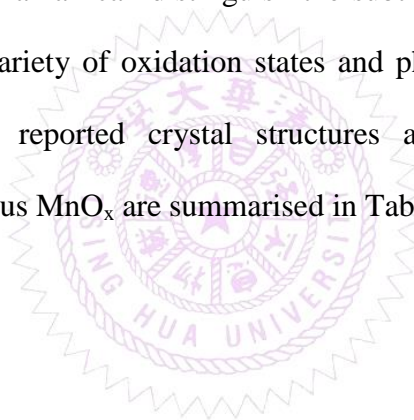


**Figure 2–18** Schemes for Rayleigh (elastic) scattering, Stokes (inelastic) scattering, anti–Stokes (inelastic) scattering and fluorescence.

Moreover, the use of *in situ* measurement techniques can provide ‘real’ and ‘instant’ information of the samples without any effects from post-treatment process. The *in situ* measurements can be done by applying different thermal, chemical and electrochemical conditions. Thus, *in situ* Raman spectroscopy has been used for different materials and various applications. For example, *in situ* Raman has been extensively used to study electrochemical doping, electronic structures, and

oxidation/reduction behaviours of carbonaceous materials [149–156]. Raman spectroscopy is a powerful technique to characterise short-range order of surface molecular species (especially for covalent character of the metal–oxygen bond) [124, 157]. Therefore, *in situ* Raman has also been used for understanding metal–oxygen bonding in oxide–based materials [158–162] even though the oxides are not well crystallised.

Accordingly, Raman analyses have been widely used to characterise various manganese oxides, since Raman can distinguish the subtle differences of vibrational modes of  $\text{MnO}_x$  with a variety of oxidation states and phases [124–126, 148, 163–171]. For example, the reported crystal structures and corresponding Raman vibrational modes of various  $\text{MnO}_x$  are summarised in Table 2–1.



UNIVERSITY OF  
LIVERPOOL



**Table 2–1** The reported crystal structures and Raman vibrational modes of MnO<sub>x</sub> in literature.

Compound	Mineral	Lattice parameter (Å)	Raman vibrational modes (cm <sup>-1</sup> )
MnO <sub>2</sub> 1D tunnel			
α-MnO <sub>2</sub>	Hollandite with Ba <sup>2+</sup> in the (2×2) tunnels	Tetragonal ( <i>I4/m</i> ) a=9.96; c=2.85 [164]	259 <sup>w</sup> , 410 <sup>w</sup> , 507 <sup>m</sup> , 586 <sup>m</sup> , 628 <sup>m</sup> [164] 180 <sup>s</sup> , 380 <sup>b</sup> , 483 <sup>m</sup> , 570 <sup>s</sup> , 635 <sup>s</sup> [165] 185 <sup>s</sup> , 392 <sup>w</sup> , 582 <sup>s</sup> , 649 <sup>m</sup> [163]
α-MnO <sub>2</sub>	Coronadite with Pb <sup>2+</sup> in the (2×2) tunnels	Tetragonal [164]	332 <sup>w</sup> , 388 <sup>w</sup> , 495 <sup>w</sup> , 585 <sup>m</sup> , 626 <sup>s</sup> [164]
β-MnO <sub>2</sub>	Pyrolusite (1×1)	Tetragonal ( <i>P4<sub>2</sub>/mnm</i> ) a=4.39; c=2.87 [164]	324 <sup>w</sup> , 376 <sup>w</sup> , 486 <sup>w</sup> , 538 <sup>s</sup> , 665 <sup>s</sup> , 750 <sup>w</sup> [126] 319 <sup>w</sup> , 377 <sup>w</sup> , 486 <sup>w</sup> , 538 <sup>s</sup> , 665 <sup>s</sup> , 750 <sup>w</sup> [164] 523 <sup>m</sup> , 576 <sup>m</sup> , 650 <sup>m</sup> [125] 186 <sup>m</sup> , 330 <sup>w</sup> , 390 <sup>w</sup> , 518 <sup>w</sup> , 582 <sup>s</sup> , 630 <sup>m</sup> , 737 <sup>w</sup> [166]
R-MnO <sub>2</sub>	Ramsdellite (1×2)	Orthorhombic ( <i>Pbnm</i> ) a=4.53; b=9.27; c=2.87 [164]	294 <sup>w</sup> , 518 <sup>w</sup> , 580 <sup>m</sup> , 630 <sup>m</sup> , 680 <sup>w</sup> , 740 <sup>w</sup> [126] 275 <sup>w</sup> , 387 <sup>m</sup> , 490 <sup>w</sup> , 522 <sup>s</sup> , 575 <sup>s</sup> , 630 <sup>sh</sup> , 648 <sup>m</sup> , 742 <sup>w</sup> [164] 392 <sup>m</sup> , 490 <sup>f</sup> , 523 <sup>m</sup> , 576 <sup>s</sup> , 650 <sup>m</sup> , 775 <sup>w</sup> [125]
γ-MnO <sub>2</sub> (EMD)	Nsutite <sup>a</sup> (1×1)/(1×2)	Complex tunnel (hexagonal) a=9.65; c=4.43 [164]	With pyrolusite intergrowth Pr=29%: 264, 337, 379, 491, 520, 572, 631, 670, 738 [164] 280, 382, 458, 515, 572, 634, 732 [164] 278 <sup>m</sup> , 494 <sup>m</sup> , 527 <sup>m</sup> , 582 <sup>s</sup> , 658 <sup>s</sup> , 770 <sup>b</sup> [163]
	Cryptomelane (2×2)		183 <sup>w</sup> , 310 <sup>w</sup> , 370 <sup>w</sup> , 475 <sup>w</sup> , 510 <sup>w</sup> , 578 <sup>m</sup> , 650 <sup>s</sup> , 745 <sup>w</sup> [167]
Mn <sub>6</sub> O <sub>18</sub> ·xH <sub>2</sub> O	Todorokite (3×3)	Monoclinic [164] P2/m [148]	263 <sup>w</sup> , 358 <sup>w</sup> , 590 <sup>w</sup> , 641 <sup>s</sup> [164]
Mn <sub>5</sub> O <sub>10</sub> ·xH <sub>2</sub> O	Romanechite	Monoclinic [164]	284 <sup>w</sup> , 372 <sup>w</sup> , 515 <sup>w</sup> , 578 <sup>s</sup> , 643 <sup>m</sup> ,



	(2×3) (NMD)	C2/m [148]	721 <sup>w</sup> [164]
MnO <sub>2</sub> 2D layer			
δ-MnO <sub>2</sub>	Birnessite MnO <sub>2</sub> (1×∞)	Hexagonal a=2.85; c=7.25; d <sub>i</sub> =7.25 [172]	296 <sup>w</sup> , 383 <sup>w</sup> , 506 <sup>m</sup> , 575 <sup>s</sup> , 623 <sup>m</sup> , 646 <sup>s</sup> , 732 <sup>w</sup> [126] 296 <sup>w</sup> , 485 <sup>sh</sup> , 506 <sup>m</sup> , 575 <sup>s</sup> , 646 <sup>s</sup> , 730 <sup>w</sup> [148] 296 <sup>w</sup> , 303 <sup>w</sup> , 506 <sup>m</sup> , 575 <sup>s</sup> , 656 <sup>s</sup> , 730 <sup>w</sup> [164] 503 <sup>w</sup> , 578 <sup>f</sup> , 650 <sup>f</sup> [18] 506 <sup>m</sup> , 565 <sup>s</sup> , 648 <sup>b</sup> [165]
δ-MnO <sub>2</sub>	Na-birnessite MnO <sub>2</sub> (1×∞)	Monoclinic (C2/m) a=5.17; b=2.85; c=7.31; d <sub>i</sub> =c sinβ= 7.11; β=103.2° [172]	500 <sup>m</sup> , 578 <sup>s</sup> , 640 <sup>s</sup> [148] Peak deconvolution: 150 <sup>w</sup> , 196 <sup>w</sup> , 282 <sup>w</sup> , 344 <sup>w</sup> , 405 <sup>w</sup> , 495 <sup>m</sup> , 570 <sup>s</sup> , 610 <sup>s</sup> , 651 <sup>s</sup> [168] 281 <sup>m</sup> , 406 <sup>m</sup> , 509 <sup>w</sup> , 581 <sup>s</sup> , 639 <sup>s</sup> [169]
δ-MnO <sub>2</sub>	Li-birnessite MnO <sub>2</sub> (1×∞)	Monoclinic (C2/m) a=5.13; b=2.85; c=7.12; d <sub>i</sub> =c sinβ= 6.94; β=103° [148]	280 <sup>m</sup> , 378 <sup>w</sup> , 410 <sup>m</sup> , 490 <sup>sh</sup> , 510 <sup>m</sup> , 585 <sup>s</sup> , 625 <sup>s</sup> [148]
MnO <sub>2</sub> 3D network			
λ-MnO <sub>2</sub>	Spinel (1×1)	Cubic (Fd3m) a=8.04 [164]	460 <sup>w</sup> , 497 <sup>w</sup> , 592 <sup>s</sup> [164]
Other valence states of MnO <sub>x</sub>			
α-Mn <sub>2</sub> O <sub>3</sub>	Bixbyite	Cubic (Ia3) a=9.41 [164]	192 <sup>w</sup> , 314 <sup>m,b</sup> , 404 <sup>w</sup> , 481 <sup>w</sup> , 592 <sup>m</sup> , 645 <sup>w</sup> , 698 <sup>w</sup> [164] 509 <sup>m</sup> , 581 <sup>s</sup> , 630 <sup>w</sup> , 650 <sup>w</sup> [125] 194 <sup>w</sup> , 307 <sup>w</sup> , 653 <sup>w</sup> , 697 <sup>w</sup> [170]
γ-Mn <sub>2</sub> O <sub>3</sub>		Tetragonal [164]	263 <sup>w</sup> , 308 <sup>w</sup> , 512 <sup>w</sup> , 631 <sup>s</sup> , 670 <sup>sh</sup> [164]
Mn <sub>3</sub> O <sub>4</sub>	Hausmannite (spinel)	Tetragonal (I4 <sub>1</sub> /amd) a=9.81; c=2.85 [164]  Tetragonal (I4 <sub>1</sub> /amd) a=5.746; c=9.463 [171]	310 <sup>w</sup> , 357 <sup>w</sup> , 485 <sup>w</sup> , 579 <sup>w</sup> , 653 <sup>s</sup> [164] 317 <sup>w</sup> , 370 <sup>w</sup> , 658 <sup>s</sup> [166] 320 <sup>w</sup> , 370 <sup>w</sup> , 659 <sup>s</sup> [18] 289 <sup>w</sup> , 315 <sup>m</sup> , 370 <sup>m</sup> , 477 <sup>w</sup> , 660 <sup>s</sup> [170] 292 <sup>w</sup> , 321 <sup>w</sup> , 376 <sup>w</sup> , 479 <sup>w,b</sup> , 659 <sup>s</sup> [171]

MnO	Manganosite	Cubic ( <i>Fm3m</i> ) a=4.44 [164]	250 <sup>w</sup> , 531 <sup>m</sup> , 591 <sup>w</sup> , 654 <sup>m</sup> [164]
MnOOH	Groutite	Orthorhombic ( <i>Pbnm</i> ) a=4.56; b=10.70; c=2.87 [164]	142 <sup>m</sup> , 213 <sup>w</sup> , 253 <sup>w</sup> , 352 <sup>w</sup> , 384 <sup>m</sup> , 528 <sup>m</sup> , 552 <sup>s</sup> , 615 <sup>m</sup> , 648 <sup>w</sup> [164]
In Raman peak intensity: w, m and s represent weak, medium and strong In Raman peak shape: b, f and sh represent broad, flat and shoulder			

Table 2–1 clearly demonstrates Raman spectroscopy is a powerful tool to distinguish various MnO<sub>x</sub> since it can detect the subtle differences of manganese–oxygen bonds in different MnO<sub>x</sub>. And the Raman spectra measured in literature offer the fingerprint of various MnO<sub>x</sub>. For example, the hausmannite Mn<sub>3</sub>O<sub>4</sub> (denoted as Mn<sup>3+</sup>Mn<sup>2+</sup><sub>2</sub>O<sub>4</sub> in spinel) is a normal tetragonal spinel structure with space group I4<sub>1</sub>/amd (*D*<sub>4h</sub><sup>19</sup>). The elementary unit cell contents Mn<sub>4</sub>Mn<sub>8</sub>O<sub>16</sub>. Factor–group analysis predicts 10 infrared–active modes (4A<sub>u</sub> + 6E<sub>u</sub>) and 14 Raman–active modes (2A<sub>1g</sub> + 2B<sub>1g</sub> + 4B<sub>2g</sub> + 6E<sub>g</sub>) [164]. This compound is highly stable under the laser beam. The Raman active bands of hausmannite Mn<sub>3</sub>O<sub>4</sub> were observed at 289, 315, 370, 477, and 660 cm<sup>-1</sup>. Bands at 310–320 and 360–370 cm<sup>-1</sup> are the bending mode of Mn<sub>3</sub>O<sub>4</sub>, while 650–660 cm<sup>-1</sup> is the characteristic of all the spinel structures (such as Fe<sub>3</sub>O<sub>4</sub>) that the A<sub>1g</sub> mode corresponds to the Mn–O breathing vibration of Mn<sup>2+</sup> in tetrahedral coordination [18, 164].

For MnO<sub>2</sub>, it was reported that all MnO<sub>2</sub> structures can be considered to be a close–packed network of oxygen atoms in which Mn<sup>4+</sup> cations (ionic radius of 0.53 Å) are differently distributed [126, 148, 164]. These distributions are conveniently described by filled MnO<sub>6</sub> octahedra sharing opposite octahedral edges to form endless chains, which can in turn be linked to neighbouring octahedral chains by sharing corners or edges. MnO<sub>x</sub> can be classified according to the number of MnO<sub>6</sub> units and

the number of  $\text{MnO}_6$  octahedral chains between two basal layers to form tunnel,  $T_{m,n}$ , openings [164].

Layered birnessite structure, denoted as  $T_{1,\infty}$ , where  $\text{MnO}_6$  octahedral layers was reported to have a vacancy in one over every six octahedral sites [148]. The interlamellar space contained cations more or less hydrated.  $\text{MnO}_{1.85} \cdot 0.6\text{H}_2\text{O}$  birnessite supports this layered structure, in which  $\text{Mn}^{2+}$  ions together with water molecules occupy the interlayer space in order to counter balance the charge defects in  $\text{MnO}_6$  sheets (i.e, the sequence along the c-axis:  $\text{O}-\text{Mn}^{4+}-\text{O}-\text{Mn}^{2+}-\text{H}_2\text{O}-\text{Mn}^{2+}-\text{O}-\text{Mn}^{4+}-\text{O}$ ) [148, 164]. The correlation between the frequency position of the Raman-active modes and the degree of polymerisation shows that  $\text{MnO}_{1.85} \cdot 0.6\text{H}_2\text{O}$  birnessite has an average of 4.8 shared edges per  $\text{MnO}_6$  octahedron [126, 164].

According to the group theory calculation reported by Julien *et al.* [148], Na-birnessite  $\text{MnO}_2$  ( $\text{Na}_{0.32}[\text{Mn}^{4+}]_{0.68}[\text{Mn}^{3+}]_{0.32}\text{O}_2 \cdot 0.6\text{H}_2\text{O}$ ) with monoclinic  $C2/m$  space group ( $Z = 4$ ), i.e.  $C_{2h}^3$  spectroscopic symmetry, are predicted to show 9 Raman-active modes with 3  $A_g$ + 6  $B_g$  species and 12 infrared-active modes with 4  $A_u$ +8  $B_u$  species. Experimental results show that seven peaks are detected in the Raman spectrum of the monoclinic Li-birnessite  $\text{MnO}_2$ , while three bands are recorded in the Raman spectrum of Na-birnessite  $\text{MnO}_2$ . The discrepancy between group factor analysis and Raman data is probably attributed to the defect chemistry and the local disorder of the birnessite structure. Nevertheless, Dias *et al.* [168] reported the spectra of Na-birnessite  $\text{MnO}_2$  can be deconvoluted by 9 Lorentzian curves.

Interestingly, Raman spectroscopy can distinguish cation intercalated within layer spaces of birnessite  $\text{MnO}_2$  due to the structural change of birnessite  $\text{MnO}_2$  upon the intercalation process. For layer birnessite  $\text{MnO}_2$ , the Raman active bands for  $\text{MnO}_2$  are at 500–510, 575–585, and 625–650  $\text{cm}^{-1}$ , which represent Mn–O stretching

vibration of  $\text{MnO}_6$  octahedra, Mn–O stretching vibration of the basal plane of  $\text{MnO}_6$  sheets and the symmetric stretching vibration of Mn–O of the  $\text{MnO}_6$  group, respectively [18, 148]. For Li– (or Na–) birnessite  $\text{MnO}_2$ , the bands below  $300\text{ cm}^{-1}$  and within  $300\text{--}500\text{ cm}^{-1}$  were indicated as stretching modes of  $\text{LiO}_6$  (or  $\text{NaO}_6$ ) octahedron and  $\text{LiO}_4$  (or  $\text{NaO}_4$ ) tetrahedron, since Li (or Na) ions occupy the trigonal prismatic sites of monoclinic  $\text{Li}_x\text{MnO}_2$  or  $(\text{Na}_x\text{MnO}_2)$  [148, 168, 169]. Besides, Zhou *et al.* [169] observed two well-defined peaks at 281 and  $406\text{ cm}^{-1}$  for Na–birnessite  $\text{MnO}_2$ , corresponding to the stretching modes of  $\text{NaO}_6$  octahedron and  $\text{NaO}_4$  tetrahedron. On the other hand,  $\text{Na}^+$  ions incorporate into birnessite  $\text{MnO}_2$  lattice during the reduction process leads to shorter Mn–O chemical bonds of the  $\text{MnO}_6$  layer and partial reduction of  $\text{Mn}^{4+}$ . As a result, the stiffened Mn–O bond on the basal plane leads to a shift toward high wavenumber (i.e., ca.  $575$  to  $578\text{ cm}^{-1}$ ). And the band related to symmetric stretching of Mn–O of  $\text{MnO}_6$  shifts toward lower wavenumber (i.e., ca.  $646$  to  $640\text{ cm}^{-1}$ ) is attributed to the inherent nature of  $\text{Mn}^{3+}$  and the softening the Mn–O bond along the interlayer direction [146, 148].

## 2.6 Electrochemically Activated Manganese Oxide

Studies on electrochemically activated  $\text{MnO}_x$  have been reported in literature [17–23], which oxidation of hausmannite  $\text{Mn}_3\text{O}_4$  to either amorphous or birnessite  $\text{MnO}_2$  in neutral aqueous electrolyte can be achieved by electrochemical activation methods. The formed  $\text{MnO}_2$  (i.e., electrochemically activated  $\text{MnO}_x$ ) produces an improved capacitive performance due to the redox reaction (pseudocapacitance) between Mn(IV) and Mn(III). Therefore, the electrochemically activated  $\text{MnO}_x$  is another approach for  $\text{MnO}_x$  material which can be applied either in pseudocapacitors or in asymmetric-type ECs.

In 2004, Broughton and Brett [102] reported sputtered Mn/MnO thin film can be anodic oxidation to higher Mn valence states and further provides pseudocapacitance of the  $\text{MnO}_x$  thin film. Followed this study, the same group found the improved capacitive performance after anodic oxidation is related to the newly-formed amorphous  $\text{MnO}_2$  surface film. The surface morphology changes from a fully dense film of Mn/MnO to a porous surface layer of  $\text{MnO}_2$  [119]. Furthermore, the authors found this porous  $\text{MnO}_2$  layer only exists in the outermost surface film, while the inner layer is partly crystalline  $\text{Mn}_3\text{O}_4$ . Based on the Pourbaix diagram, the authors proposed the anodic oxidation of Mn/MnO in neutral aqueous electrolyte leads to the formation of  $\text{Mn}_3\text{O}_4$ , then  $\text{Mn}_2\text{O}_3$  and further to  $\text{MnO}_2$  [173]. XPS Mn 3s spectra confirmed the sequence of oxidation is as follows: 2+, 2+/3+, 3+ and eventually to 4+.



UNIVERSITY OF  
LIVERPOOL

**Table 2–2** Reported material characterisation analyses on electrochemical activation from Mn<sub>3</sub>O<sub>4</sub> to MnO<sub>2</sub>.

Synthetic method	Post treatment	Total time	Analyses during activation <sup>a</sup>	Identified activated MnO <sub>x</sub>	references
Electrostatic spray deposition from Mn(CH <sub>3</sub> COO) <sub>2</sub> precursor at 260 °C by 10 kV	Annealing at 900 °C for 10 hr	>10 hr	XRD, XPS, SEM	Birnessite MnO <sub>2</sub>	[17]
Electrostatic spray deposition from MnCl <sub>2</sub> precursor by 12 kV	Annealing at 200–400 °C for 3 hr	>3 hr	XRD, XANES (Mn–K edge), Raman	Amorphous MnO <sub>2</sub>	[18]
Chemical bath deposition from MnSO <sub>4</sub> and urea precursor for 12 hr	N/A	~12 hr	XRD, SEM, Raman, contact angle	Birnessite MnO <sub>2</sub>	[19]
Thermal reduction of electrolytic manganese dioxide at 1050 °C for 72 hr	Ball–milled at 1000 rpm for 10 hr with acetone	~82 hr	SEM, XRD, XPS	Birnessite MnO <sub>2</sub>	[20]

<sup>a</sup> Except for the electrochemical analyses, the methods used for identifying as–prepared Mn<sub>3</sub>O<sub>4</sub> and activated MnO<sub>2</sub>.

In addition to the oxidation of Mn/MnO thin film, studies on the oxidation of hausmannite  $\text{Mn}_3\text{O}_4$  to  $\text{MnO}_2$  via cyclic voltammetric cycling in  $\text{Na}_2\text{SO}_4$  have been reported [17–23]. The as-prepared hausmannite  $\text{Mn}_3\text{O}_4$  can be obtained by electrostatic spray deposition from Mn(II) precursor, chemical bath deposition from Mn(II) and urea precursor, hydrothermal of oxygen saturated Mn(II) precursor and thermal reduction of electrolytic manganese dioxide. After hundreds of CV cycles, hausmannite  $\text{Mn}_3\text{O}_4$  can be activated to have better capacitance. According to the reported studies, the material characterisation methods, including XRD, SEM, TEM, XPS, XANES, Raman and contact angle, have been used to analyse the structure, morphology and oxidation state of  $\text{MnO}_x$  during activation process (as shown in Table 2–2). The electrochemically activated  $\text{MnO}_x$  is reported as  $\text{MnO}_2$ . Mostly, the identified activated  $\text{MnO}_x$  is birnessite  $\text{MnO}_2$ , while amorphous  $\text{MnO}_2$  has also been reported as electrochemically activated  $\text{MnO}_x$ .

Komaba *et al.* [20] reported the morphology changes from smooth and homogeneous of  $\text{Mn}_3\text{O}_4$  to a porous nanostructured layer of  $\text{MnO}_2$  upon CV cycling. The authors proposed that the porous surface layer is the re-deposition of dissolved Mn(II) (from hausmannite  $\text{Mn}_3\text{O}_4$  crystalline structure) onto the electrode surface as  $\text{MnO}_2$  during the activation process (as shown in Figure 2–19). Besides, the insignificant electrochemical activation of  $\text{Mn}_2\text{O}_3$  comparing with  $\text{Mn}_3\text{O}_4$  was found. Therefore, dissolution of Mn(II) from  $\text{MnO}_x$  crystalline is believed to be a key step for the electrochemical activation process. Furthermore, XPS C 1s spectra demonstrated the decrease of carbon additive intensity, suggesting the re-deposited  $\text{MnO}_2$  layers homogeneously cover the electrode surface. And XPS Na 1s spectra reveal the incorporation of Na into  $\text{MnO}_2$  lattice for activated  $\text{MnO}_x$ . As shown in Figure 2–20, XRD patterns clearly demonstrate the layered structure  $\text{MnO}_2$  formed after electrochemical activation. Therefore, the authors reported birnessite  $\text{MnO}_2$  is



formed after electrochemical activation process, where the  $\text{Na}^+$  ions would incorporate into  $\text{MnO}_2$  lattice during charge–discharge process.

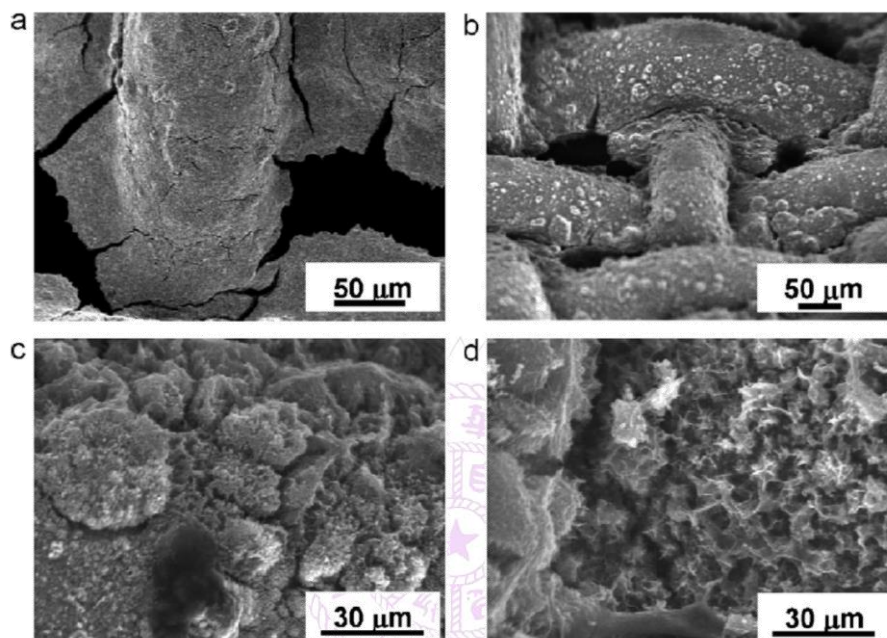


**Figure 2–19** SEM photos of the milled  $\text{Mn}_3\text{O}_4$  electrode surface (a) before and after electrochemical cycle test; after (b) 10, (c) 50 and (d) 200 cycles in 0.1 M  $\text{Na}_2\text{SO}_4$  aqueous solution [20].

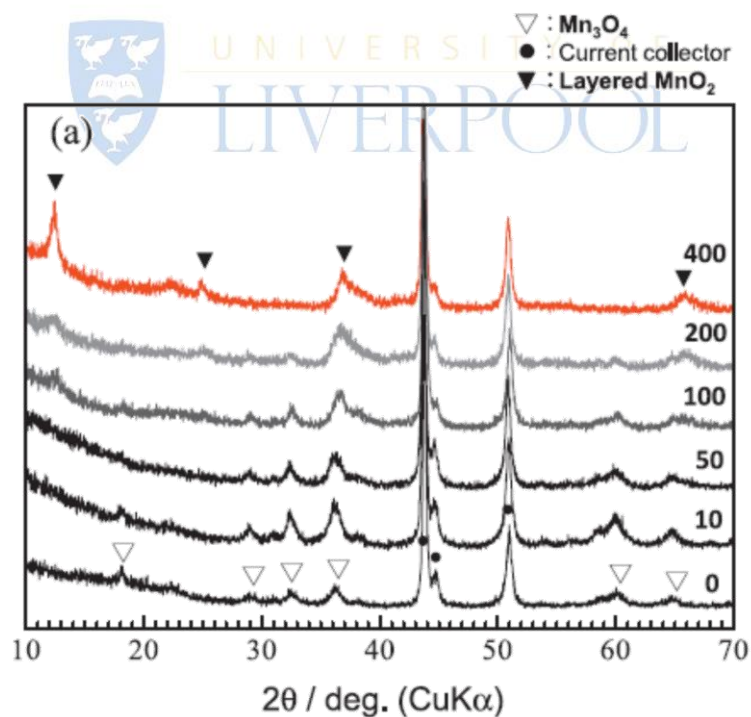


**Figure 2–20** XRD patterns of the ball–milled  $\text{Mn}_3\text{O}_4$  at different cycling stages. Cycle numbers are indicated in the figure [20].

However, the obtained  $\text{MnO}_x$  films by sputter deposition and electrostatic spray deposition are generally less than  $250 \mu\text{g cm}^{-1}$  [17, 18, 23, 102, 119, 173], in which the mass loading are too light to have practical energy storage applications. Therefore, how to obtain  $\text{Mn}_3\text{O}_4$  in a large scale is a key point for this type of pseudocapacitors. For example, Komaba *et al.* [20] successfully used thermal reduction of electrolytic manganese dioxide at  $1,050^\circ\text{C}$  for 72 hours to obtain  $\text{Mn}_3\text{O}_4$  in a large scale. After ball-milling at 1,000 rpm for 10 hours with acetone, the higher porosity of  $\text{Mn}_3\text{O}_4$  and thus better capacitive performance (enhanced by ca. 6 times) can be obtained. The electrochemically activated  $\text{MnO}_x$  exhibits ca.  $190 \text{ F g}^{-1}$  at  $10 \text{ mV s}^{-1}$  in  $1 \text{ M Na}_2\text{SO}_4$ , which is electrochemically stable for 2,000 cycles. Besides, ~85% capacitance retention is obtained when the mass increase from 2.5 to 8 mg. Hu *et al.* [22] reported a low temperature hydrothermal synthesis at  $120^\circ\text{C}$  for 12 hours from oxygen saturated  $\text{Mn}(\text{CH}_3\text{COO})_2$  precursor is a simple and energy-saving method to obtain  $\text{Mn}_3\text{O}_4$ . The activation process can be achieved with 200 CV cycles between 0 and 1 V (vs. Ag/AgCl) in  $1 \text{ M Na}_2\text{SO}_4$ , which gives a good power performance (i.e., ca.  $170 \text{ F g}^{-1}$  at  $500 \text{ mV s}^{-1}$ ) and electrochemical stability (1,500 cycles). It has been found that the electrochemical activation of  $\text{MnO}_x$  is affected by the  $\text{MnO}_x$  oxidation states, activation potential window, electrolyte cation species and electrolyte concentrations [20].

## 2.7 Redox Mechanism of $\text{NiOOH}/\text{Ni}(\text{OH})_2$

Nickel hydroxide,  $\text{Ni}(\text{OH})_2$ , has been studied for many decades, which is widely applied to alkaline rechargeable batteries [25–27], supercapacitors [28–30], sensors [174, 175], electrochromic devices [176–178] and electrocatalytic reactions [179–181]. Bode diagram describes the relationship between different phases of  $\text{Ni}(\text{OH})_2$  and  $\text{NiOOH}$  [182] (Figure 2–21). According to the diagram, two predominant redox

reactions are described,  $\gamma\text{-NiOOH}/\alpha\text{-Ni(OH)}_2$  and  $\beta\text{-NiOOH}/\beta\text{-Ni(OH)}_2$ , where both  $\text{Ni(OH)}_2$  and  $\text{NiOOH}$  are involved in these two redox reactions.

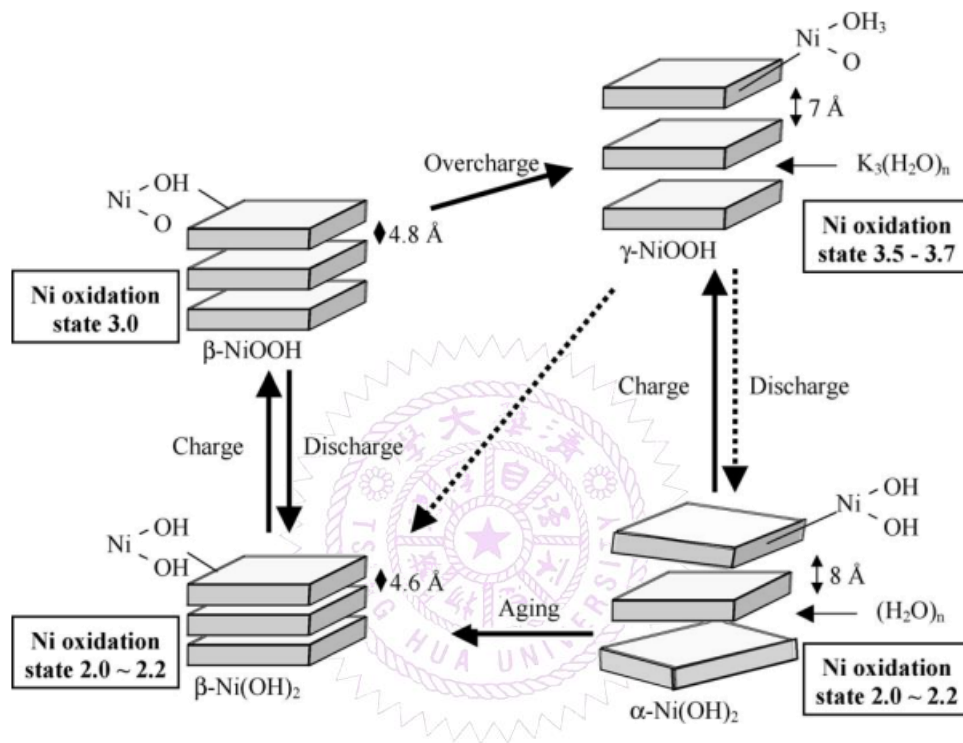


**Figure 2–21** Bode diagram of  $\text{Ni(OH)}_2$  and  $\text{NiOOH}$  [183].

In general,  $\alpha\text{-Ni(OH)}_2$  represents a set of disordered nickel hydroxides, with  $\text{Ni(OH)}_2$  layers randomly oriented and separated by intercalated water molecules and/or anions. The intercalated water molecules act as an ‘amorphous glue’ holding the randomly stacking of  $\text{Ni(OH)}_2$  layers, which is well known as ‘turbostratic’ structure [184].  $\beta\text{-Ni(OH)}_2$  is the phase in the absence of intercalated water molecules, which is thermodynamically stable and exists as mineral theophrastite in nature. The inter-slab distance of  $\alpha\text{-Ni(OH)}_2$  is ca. 8 Å, which is similar to  $\gamma\text{-NiOOH}$  (7 Å) in comparison with  $\beta\text{-Ni(OH)}_2$  (4.6 Å) and  $\beta\text{-NiOOH}$  (4.8 Å) [183]. Moreover, the mean oxidation state of nickel atom in  $\gamma\text{-NiOOH}$  ranges from 3.3 to 3.75 [183, 185–187], obviously larger than that of  $\beta\text{-NiOOH}$ , ca. 3.0 [183, 188]. Accordingly, the

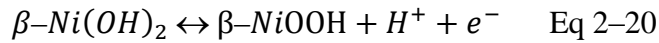
charge capacity and specific capacitance of the  $\gamma$ -NiOOH/ $\alpha$ -Ni(OH)<sub>2</sub> redox couple is higher than that of  $\beta$ -NiOOH/ $\beta$ -Ni(OH)<sub>2</sub>.

Except for these two redox reactions, overcharging of  $\beta$ -NiOOH to  $\gamma$ -NiOOH is also indicated in the diagram. Oliva *et al.* [187] reported that the reasons for  $\gamma$ -NiOOH does not directly from  $\beta$ -Ni(OH)<sub>2</sub> upon oxidation are mainly related to the kinetics and steric hindrance. The oxidation of  $\beta$ -Ni(OH)<sub>2</sub> to  $\beta$ -NiOOH only involves the removal of one proton and one electron, with no other structural change except a slight variation of crystal cell parameter. However, the oxidation of  $\beta$ -Ni(OH)<sub>2</sub> to  $\gamma$ -NiOOH requires the intercalation of H<sub>2</sub>O molecules, the exchange of protons and alkali ions and a sheet glide. As a consequence, a higher energy barrier exists and  $\beta$ -NiOOH is first obtained,  $\gamma$ -NiOOH appearing ultimately upon overcharging or ageing in KOH.

On the other hand, the occurrence of  $\alpha$ -Ni(OH)<sub>2</sub> ageing into  $\beta$  phase can be achieved either by chemical or electrochemical routes. Biphasic mechanism was reported as the mechanism of  $\alpha$  phase ageing into  $\beta$  phase when  $\alpha$ -Ni(OH)<sub>2</sub> is in contact with water, suggesting that turbostratic Ni(OH)<sub>2</sub> dissolves into water slowly and followed by nucleation and growth of  $\beta$ -Ni(OH)<sub>2</sub> from the solution [187]. The reason for the ageing process originates from the more thermodynamically stable structure of  $\beta$ -Ni(OH)<sub>2</sub> (i.e., the chemical potential is the driving force for the phase transformation). However, phase transformation of  $\alpha$ -Ni(OH)<sub>2</sub> in water solution takes a relatively long time period (ca. 43 days) [189]. With regard to the phase transformation induced by electrochemical methods in alkaline solution, the ageing process occurs much quicker in KOH (ca. few hours) [190], suggesting a different phase transformation mechanism from the proposed 'biphasic mechanism'.

EQCM is an effective technique to examine the electrochemical kinetics of redox couples involving ion-exchange because it measures the electrochemical responses

and accompanying mass changes simultaneously. Thus, EQCM studies on the redox mechanism of NiOOH/Ni(OH)<sub>2</sub> have been widely investigated for decades. In fact, some redox models have been suggested, depending on whether H<sup>+</sup> transport or OH<sup>-</sup> transport dominates and whether the mass uptake is related to the nature of cation or not [183, 187]. For β-NiOOH/β-Ni(OH)<sub>2</sub>, the redox mechanism was proposed to be the involvement of proton and electron only [187, 190]:



With regard to γ-NiOOH/α-Ni(OH)<sub>2</sub>, the inter-slab distance is much larger than β phases. It leads to the insertion of cations into the inter-slab space during redox reaction. Therefore, the redox transition also involves the uptake/loss of cation, thus, the redox mechanism is much more complicated. Cheek *et al.* [191] found the mass increase at the end of oxidation process in various 1 M solutions (LiOH, NaOH, KOH, RbOH and CsOH) is in good agreement with the linear relationship of atomic weight of alkali metal cations examined by EQCM (Figure 2-22). Therefore, the model assumes the hydration sphere of water molecules around the alkali metal cation is essentially striped away (as bare cation) upon entering the Ni(OH)<sub>2</sub> structure. On the other hand, Cordoba-Torresi *et al.* [192] found only small difference in the mass increases in 1M LiOH and KOH (Figure 2-23). The proposed redox model is based on the different hydrated coordination numbers of Li<sup>+</sup> and K<sup>+</sup>, i.e., Li<sup>+</sup>(H<sub>2</sub>O)<sub>3</sub> and K<sup>+</sup>(H<sub>2</sub>O)<sub>1</sub>, inserting into Ni(OH)<sub>2</sub>. The mass balance and charge balance equations were also used to understand the stoichiometric composition of γ-NiOOH at the end of oxidation process.

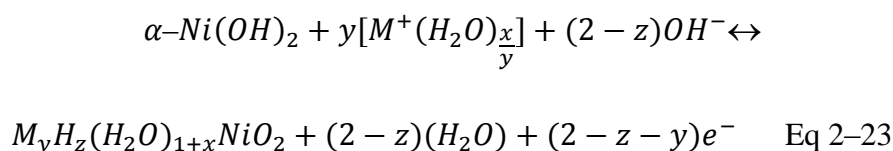
$$\Delta m = n(yAW_{M^+} + xMW_{H_2O} - (2 - z)AW_{H^+}) \quad \text{Eq 2-21}$$

$$q = nF(2 - z - y) \quad \text{Eq 2-22}$$

where  $\Delta m$  is the mass change in the oxidation process;  $n$  is the mole number of



$\text{Ni}(\text{OH})_2$ ;  $AW_M^+$  is the atomic weight of cation;  $MW_{H_2O}$  is the molecular weight of water;  $AW_H^+$  is the atomic weight of proton;  $q$  is the total charge in the oxidation process;  $F$  is the Faraday constant. The  $\gamma\text{-NiOOH}/\alpha\text{-Ni}(\text{OH})_2$  redox mechanism was therefore proposed as following:



where  $M^+$  is the cation. According to this redox model, the exact composition of  $\gamma\text{-NiOOH}$  cannot be determined because three independent parameters cannot be solved by only two equations. The authors circumvent this issue by proposing different hydrated coordination numbers of  $\text{Li}^+$  and  $\text{K}^+$ , i.e.,  $\text{Li}^+(\text{H}_2\text{O})_3$  and  $\text{K}^+(\text{H}_2\text{O})_1$ , inserting into  $\text{Ni}(\text{OH})_2$ . Besides, the authors found the continuous mass increase at the end of each cycle during cycling. However, the reasons for (and the effects of) this phenomenon was not discussed in this work. Nevertheless, the drastically different features in mass change between  $\gamma\text{-NiOOH}/\alpha\text{-Ni}(\text{OH})_2$  and  $\beta\text{-NiOOH}/\beta\text{-Ni}(\text{OH})_2$  makes EQCM to be a powerful tool to distinguish the redox behaviours between these two.

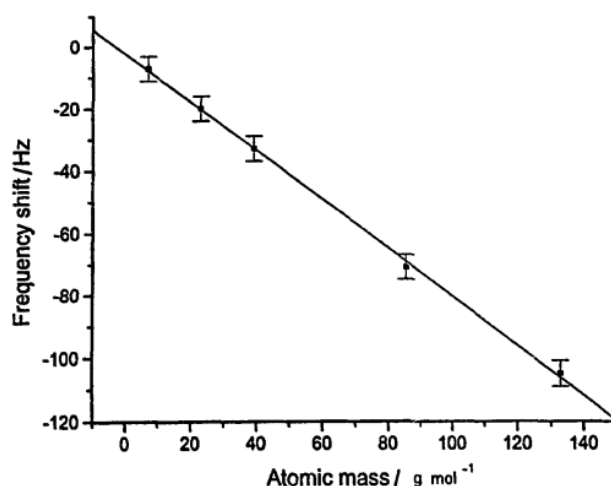


**Figure 2-22** Plot of frequency shift versus atomic number of alkali metal for  $\alpha\text{-Ni}(\text{OH})_2$  film [191].

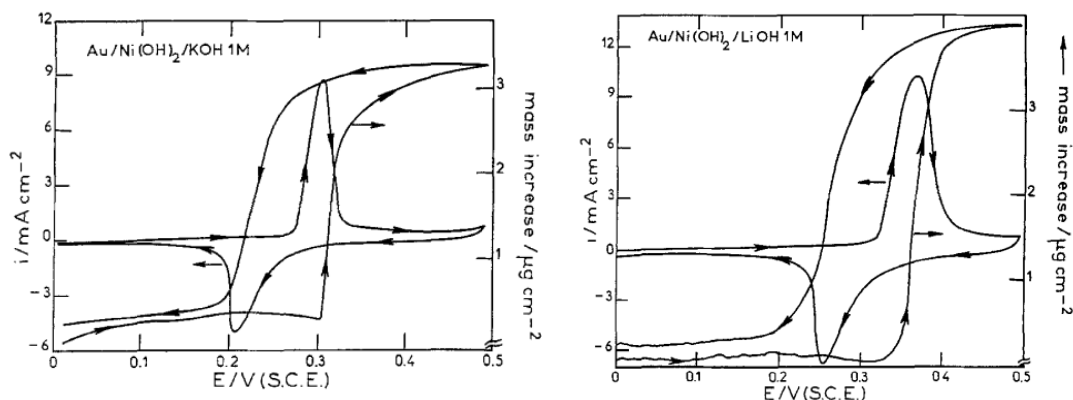


**Figure 2-23** E/i and E/ $\Delta m$  potentiodynamic profiles recorded with  $\alpha$ -Ni(OH)<sub>2</sub> film in 1M KOH (left) and LiOH (right) solution,  $v = 0.01 \text{ V s}^{-1}$  [192].

Years later, DFT calculation was introduced to determine the energetically stable  $\gamma$  phase. Van der Ven *et al.* [188] proposed the energetically stable  $\gamma$ -NiOOH phase with intercalated Na<sup>+</sup> or K<sup>+</sup> as  $\gamma$ -M<sub>0.33</sub>H<sub>y</sub>(H<sub>2</sub>O)<sub>0.66</sub>NiO<sub>2</sub> (where M is Na<sup>+</sup> or K<sup>+</sup>), which can be obtained by overcharging  $\beta$ -NiOOH or chemical synthesis routes [185, 187]. The Ni valence state is dependent on y value, which can range from 0 to 1.33. The intercalated cation can stably reside at the centre of a rectangle of oxygen atoms (two oxygen atoms from each O-Ni-O slab above and below) in a AABBCO oxygen stacking sequence of  $\gamma$ -NiOOH phase instead of the centre of a prismaticly coordinated (by oxygen atoms) interstitial site [188]. The intercalated cation and H<sub>2</sub>O is 0.33 and 0.66 per Ni, respectively, in the stable  $\gamma$ -NiOOH structure. Therefore, the results offer an explanation for the oxidation state of Ni equals to 3.66 for the charged  $\gamma$ -NiOOH. However, this composition of  $\gamma$  phase obtained from DFT calculation is based on the thermodynamics. One cannot guarantee the ‘real’  $\gamma$  composition upon potential cycling (kinetics) is the same as the one calculated from thermodynamics. Besides, several factors were ignored in this work, such as zero-potential energy, mainly due to the restricted knowledge database in 2006.



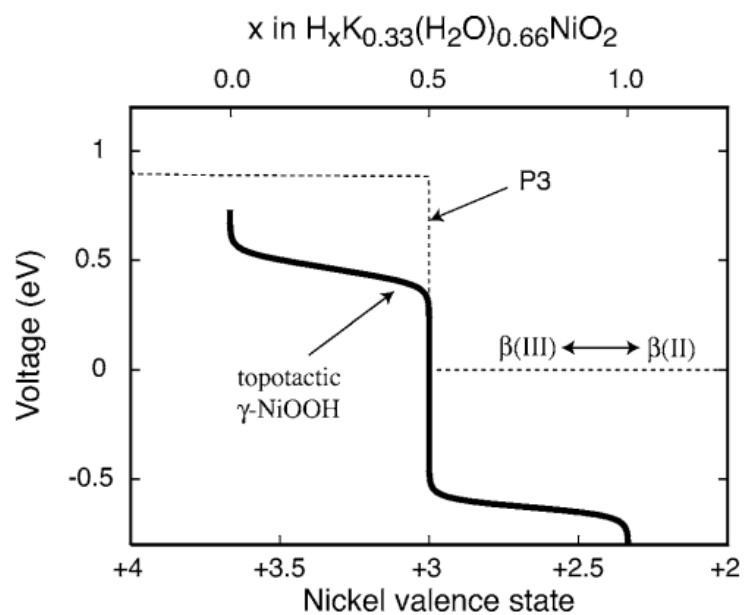
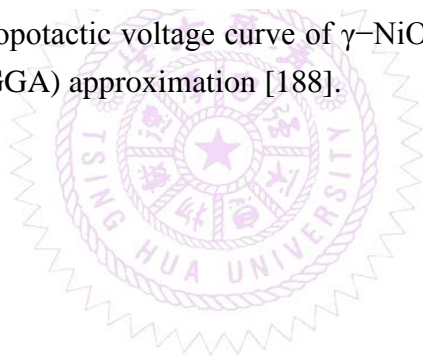


**Figure 2–24** Calculated topotactic voltage curve of  $\gamma$ -NiOOH within the generalised gradient approximation (GGA) approximation [188].



UNIVERSITY OF  
LIVERPOOL

# Chapter 3

## Experimental Methods

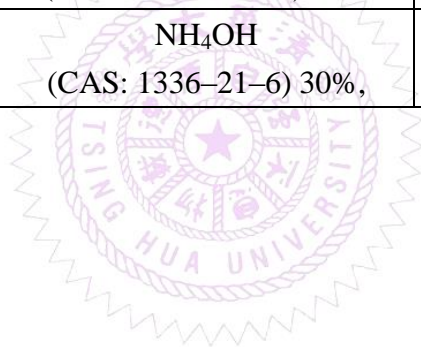
### 3.1 Chemicals and Instruments

#### 3.1.1 Chemicals

The chemicals used in this work are summarised in the following table.

Chemicals	Molecular formula	Supply	Country
Manganese acetate	$\text{Mn}(\text{CH}_3\text{COO})_2 \cdot 4\text{H}_2\text{O}$ (CAS: 6156-78-1) $\geq 99\%$	Sigma-Aldrich	USA
Sodium sulfate	$\text{Na}_2\text{SO}_4$ (CAS: 7757-82-6) $\geq 99\%$	Sigma-Aldrich	USA
Sodium nitrate	$\text{NaNO}_3$ (CAS: 7631-99-4) 95-98%	J.T. Baker	USA
Sulfuric acid	$\text{H}_2\text{SO}_4$ (CAS: 7664-93-9) $\geq 99\%$	Sigma-Aldrich	USA
Potassium permanganate	$\text{KMnO}_4$ CCAS: 7722-64-7) $\geq 99\%$	Sigma-Aldrich	USA
Methanol	$\text{CH}_3\text{OH}$ (CAS: 67-56-1) $\geq 99\%$	J.T. Baker	USA
Hydrogen peroxide	$\text{H}_2\text{O}_2$ (CAS: 7722-84-1) 30 wt. % in $\text{H}_2\text{O}$	Fluka Chemika	Japan
Activated carbon ACS-679	C	China Steel Chemical Corporation	Taiwan
XC-72	C	Cabot corporation	USA
Polyvinylidene fluoride (PVDF)	$(-\text{CH}_2\text{CF}_2-)_n$	Fluka Chemika	Japan
Poly(vinylidene fluoride-hexafluoropropylene) co-polymeric binder (Kynar-flex)	$(-\text{CH}_2\text{CF}_2-)_x$ $[-\text{CF}_2\text{CF}(\text{CF}_3)-]_y$	Arkema	France

Chemicals	Molecular formula	Supply	Country
1-Methyl-2-pyrrolidone (NMP)	$C_5H_9NO$ (CAS: 872-50-4) 99.5%	Sigma-Aldrich	USA
Nickel chloride	$NiCl_2 \cdot 6H_2O$ (CAS: 7791-20-0) $\geq 96\%$	SHOWA	Japan
Lithium hydroxide	$LiOH \cdot H_2O$ (CAS: 1310-66-3) 98.88%	TEDIA	USA
Sodium hydroxide	$NaOH$ (CAS: 1310-73-2) $\geq 97\%$	SHOWA	Japan
Potassium hydroxide	$KOH$ (CAS: 1310-58-3) $\geq 85\%$	SHOWA	Japan
Cesium hydroxide	$CsOH \cdot H_2O$ (CAS: 35103-79-8) 96%	Alfa Aesar	USA
Ammonia hydroxide	$NH_4OH$ (CAS: 1336-21-6) 30%,	J.T. Baker	USA



UNIVERSITY OF  
LIVERPOOL

### 3.1.2 Instruments

The instruments used in this work are summarised in the following table.

Instrument	Module	Supply	Country
Potentiostat	CHI 660C	CH instruments	USA
Potentiostat	CHI 4051C	CH instruments	USA
Potentiostat	EC-Lab MPG2	BioLogic Science instruments	France
Impedance spectrum analyser	IM6	ZAHNER	Germany
Inductance–Capacitance–Resistance meter (LCR meter)	LCR HiTester 3522–50T	Hioki	Japan
Microwave system	Discover SP system	CEM	USA
Reagent water system	MILLI–Q SP at 18M $\Omega$ –cm	MILLI–Q	Japan
Water thermostat	HAAKE DC3 and K20	Thermo Electron Corporation	USA

The instruments used for material characterisation are summarised in the following table.

Technique	Module	Supply	Country
XRD	MXP 18, Cu K $\alpha$ , $\lambda=1.54 \text{ \AA}$	Mac Science	UK
XRD	D8 advance, Mo K $\alpha$ , $\lambda=0.709 \text{ \AA}$	Bruker	USA
SEM	JSM–6610	JEOL	Japan
TEM	Philips Tecnai F20 G2	FEI Corporation	USA
BET	NOVA N1200e	Quantachrome instruments	USA
Raman	Renishaw inVia, using a He–Ne laser (632.8 nm) focused through an inverted microscope (Leica), via a 50 $\times$ objective lens (Leica)		
XPS	a PSP Vacuum Technology electron energy analyser (angle integrating $\pm 10^\circ$ ) and a dual anode Mg K $\alpha$ (1253.6 eV) X–ray source		

## 3.2 Experimental

### 3.2.1 Preparation of Graphene Oxide

Graphene oxide (GO) was prepared by the modified Hummer's method, i.e., the natural graphite powder was oxidised by  $\text{KMnO}_4$  in concentrated  $\text{H}_2\text{SO}_4$ . First, 0.25 g  $\text{NaNO}_3$  was added into 10 mL 95–98%  $\text{H}_2\text{SO}_4$  and stirred until  $\text{NaNO}_3$  powder dissolved. Then, 0.2 g graphite powder was added gradually while stirring. After that, 1 g  $\text{KMnO}_4$  was added into the solution to oxidise graphite. The above mixture was under sonication for 1 hr and then, 20 mL deionised water was added slowly into the mixture. The reaction was terminated by adding few  $\text{H}_2\text{O}_2$  drops. The solid product was separated via centrifugation at 11,000 rpm, washed repeatedly with deionised water. Afterwards, the obtained solutions were either well dispersed in deionised water (GO/ $\text{H}_2\text{O}$ ) or methanol (GO/methanol) with the concentration about 2 mg/ml.

### 3.2.2 Preparation of Manganese Oxide

0.5 g manganese acetate was dissolved in 10 ml GO/methanol solution and stirred for 2hr. The mixture solution was dropped onto a 9 cm–diameter Petri dish (with 1 ml each Petri dish) and were heated under an air flow at a ramping rate of  $1\text{ }^\circ\text{C min}^{-1}$  to  $300^\circ\text{C}$  and then cooled down to room temperature. The resultant manganese oxide powders were collected and ground afterward. The powders were then made into slurry for casting onto current collectors. The composition of slurry is shown in the next section.

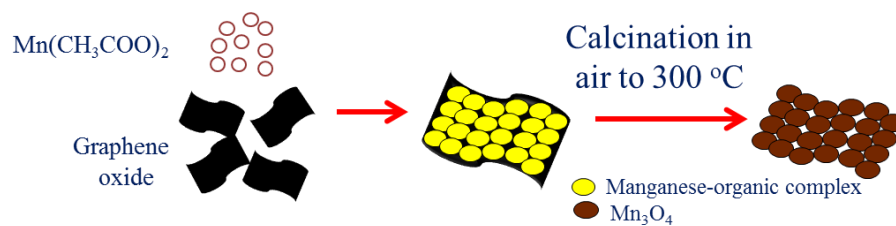


**Figure 3–1** Schematic diagram of Mn<sub>3</sub>O<sub>4</sub> synthetic process.

### 3.2.3 Microwave–Assisted Hydrothermal Reduction of Graphene Oxide

10 ml GO/H<sub>2</sub>O solution was diluted with 10 ml deionised water and then transferred to microwave reaction tube. The microwave–assisted hydrothermal reduction process was operated at 190 °C and 200 W for 10 min. After cooling down to room temperature, the as–obtained solution (black colour) was filtered and washed by deionised water repeatedly. Finally, the reduced graphene oxide (RGO, in powder form) was collected after dried in 85 °C oven overnight.

### 3.2.4 Graphite Substrate Pretreatment

The graphite substrates (provided by Well Hand Industrial Corporation, Taiwan) were cut into the size of 10 mm × 10 mm with the thickness about 3~5 mm. These substrates were first abraded with ultrafine SiC paper grit 400 and grit 800 and then the substrates were drilled a hole on the side for sheathing a copper wire on each substrate. The as–obtained current collectors were rinsed in an ultrasonic bath of deionised water for 10 min and then etched in a 0.5 M H<sub>2</sub>SO<sub>4</sub> solution at room temperature for 10 min. Finally, it will be rinsed in the ultrasonic bath of deionised water for 30 min to wash off all the residuals. Finally, the current collectors were dried in 85 °C oven overnight.



### 3.2.5 Electrodeposition of Ni(OH)<sub>2</sub>

Ni(OH)<sub>2</sub> at present work was synthesized by cathodic deposition from a deposition bath consist of 40 mM NaNO<sub>3</sub> and 20 mM NiCl<sub>2</sub>•6H<sub>2</sub>O at 70°C. Galvanostatic technique was applied with a fixed current at 1 mA for 750 s. Graphite substrates were used as the working electrode, and the surface area and pretreatments were followed the previous procedure. Three-electrode system was used. The reference and counter electrode were Ag/AgCl (Argenthal, 3 M KCl, 0.207 V vs. SHE at 25C) and a platinum wire (99.95%, 0.5 mm in diameter and 8 cm in length), respectively.

### 3.3 Electrochemical Analyses

Electrochemical characteristics were obtained by electrochemical analyser systems, CHI 660C or CHI 4053a (CH instruments, USA) or EC-Lab MPG2 (BioLogic Science instruments, France). The three-electrode compartment system was used to characterise the electrode materials with an Ag/AgCl electrode (Argenthal, 3 M KCl, 0.207 V vs. SHE at 25 °C) and a platinum wire as reference and counter electrode, respectively. The prototype EC full cells, including symmetric EDLCs and asymmetric ECs were tested in a two-electrode configuration without adding separator between two electrodes. All solutions used in this work were prepared with deionized water produced by a reagent water system (Milli-Q SP, Japan) at 18 MΩ cm. The alkaline electrolytes used for electrochemical characterization was maintained at 25 °C by a water thermostat (Haake DC3 and K20), and degassed with purified N<sub>2</sub> for 30 min before measurements.

In Chapter 4, commercial activated carbon ACS-679, without any treatments

was used as electroactive material. After mixing AC (70%) with poly(vinylidene difluoride) (PVDF, 30%) in N-methylpyrrolidinone (NMP) solvent, the slurry was coated onto graphite substrates to form electrode. There are three types of AC-based EDLCs discussed in Chapter 4; the first cell (cell A) consists of charge-balanced negative and positive electrodes where their mass loading of AC is equal to 0.4 and 0.6 mg cm<sup>-2</sup>, respectively. The second one (cell B) consists of a positive electrode with its charges two times of that on the negative electrode (i.e., 0.25 and 0.75 mg cm<sup>-2</sup> for the negative and positive electrodes, respectively). The third EDLC (cell C) consists of a negative electrode with its charges two times of that on the positive electrode (i.e., 0.57 and 0.43 mg cm<sup>-2</sup> for the negative and positive electrodes, respectively). Note that the total mass loading of AC in each EDLC was controlled as 1.0 mg and the exposed geometric area of both positive and negative electrodes is 1 cm<sup>2</sup>. The electrolyte was 0.5 M Na<sub>2</sub>SO<sub>4</sub> degassed with purified nitrogen (or argon) gas flow before and during the measurements.

In Chapter 5, as-prepared MnO<sub>x</sub> powders (Mn<sub>3</sub>O<sub>4</sub> described in Chapter 3.2.2) (70%) were mixed with PVDF (20%) and XC-72 powders (10%) for 30 min and NMP solvent was added to form a slurry. Reduced graphene oxide (RGO) was obtained by microwave-assisted hydrothermal reduction of graphene oxide (described in Chapter 3.2.3). Both the slurry and RGO were coated separately onto graphite substrates to form electrodes. The mass loading of Mn<sub>3</sub>O<sub>4</sub> and RGO is 0.70 and 1.04 mg cm<sup>-2</sup>, respectively and the exposed area of all electrodes is 1 cm<sup>2</sup>. For the two-electrode mode, a full cell without separator consisting of RGO (negative electrode) and activated MnO<sub>x</sub> (positive electrode) was measured. The open-circuit potentials of RGO and activated Mn<sub>3</sub>O<sub>4</sub> are -0.1 and 0.1 V (vs. Ag/AgCl), respectively. The electrolyte was 0.5 M Na<sub>2</sub>SO<sub>4</sub> degassed with purified nitrogen (or argon) gas flow before and during the measurements.

In Chapter 6, the working electrodes were prepared by casting the slurry composed of as-prepared  $\text{MnO}_x$  (70%), XC-72 powders (20%) and poly(vinylidene fluoride-hexafluoropropylene) co-polymeric binder (Kynar-flex, Arkema) powders (10%) onto graphite electrodes. Total mass of each electrode is 0.71 mg. The electrolyte was 0.5 M  $\text{Na}_2\text{SO}_4$  degassed with purified nitrogen (or argon) gas flow before and during the measurements.

In Chapter 7, the alkaline electrolytes were LiOH, NaOH, KOH, CsOH and  $\text{NH}_4\text{OH}$  in 1 M concentration. The working electrodes were prepared by cathodic deposition of  $\text{Ni}(\text{OH})_2$  according to previous section.

All the calculations of specific capacitance were calculated based on the total mass of active materials (including polymeric binder) on either working electrode for three-electrode compartment or both of positive and negative electrodes for two-electrode configurations. The specific energy and power were also calculated based on the two-electrode configurations with considering total mass of active materials (including polymeric binder) on both positive and negative electrodes.

### 3.3.1 Cyclic Voltammetry (CV)

Cyclic voltammetry technique was employed as the preliminarily analytic method in this study. The working electrode (or a full cell) is cycled within a potential window, where the potential applied on the working electrode (or a full cell) is continuously changed with a constant scan rate. An ideally capacitive electrode exhibits the amount of stored charge proportional to potential ( $C=\Delta Q/\Delta V$ ), i.e., the current response is constant and proportional to scan rate within the electrochemically stable potential window ( $I=C \Delta V/\Delta t$ ). Therefore, a rectangular and symmetric shape along x-axis (electrode potential) can be observed in CV.

The specific capacitance of material can be calculated from the cyclic voltammograms based on the following equation:

$$C_s = \frac{Q}{\Delta V \cdot m} = \frac{\int i(dV/v)}{\Delta V \cdot m} = \frac{\int idt}{\Delta V \cdot m} \quad \text{Eq 3-1}$$

$$C_s = \frac{C_{s,p} + C_{s,n}}{2} \quad \text{Eq 3-2}$$

Where  $C_s$  is the average specific gravimetric capacitance ( $\text{F g}^{-1}$ ) obtained from positive ( $C_{s,p}$ ) and negative ( $C_{s,n}$ ) sweeps.  $Q$  (C) is the voltammetric charge in one sweep,  $\Delta V$  (V) is the potential window,  $m$  is the mass (g) of sample being coated on current collector,  $v$  is the scan rate ( $\text{V s}^{-1}$ ).

The charge ratio of positive and negative sweeps can be calculated by the under-curve-area to preliminarily understand the electrochemical reversibility of ECs. Besides, CVs measured at a huge range of scan rates can be also applied to conduct the kinetic analyses, which allow to distinguish capacitive (surface or near-surface) and diffusive (inner surface or in the bulk) charge storage contribution of total voltammetric charge [32, 193].

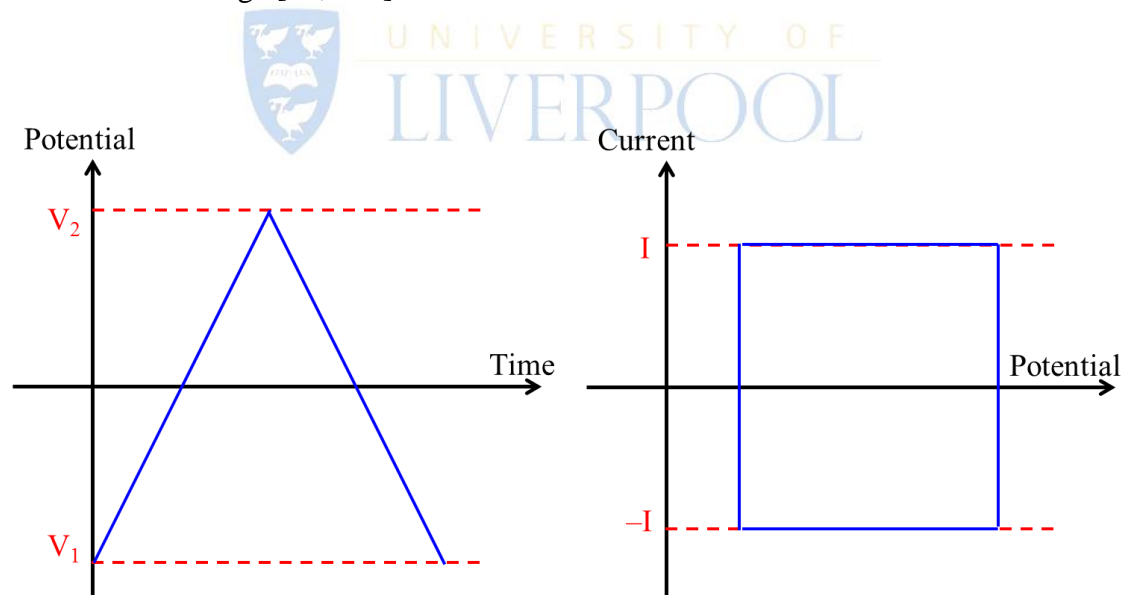


**Figure 3-2** (a) Cyclic voltammetric sweep and (b) the corresponding ideal capacitive performance.

In this work, CVs were used to preliminarily understand the electrochemical behaviours of electroactive materials. In Chapter 4 and 5, the charge ratios of positive and negative sweeps were calculated by the under-curve-area to firstly evaluate the electrochemical reversibility of full-cell ECs. In Chapter 6, CV was conducted to activate as-prepared  $\text{MnO}_x$  for 500 cycles.

### 3.3.2 Chronopotentiometry (CP)

Constant current charge-discharge method was used to analyse the capacitive performance of prototype EC full cells, including symmetric EDLCs and asymmetric ECs. The specific capacitance EC full cells were measured from the galvanostatic discharge curves on the basis of the following equation:

$$C_s = \frac{Q_d}{\Delta V \cdot W_T} = \frac{I t_d}{\Delta V \cdot W_T} \quad \text{Eq 3-3}$$

where  $I$  (A),  $t_d$  (s) and  $Q_d$  (C) represent the discharge current, discharge time and the charge obtained from the discharge of the EC full cells.  $W_T$  is the total weight of active material on the two electrodes.

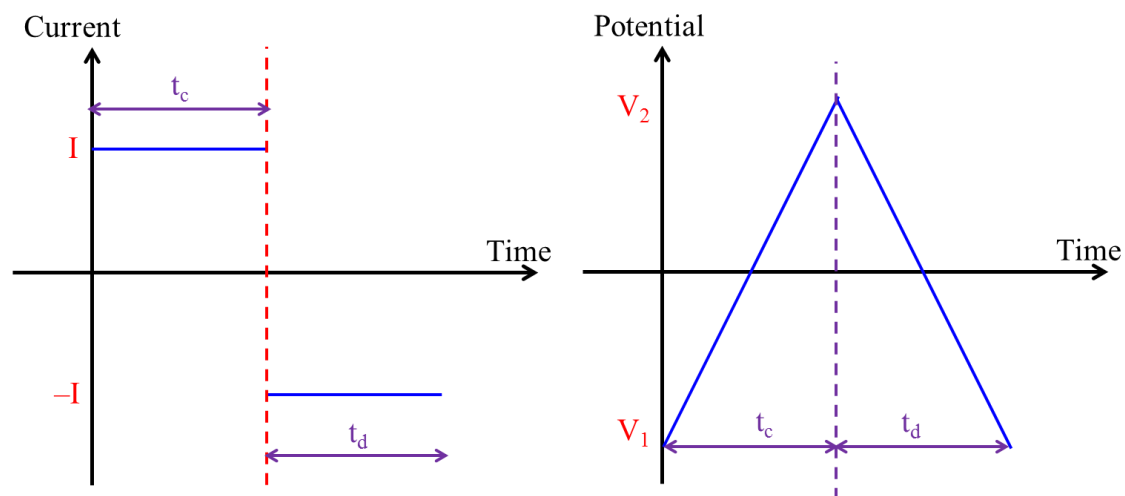


**Figure 3-3** (a) Constant current charge-discharge function and (b) the corresponding ideal capacitive performance.

The current and energy efficiency were calculated based on the constant current charge–discharge profiles of full cells according to the equations:

$$\text{Current Efficiency (CE)} = \frac{Q_d}{Q_c} \quad \text{Eq 3-4}$$

$$\text{Energy Efficiency (EE)} = \frac{\int V t_d}{\int V t_c} \quad \text{Eq 3-5}$$

where  $Q_d$  and  $Q_c$  are the total electrical quantity of discharge and charge (C), respectively.  $V$  is the potential (V) and  $t_d$  and  $t_c$  are the time of discharge and charge (s), respectively. Therefore,  $Vt_d$  and  $Vt_c$  stand for the area of galvanostatic charge–discharge curves integrated from discharge and charge region, respectively. Besides, the individual potentials of positive and negative electrodes were monitored during the constant current charge–discharge of full cells. The potential windows of the individual electrodes are important to understand the electrochemical behaviours during the full cells charge–discharge process. The specific energy ( $\text{Wh kg}^{-1}$ ) and power ( $\text{W kg}^{-1}$ ) of a full cell can be evaluated on the basis of Eq 3–6 and 3–7:

$$\text{Specific Energy (SE)} = \frac{C_s(\Delta V)^2}{2} \times \frac{1000}{3600} \quad \text{Eq 3-6}$$

$$\text{Specific Power (SP)} = \frac{SE}{t_d} \times 3600 \quad \text{Eq 3-7}$$

where SE and SP represent the specific energy and power of the device.  $C_s$  and  $V$  are the specific capacitance and operating cell voltage of the device, respectively.

In this work, the charge–discharge measurements were started from 0 V to the cell voltage for two–electrode configurations. Current and energy efficiency were calculated at various current loading rates ( $2\text{--}30 \text{ A g}^{-1}$ ) in order to know the charge and energy loss during charge–discharge measurements. Specific energy and power were also calculated at various current loading rates in order to estimate energy stored in devices.



### 3.3.3 Electrochemical Impedance Spectroscopy (EIS)

Electrochemical impedance spectroscopy is usually measured by applying an AC potential (sinusoidal potential excitation) to an electrochemical cell and then measuring the current through the cell. EIS is normally measured by using a small AC excitation signal in order to have 'pseudo-linear' current responses. In a linear (or pseudo-linear) system, the current responses to a sinusoidal potential will be a sinusoid at the same frequency with phase shifted. Typically, a small AC signal (e.g. 10 mV) is applied to the cell, therefore, the system is usually pseudo-linear that avoid generating harmonics.

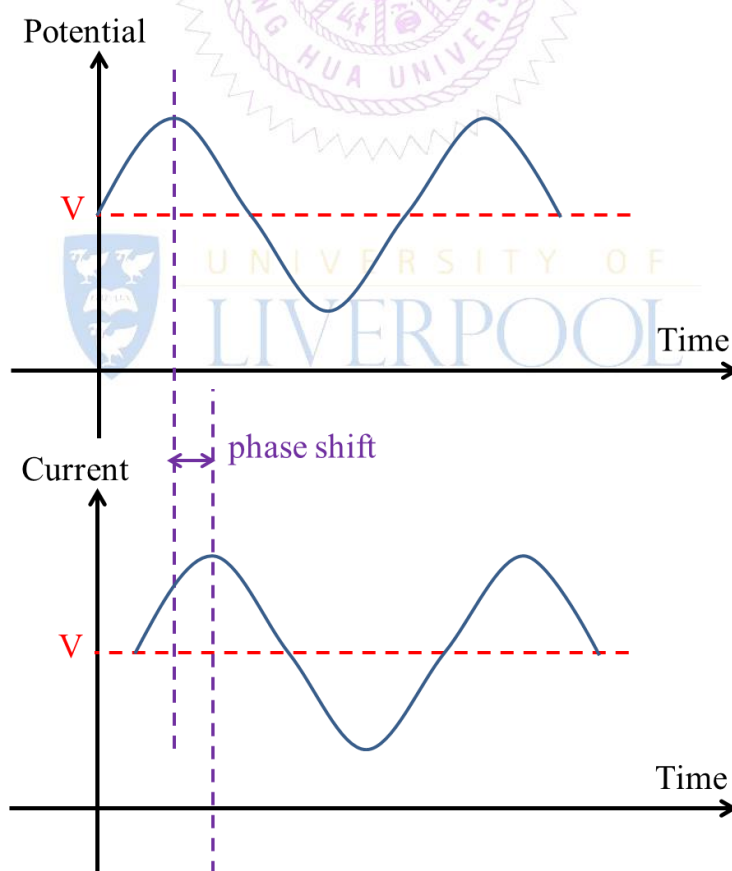


**Figure 3–4** Scheme for electrochemical impedance spectroscopy.

The EIS results were presented by Bode plot (impedance and phase angle to frequency), Nyquist plot (real part of impedance to imaginary part of impedance) and frequency dependence of specific capacitance figure (specific capacitance to frequency). For full cells, the frequency dependence of specific capacitance values can be calculated based on the imaginary part of impedance:

$$C_s = \frac{-1}{2\pi f W_T Z''} \quad \text{Eq 3-8}$$

where  $Z''$  is the imaginary part of impedance under the frequency  $f$ .

In this work, an impedance spectrum analyser, IM6 (ZAHNER, Germany), with Thales software was employed to measure and analyse the EIS spectra. The ac potential amplitude was equal to 10 mV with its frequency from 0.1 Hz to 100 kHz under a potentiostat mode (i.e., constant potential method). Impedance spectra were measured when the biased potentials were set for 30 seconds. The impedance spectra were used to know the capacitive performance of electroactive materials (i.e.,  $\text{MnO}_x$  and RGO) and full cells.

Due to the porous nature of carbon materials, the equivalent-circuit model for the carbon materials under three-electrode compartment (shown in Figure 3-5a) is composed of a series of solution resistance ( $R_s$ ), porous-electrode element and double-layer capacitance ( $C_{dl}$ ). For carbon-based EDLCs, the double-layer capacitance can be replaced by the effective cell capacitance ( $C_{cell}$ ). The porous-electrode element consists of two resistances of porous electrodes, including the ionic resistance within carbon pores ( $R_p$ ) and electrical resistance of bulk carbon ( $R_c$ ). For pseudocapacitors, the equivalent-circuit model is shown in Figure 3-5b where  $R_s$ ,  $R_{ct}$ ,  $W_f$ ,  $C_{dl}$  and  $C_f$  are solution resistance, charge-transfer resistance, finite diffusion impedance, double-layer capacitance and film Faradaic pseudocapacitance, respectively. Charge-transfer resistance represents the Faradaic redox reaction of

pseudocapacitive materials, while finite diffusion impedance stands for the diffusion of ions within the electroactive material followed by charge transfer at the interface. All the capacitance elements were fitted by a constant phase element (CPE), which is an equivalent-circuit component for modelling the imperfect capacitive behaviour. The rotation of the impedance semicircles by an angle of  $(1-\alpha)90^\circ$  for a CPE is attributed to the roughness of the electrode surfaces or the redox kinetics of active materials [194, 195]. The equivalent-circuit model for RGO//MnO<sub>x</sub> (or RGO//RuO<sub>2</sub>) asymmetric ECs is shown in Figure 3–5c, where both double-layer and pseudocapacitive behaviours are included in this model.

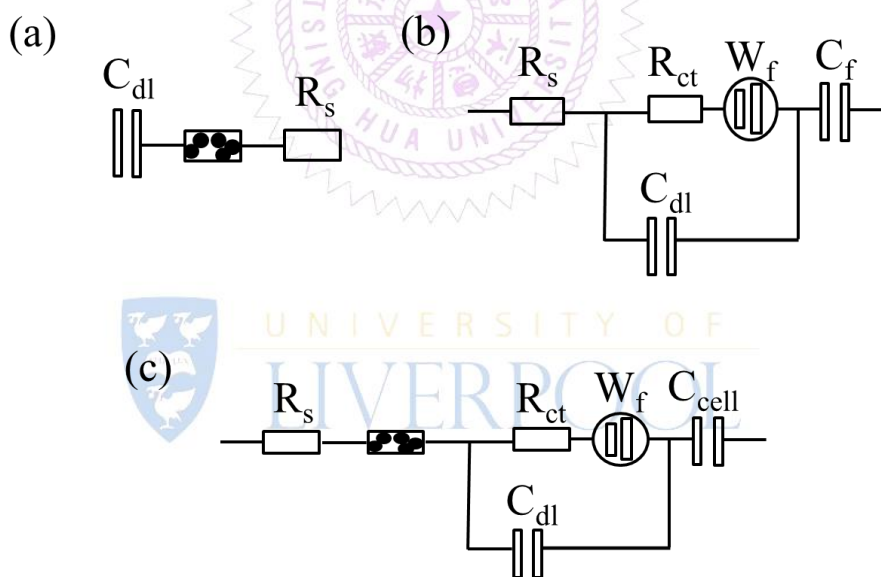


**Figure 3–5** The equivalent-circuit models used for (a) EDLCs, (b) pseudocapacitors and (c) RGO//MnO<sub>x</sub> (or RGO//RuO<sub>2</sub>) asymmetric ECs.

### 3.3.4 Inductance–Capacitance–Resistance Meter (LCR)

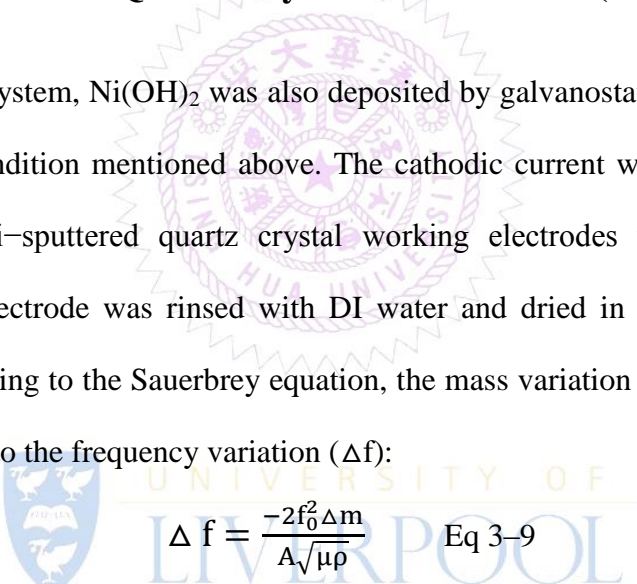
Inductance–Capacitance–Resistance meter (LCR meter) was also applied to measure the impedance and capacitive behaviour (phase angle) of full cells in the same condition as EIS analyses (i.e., ac potential amplitude = 10 mV at potentiostat

mode with the frequency from 0.1 Hz to 100 kHz). The measurements were done by averaging at least 16 data points in the range of 100–100 kHz and at least 4 data points in the range of 0.1–100 Hz.

In this work, LCR meter (HiTester 3522–50T, Hioki, Japan) was also applied to measure the impedance and capacitive behaviour (phase angle) of the EDLCs in the same frequency range as EIS analyses.

### 3.3.5 Electrochemical Quartz Crystal Microbalance (EQCM)

For EQCM system, Ni(OH)<sub>2</sub> was also deposited by galvanostatic technique from the same bath condition mentioned above. The cathodic current was fixed at 20 μA for 500 s. Au/Ti-sputtered quartz crystal working electrodes were used. After deposition, the electrode was rinsed with DI water and dried in an oven at 85 °C overnight. According to the Sauerbrey equation, the mass variation of electrode (Δm) can be correlated to the frequency variation (Δf):


$$\Delta f = \frac{-2f_0^2 \Delta m}{A\sqrt{\mu\rho}} \quad \text{Eq 3-9}$$

where  $f_0$  is the resonant frequency of the quartz crystal (7.995 MHz), A is the piezoelectric active area (0.196 cm<sup>2</sup>),  $\mu$  is shear modulus of quartz (2.947 × 10<sup>11</sup> g cm<sup>-1</sup>s<sup>-2</sup>) and  $\rho$  is the density of crystal (2.648 g cm<sup>-3</sup>).

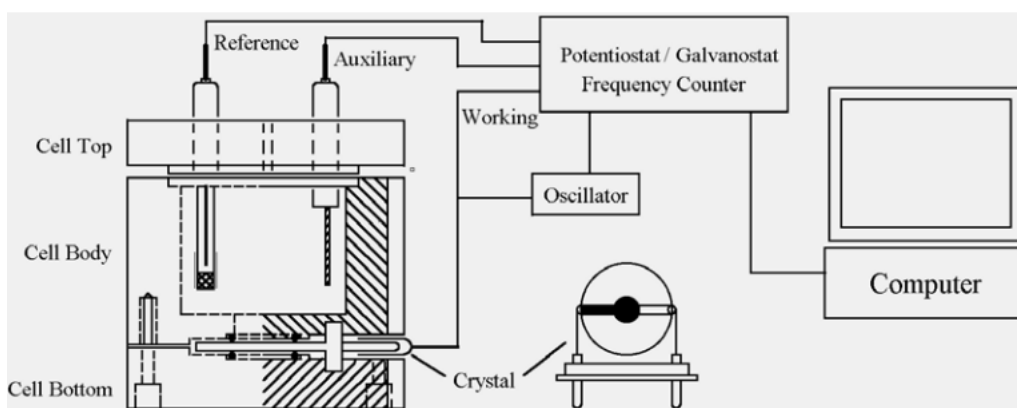


**Figure 3–6** Schematic diagram of electrochemical quartz crystal microbalance apparatus.

### 3.4 Textural Analysis

#### 3.4.1 X–ray Diffraction (XRD)

X–ray diffraction is a versatile, non–destructive technique that reveals detailed information about the chemical composition and crystallographic structure of materials. A crystal consists of a periodic arrangement of the unit cell into a lattice. The unit cell can contain a single atom or atoms in a fixed arrangement. X–rays are produced whenever high–speed electrons (from cathode, a hot W filament) collide with a metal target (such as Cu, Mo, Mg, Al etc.). According to Bragg's law,

$$2d_{hkl}\sin\theta_{hkl} = n\lambda \quad \text{Eq 3–10}$$

where  $n$  is any integer and  $(h, k, l)$  represent the Miller indices. Diffraction occurs only when Bragg's Law is satisfied for constructive interference from lattice plane  $(h, k, l)$  with spacing ' $d_{hkl}$ '.

In this study, XRD was utilised to identify the crystalline structure of as–prepared  $\text{MnO}_x$  via a  $\text{Cu K}\alpha$  source with  $\lambda=1.54 \text{ \AA}$  (MXP 18, Mac Science, UK) and activated  $\text{MnO}_x$  through a  $\text{Mo K}\alpha$  source with  $\lambda=0.709 \text{ \AA}$  (D8 advance, Bruker, USA).

### **3.4.2 Scanning Electron Microscopy (SEM)**

Scanning electron microscopy (SEM) can be used to characterise the surface morphology (topographic images) of a wide range of materials on a nanometer to micrometer scale. The electrons generated by electron guns with the energy in the range of 0.1–30 keV. The electron beam interacts with the specimen to a depth of ca. 1  $\mu\text{m}$  to produce information about the surface morphologies, composition (by Energy–dispersive X–ray Spectroscopy, EDS analysis) and element distribution of materials (by surface mapping). According to the interactions between electron beam and specimen, two types of signals are produced, backscattered electrons by elastic scattering and secondary electrons by inelastic scattering. The former strongly depends on the atomic number of material species, while the latter is generated by the interaction between energetic electron beam and weakly bound conduction band electrons in metal or outer shell valence electrons in semiconductors and insulators. In the most common or standard detection mode, secondary electron imaging (SEI), the SEM can produce very high–resolution images of a sample surface with resolution about 1 to 5 nm.

In this study, scanning electron microscopy (JSM–6610, JEOL, Japan) was used to probe the surface morphology of  $\text{MnO}_x$  during the electrochemical activation process.

### **3.4.3 Transmission Electron Microscopy (TEM)**

Transmission electron microscopy (TEM) is a microscopy technique whereby an electronic beam is transmitted through an ultrathin specimen, interacting with the specimen as electron passes through sample. TEM technique is capable of imaging at



a significantly high resolution of sample surface due to the small de-Broglie wavelength of electrons (i.e., high energy electrons generated by accelerating voltage from 100 to 1,000 kV). An image is formed from the electrons transmitted through the specimen, magnified and focused by an objective lens and appears on an imaging screen. Selected area electron diffraction (SAED) patterns can be obtained by adjusting the magnetic lenses (i.e., the back focal plane of the lens rather than the imaging plane is placed on the imaging apparatus).

In this study, FE-TEM (Philips Tecnai F20 G2, FEI Corporation, USA) was utilised to reveal the particle size of as-prepared and activated  $\text{MnO}_x$ . The as-prepared  $\text{MnO}_x$  was prepared by dissolving as-prepared  $\text{MnO}_x$  powder into ethanol solvent. And the activated  $\text{MnO}_x$  was prepared by sonicating  $\text{MnO}_x$  composite electrodes (after electrochemical activation) in acetone solvent. For both cases,  $\text{MnO}_x$ /solvents were applied 2–3 drops onto Cu TEM grids (Holey carbon films on 300 mesh copper grids, Agar Scientific, UK) and finally dried in oven at 85 °C. SAED was also used to probe the crystalline structure of  $\text{MnO}_x$  samples.



#### **3.4.4 Nitrogen Adsorption/desorption Isotherms**

BET theory was proposed by Brunauer, Emmett and Teller, which considers the possible multilayer physisorption of gas molecules on a solid surface. The concept of the theory is an extension of the Langmuir theory, which is a theory for monolayer molecular adsorption, to multilayer adsorption with the following hypotheses: (a) gas molecules physically adsorb on a solid in layers infinitely; (b) there is no interaction between each adsorption layer; and (c) the Langmuir theory can be applied to each layer. The BET method is widely used in surface science for the calculation of surface areas of porous materials by physical adsorption of gas molecules under its cryogenic

temperature (e.g. N<sub>2</sub> adsorption/desorption isotherms in 77 K).

In this study, N<sub>2</sub> adsorption/desorption isotherm was measured by NOVA N1200e (Quantachrome instruments, USA) to obtain the specific surface area (by BET method) of as-prepared MnO<sub>x</sub>.

### 3.4.5 Raman Spectroscopy

The wavelength of laser sources ranges from infrared to ultraviolet, while the most commonly used is visible region (e.g. 514, 532, 633, 785 nm etc.). In this study, Raman spectra were recorded with Raman microscope (Renishaw inVia), using a He-Ne laser (632.8 nm) focused through an inverted microscope (Leica), via a 50× objective lens (Leica). Elastic scattering (Rayleigh scattering) is filtered out, while the rest of the collected light is back-scattered through the objective and then passes through a notch filter. The light further passes through a grating spectrometer (1800 gr mm<sup>-1</sup>), and the signals finally are collected by a sensitive charge couple device (CCD).



UNIVERSITY OF  
LIVERPOOL

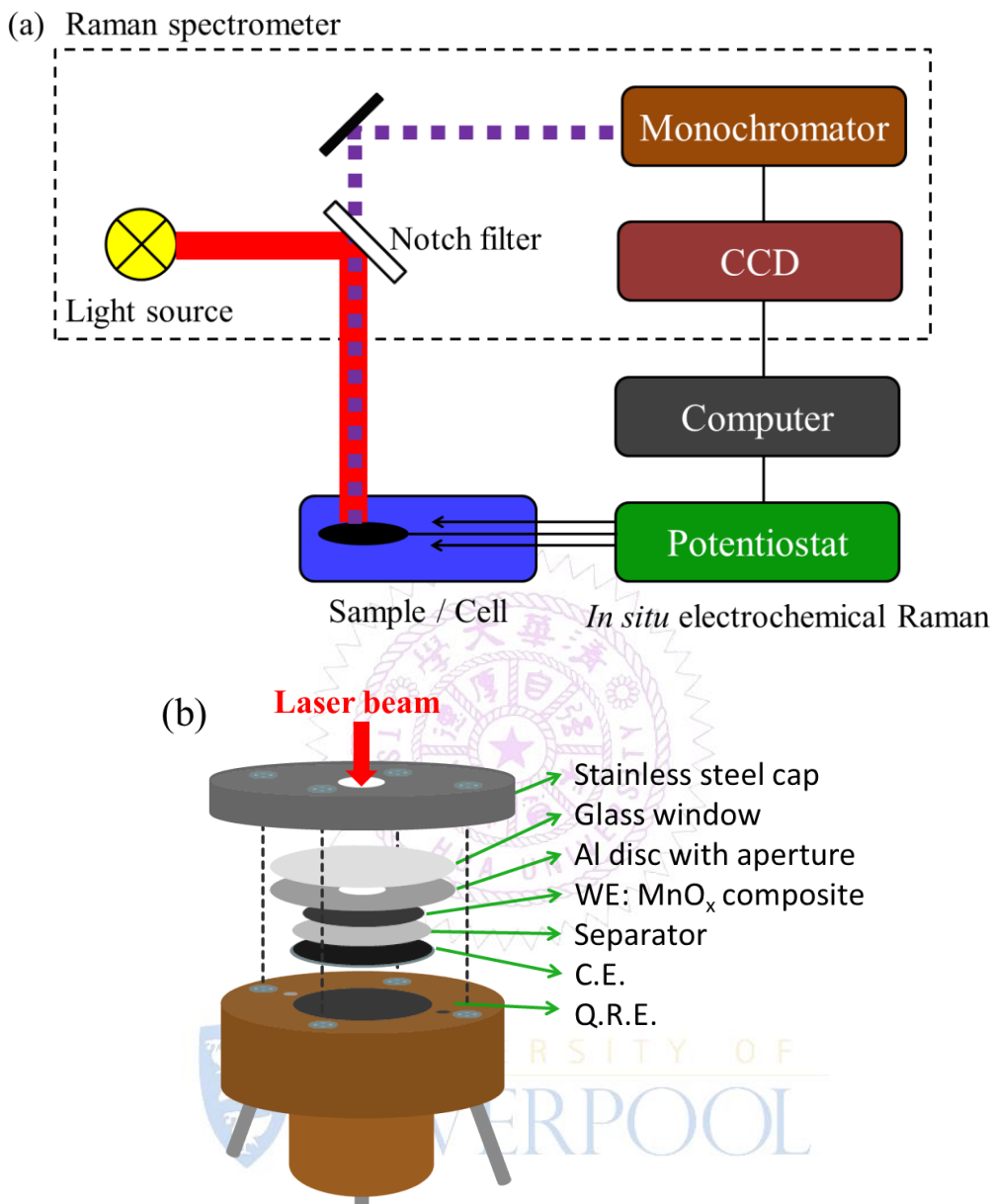


**Figure 3–7** (a) schematic diagram of *in situ* electrochemical Raman instrument and (b) the configuration of *in situ* Raman cell.

In Chapter 6, the use of *in situ* measurement techniques are important in understanding the Mn<sub>3</sub>O<sub>4</sub> activation process and charge storage mechanism in neutral aqueous electrolytes since the dried electrodes used in *ex situ* techniques may not represent the true state during electrochemical analyses. For *in situ* Raman cell configuration in Chapter 6, the working electrode was free-standing sample film composed of as-prepared MnO<sub>x</sub> (30%), XC-72 (173 m<sup>2</sup>g<sup>-1</sup>; 20%) and

poly(vinylidene fluoride–hexafluoropropylene) co–polymeric binder (Kynar–flex) powders (50%). The counter electrode was prepared by casting activated carbon ACS–679 (with 20% poly(vinylidene fluoride–hexafluoropropylene) co–polymeric binder powders) onto an Al current collector, while activated carbon free–standing film composed of ACS–679 activated carbon (40%) and Kynar–flex powders (60%) was served as the quasi–reference electrode (QRE) [196]. The three–electrode compartments were sealed in the *in situ* Raman cell with adequate amount of electrolyte (4–5 drops) [150]. The mass based on  $Mn_3O_4$  of working electrode and activated carbon of counter electrode were ca. 1 mg and 15 mg, respectively. Note that the potential of quasi–reference electrode (QRE) were tested in a beaker cell, the CV profile of  $MnO_2$  between  $-0.1$  and  $1.1$  V was extremely similar to the CV measured against an Ag/AgCl in the range between 0 and  $1.2$  V, indicating that the potential difference of QRE and Ag/AgCl is ca.  $0.1$  V (Figure 3–8). The electrolyte was  $0.5$  M  $Na_2SO_4$  degassed with purified argon gas flow before the measurements. *In situ* Raman spectra were measured at different potentials with an interval of  $200$  mV, starting from  $0.1$  V vs. QRE to  $1.1$  V (positive sweep, PS) and then back from  $0.9$  V to  $-0.1$  V (negative sweep, NS). Therefore, 12 spectra were obtained from each *in situ* Raman cycle. For each spectrum, the working electrode was pre–polarised for  $3$  min and held the potential during the spectral acquisition with the range of  $250$ – $750$   $cm^{-1}$ . The formation of  $Mn_3O_4$  triggered by an increase in lattice temperature due to local heating by laser has been widely reported [124–126]. In order to avoid this factor, the laser exposed to sample surface was controlled via the use of an appropriate filter to keep below a maximum power of  $0.37$  mW.

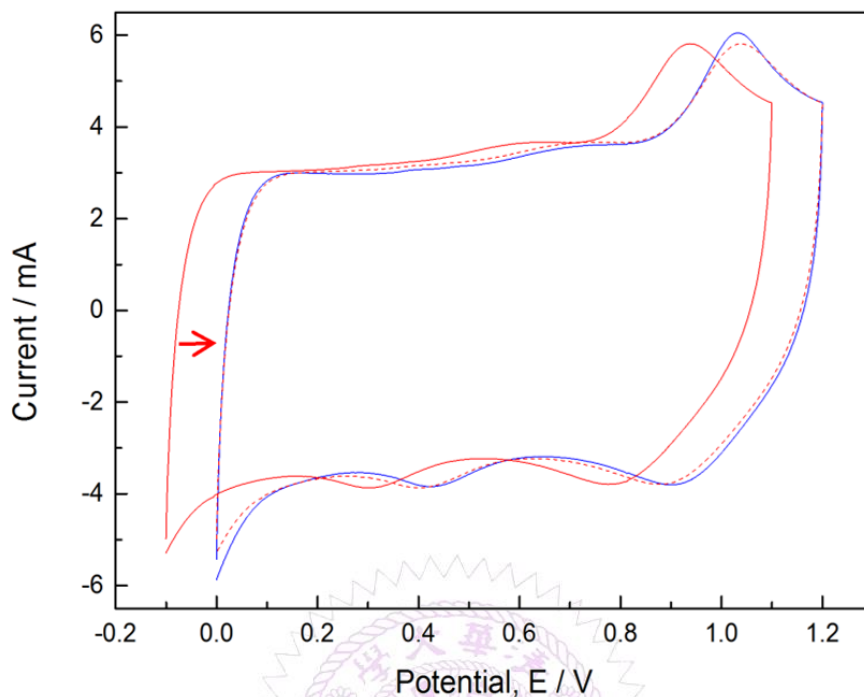


**Figure 3–8** CV of  $\text{MnO}_x$  measured at a sweep rate of  $25 \text{ mV s}^{-1}$  in  $0.5\text{M Na}_2\text{SO}_4$  against Ag/AgCl (blue) and quasi–reference electrode (red). The dash curve is measured against quasi–reference electrode after shifting by  $+0.1 \text{ V}$ .

For *ex situ* Raman experiments in Chapter 6, the working electrodes were prepared by casting the slurry composed of as–prepared  $\text{MnO}_x$  (70%), XC–72 (20%) and Kynar (10%) onto graphite electrodes. Total mass of each electrode is 0.71 mg, which is used for calculating specific capacitance. The cyclic voltammograms (CV) were measured at  $25 \text{ mV s}^{-1}$  between 0 and 1.2 V (vs. Ag/AgCl). The  $\text{MnO}_x$ –coated working electrodes were potential–cycled for 5, 10, 50, 100, 150, 200 and 500 cycles to elucidate the activation process. After CV cycling, the  $\text{MnO}_x$ –coated electrodes were gently washed by deionised water and dried in  $85^\circ\text{C}$  oven overnight.

In Chapter 7, *in situ* Raman spectra were recorded with Raman microscope (Renishaw inVia), using a He–Ne laser (632.8 nm) focussed through an inverted microscope (Leica), via a  $50\times$  objective lens (Leica). The working electrode was chemically synthesised  $\alpha\text{-Ni(OH)}_2$  [197] casting on Ni electrode surface. The reference and counter electrode were Ag/AgCl (3M NaCl) and Pt wire, respectively.

*In situ* Raman spectra were measured at rest status just after CV cycling ( $10 \text{ mVs}^{-1}$ ) between 0 and 0.45 V in alkaline electrolytes (1M LiOH, NaOH, and KOH). For each spectrum, the acquisition time is 50 seconds in the range of  $3400\text{--}3800 \text{ cm}^{-1}$  with 5 accumulations. The laser exposed to sample surface was controlled via the use of an appropriate filter to a maximum power of 3.7 mW.

Lorentz line shape is used for Raman spectra fitting in this work. It can be represented as following:

$$F(\nu) = \frac{\Gamma}{(\nu-\nu_0)^2+\Gamma^2} \quad \text{Eq 3-11}$$

where  $\nu$  is the Raman shift;  $\nu_0$  and  $\Gamma$  are position and FWHM of Raman band, respectively. The band fitting process was conducted through Renishaw WiRE 4.0 software.

### 3.4.6 X-ray Photoelectron Spectroscopy (XPS)

X-ray Photoelectron Spectroscopy (XPS) is also known as electron spectroscopy for chemical analysis (ESCA), which is a surface-sensitive analysis tool. It is widely used to understand the chemical composition and chemical environment (structure) of materials. The electrons are photo-emitted by incident X-rays (photons) and the electron kinetic energy and number of electrons that escape within 10 nm of material surface are analysed under an ultra-high vacuum condition. From XPS spectra, chemical shifts reveal the formal oxidation state and its neighbouring atoms. Therefore, the near surface chemical environment (structure) of specimen can be analysed.

In this study, XPS measurements were performed in a standard ultrahigh vacuum surface science chamber ( $2 \times 10^{-10}$  mbar) a PSP Vacuum Technology electron energy



analyser (angle integrating  $\pm 10^\circ$ ) and a dual anode Mg K $\alpha$  (1253.6 eV) X-ray source for measurements on Mn 3s, Mn 2p, O 1s, C 1s and Na 1s of MnO<sub>x</sub> samples.

### 3.4.7 X-ray Absorption Spectroscopy (XAS)

X-ray Absorption Spectroscopy (XAS) is a widely used technique for determining the atomic local structure and electronic state of matter. When the X-rays hit a sample, the oscillating electric field of the electromagnetic radiation interacts with the core-level electrons bound in an atom. Either emission of fluorescence or Auger electrons is followed by photoelectron emission by the absorption of X-rays into core-level electrons. Therefore, X-ray Absorption Near-Edge Structure (XANES) is commonly used to estimate the oxidation state of metals through the absorption edge.

The XAS in this work was measured in Beamline B18 of Diamond Light Source. The Si(111) double crystal was used to monochromatise the X-ray photon energy. The samples were prepared into pellets (diameter = 13 mm) and measured in transmission mode. The XAS energy was calibrated by using the first inflection point of Mn K-edge region of a metallic Mn foil (6539 eV) recorded simultaneously in each scan. The mean Mn oxidation state of MnO<sub>x</sub> was assigned as the second inflection point of Mn K-edge region [18]. The correlation of Mn K-edge energy and the mean Mn oxidation state was established on the basis of 4 standard MnO<sub>x</sub> samples (MnO, Mn<sub>3</sub>O<sub>4</sub>, Mn<sub>2</sub>O<sub>3</sub> and MnO<sub>2</sub>). The linear relationship was found in the regression model with reliable R<sup>2</sup> value (0.9996). Therefore, the mean Mn oxidation state of our manganese oxides can be calculated according to the established regression model.

# Chapter 4

## Important Parameters Affecting the Cell Voltage of Aqueous Electric double-Layer Capacitors (EDLCs)

### 4.1 Motivation

As discussed in Chapter 1, the electrochemically stable potential window of carbons can be improved by applying neutral aqueous electrolytes (such as  $\text{Li}_2\text{SO}_4$ ,  $\text{Na}_2\text{SO}_4$  etc.) [44, 58]. However, the important factors, such as open-circuit potential, have not been discussed before. In literature, most of the symmetric ECs were assembled by two electrodes with identical material with the same mass loading. Therefore, in this chapter, activated carbon (ACS-679) was employed as an electroactive material to demonstrate the necessity of charge-balanced condition of symmetric ECs in order to improve the utilisation of electrochemically stable potential window of electroactive material. In principle, the open-circuit potential effect and charge-balanced condition can be applicable to all the symmetric ECs no matter what kind of material is used as electroactive material. In this chapter, the open-circuit potential and electrochemically stable potential window of activated carbon were firstly measured by a three-electrode compartment in neutral aqueous medium (i.e., 0.5 M  $\text{Na}_2\text{SO}_4$ ). Secondly, two activated carbon electrodes were assembled as an EDLC under charge-balanced condition, where the charge-balanced EDLC was employed to evaluate the highest acceptable cell voltage by means of electrochemical analyses, including cyclic voltammogram, constant current charge-discharge, electrochemical impedance spectroscopy and inductance-capacitance-resistance

meter measurements. Finally, charge–unbalanced EDLCs were used to demonstrate the necessity of charge–balance condition in symmetric ECs.

## 4.2 Open–circuit Potential Effect on EDLCs

In constructing an aqueous EDLC, two key parameters, i.e., the stable open–circuit potential ( $E_{\text{OCP}}$ ) and charge capacity in the working potential window of the positive and negative electrodes, have to be carefully evaluated in order to fully extend the cell voltage. Figure 4–1a shows the CV curve of activated carbon in 0.5 M  $\text{Na}_2\text{SO}_4$  (inset shows its corresponding stable  $E_{\text{OCP}}$ ). The stable  $E_{\text{OCP}}$  of activated carbon is  $-0.04$  V (vs. Ag/AgCl). The reason why charge–balanced but not capacitance–balanced on the positive and negative electrodes has to be considered is illustrated in Figure 4–1b where stable  $E_{\text{OCP}}$  of the electrode material was set at the one–third and middle points of the potential window of solvent decomposition. Clearly, the cell voltage is only two thirds of potential window of solvent decomposition if stable  $E_{\text{OCP}}$  of the electrode material was located at P (one–third point) and the electrode material is ideal for EDLCs (i.e., constant specific capacitance in the whole potential window of solvent decomposition). Furthermore, the charge capacity of each electrode is a function of the potential change on each electrode in a supercapacitor although the specific capacitance of electrode materials is an important index for the energy density of the resultant devices.

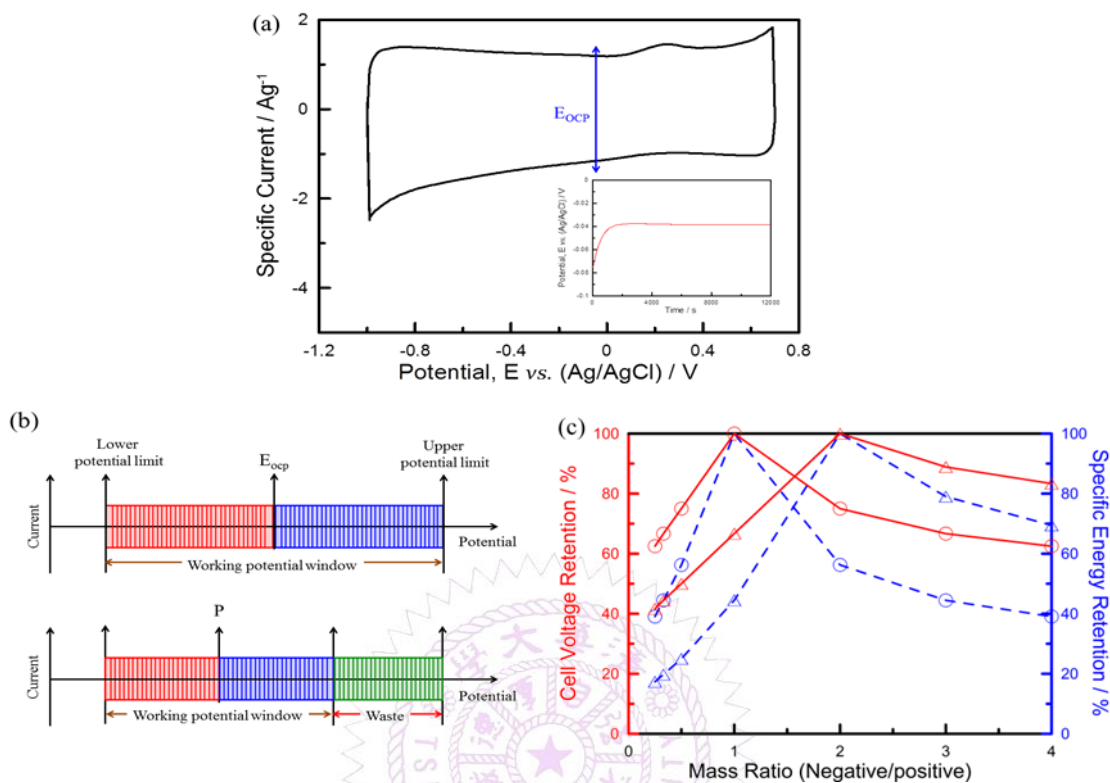


**Figure 4-1** (a) Cyclic voltammograms of AC (in three-electrode mode) measured at  $25 \text{ mV s}^{-1}$  in  $0.5 \text{ M Na}_2\text{SO}_4$  and (b) available working potential window for  $E_{\text{OCP}}$  of the electrode material at the middle and one-third points (located at P) of the potential window under equal mass loading of positive and negative electrodes and (c) mass ratio (positive/negative) dependence of cell voltage and specific retention for  $E_{\text{OCP}}$  at middle (circle) and one-third points (triangular) cases. Inset in (a) shows corresponding  $E_{\text{OCP}}$  of AC.

In fact, stable  $E_{\text{OCP}}$  of carbon materials in aqueous media is a strong function of the type and density of surface functional groups on carbons as well as the pH value and oxygen content of the electrolytes [198]. In addition, the type and density of surface functional groups on carbons are probably affected by the preparation method, history of pre-treatments, storage, etc. [47, 59]. This drawback might be circumvented by means of thermal removal of surface functional groups on carbons while the hydrophobic nature of bare carbon will depress the electrolyte-accessible surface area significantly. Accordingly, it is hard to obtain a high electrolyte-accessible surface area carbon with its stable  $E_{\text{OCP}}$  at the middle point of the potential

window of water decomposition. Hence, even when the double-layer capacitance of a carbon is independent of the applied potential, the charges being stored on the positive and negative electrodes are not equal (see the case for stable  $E_{OCP}$  at point P in Figure 4-1b). Consequently, stable  $E_{OCP}$  of carbons in the electrolyte has to be measured before constructing the EDLC.

Note that the ‘stable  $E_{ocp}$ ’ mentioned here is different from potential of zero charge (PZC), which is defined by IUPAC as the potential of an electrode (against a defined reference electrode) at which the surface charge is zero, indicating the absence of specific adsorption other than that of the solvent. On the other hand,  $E_{ocp}$  is the potential at which there is no current flow through the carbon electrode. With regard to the ‘stable  $E_{ocp}$ ’, it represents the potential at which the adsorption of ions and/or solvent reaching to a stable value after immersion of carbon electrode into electrolyte medium for a period of time. Therefore, the ‘stable  $E_{ocp}$ ’ is used as the key parameter to estimate the charge storage in positive and negative electrodes in EDLCs.

As the stable  $E_{OCP}$  of carbons in aqueous electrolytes has been measured, the charge stored on the positive and negative electrodes is determined by the mass loading of carbon and the specific capacitance in the working potential window (see Figure 4-1c). As mentioned in the previous paragraph, the specific capacitance of carbons is significantly affected by the type and density of surface functional groups on carbons meanwhile the pseudocapacitance is generally changed by varying the electrode potential and electrolyte [32, 47, 59, 199]. Since the specific capacitance in the working potential window for carbons of interest in the electrolytes is generally fixed when the electrode materials and electrolytes are proposed, the mass loading can be used to adjust the charge stored on both positive and negative electrodes. Accordingly, it is not suitable to employ the same mass loading on both sides of a

current collector in a bipolar design of symmetric ECs.

In fact, charge balance on the positive and negative electrodes of EDLCs is necessary to achieve the overall utilisation of stable potential window of the active materials [7]. Thus, carbon-based EDLCs have been proposed to reach the high cell voltage [7, 58, 199, 200], high power [200], low cost [47, 199] and long life-time benefits [7, 199]. To our best knowledge, 2.0 V has been proposed to be the highest cell voltage for symmetric ECs in aqueous solutions from the literature, which is comparable to the cell voltage of an asymmetric design consisting of positive  $\text{MnO}_2$  and negative carbon electrodes [16, 103]. On the other hand, how to precisely balance the charge stored in the positive and negative electrodes is determined by the correct potential window of water decomposition proposed for the carbons of interest. Accordingly, the charge capacity in the working potential window of the positive and negative electrodes has to be correctly evaluated in the second step of constructing symmetric ECs. The challenge here is how to evaluate the highest tolerable cell voltage and the realistic specific energy. Furthermore, obtaining the reliable cell voltage of symmetric ECs is vital for the lifetime and safety concerns of devices, especially when ECs are connected in series to increase the device voltage.

From the above viewpoints, EDLCs with charge-balanced positive and negative electrodes will reach a higher acceptable cell voltage than the charge-unbalanced cases. To demonstrate this idea, an EDLC consisting of two activated carbon electrodes is used as the model EC to set up the criteria appointing the highest acceptable cell voltage for realistic application of EDLCs through comparisons of CVs, charge-discharge curves, EIS and LCR meter examinations. The investigations were conducted in a neutral aqueous solution (0.5 M  $\text{Na}_2\text{SO}_4$ ) without compromising specific energy, power and cycle-life.



### 4.3 Establish Criteria for Aqueous EDLCs

From Figure 4–1a, AC generally shows capacitive response in aqueous neutral media (0.5 M Na<sub>2</sub>SO<sub>4</sub>) between –1 to 0.7 V (vs. Ag/AgCl) with the stable open–circuit potential at –0.04 V. Accordingly, the stable open–circuit potential determines the charge ratio within negative and positive potential windows as 60/40. Therefore, cell A consists of charge–balanced negative and positive electrodes where their mass loading of AC is equal to 0.4 and 0.6 mg cm<sup>–2</sup>, respectively. This charge–balanced EDLC is used to establish criteria for appointing the highest acceptable cell voltage for aqueous EDLCs. The typical CV curves of AC–based negative and positive electrodes are shown in Figure 4–2a. Clearly, the voltammetric charges on both positive and negative electrodes are approximately the same. Both CV curves show the ideal capacitive behaviour, which are extremely rectangular without observable redox peaks. Accordingly, an EDLC consisting of the above two electrodes will show ideal capacitive behaviour in a cell voltage of 1.7 V. Note in Figure 4–2b that the CV responses for the above EDLC under the two–electrode mode (i.e., cell A) with the positive shift in the upper potential limit are overlapped in the potential region of interest at the upper potential limit of CV is lower than or equal to 2.0 V. In addition, these CV curves are typically capacitive (i.e., rectangular), revealing the excellent reversibility of this EDLC. Accordingly, the cell voltage is able to be extended to 2.0 V for this charge–balanced EDLC and the cell voltage roughly obtained from CV in Figure 4–1a seems to be under–estimated. This statement is supported by the symmetric charge–discharge curves of cell A at cell voltages ≤ 2.0 V, shown in Figure 4–2c.

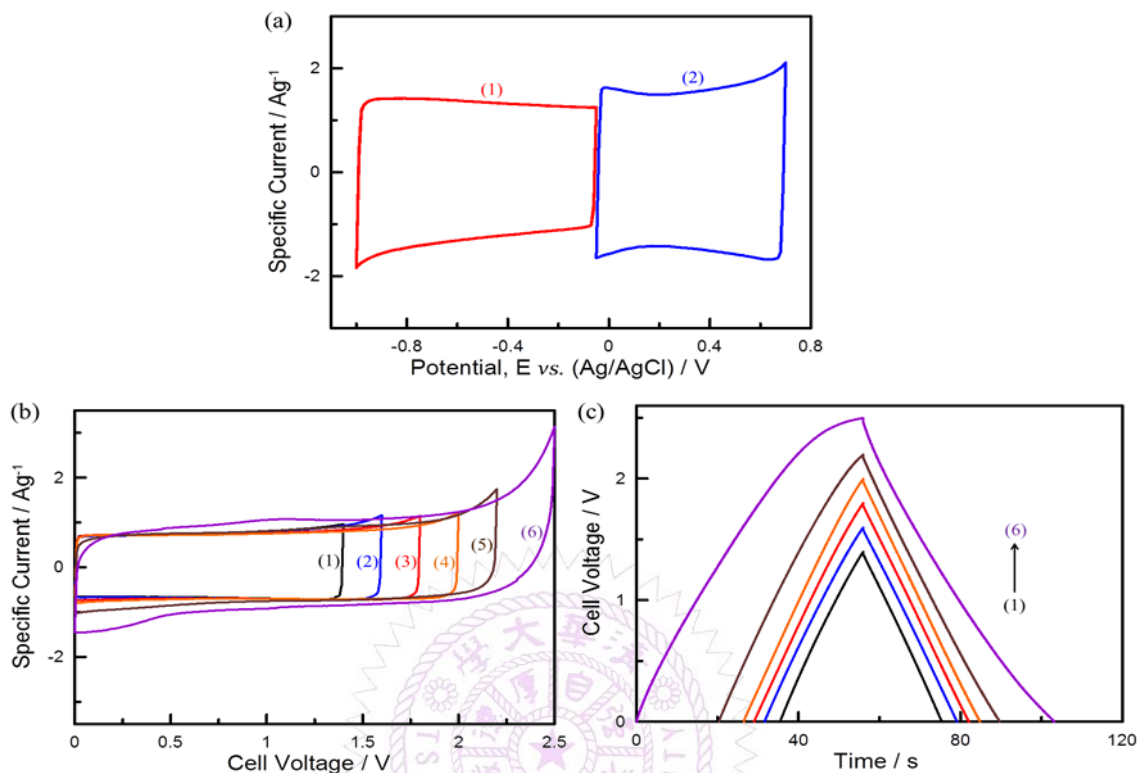


**Figure 4–2** (a,b) Cyclic voltammograms of charge–balanced cell A at  $25 \text{ mV s}^{-1}$  and (c) constant–current charge–discharge curves of charge–balanced cell A at  $2 \text{ A g}^{-1}$  with different cell voltages for (a,1) negative and (a,2) correspondingly charge–balanced positive electrode and (b,c) the activated carbon symmetric EC with cell voltage of (1) 1.4, (2) 1.6, (3) 1.8, (4) 2.0, (5) 2.2, (6) 2.5 V in  $0.5 \text{ M Na}_2\text{SO}_4$ .

On the other hand, while extending the upper potential limit of CV to 2.2 and 2.5 V, relatively distorted CV curves with oxidation peaks in the highly positive potential range are obtained in Figure 4–2b. Due to the irreversibly oxidation at potentials positive than 2.0 V, a cathodic plateau from ca. 1.0 to 0 V is visible on the negative sweep of curve 5, indicating the significant irreversibility. On curve 6, the totally irreversible behaviour is found at potentials positive to 2.25 V on both positive and negative sweeps. This irreversibility results in the obvious increase in the background currents on both positive and negative sweeps, indicating the obvious instability of AC in this potential region. Similar results are also found in Figure 4–2c, revealing lower columbic efficiencies (CEs) at cell voltages above 2.0 V; i.e., CEs

equal to 93 and 84 % at the cell voltage of 2.2 and 2.5 V, respectively. When the charge–discharge current density was fixed at 2 A g<sup>-1</sup>, the energy efficiency (EE) of cell A with the cell voltage = 1.4, 1.6, 1.8 and 2.0 V are 89, 89, 91 and 90%, respectively (see curve 2 in Figure 4–3a). However, a sudden decrease in EE to 80 and 57% at the cell voltage equal to 2.2 and 2.5 V, respectively, reveals the unsuitability in setting the cell voltages above 2.0 V.

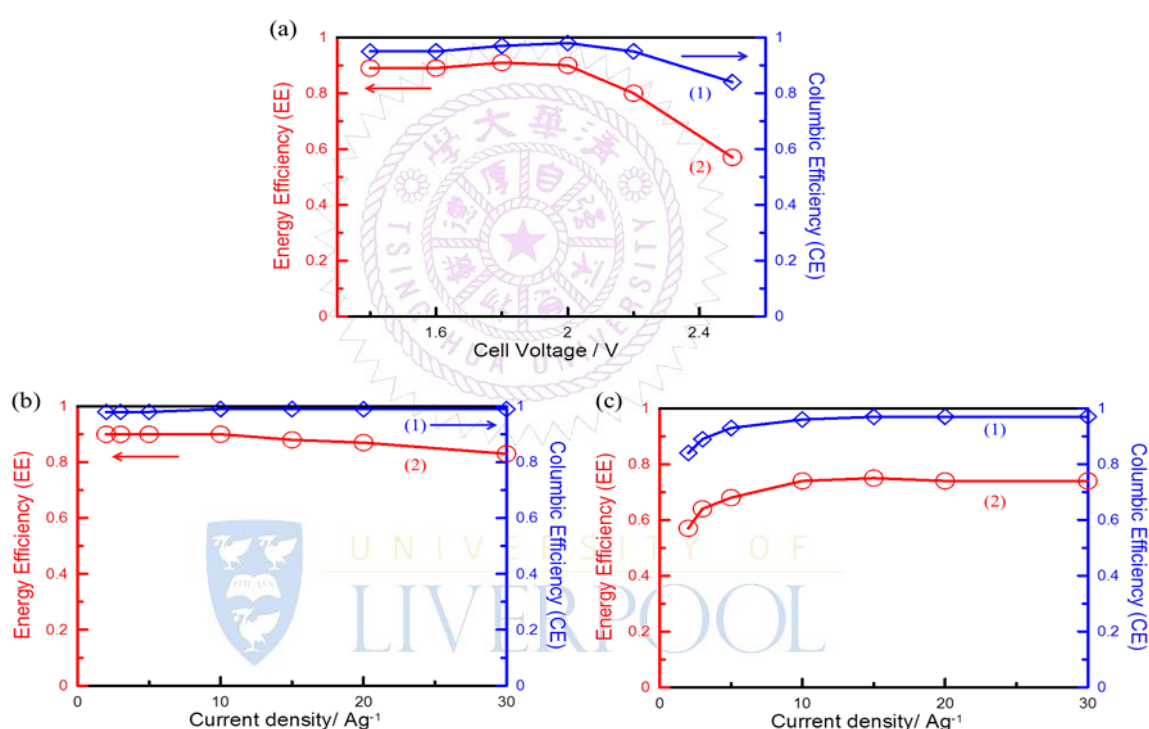


**Figure 4–3** (a,1) columbic efficiency (CE) and (a,2) energy efficiency (EE) of charge–balanced cell A measured at 2 A g<sup>-1</sup> with different cell voltages and (1) columbic efficiency (CE) and (2) energy efficiency (EE) of charge–balanced cell A measured at (b) 2.0 and (c) 2.5 V with different current density in 0.5 M Na<sub>2</sub>SO<sub>4</sub>.

The above irreversibility in the charge–discharge curves of a full cell can be affirmed by the correspondingly individual charge–discharge curves of both positive and negative electrodes. In Figure 4–4a, the corresponding charge and discharge curves of both positive and negative electrodes show the ideally symmetric triangular

shape when the cell voltage is set at 2 V. The upper and lower potential limits of the charge–discharge curves on the positive and negative electrodes are equal to 0.87 and –1.13 V (vs. Ag/AgCl), respectively. These potentials are respectively more positive and negative than the upper and lower potential limits of CV shown in Figure 4–1a. Hence, the wider cell voltage of this EDLC is due to the simultaneous extension of the working potential windows of AC in both positive and negative electrodes. In Figure 4–4b, the relatively irreversible behaviour of cell A at cell voltages above 2.0 V mainly comes from the slight change in the slope on the charge curve of the positive electrode at potentials positive than 0.87 V (vs. Ag/AgCl) although minor hydrogen adsorption occurs on the negative electrodes at potentials negative to –1.13 V on the charge curve, too. In Figure 4–4c, as the cell voltage was set at 2.5 V, however, much worse irreversible behaviour on both positive and negative electrodes is visible meanwhile the slopes of charge and discharge curves are not constant, indicating the involvement of pseudocapacitance after the 5–cycle charge–discharge test. From the above results and discussion, the simultaneous measurement of the charge–discharge behaviour of the positive and negative electrodes for a full cell is good for judging the source of irreversibility.

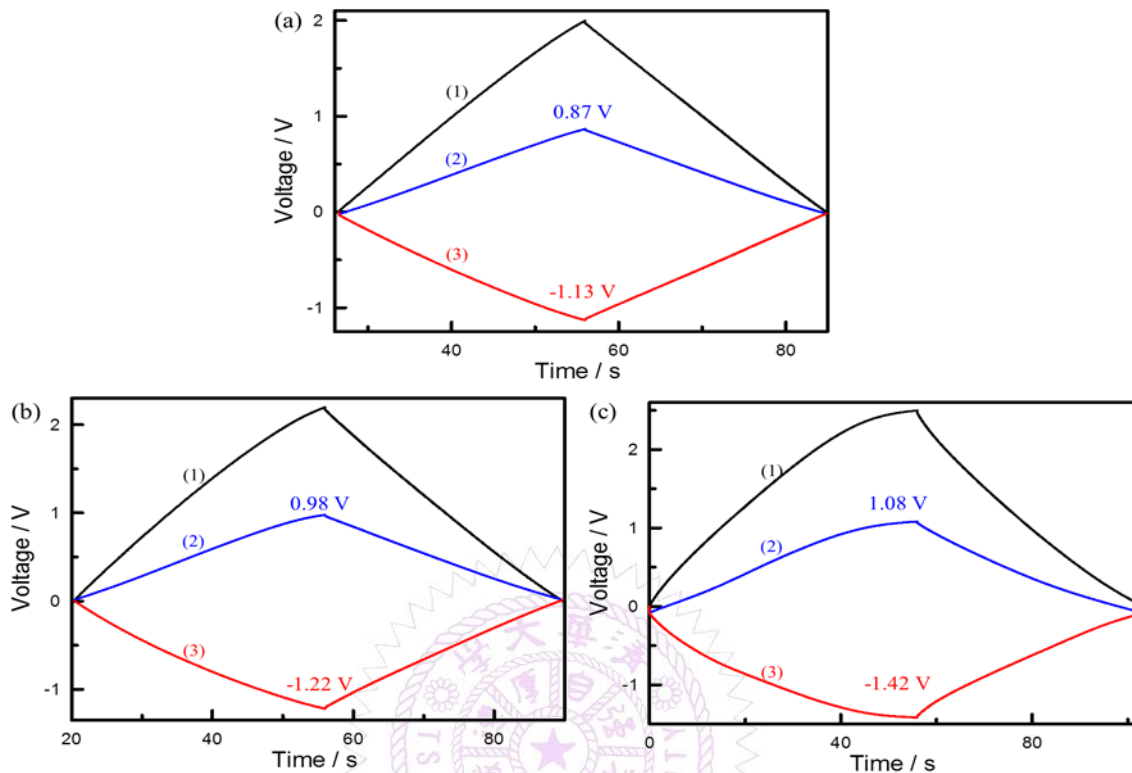


**Figure 4-4** constant-current charge-discharge curves of cell A measured at (a) 2.0, (b) 2.2 and (c) 2.5 V. Charge-discharge curves of (1) a full cell and the corresponding (2) positive and (3) negative electrode.

From a comparison of Figure 4-3b and 4-3c, the EE values obtained at different current densities with a cell voltage of 2 V are all higher than those with a cell voltage of 2.5 V. The above loss in both energy and columbic efficiencies reveals the unacceptable cell voltage of 2.5 V. Interestingly, the EE value monotonously decreases with increasing the current density of charge-discharge when the cell voltage is set at 2 V while the EE value at 2.5 V reaches a maximum and keeps almost constant at the current densities  $\geq 10 \text{ A g}^{-1}$ . The above unusual results can be explained by following reasons. In the first case with a cell voltage of 2.0 V, the columbic efficiency of cell A is very high and approximately independent of the charge-discharge current density. Thus,  $iR$  drop becomes the main factor determining the energy efficiency of the device though the equivalent series resistance (ESR) of

this aqueous EDLC is low. Since a higher  $iR$  drop is obtained at a higher current density, a monotonous decrease in the EE value with the current density is reasonably obtained (e.g., EE = 90.2 and 87.4% at 10 and 20 A g<sup>-1</sup>, respectively). In the second case with a cell voltage of 2.5 V, a shorter charge (and discharge) time is spent in the high cell voltage region from 2 to 2.5 V when a higher charge–discharge current density is applied. Accordingly, the contribution of the irreversible process in this cell voltage region to CE and EE decreases with shorter charge and discharge times (i.e., at a higher current density). This phenomenon emphasises the dominant effect of the irreversibility in the high cell voltage range for cell A on CE and EE because the contribution from  $iR$  drop discussed in the first case to EE still exists in this case. Therefore, the EE value for the EDLC with a cell voltage of 2.5 V reaches a maximum (74%) at 10 A g<sup>-1</sup> and then maintains at a similar value with further increasing the current density. Note in Figure 4–3c that the columbic efficiency (CE) is larger than 92% when the current density is equal to/above 5 A g<sup>-1</sup> even though 2.5 V has been identified to be an unsuitable cell voltage. Accordingly, CE cannot be considered to be a criterion to judge the suitable cell voltage of this EDLC.

The EIS spectra of the above AC–based EDLC measured at different cell voltages are shown in Figure 4–5a since the capacitance of high–area carbons (e.g., AC and reduced graphene oxide) is mainly contributed from the double–layer process [4, 32]. The equivalent–circuit model for a porous carbon material is a series of solution resistance, porous–electrode element (with electrolyte and solid resistances in pores) and double–layer capacitance due to the inherent porous nature of carbon [24]. By combining the two individual double–layer electrodes in series (i.e., the full cell), the equivalent–circuit model for the above EDLC (see inset in Figure 4–5a) is composed of a series of solution resistance ( $R_S$ ), porous–electrode element and effective cell capacitance ( $C_{\text{cell}}$ ) if the irreversible process found in the high cell



voltage region is negligible. This statement is supported by the capacitor-like responses in the low-frequency end (although the phase angle is not  $90^\circ$ ) when the cell voltage is equal to/lower than 2.0 V. However, there are 2 and 3 outliers deviated from the fitting curves in the low-frequency end when the cell voltages are set at 2.2 and 2.5 V, respectively, revealing the significant divergence from the capacitor-type behaviour. Again, cell voltages above 2.0 V are concluded to be unsuitable.

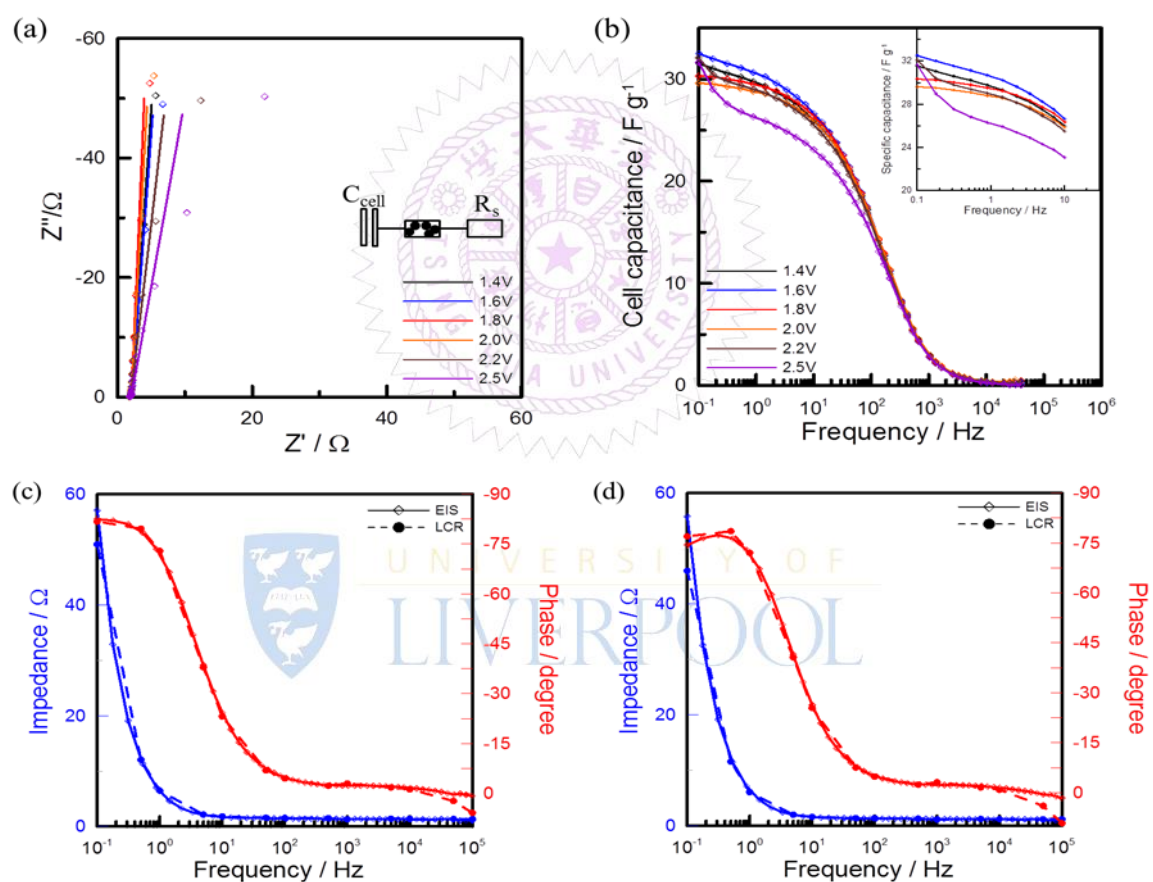


**Figure 4-5** (a) EIS spectra and (b) frequency dependence of specific capacitance for charge-balanced cell A at 25 °C in 0.5 M  $\text{Na}_2\text{SO}_4$  at different cell voltages. Inset in (a) shows the corresponding equivalent circuit model, inset in (b) enlarges the lower frequency region. Bode plots measured by EIS and LCR at (c) 2.0 and (d) 2.2 V.

**Table 4–1** Fitted values of all elements in the equivalent–circuit model shown in the inset of Figure 4–5a from the impedance spectra in Figure 4–5a for charge–balanced cell A.

$E_{\text{cell}}$	1.4 V	1.6 V	1.8 V	2.0 V	2.2 V	2.5 V
$R_s/\Omega$	0.56	0.56	0.56	0.56	0.56	0.56
$R_p/\Omega$	15.21	14.92	14.12	14.05	13.86	13.59
$R_b/\Omega$	1.67	1.66	1.56	1.56	1.59	1.60
$C_{\text{cell}}/(\text{mF})^\alpha$	22.93	23.00	25.75	24.99	18.48	13.21
$\alpha$	0.96	0.96	0.98	0.97	0.93	0.89

On the basis of the EIS spectra in Figure 4–5a, the fitting values of all elements in the full cell model are summarised in Table 4–1.  $R_s$  obtained at different cell voltages is the same (0.56  $\Omega$ ), ascribed to the constant distance between positive and negative electrodes.  $R_p$  and  $R_b$  represent electrolyte and bulk solid resistances in the porous–electrode element, which represent the resistance values inside the pores of AC. Both resistances remain in the same level around 14.3 and 1.6  $\Omega$ , respectively. The significant difference between  $R_p$  and  $R_b$  suggests that the ionic resistance within AC is significantly higher than the electrical resistance of AC.  $C_{\text{cell}}$  measured at 1.4 and 1.6 V are similar (22.93 and 23.00 mF) with  $\alpha$  of 0.96, close to ideal–capacitor behaviour ( $\alpha = 1$ ). Interestingly,  $C_{\text{cell}}$  slightly increases to 25.75 mF with  $\alpha$  of 0.98 when the cell voltage is equal to 1.8 V, probably resulting from the additional reversible pseudocapacitive responses of AC on the positive electrode although H adsorption/desorption on the negative electrode might provide certain additional capacitance. From the CV curve in the three–electrode mode, AC–coated electrodes are merely operated to 0.7 V (vs. Ag/AgCl) in the initial cycles. However, from the above result, the upper limit of the operation potential window for the AC positive

electrode can reach 0.87 V (vs. Ag/AgCl), which enlarges almost 0.2 V in the positive potential region. This phenomenon suggests that defects (e.g., edge/amorphous carbon sites) of AC might be easily oxidised in this potential region during the initial period while the AC surface is stabilised with the above oxidation. When the cell voltage is increased to 2.0 V,  $C_{\text{cell}}$  and  $\alpha$  are very similar (24.99 mF and 0.97, respectively), revealing the acceptable cell voltage of 2.0 V. With further extending the cell voltage to 2.2 and 2.5 V, on the other hand,  $C_{\text{cell}}$  significantly drops to 18.48 and 13.21 mF (ca. 26% and 47% loss in the effective cell capacitance), respectively. In addition, the  $\alpha$  values at 2.2 and 2.5 V are overestimated inevitably since the fitting data in the low-frequency end for the capacitor element significantly deviate from the real EIS responses when the cell voltages are set at 2.2 or 2.5 V. From the EIS results, the effective  $C_{\text{cell}}$  strongly depends on the cell voltage, which cannot be observed by means of CV and charge-discharge analyses. The cell capacitances calculated from the imaginary part of the impedance spectrum (in Figure 4-5a) as the functions of frequency are shown in in Figure 4-5b [201]. Obviously, the cell capacitances increase with descending the applied frequency and the capacitive behaviour is visible at frequencies below 10 Hz. When the cell voltages are equal to/lower than 2.0 V, the curves in the low frequency range (from 10 to 0.1 Hz) are almost horizontal, revealing the cell capacitances reach stable values. However, as the cell voltages are set at 2.2 and 2.5 V, the cell capacitances further increase at 0.31 and 0.54 Hz, respectively, consistent with the phase angle declining in the low-frequency range. In fact, larger voltammetric current densities are clearly found on the CV curves of this cell with unacceptable cell voltages (e.g., 2.2 and 2.5 V) while this effect results from the significant contributions of irreversible reactions (e.g., oxygen evolution reaction and hydrogen evolution reaction) at positive and/or negative electrodes. Accordingly, the higher cell capacitance obtained from CV and EIS analyses cannot be entirely utilised

in charge storage/delivery since a significant decrease in the effective cell capacitance is found when the cell voltage is changed from 2.0 to 2.2 or 2.5 V.

The Bode plots measured by the EIS analyser and LCR meter at 2.0 (in Figure 4-5c) and 2.2 V (in Figure 4-5d) are almost identical in the impedance and phase angle for cell A (a symmetric EDLC). Accordingly, cell A successfully works as a capacitor although the inductance-like behaviour in the high-frequency range (100k–10k Hz) ascribes to the susceptible detection of the curled conductive wires of LCR meter. Note that the phase angle in the low-frequency range is still high (without declining) at a cell voltage of 2.0 V while the phase angle decreases as the frequencies are lower than 0.31 Hz at 2.2 V. The phase-angle-declining phenomenon in the low-frequency range corresponds to the deviation points (outliers) in Nyquist plot (in Figure 4-5a) at cell voltages  $\geq 2.2$  V, revealing that cell A significantly deviates from the original capacitive behaviour at unsuitable cell voltages (i.e., cell voltages  $> 2.0$  V).

From the cell capacitance and EE retention shown in Figure 4-6, the charge-balanced cell A with stable operation at 2.0 V is substantiated with the stable cell capacitance and EE retention (ca. 96% and 90%, respectively). For the case operated at 2.2 V for 600 cycles, the constant-current charge-discharge curve shows the irreversible responses which are much worse than the first cycle. Note that the cell capacitance increases in the first 20 cycles and the cell capacitance subsequently decays to 97% of the initial capacitance value at the 600th cycle. The increase of cell capacitance in the first 20 cycles actually results from the oxidation on the positive electrode with its electrode potential at the full-charge state shifted from 0.98 to 1.14 V (vs. Ag/AgCl). Moreover, the potential of the positive electrode at the full-charge state monotonously increases to 1.24 V (vs. Ag/AgCl) at the 600th cycle. On the contrary, the potential of the positive electrode at the full-charge state is very stable in

the 600-cycle test for the case operated at 2.0 V. Although the cell capacitance increases at 2.2 V during the first tens of cycles, low EE values (about 60%) reveal the irreversible characteristics. Due to the excess oxidation at potentials positive than 0.9 V during the charge-discharge cycles at a cell voltage of 2.2 V, the open-circuit potential of positive electrode will gradually increase to higher potentials, resulting in the further increase in the potential of positive electrode at the full-charge state. The above results imply that for the AC-based, aqueous EDLCs, influences of the irreversible reactions on the positive electrode are more serious than those on the negative electrode.

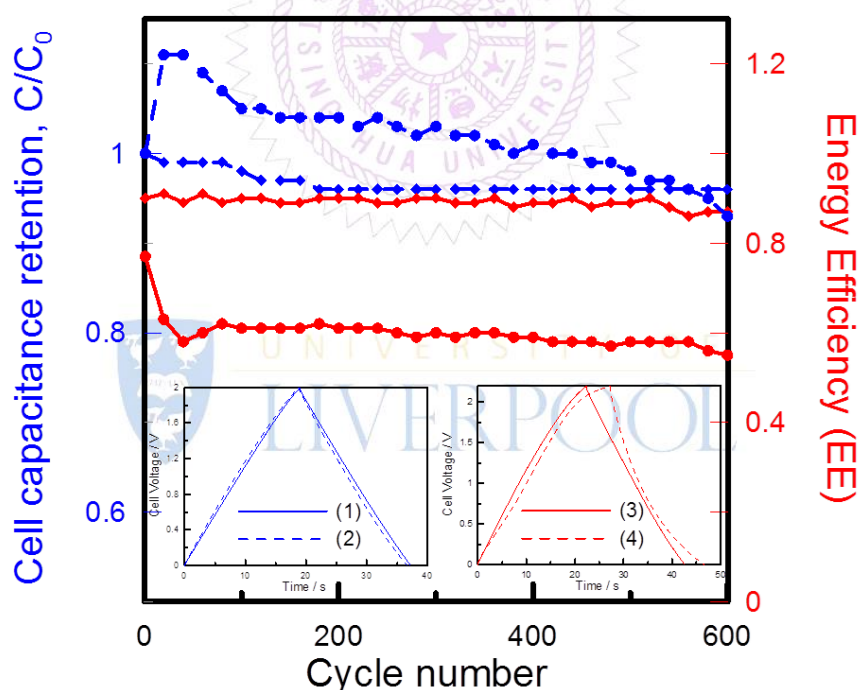


**Figure 4-6** Cell capacitance retention (dash) and energy efficiency retention (solid line) measured at 2.0 (diamond) and 2.2 V (circle) of charge-balanced cell A. Inset shows the constant-current charge-discharge curves of (1) the first and (2) the 600<sup>th</sup> cycle at 2.0 V and (3) the first and (4) the 600<sup>th</sup> cycle at 2.2 V.

According to all the above electrochemical analyses, 2.0 V is proposed to be the highest practical cell voltage of cell A (an aqueous AC-based EDLC under the

charge-balanced condition) in 0.5 M Na<sub>2</sub>SO<sub>4</sub>. All of the above results indicate the most important criterion is the phase angle of resultant cell capacitance (i.e., -85° in the complex plan) meanwhile sufficient evidences show that certain other parameters can be used as approximate indicators, such as (1) EE > 90% at 2 A g<sup>-1</sup>, (2) a slight decrease in EE with increasing the charge-discharge current density (no maximum in EE with increasing the charge-discharge current density), (3) the cell voltage where a significant drop in effective cell capacitance is found and (4) the capacitance-ascent phenomenon in the low frequency range (< 1 Hz).

#### 4.4 Necessity of Charge Balance in EDLCs

Cell B is the first example of charge-unbalanced EDLC, in which the positive/negative charge ratio is equal to 2. In order to illustrate the importance of charge balance, the influences of the charge-unbalanced AC-based EDLCs on the acceptable cell voltage are investigated. In this section, charges stored on the positive electrode are twice of those on the negative one (i.e., cell B) and the typical CV curves of the positive and negative electrodes are shown in Figure 4-7a. The CV curves of cell B are shown in Figure 4-7b, which show the capacitive responses (rectangular CV curves) at the cell voltages varied from 1.0 to 1.4 V. However, the CV curve with the upper limit of CV = 1.6 V shows a small plateau from 0.8 to 0 V on the negative sweep. This plateau on the negative sweep indicates the irreversible characteristics at a cell voltage of 1.6 V though the oxidation peak in the high positive potential range is not conspicuous. Extending the cell voltage to 1.7 V, a distorted CV curve is visible, revealing the poor capacitive behaviour. This statement is supported by the asymmetric charge-discharge curves at 1.7 V shown in Figure 4-7c where the declining slope found in the high cell voltage range during the charge process is



attributable to the charging difficulty to such a high cell voltage.

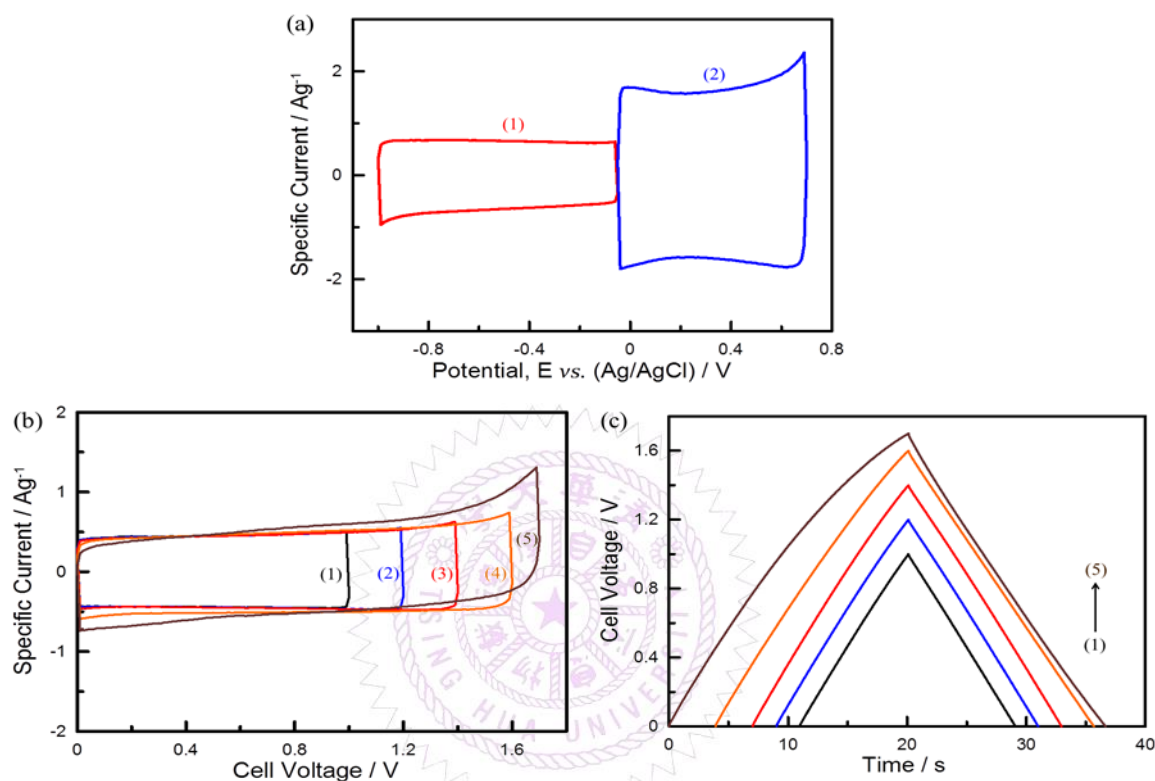


**Figure 4-7** (a,b) Cyclic voltammograms of cell B at  $25 \text{ mV s}^{-1}$  and (c) constant-current charge-discharge curves at  $2 \text{ A g}^{-1}$  with different cell voltages for (a,1) negative and (a,2) corresponding positive electrode of cell B with cell voltage of (1) 1.0, (2) 1.2, (3) 1.4, (4) 1.6, (5) 1.7 V in  $0.5 \text{ M Na}_2\text{SO}_4$ .

The trends of EE and CE against the cell voltage for cell B (see Figure 4-8a) are similar to those for the charge-balanced case but a smaller acceptable cell voltage is obtained. The EE values measured at  $2 \text{ A g}^{-1}$  for the charge-unbalanced cell are about 95~94% at the cell voltages varied from 1.0 to 1.4 V, which tallies with one of the approximate indicators (i.e.,  $\text{EE} > 90\%$  at  $2 \text{ A g}^{-1}$ ). From Figure 4-8b and 4-8c, EE monotonously descends with the current density when the cell voltages are equal to/below 1.4 V, while a maximum value of EE is obtained at  $10 \text{ A g}^{-1}$  measured at 1.6 V (see Figure 4-8c). The above phenomena also correspond to one of the approximate indicators (i.e., no maximum in EE with increasing the charge-discharge current

density). Based on all the results and discussion in this section, the potential utilisation of the positive electrode in cell B is lower than that in cell A, leading to a narrower cell voltage of cell B since the charges stored on both electrodes are not the same. From Figure 4–9a, as the cell voltage is equal to 1.4 V, the upper potential limit of the positive electrode reaches 0.43 V (vs. Ag/AgCl) while the lower potential limit of the negative one approaches –0.97 V (vs. Ag/AgCl) which is less negative than that obtained at 2.0 V for cell A (i.e., –1.13 V vs. Ag/AgCl). By extending the cell voltage to 1.6 V (see Figure 4–9b), an unequal potential–extending phenomenon is clearly observed (0.03 and –0.17 V for the positive and negative electrodes, respectively). As a result, slightly irreversible behaviour occurs at potentials around –1.14 V for the negative electrode, leading to the highest acceptable cell voltage of 1.4 V for cell B.

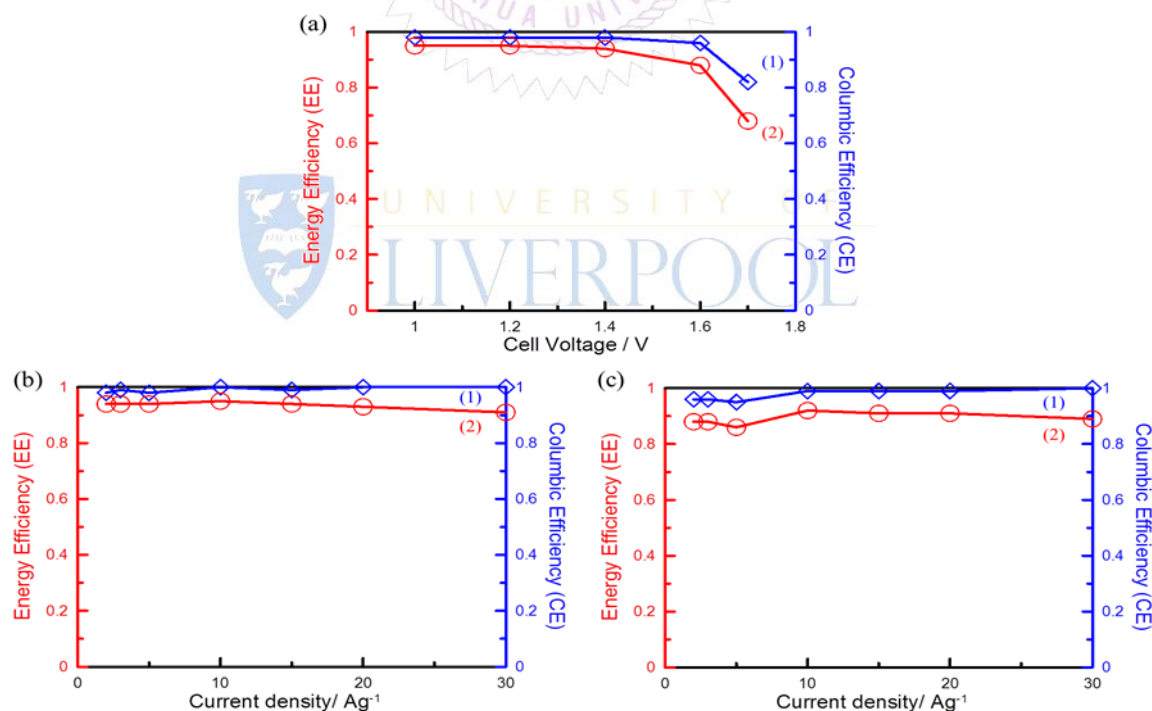


**Figure 4–8** (1) columbic efficiency (CE) and (2) energy efficiency (EE) measured at (a) 2 A g<sup>-1</sup> with different cell voltages and at (b) 1.4 and (c) 1.6 V with different current density of cell B in 0.5 M Na<sub>2</sub>SO<sub>4</sub>.

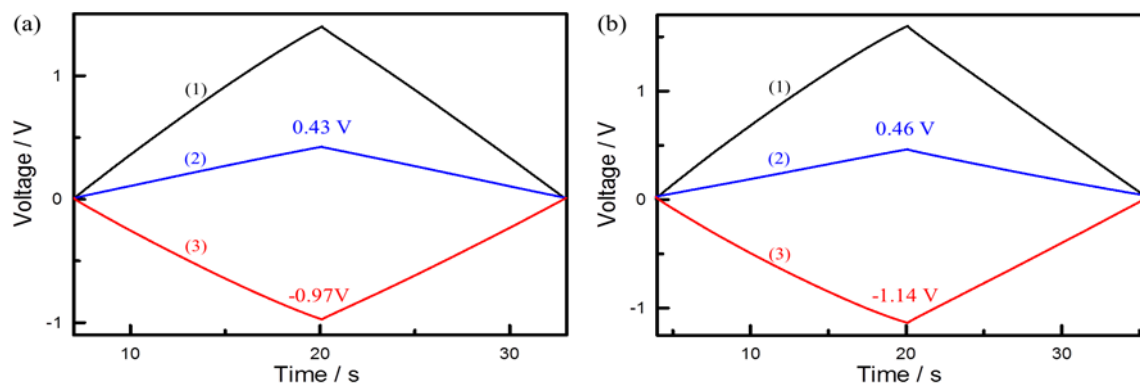


**Figure 4-9** Constant-current charge-discharge curves of cell B measured at (a) 1.4 and (b) 1.6 V. Charge-discharge curves of (1) a full cell and the corresponding (2) positive and (3) negative electrode.

The EIS spectra for cell B are shown in Figure 4-10a. The results show the capacitor-like behaviour at all acceptable cell voltages (i.e., equal to/lower than 1.4 V) while some outliers show up in the low-frequency end (0.1 Hz) at the unacceptable cell voltages. Values of all the elements in the full-cell equivalent-circuit model for cell B are summarised in Table 4-2. Again, the effective  $C_{\text{cell}}$  strongly depends on the cell voltage and decreases with enlarging the cell voltage. However, from the criterion of phase angle ( $-85^\circ$  in the complex plan) of resultant cell capacitance, 1.4 V is proposed to be the highest acceptable cell voltage, which corresponds to the result from all the indicators. The effective cell capacitance loss of cell B between 1.4 and 1.6 V is 11.5% (from 12.11 to 10.72 mF in Table 4-2). From the curves for the dependence of the specific capacitance on the applied frequency in Figure 4-10b, the capacitance ascent phenomenon in the low-frequency range is clearly found on the curves with cell voltages  $> 1.4$  V. These results and discussion support the applicability of the phase-angle criterion as well as the approximate indicators proposed in the charge-balanced case.

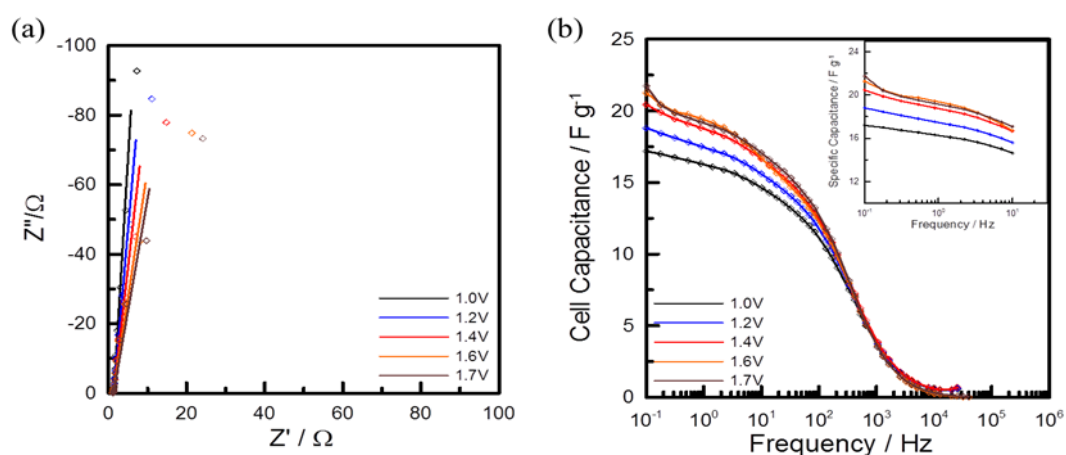


**Figure 4–10** (a) EIS spectra and (b) frequency dependence of specific capacitance for cell B at 25 °C in 0.5 M Na<sub>2</sub>SO<sub>4</sub> at different cell voltages. Insets in (b) enlarge the lower frequency region.

**Table 4–2** Fitted values of all elements in the equivalent–circuit model shown in the inset of Figure 5a from the impedance spectra in Figure 4–10a for cell B.

$E_{\text{cell}}$	1.0 V	1.2 V	1.4 V	1.6 V	1.7 V
$R_s/\Omega$	0.64	0.64	0.64	0.64	0.64
$R_p/\Omega$	10.91	10.87	10.84	9.93	9.90
$R_b/\Omega$	0.95	0.96	0.97	0.84	0.92
$C_{\text{cell}}/(\text{mF})^\alpha$	12.89	12.52	12.11	10.72	9.85
$\alpha$	0.97	0.95	0.94	0.91	0.90

Cell C is the second example of charge–unbalanced EDLC, in which the positive/negative charge ratio is equal to 0.5. Figure 4–11a shows the typical CV curves of the negative and positive electrodes with the charge ratio of the positive/negative electrodes equal to 0.5. The CV curves of cell C (an AC–based EDLC assembled with the above two electrodes) are shown in Figure 4–11b, which show the rectangular shapes at 1.0 and 1.2 V while those with the voltage windows from 1.4 to 1.7 V exhibit a significant irreversible oxidation in highly positive voltage

range. A similar trend for the observation of an irreversible oxidation in the highly positive voltage range on the charge–discharge curves of this cell is also found in Figure 4–11c. From the charge–discharge curves with the cell voltages  $\geq 1.6$  V, the declining slope in the high cell voltage range during the charging process is attributable to the difficulty in charging to such a high cell voltage.

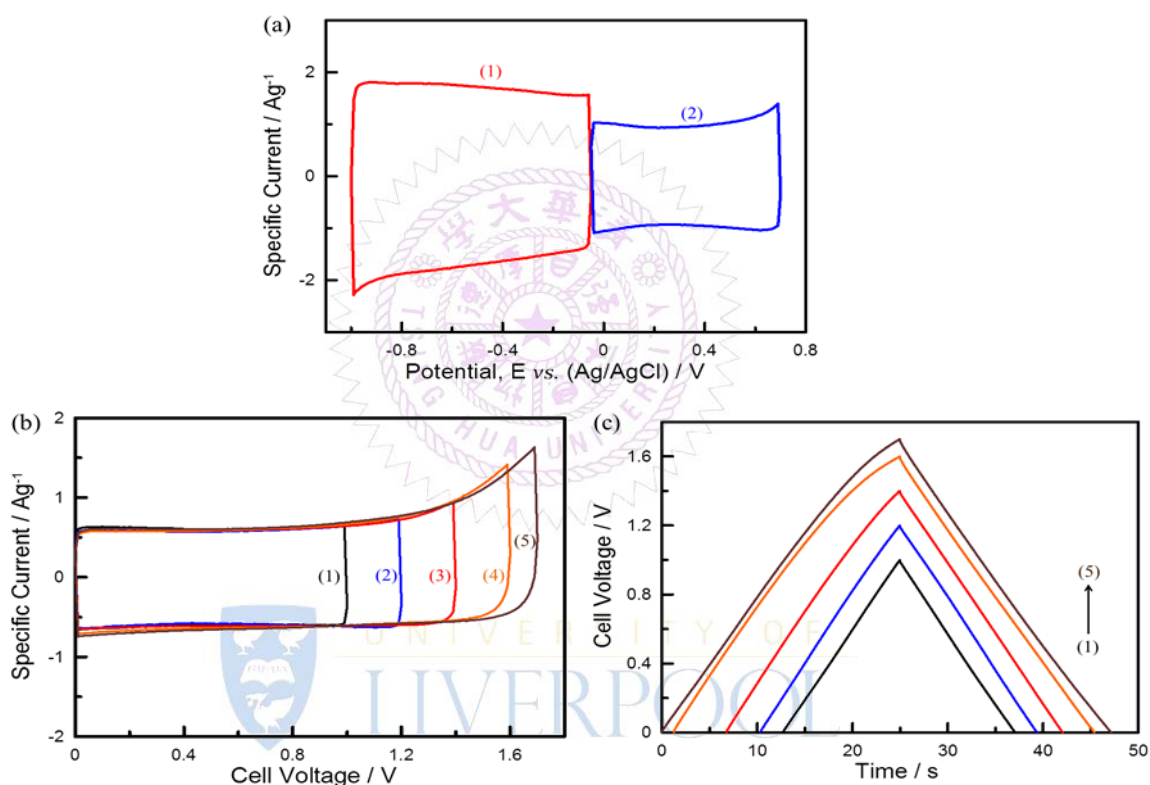


**Figure 4–11** (a,b) Cyclic voltammograms of cell C at  $25 \text{ mV s}^{-1}$  and (c) constant-current charge–discharge curves at  $2 \text{ A g}^{-1}$  with different cell voltages for (a,1) negative and (a,2) corresponding positive electrode of cell C with cell voltage of (1) 1.0, (2) 1.2, (3) 1.4, (4) 1.6, (5) 1.7 V in  $0.5 \text{ M Na}_2\text{SO}_4$ .

The dependence of EE and CE for cell C on the cell voltage (see Figure 4–12a) is similar to the findings for cells A and B with the exception that EE and CE values increase with extending the cell voltage from 1.6 to 1.7 V. This slight increase in EE and CE may be due to the formation of certain surface functional groups contributing pseudocapacitance when the positive electrode was subjected to the irreversible

oxidation reaction during the charge–discharge in the highly positive cell voltage region. This effect will compensate the charge difference between positive and negative electrodes and slightly increase the EE and CE values by extending the cell voltage from 1.6 to 1.7 V. The above statements are supported by the visible oxidation reaction in the CV and charge–discharge analyses. Note that for cell C, the EE values measured at  $2 \text{ A g}^{-1}$  are 97 and 96% for 1.0 and 1.2 V, respectively, which correspond to the approximate indicator of  $\text{EE} > 90\%$  at  $2 \text{ A g}^{-1}$ . From the dependence of EE on the charge–discharge current density, the feature of monotonous decrease in EE is visible at the cell voltage of 1.2 V (see Figure 4–12b), while the presence of a maximum EE at  $10 \text{ A g}^{-1}$  is found at the cell voltage equal to 1.6 V (see Figure 4–12c). These phenomena also correspond to the approximate indicator of no maximum in EE with increasing the charge–discharge current density. In fact, the corresponding electrode potentials of positive and negative electrodes reach 0.66 and  $-0.54 \text{ V}$  (vs. Ag/AgCl) when cell voltage of cell C is set at 1.2 V (see Figure 4–13a). However, the irreversible behaviour can be found on the positive electrode with an upper potential limit of 1.02 V (vs. Ag/AgCl) when the cell voltage is 1.6 V (see Figure 4–13b) though the negative electrode shows ideally capacitive behaviour in the potential region less negative than  $-0.58 \text{ V}$  (vs. Ag/AgCl). Similar to the findings in section 4.2, an unequal potential–extending phenomenon is also found (0.36 and  $-0.04 \text{ V}$  for the positive and negative electrodes, respectively) when the cell voltage is extended from 1.2 to 1.6 V. As a result, the irreversible oxidation reaction at potentials positive than 0.87 V on the positive electrode does indicate an unacceptable cell voltage of 1.6 V, although the negative electrode can be extended to as negative as  $-1.13 \text{ V}$  in cell A. Due to the progressive oxidation and formation of oxygen–containing functional groups on the positive electrode at the cell voltages varied from 1.2 to 1.6 V, the capacitive performances of cell C sometimes are acceptable on the



basis of certain approximate indicators, but questionable for the long-term charge-discharge requirement. Accordingly, the acceptable cell voltage of cell C is significantly reduced from 2.0 to 1.2 V.

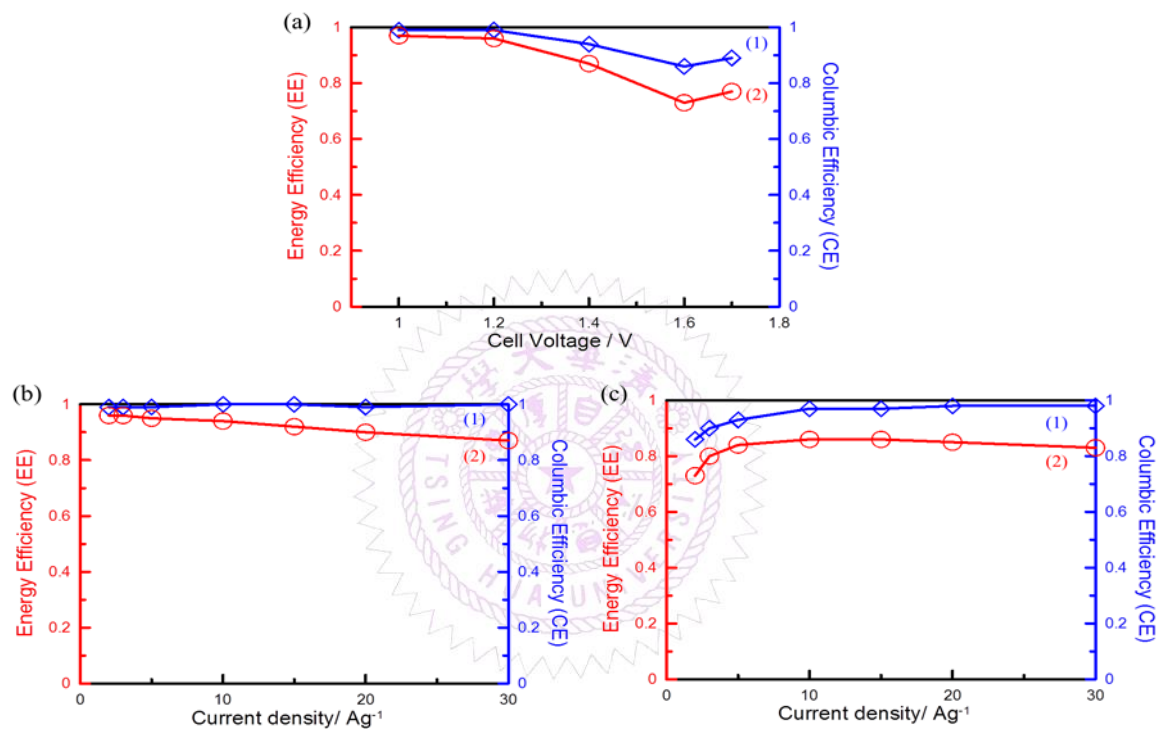


**Figure 4-12** (1) columbic efficiency (CE) and (2) energy efficiency (EE) measured at (a) 2 A g<sup>-1</sup> with different cell voltages and at (b) 1.2 and (c) 1.6 V with different current density of cell C in 0.5 M Na<sub>2</sub>SO<sub>4</sub>.

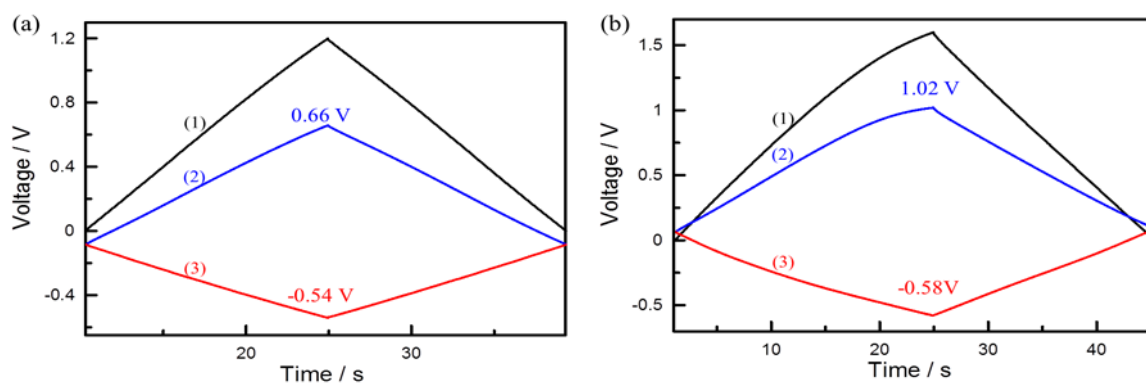


**Figure 4-13** Constant-current charge-discharge curves of cell C measured at (a) 1.2 and (b) 1.6 V. Charge-discharge curves of (1) a full cell and the corresponding (2) positive and (3) negative electrode.

Figure 4–14a shows the typical EIS spectra of cell C. Clearly, capacitor–like responses are visible at the cell voltages lower than/equal to 1.2 V, while there are some outliers in the low–frequency end (0.1 Hz) at the cell voltages above 1.2 V. The values of all elements constructed in the full–cell equivalent–circuit model are summarised in Table 4–3. The effective cell capacitance loss for cell C is 15.8% (from 17.15 to 14.44 mF) when the cell voltage is shifted from 1.2 to 1.4 V, which is higher than that for cell B (11.5 %), which might ascribe to the more serious irreversibility at potentials positive than 0.87 V on the positive electrode in comparison with the hydrogen adsorption/desorption responses on the negative electrode discussed for cell B. From the criterion of phase angle ( $-85^\circ$  in the complex plan) of resultant cell capacitance, 1.2 V is proposed to be the highest acceptable cell voltage, which also matches the criteria from all approximate indicators. From the dependence of specific capacitance on the applied frequency in Figure 4–14b, the capacitance ascent phenomenon in the low–frequency range is also observed on the curves measured at the cell voltages above 1.2 V.

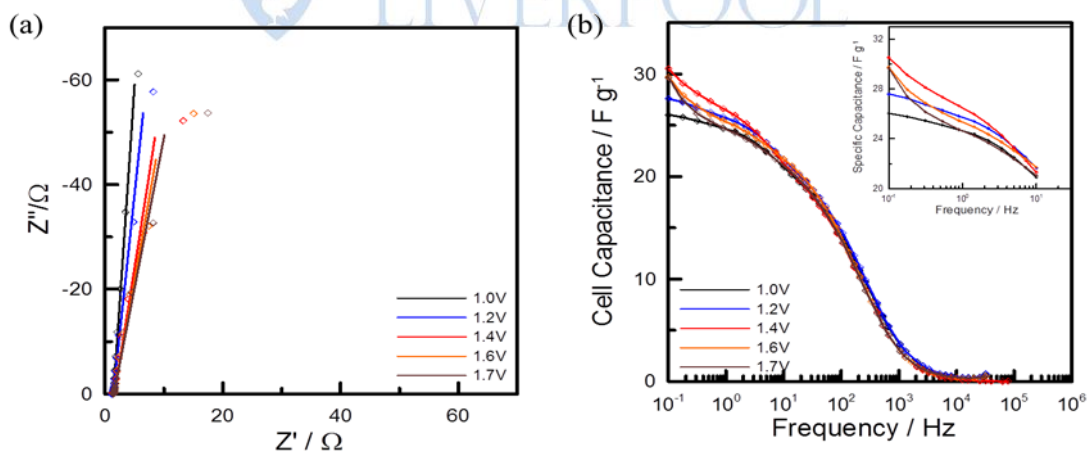


**Figure 4–14** (a) EIS spectra and (b) frequency dependence of specific capacitance for cell C at 25 °C in 0.5 M Na<sub>2</sub>SO<sub>4</sub> at different cell voltages. Insets in (b) enlarge the lower frequency region.

**Table 4–3** Fitted values of all elements in the equivalent–circuit model shown in the inset of Figure 4–5a from the impedance spectra in Figure 4–14a for cell C.

$E_{\text{cell}}$	1.0 V	1.2 V	1.4 V	1.6 V	1.7 V
$R_s/\Omega$	0.65	0.65	0.65	0.65	0.65
$R_p/\Omega$	12.43	12.43	9.73	13.59	13.31
$R_b/\Omega$	1.13	1.14	0.88	1.40	1.39
$C_{\text{cell}}/(\text{mF})^\alpha$	19.08	17.15	14.44	12.82	11.63
$\alpha$	0.96	0.94	0.91	0.90	0.89

#### 4.5 Overall Capacitive Performances of Charge–balanced and –unbalanced EDLCs

The retentions of cell capacitance and energy efficiency as well as the electrode potential stability against the charge–discharge cycle for both cells B and C are also examined here. Note that cells B and C reach their respectively stable cell capacitance and energy efficiency within 600 charge–discharge cycles (see Figure 4–15). However, the potential limits of both positive and negative electrodes under the full–charge state slightly changes during the initial hundreds of cycles in both cases. For example, in Figure 4–15a, the potential limits of negative and positive electrodes respectively reach  $-1.14$  and  $0.49$  V at the full–charge state for the first charge process while the potential limits of negative and positive electrodes gradually shift to  $-0.88$  and  $0.72$  V at the full–charge state for the 600<sup>th</sup> charge process. This shift in the working potential windows of positive and negative electrodes will stabilise the capacitive performances of cell B through the parallel shift in the starting charge potential by compensating the charge–inequality between positive and negative electrodes. In other words, during the charging process, the irreversible reaction in the negative potential region will consume the charges stored on the positive electrode,

leading to the movement of the upper potential limit of the positive electrode. In the following discharge process, the working potential window of the negative electrode is slightly extended to the positive potential range because of its lower charges in comparison with the positive electrode. Hence, the starting charge potentials of both electrodes are positively shifted from  $-0.06$  to  $0.24$  V during the 600-cycle charge-discharge test for cell B. Similarly, in Figure 4-15b, the starting charge potential of both electrodes are negatively shifted from  $-0.02$  to  $-0.09$  V in another 600-cycle charge-discharge test since the charges on the negative electrode is twice of that on the positive one for cell C. In this case, the potential limits of negative and positive electrodes gradually shift to  $-0.62$  and  $0.78$  V at the full-charge state for the 600<sup>th</sup> charge process. Although cells B and C (charge-unbalanced EDLCs) can reach their stable charge-discharge state, cell capacitance and energy efficiency in hundreds of charge-discharge cycles, the EE value and phase angle of resultant cell capacitance obtained at the cell voltage =  $1.6$  V for Figure 4-15a (and  $1.4$  V for Figure 4-15b) do not follow the criteria set in the Chapter 4.3 (i.e.,  $EE > 90\%$  at  $2 \text{ A g}^{-1}$  and  $-85^\circ$  in the complex plan), indicative of the deteriorated capacitive behaviour.

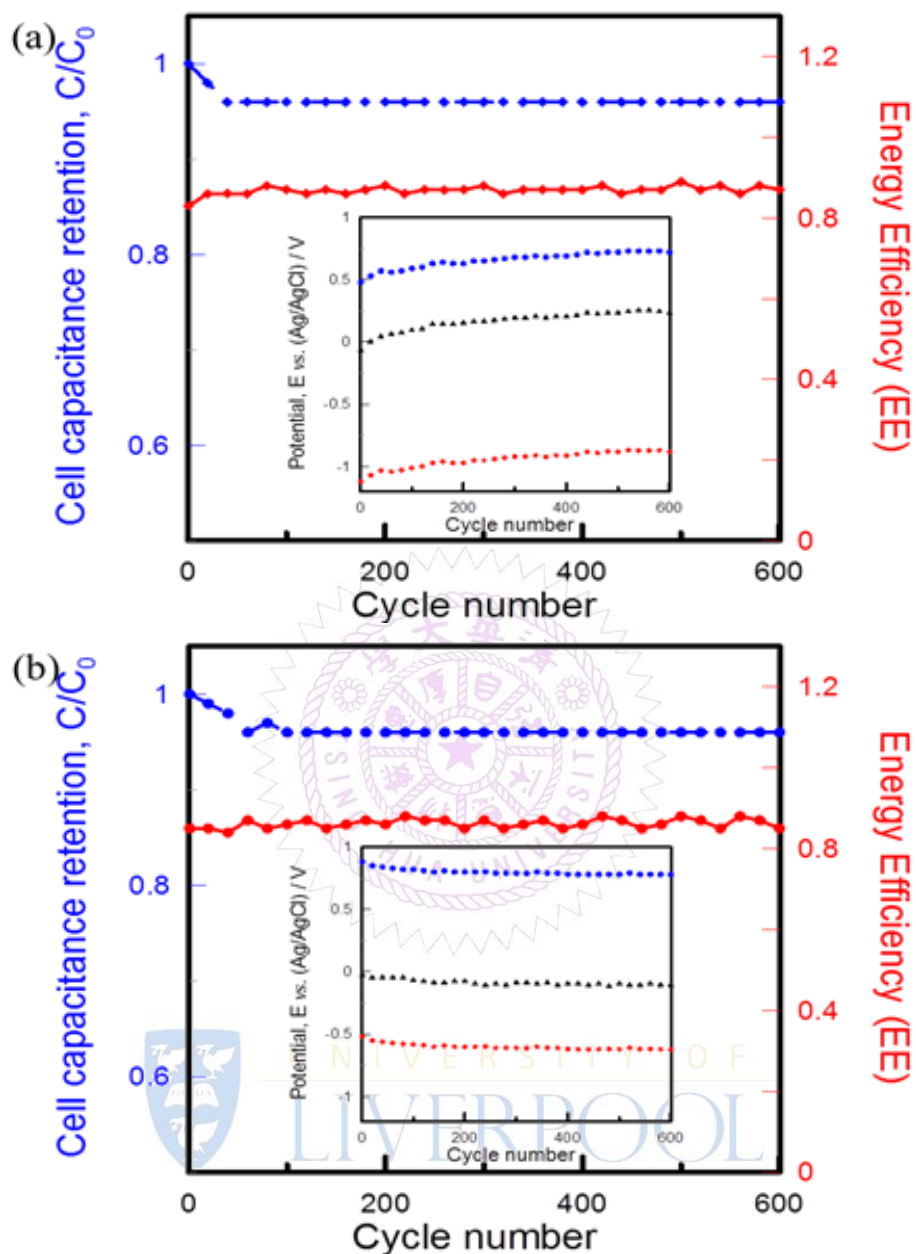


**Figure 4-15** Cell capacitance retention (dash) and energy efficiency retention (solid line) measured at (a) 1.6 V of cell B and (b) 1.4 V of cell C. Inset shows the 600-cycle potential stability at full-charge state of positive (blue) and negative (red) electrodes with the starting potential (black) for each cycle.

From the above results, the necessity of charge balance between negative and positive electrodes in order to reach the overall utilisation of electrochemically stable potential window and further perform the highest acceptable cell voltage for symmetric EDLCs is verified. The criteria set up in this work are feasible and reliable

due to all the electrochemical analyses are mutually verified. Note that from a comparison of cells B and C operated at the same cell voltage of 1.6 V (see Figure 4-7b and 4-7c, Figure 4-11b and 4-11c), the irreversibility seems to be more obvious for cell C (i.e., the charges on the negative electrode are twice of that on the positive one) although both cells B and C can reach their stable charge-discharge state, cell capacitance and energy efficiency in hundreds of charge-discharge cycles.

The specific energy and power of the asymmetric supercapacitors have been calculated from the charge-discharge curves. The specific energy and power of a full cell can be evaluated on the basis of Eq 3-6 and 3-7. Based on the same total weight of ACs on the positive and negative electrodes (e.g., 1 mg per cell), the specific energy and power of cells A-C are shown in Figure 4-16. For cell A with a highest acceptable cell voltage of 2.0 V, the specific energy and power are equal to 16.2 Wh kg<sup>-1</sup> and 2 kW kg<sup>-1</sup> at 2 A g<sup>-1</sup>. In addition, the capacitance retention obtained from the charge-discharge profile at 30 A g<sup>-1</sup> is as high as 90 % with a high EE value (> 80%). Therefore, this charge-balanced EDLC is capable of high-power discharge with the specific power of 30 kW kg<sup>-1</sup> at 30 A g<sup>-1</sup>. For cells B and C charged-discharged at 2 A g<sup>-1</sup>, the specific energy significantly reduces to 5.0 and 4.8 Wh kg<sup>-1</sup>, respectively meanwhile their specific power is about 1.4 and 1.2 kW kg<sup>-1</sup>, respectively. Although the highest acceptable cell voltages of charge-unbalanced cells B and C are equal to 1.4 and 1.2 V, respectively, their specific energy ratio is only 1.04 because the effective cell capacitance of cell C (24.2 F g<sup>-1</sup>) is higher than that of cell B (18.5 F g<sup>-1</sup>). This difference is attributable to the significant pseudocapacitance of the oxygen-containing functional groups generated in the irreversible oxidation reaction on the positive electrode for cell C while the irreversible oxidation might be indicative of the deterioration of ACs. Since the specific energy and power based on the device mass can be estimated from the above values evaluated from the total active material



mass by dividing a suitable factor [2], the estimated specific energy and power based on the device mass are about  $4.6 \text{ Wh kg}^{-1}$  and  $800 \text{ W kg}^{-1}$  at  $2 \text{ A g}^{-1}$  for cell A. With regarding to cells B and C, the specific energy and power are about  $1.4 \text{ Wh kg}^{-1}$  and  $500 \text{ W kg}^{-1}$ .

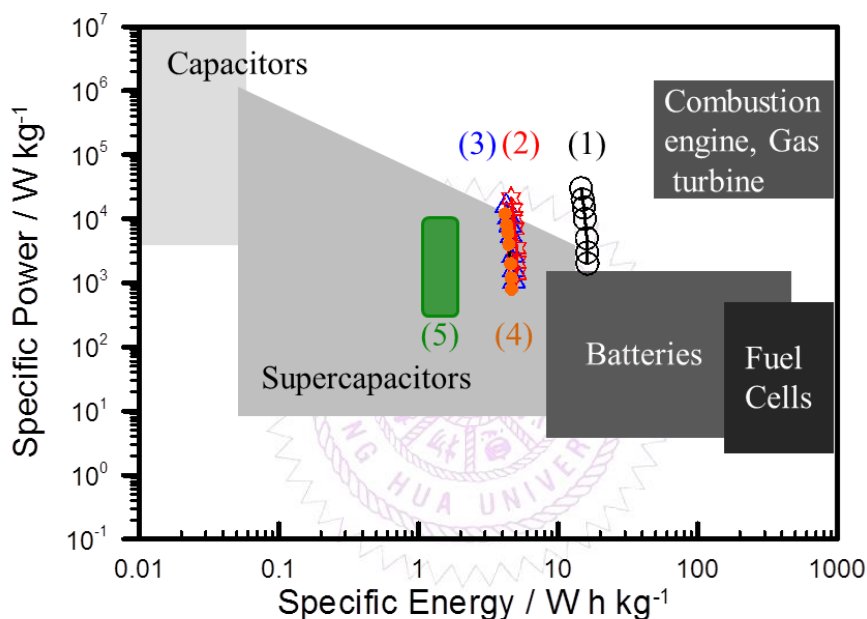


**Figure 4–16** The specific energy and power of (1) charge–balanced cell A (circle), (2) cell B (star) and (3) cell C (triangular) based on the total mass of active material. The estimated specific energy and power of (4) cell A (dot) and (5) cells B and C on the basis of the device mass [2].

## 4.6 Conclusion

For charge–balanced activated carbon–based EDLCs, the capacitor–like behaviour at the cell voltage of 2.0 V (with the specific energy and power of  $16.2 \text{ Wh kg}^{-1}$  and  $2 \text{ kW kg}^{-1}$  at  $2 \text{ A g}^{-1}$  on the basis of total AC mass) is observable by means of CV, constant–current charge–discharge, EIS analyses and the LCR meter examination. All the electrochemical analyses are consistent and mutually verify that the most

important criterion is the phase angle of resultant cell capacitance (i.e.,  $-85^\circ$  in the complex plan) while sufficient evidence shows that four other criteria can be considered to be approximate indices: (1) energy efficiency (EE)  $> 90\%$  at  $2 \text{ A g}^{-1}$ , (2) no maximum in EE with increasing the charge–discharge current density, (3) the cell voltage where a significant drop in effective cell capacitance is found and (4) the capacitance–ascent phenomenon in the low–frequency range ( $< 1 \text{ Hz}$ ). Moreover, the effect of stable open–circuit potential of electroactive material demonstrates that the capacitance–balanced condition cannot guarantee to reach the highest acceptable cell voltage for symmetric EDLCs. From the charge–unbalanced EDLC studies, the necessity of charge–balance condition between negative and positive electrodes in order to reach the highest acceptable cell voltage for symmetric EDLCs is verified. At  $2 \text{ A g}^{-1}$ , the specific energy and power (based on the total AC mass) significantly reduce to ca.  $4.8\sim 5.0 \text{ Wh kg}^{-1}$  and  $1.2\sim 1.4 \text{ kW kg}^{-1}$ , respectively when the positive/negative charge ratio is 0.5 or 2. This concept is on the basis of electrochemical charge–balance principle, therefore, it is believed to be applicable to all the symmetric ECs no matter what kind of material used as electroactive material.

## Chapter 5

# Criteria for Appointing the Highest Acceptable Cell Voltage of RGO//MnO<sub>x</sub> Asymmetric ECs

### 5.1 Motivation

As discussed in Chapter 1, cell voltage and specific energy of aqueous ECs can be significantly enhanced by asymmetric–design, i.e., choosing appropriate materials with complementary potential windows as electroactive materials on positive and negative electrodes. One of the good examples is carbon//MnO<sub>x</sub> asymmetric ECs since potential window of MnO<sub>x</sub> (positive electrode) in neutral aqueous media is complementary of carbon materials (negative electrode). Besides, these two electroactive materials are low cost, environmentally friendly and applicable to non–toxic and non–corrosive electrolytes. Therefore, carbon//MnO<sub>x</sub> asymmetric ECs have been widely studied recently. However, researchers usually consider the decomposition potential, i.e., electrolyte oxidation or reduction at the positive or negative electrode, respectively, based on cyclic voltammogram (or constant–current charge–discharge) at various scan rates (or current densities). Such a criterion is generally applicable but sometimes the decomposition potentials of electrolytes are not very definitely clear, especially for the asymmetric type. There is no study considering the criteria for appointing the highest acceptable cell voltage of asymmetric ECs. Hence, in this chapter, an example of RGO//MnO<sub>x</sub> asymmetric ECs was used to develop new criteria for appointing the highest acceptable cell voltage of asymmetric ECs, which is useful to evaluate the specific energy of devices. This is definitely practical and academic importance in the field of supercapacitors. In

addition to RGO//MnO<sub>x</sub> asymmetric ECs, RGO//RuO<sub>2</sub> was also used to verify the validity of the proposed criteria. Note that MnO<sub>x</sub> and RuO<sub>2</sub> are both pseudocapacitive materials with high electrochemical reversibility. Asymmetric ECs consisting of carbons and battery-like oxide-based materials (i.e., AC//Ni(OH)<sub>2</sub>) have been discussed in other work [202].

## **5.2 Establish Criteria for RGO//MnO<sub>x</sub> Asymmetric ECs by Electrochemical Methods**

The activation of Mn<sub>3</sub>O<sub>4</sub> was performed by CV at 100 mV s<sup>-1</sup> between 0 to 1 V (vs. Ag/AgCl) for 50 cycles in 0.5 M Na<sub>2</sub>SO<sub>4</sub>. Typical CV curves of RGO and activated Mn<sub>3</sub>O<sub>4</sub> in neutral media are shown in Figure 5-1. An ideal capacitive behaviour is obtained for RGO between -1 and 0.1 V, which is extremely rectangular without observable redox peaks. Similarly, ideal capacitive responses are evident for activated MnO<sub>x</sub> which has a complementary potential window to RGO. The charges stored in the negative and positive electrodes must balance in order to efficiently extend the cell voltage of this asymmetric EC [10].

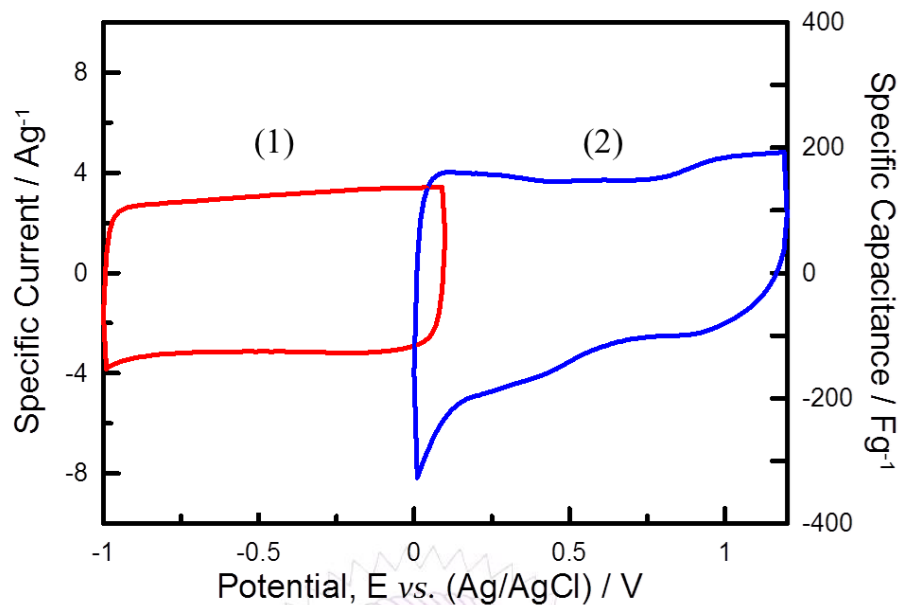


**Figure 5–1** CVs measured under three–electrode mode at  $25 \text{ mV s}^{-1}$  for (1) RGO and (2) activated  $\text{MnO}_x$  in  $0.5 \text{ M Na}_2\text{SO}_4$ .

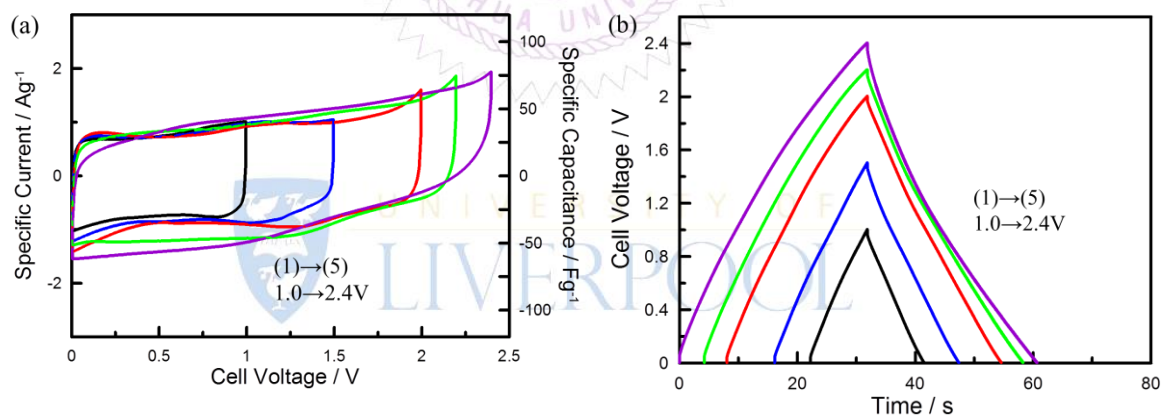


**Figure 5–2** (a) CVs at  $25 \text{ mV s}^{-1}$  and (b) constant–current charge–discharge curves at  $3 \text{ A g}^{-1}$  of an asymmetric EC consisting of RGO and activated  $\text{MnO}_x$ .

To confirm the successful construction of an asymmetric EC, typical CVs and charge–discharge curves in different cell voltages are shown in Figure 5–2a and 2b, respectively. In Figure 5–2a, rectangular curves with the cell voltage varying from 1.0 to 2.2 V are visible and the charge ratio of positive and negative sweeps gradually decreases from 0.997 to 0.918. Extending the cell voltage to 2.4 V leads to

undesirable lower columbic charge ratios and relatively distorted CV curves. The same results are verified in the constant-current charge-discharge profiles in Figure 5-2b. The nearly symmetric triangular charge-discharge curves with cell voltages between 1.0 and 2.2 V show excellent supercapacitor behaviour while the reversibility of the cell with 2.4 V is relatively worse. Note that the current efficiency (CE) is larger than 0.90 for all curves as shown in Figure 5-3a. However, from the area under the charge-discharge profiles, the energy efficiency (EE) of this cell with cell voltage = 1.0, 1.5 and 2.0 V are 0.84, 0.81 and 0.76, respectively (at  $3 \text{ A g}^{-1}$ ). A further decrease in EE to 0.71 and 0.61 when cell voltages are equal to 2.2 and 2.4 V reveals the significant irreversibility at cell voltages  $> 2.2 \text{ V}$  (Figure 5-3a). Accordingly, CE cannot be considered to be a criterion to judge the suitable cell voltage of asymmetric ECs. Moreover, the dependence of EE and CE on the charge-discharge rate at 2.0, 2.2, 2.4 V are shown in Figure 5-3b-d. Clearly, the CE is high in the high-rate region while EE reaches a maximum in the current density region of investigation.





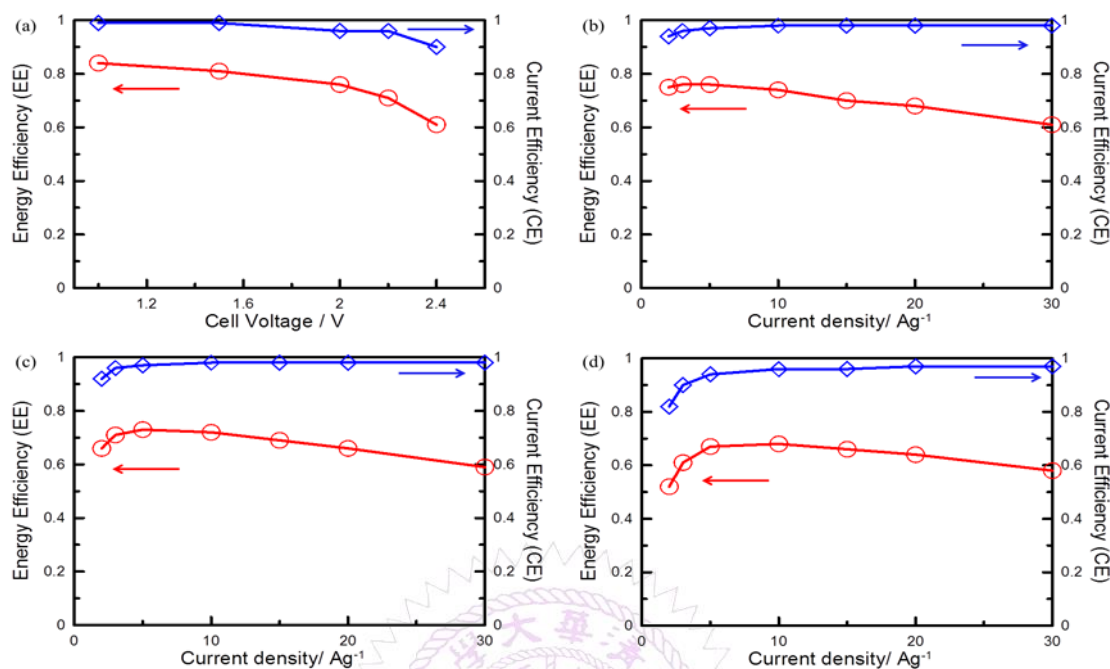


**Figure 5–3** (a) the cell voltage dependence of energy efficiency (EE) and current efficiency (CE) of RGO//MnO<sub>x</sub> at 3 A g<sup>-1</sup>. And the current density dependence of EE and CE with cell voltage of (b) 2.0, (c) 2.2 and (d) 2.4 V.

For the arbitrary evaluation criterion limit values, the constant-current charge-discharge results for the full cell as well as the corresponding individual electrode potentials of MnO<sub>x</sub> and RGO confirm that our evaluation criteria work very well. Figure 5–4 shows typical results for a full cell (in black) with its cell voltage of (a) 1.0, (b) 1.5, (c) 2.0, (d) 2.2, (e) 2.4 V, as well as the corresponding electrode potentials of individual activated MnO<sub>x</sub> (in blue) and RGO (in red) electrodes. The potential limits (vs. Ag/AgCl) of individual MnO<sub>x</sub> and RGO electrodes are listed in Table 5–1. From the individual electrode potentials of RGO and activated MnO<sub>x</sub>, irreversible behaviour is found at potentials above 1.0 V for activated MnO<sub>x</sub> and negative than -1.2 V for RGO. The lower efficiency was reported to be dissolution of manganese oxide (e.g., Mn(VI)/Mn(IV) at potentials > 1.0 V and HER at potentials < -1.2 V in AC//MnO<sub>x</sub> asymmetric ECs [80, 81].

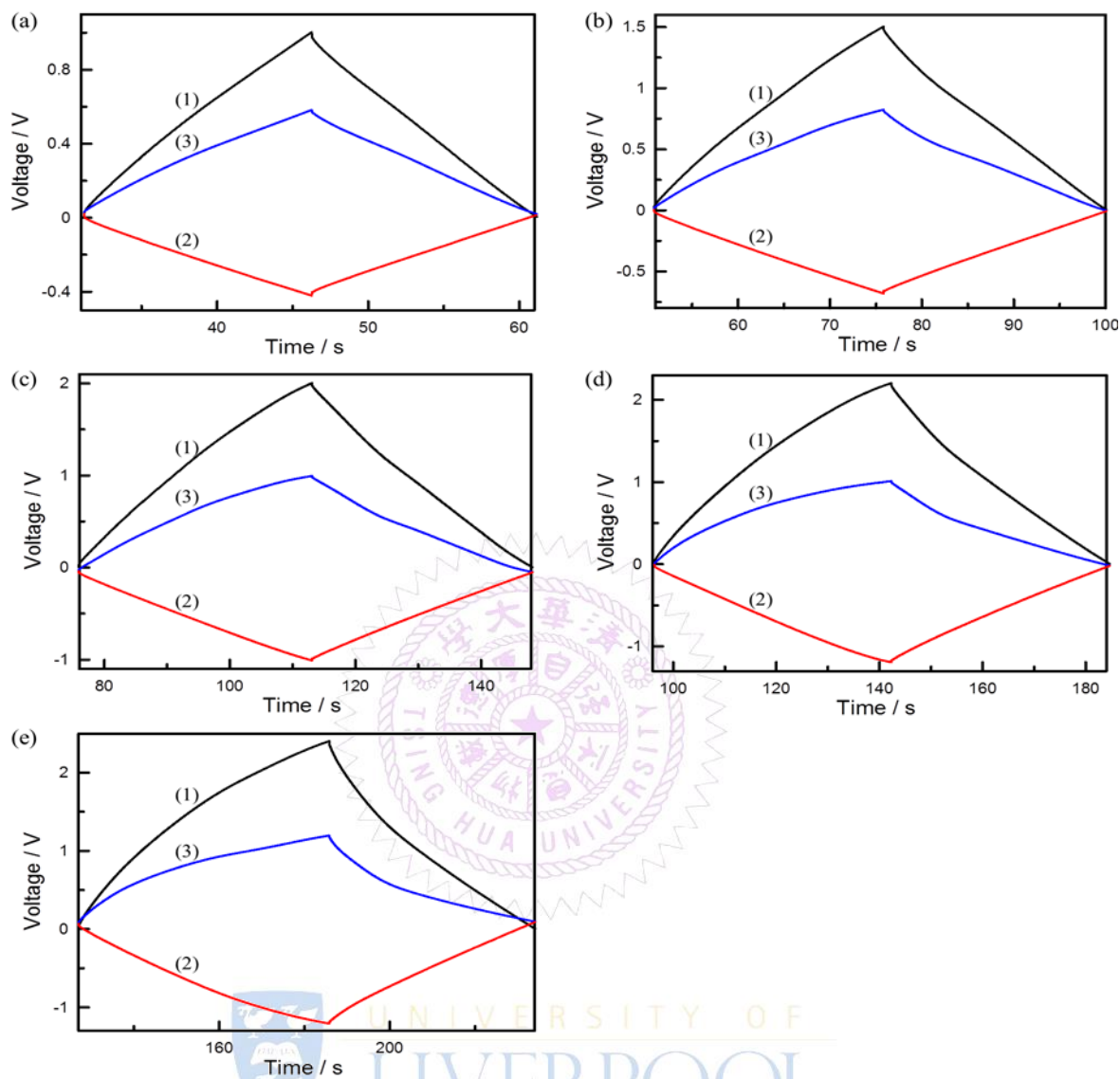


**Figure 5-4** Constant-current charge-discharge curves for an asymmetric EC (black) with the cell voltage of (a) 1.0, (b) 1.5, (c) 2.0, (d) 2.2, (e) 2.4 V and the corresponding charge-discharge curves of individual activated MnO<sub>x</sub> (blue) and RGO (red) electrodes.

**Table 5–1** The potential limits (vs. Ag/AgCl) of RGO and activated MnO<sub>x</sub>.

Cell Voltage (V)	Potential of RGO	Potential of activated MnO <sub>x</sub>
1.0	–0.42	0.58
1.5	–0.68	0.82
2	–1.01	0.99
2.2	–1.19	1.01
2.4	–1.21	1.20

The EIS results from individual MnO<sub>x</sub> and RGO electrodes are employed to extend the circuit models for the full cell. Accordingly, we measured the EIS spectra for the individual MnO<sub>x</sub> and RGO electrodes under the three–electrode mode. The capacitance of RGO is mostly contributed from the double–layer process [38, 41]. Due to the porous nature, the equivalent–circuit model for graphene is a series of solution resistance ( $R_{S,1}$ ), porous–electrode element (with electrolyte and solid resistances in pores) and double–layer capacitance ( $C_{dl,1}$ ) as shown in Figure 5–5a. The presence of the depressed semicircle in the high–frequency region is attributable to the porous nature of RGO, which can be fitted very well by the porous–electrode element in the equivalent–circuit model for carbon–based materials. For activated MnO<sub>x</sub>, the capacitance is mainly contributed from pseudocapacitance. Hence, the equivalent–circuit model is shown in Figure 5–5b where  $R_{S,2}$ ,  $R_{ct}$ ,  $W_f$ ,  $C_{dl,2}$  and  $C_f$  are solution resistance, charge–transfer resistance, finite diffusion impedance, double–layer capacitance and film Faradaic pseudocapacitance, respectively. The pseudocapacitance was fitted by a constant phase element (CPE) due to the nature of Faradaic reaction [194]. The rotation of the impedance semicircles by an angle of  $(1-\alpha)90^\circ$  for a CPE is attributed to the roughness of the electrode surfaces or the redox

kinetics of active materials [194, 195].

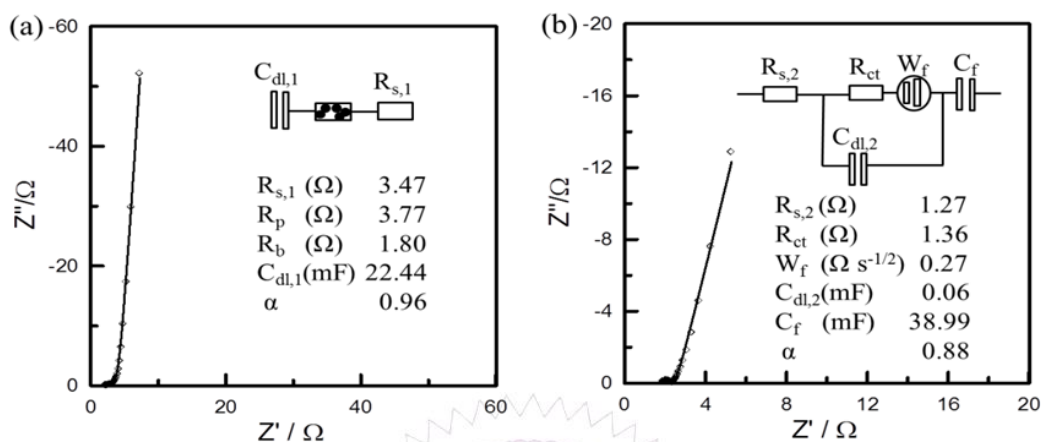


**Figure 5-5** EIS spectra measured at 25 °C in 0.5 M  $Na_2SO_4$  for individual (a) RGO at -0.1 V, (b) activated  $MnO_x$  at 0.2 V. Insets in (a) and (b) show the corresponding equivalent circuits and fitted values of elements.

The EIS spectra of the RGO/ $MnO_x$  two-electrode assembly measured at different cell voltages are shown in Figure 5-6a. Its equivalent-circuit model is constructed according to Figure 5-5a and 5-5b (see Figure 5-6b where  $R_S$  is the combined solution resistance and  $C_{cell}$  is the resultant cell capacitance). When the cell voltage is equal to/lower than 2.0 V, capacitor-like responses in the low-frequency end are obtained (curves 1-3 in Figure 5-6a), although the phase angle is not 90°. The onset frequencies for the capacitor-like response are equal to 32.4, 32.4 and 24.7 Hz when the cell voltages are 1.0, 1.5 and 2.0 V, indicating that cell voltages affect the charge-discharge responses of an asymmetric EC. A further increase in cell voltage results in the deviation in the phase angle (25° and 42° for 2.2 and 2.4 V, respectively), revealing the significant divergence from the capacitor-type behaviour. The depressed semicircle in the high-frequency region is attributable to the porous nature of graphene, leading to the depressed arc in the similar frequency region for the full cell

measurement.

From the EIS spectra in Fig 5–6a, fitting values of all elements in the full cell model are summarised in Table 5–2.  $R_S$  obtained at different cell voltages is very similar, ascribed to the distance variation between RGO and activated  $MnO_x$  electrodes.  $R_{ct}$  and  $W_f$  increase with enlarging cell voltages, attributable to a higher barrier of ion exchange during the charge–discharge process at a larger cell voltage. Note that the finite diffusion impedance ( $W_f$ ) increases from 2.34 to 10.64 and 14.78  $\Omega s^{-1/2}$  when the cell voltage is enlarged from 2.0 to 2.2 and 2.4 V, respectively, leading to the appearance of an arc or a diffusion–control response in the low–frequency end. This phenomenon suggests the involvement of redox couples with relatively worse reversibility at the cell voltage end (e.g., Mn(VI)/Mn(IV) at potentials  $> 1.0$  V and/or HER at potentials  $< -1.2$  V). Interestingly,  $C_{cell}$  measured at 1.0 V is 23.60 mF with  $\alpha = 0.93$ , indicative of almost ideal capacitor ( $\alpha = 1$ ) behaviour. Both parameters decline with increasing the cell voltage, especially when the cell voltage is over 2.0 V. The above results indicate that the effective  $C_{cell}$  strongly depends on the cell voltage, which cannot be observed by means of CV and charge–discharge analyses. Since  $\alpha$  close to 0.9 is an acceptable value, 2.0 V is proposed to be the highest practical cell voltage of the asymmetric EC consisting of RGO and activated  $MnO_x$  in 0.5 M  $Na_2SO_4$  according to all the electrochemical tests that would allow stable, with greatest specific energy and power. In fact, the decrease in  $\alpha$  might result from redox irreversibility, material degradation and significant leakage current of asymmetric ECs. If the relatively worse reversibility of Mn(VI)/Mn(IV) and HER at the cell voltage end can be improved by certain means, the highest acceptable cell voltage of this asymmetric EC will be larger than 2.0 V.

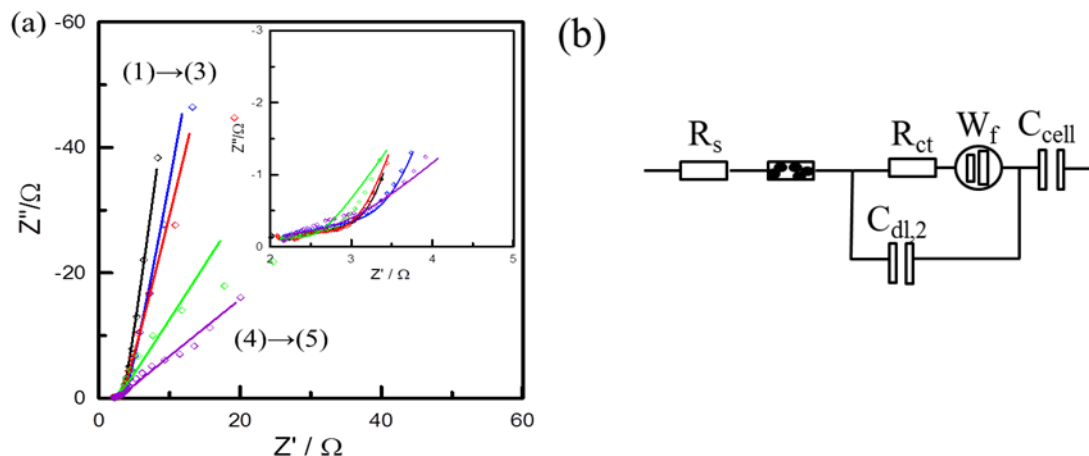


**Figure 5–6** (a) EIS spectra measured at 25 °C in 0.5 M Na<sub>2</sub>SO<sub>4</sub> with RGO//MnO<sub>x</sub> at (1) 1.0, (2) 1.5, (3) 2.0, (4) 2.2 and (5) 2.4 V. (b) the corresponding full–cell equivalent circuit. Insets in (a) shows the enlarged high frequency region.

**Table 5–2** Values of the equivalent–circuit element model in Figure 2d from the fitted impedance data shown in Figure 2c.

E <sub>cell</sub>	1.0 V	1.5 V	2.0 V	2.2 V	2.4 V
R <sub>s</sub> /Ω	2.02	2.04	1.98	1.99	2.08
R <sub>p</sub> /Ω	3.26	3.68	3.18	3.35	3.71
R <sub>b</sub> /Ω	2.25	2.91	2.19	2.31	2.55
R <sub>ct</sub> /Ω	1.87	1.93	2.05	2.19	2.32
W <sub>f</sub> /Ω s <sup>-1/2</sup>	1.19	2.03	2.34	10.64	14.78
C <sub>dl</sub> /mF	0.14	0.12	0.09	0.16	0.06
C <sub>cell</sub> /(mF) <sup>α</sup>	23.60	15.75	12.42	3.85	1.56
α	0.93	0.91	0.88	0.70	0.54

Based on the total weight of RGO and activated MnO<sub>x</sub>, the specific energy and power of the two–electrode assembly (cell voltage = 2.0 V) are 20.1 Wh kg<sup>-1</sup> and 2 kW kg<sup>-1</sup> at 2 A g<sup>-1</sup> (13.4 Wh kg<sup>-1</sup> and 30 kW kg<sup>-1</sup> at 30 A g<sup>-1</sup>) as shown in Fig 5–7.



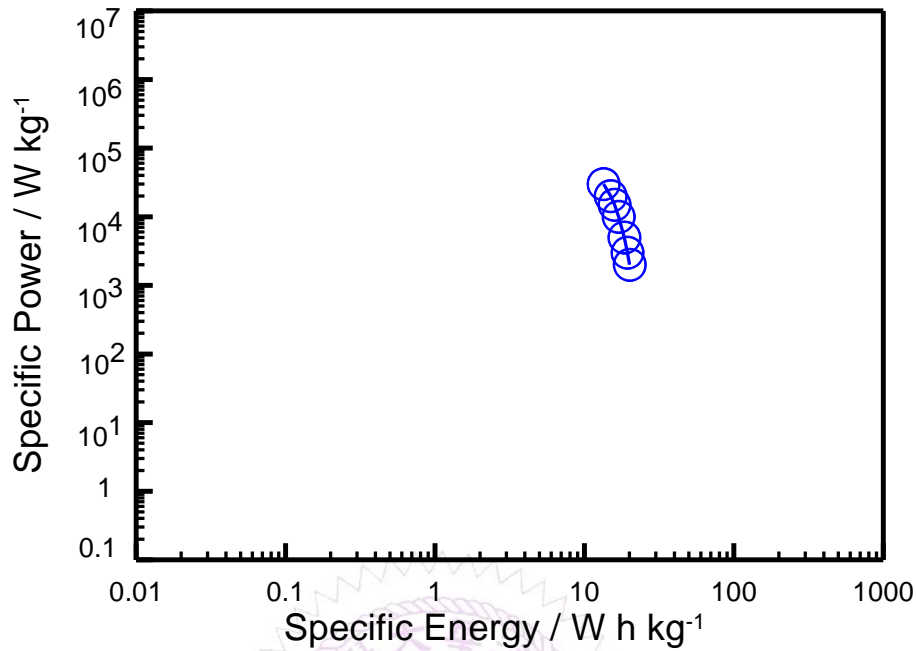


**Figure 5–7** The specific energy and power of asymmetric supercapacitor consisting of RGO and activated  $\text{MnO}_x$  operating at 2.0 V.

### 5.3 Criteria Validation by RGO// $\text{RuO}_2$ Asymmetric ECs

The main purpose of this chapter is to show the criteria for appointing the highest acceptable cell voltage of asymmetric ECs. The criteria should be applicable to other asymmetric ECs. Here, the EIS spectra of RGO// $\text{RuO}_2$  asymmetric supercapacitors were measured at different cell voltage in Fig 5–8. Values of the equivalent–circuit element model in Figure 5–6b for a RGO// $\text{RuO}_2$  are listed in Table 5–3. Apparently, the capacitor–like performance of the RGO// $\text{RuO}_2$  asymmetric EC at the cell voltage of 1.2 and 1.8 V were demonstrated by the highly reversible constant–current charge–discharge curves (in Fig 5–8a) and nearly 90 degree of impedance curves (in Fig 5–9). As for 2.2 V for the RGO// $\text{RuO}_2$  asymmetric EC, the constant–current charge–discharge curve shows an irreversible behaviour when the cell voltage  $> 2.0$  V. And RGO// $\text{RuO}_2$  asymmetric EC cannot be charged to 2.3 V. The equivalent–circuit model in Fig 5–6b is applied for fitting EIS spectra (in Fig 5–9), which clearly demonstrates

$\alpha$  significantly drop from 0.9 to 0.81 when the cell voltage increase from 1.8 to 2.2 V. The significant drop in effective cell capacitance can be clearly found (from 21.68 mF at 1.8 V to 15.53 mF at 2.2 V). Besides, the most important criterion proposed in previous section (i.e.,  $-80^\circ$  in the complex plan of resultant cell capacitance) can be applied to determine the highest acceptable cell voltage of the RGO//RuO<sub>2</sub> asymmetric EC. Therefore, the above criteria is applicable to the RGO//RuO<sub>2</sub> asymmetric system, indicating the reliability of the criteria.

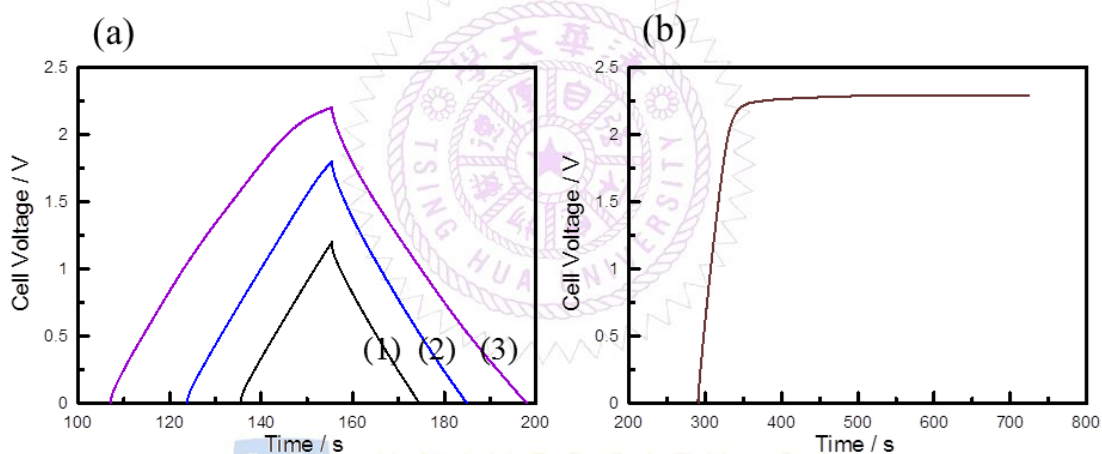


**Figure 5-8** The constant-current charge-discharge curves with the cell voltage equal to (a,1) 1.2, (a,2) 1.8, (a,3) 2.2 V and (b) 2.3 V for a RGO//RuO<sub>2</sub> asymmetric EC.

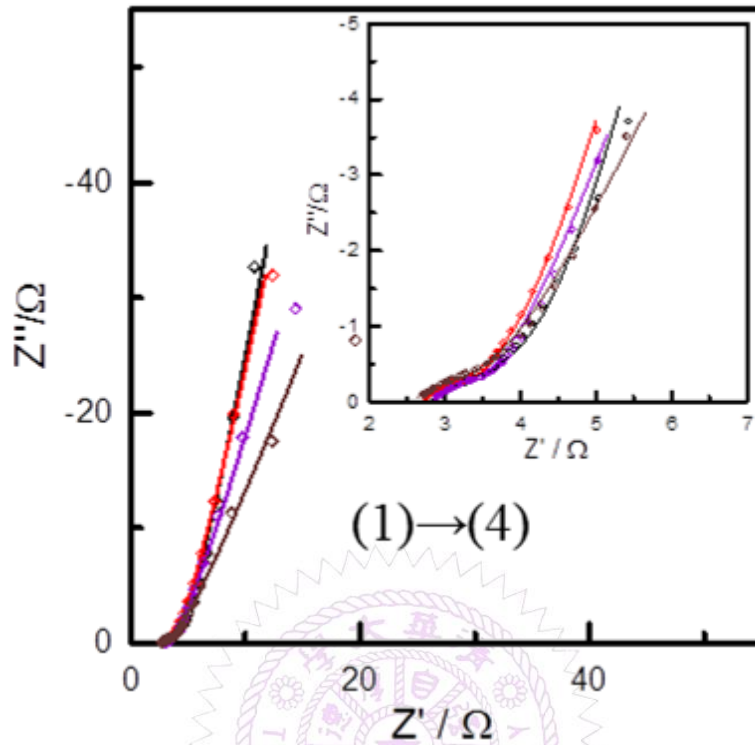


**Figure 5–9** EIS spectra measured at 25 °C in the frequency range between 0.1 and 100 kHz in 0.5 M Na<sub>2</sub>SO<sub>4</sub> for a RGO//RuO<sub>2</sub> asymmetric EC at (1) 1.2, (2) 1.8, (3) 2.2, (4) 2.3V.

**Table 5–3** Values of the equivalent–circuit element model in Figure 5–6b for a RGO//RuO<sub>2</sub> asymmetric EC.

$E_{\text{cell}}$	1.2 V	1.8 V	2.2 V	2.3 V
$R_s/\Omega$	2.66	2.59	2.66	2.56
$R_p/\Omega$	4.37	4.24	4.38	4.02
$R_b/\Omega$	3.46	3.36	3.47	3.18
$R_{\text{ct}}/\Omega$	1.44	1.59	1.62	1.80
$W_f/\Omega \text{ s}^{-1/2}$	4.53	5.06	5.53	6.82
$C_{\text{dl}}/\text{mF}$	0.32	0.39	0.33	0.29
$C_{\text{cell}}/(\text{mF})^\alpha$	22.18	21.68	15.53	9.57
$\alpha$	0.91	0.90	0.81	0.78

## 5.4 Conclusions

For an asymmetric EC consisting of RGO and activated  $\text{MnO}_x$ , the EIS results show non-capacitor like behaviour when the cell voltage is above 2.0 V, even though their CV curves (and charge-discharge profiles) are rectangular (triangular) and symmetric at a cell voltage of 2.2 V. The most important criterion for appointing the highest acceptable cell voltage of asymmetric ECs is the phase angle of resultant cell capacitance (i.e.,  $-80^\circ$  in the complex plan) while energy efficiency is an approximate indicator of capacitor or non-capacitor like behaviour. The above criteria are applicable to the RGO/ $\text{RuO}_2$  asymmetric system, indicating the reliability of the criteria. It is very useful to evaluate the practical specific energy of asymmetric ECs by understanding the highest acceptable cell voltage.



# Chapter 6

## Charge Storage Mechanism of Electrochemically Activated Manganese Oxide Composites

### 6.1 Motivation

As discussed in Chapter 2.4, the charge storage mechanism of  $\text{MnO}_2$  has been discussed by various analyses, such as X-ray photoelectron spectroscopy (XPS) [86], electrochemical quartz crystal microbalance (EQCM) [129], *in situ* powder X-ray diffraction (PXRD) [96, 143] and *in situ* X-ray absorption near-edge structure (XANES) [144, 145]. Two mechanisms have been proposed to elucidate the  $\text{MnO}_2$  charge storage process. The first is based on the surface adsorption of cations on  $\text{MnO}_2$  active sites [62], while the second involves the intercalation and expulsion of alkali metal cations and/or protons into/from  $\text{MnO}_2$  structures [63]. Alternatively,  $\text{Mn}_3\text{O}_4$  can undergo an electrochemical activation step that leads to greater capacitances [17–23]. The activation from hausmannite  $\text{Mn}_3\text{O}_4$  to birnessite  $\text{MnO}_2$  by electrochemical methods has been proposed by a series analyses of PXRD, X-ray absorption spectroscopic (XAS) and *ex situ* Raman spectroscopy [17–20, 22]. The activation process has been proposed as a complex and irreversible process and the new formed birnessite  $\text{MnO}_2$  is accepted as the material responsible for pseudocapacitive behaviour via the insertion of cations and/or protons [17, 22]. The structural disorder of electrochemically activated birnessite  $\text{MnO}_2$  has been previously remarked upon [18]. However, the charge storage mechanism of electrochemically activated  $\text{MnO}_x$  from hausmannite  $\text{Mn}_3\text{O}_4$  in neutral aqueous electrolytes has not yet

been verified.

In Chapter 5, we demonstrated that the one-pot synthesised of manganese oxide ('Mn<sub>3</sub>O<sub>4</sub>') is a practical and scalable process. This material needs approximately 100 potential cycles to activate to 'MnO<sub>2</sub>'. A wide-ranging study on a MnO<sub>x</sub> synthesised by annealing manganese (II) acetate precursor to 300 °C were presented in this Chapter, which includes *in operando* monitoring of the structural evolution during the activation process via *in situ* Raman microscopy. Other advanced material characterisation techniques, such as powder X-ray diffraction, X-ray photoelectron spectroscopy, scanning electron, transmission electron and *ex situ* Raman microscopy, were also applied to analyse the as-prepared and activated MnO<sub>x</sub> in this Chapter.

## 6.2 Chemical Synthesised As-prepared MnO<sub>x</sub>

The diffraction pattern of as-prepared MnO<sub>x</sub> (Figure 6-1a) corresponds to the PXRD pattern of hausmannite Mn<sub>3</sub>O<sub>4</sub> from the database (JCPDS CARD 24-0734). Reflections at 18.0°, 28.9°, 32.4°, 36.1° and 59.8° are recorded, which correspond to face (101), (112), (103), (211) and (224) of hausmannite Mn<sub>3</sub>O<sub>4</sub>, respectively. The sub-particles of the MnO<sub>x</sub> can be observed by TEM images (Figure 6-1c, 1d). From TEM images, the particle size of as-prepared MnO<sub>x</sub> is ca. 6–8 nm. The d-spacing of 0.499, 0.313, 0.281, 0.253, 0.208, 0.182, 0.157 and 0.146 nm can be found and calculated from the selected area electron diffraction (SAED) pattern of as-prepared MnO<sub>x</sub> (Figure 6-1b), which are consistent with the d-spacing of hausmannite Mn<sub>3</sub>O<sub>4</sub>. Moreover, the lattice spacing of 0.50, 0.31, 0.28 and 0.25 nm can be identified from the TEM image (Figure 6-1d), which correspond to face (101), (112), (103) and (211) of hausmannite Mn<sub>3</sub>O<sub>4</sub>, respectively. The diffraction peaks and d-spacing of as-prepared MnO<sub>x</sub> are compiled and compared to hausmannite Mn<sub>3</sub>O<sub>4</sub> (JCPDS CARD



24-0734) in Table 6-1, which verifies that the as-prepared  $\text{MnO}_x$  can be considered to be consisting of hausmannite  $\text{Mn}_3\text{O}_4$  [86, 95, 116, 118].

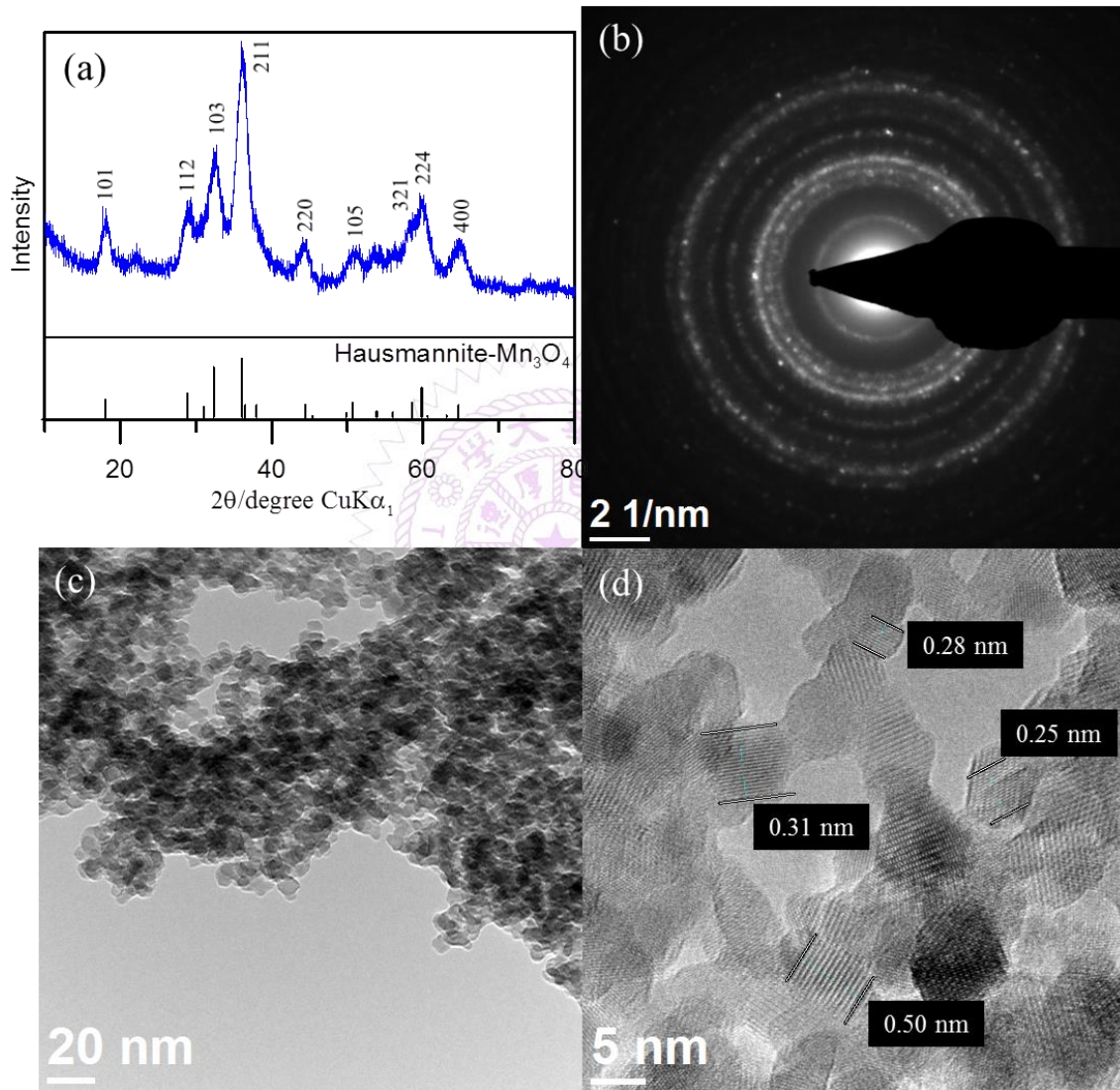


**Figure 6-1** (a) X-ray diffraction pattern, (b) SAED pattern and (c,d) TEM images of as-prepared  $\text{MnO}_x$ .

**Table 6–1** Comparisons of diffraction peaks and d–spacing calculated from the SAED pattern of as–prepared and activated MnO<sub>x</sub> with standards (hausmannite Mn<sub>3</sub>O<sub>4</sub>, JCPDS CARD 24–0734 and birnessite MnO<sub>2</sub>, JCPDS CARD 18–0802) from database.

	2θ from XRD pattern (degree)	2θ from database (degree)	d–spacing calculated from SAED pattern (nm)	d–spacing from Mn <sub>3</sub> O <sub>4</sub> database (nm)		d–spacing calculated from SAED pattern (nm)	d–spacing from MnO <sub>2</sub> database (nm)
as–prepared MnO <sub>x</sub>	18.0	18.0	0.499	0.492	activated MnO <sub>x</sub>	0.497	
	28.9	28.9	0.313	0.309		0.308	
		31.0		0.288			
	32.4	32.3	0.281	0.277		0.283	
	36.1	36.1	0.253	0.249		0.253	
						0.242	0.244
	44.3	44.4	0.208	0.204			
		49.8	0.182	0.183		0.210	0.212
	50.7	50.7		0.180		0.182	
	58.4	58.5	0.157	0.158		0.158	
59.8	59.8		0.154				
64.7	64.7	0.146	0.144	0.146			

The mean manganese oxidation state of  $\text{MnO}_x$  can be determined by the energy separation between the two peaks of Mn 3s core level spectrum [86, 95, 116, 118]. It has been reported that more interaction can occur upon photoelectron ejection since a lower valence state implies more electrons in the 3d orbital. Consequently, the energy separation between the two components of the Mn 3s multiplet will increase [86, 118]. The energy separation between these two peaks of Mn 3s spectra is 5.79, 5.50, 5.41 and 4.78 eV for reference sample of MnO,  $\text{Mn}_3\text{O}_4$ ,  $\text{Mn}_2\text{O}_3$  and  $\text{MnO}_2$ , respectively [86, 95, 118]. The peak separation is 5.23 eV obtained from Mn 3s spectrum of as-prepared  $\text{MnO}_x$  (Figure 6-2a). Therefore, the mean manganese oxidation state of as-prepared  $\text{MnO}_x$  is ca. 3.18 according to the relationship of energy separation and mean oxidation state [86, 95, 118], which implies that as-prepared  $\text{MnO}_x$  possesses a minor portion of Mn (IV) since the mean oxidation state of as-prepared  $\text{MnO}_x$  is slightly higher than  $\text{Mn}_3\text{O}_4$  (mean oxidation state = 2.67). XPS is a surface-sensitive measurement, which indicates the mean manganese oxidation state obtained from XPS results is in the proximity to the sample surface. From Mn 2p spectrum of as-prepared  $\text{MnO}_x$  (not shown here), the peaks of Mn  $2p_{3/2}$  and Mn  $2p_{1/2}$  are located at 641.91 and 653.31 eV, respectively. From the Lorentz fitting of O 1s spectrum of as-prepared  $\text{MnO}_x$  (Figure 6-2b), the peak position at 529.8, 531.3 and 532.5 eV are attributed to Mn-O-Mn (for anhydrous oxide), Mn-OH (hydroxide) and H-O-H bonds (crystalline water), respectively [86, 95, 116, 118]. The Mn-OH bonds contribute 15% (Table 6-2), which suggests the as-prepared  $\text{MnO}_x$  exhibit better capacitive performance since the hydrous property facilitates ionic exchange [95, 116].

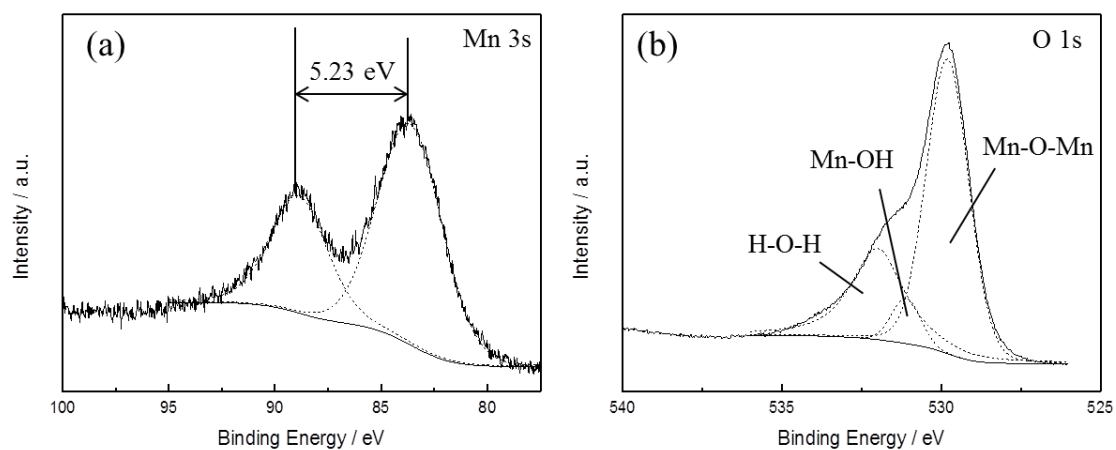


**Figure 6-2** XPS (a) Mn 3s and (b) O 1s spectra of as-prepared  $\text{MnO}_x$ .

**Table 6-2** Peak position and area percentage of O 1s spectrum of as-prepared and activated  $\text{MnO}_x$ .

O 1s		Position (eV)	Percentage (%)
Mn-O-Mn	as-prepared $\text{MnO}_x$	529.8	67
Mn-OH		531.3	15
H-O-H		532.5	18
Mn-O-Mn	activated $\text{MnO}_x$	529.9	44
Mn-OH		531.2	37
H-O-H		532.5	19

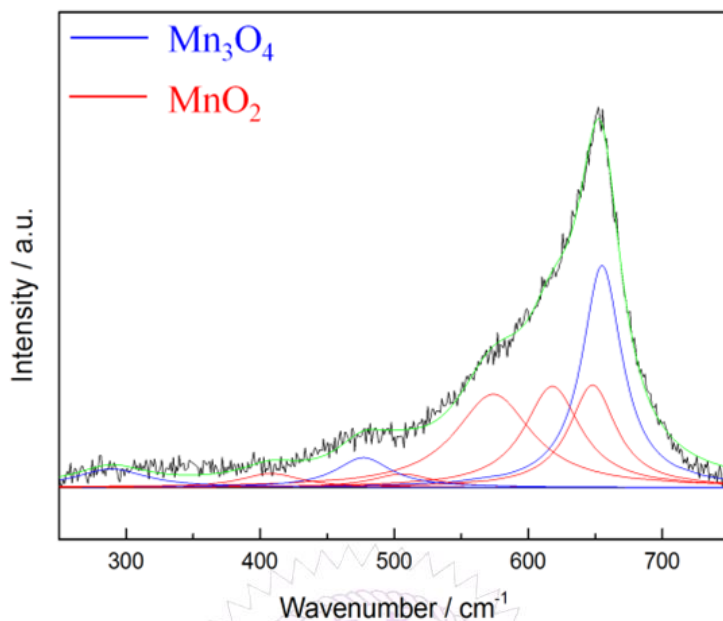


**Figure 6–3** Lorentz fitting of *ex situ* Raman spectrum of as–prepared  $\text{MnO}_x$ . Green line = envelope of total of the fitted peaks.

According to literature [170], the Raman active bands of hausmannite  $\text{Mn}_3\text{O}_4$  are observed at 289, 315, 370, 477 and  $660\text{ cm}^{-1}$ . Bands at  $310\text{--}320$  and  $360\text{--}370\text{ cm}^{-1}$  are the bending mode of  $\text{Mn}_3\text{O}_4$ , while  $650\text{--}660\text{ cm}^{-1}$  is the Mn–O breathing vibration of  $\text{Mn}^{2+}$  in tetrahedral coordination [18, 164]. In general, the Raman active bands for  $\text{MnO}_2$  are at  $500\text{--}510$ ,  $575\text{--}585$  and  $625\text{--}650\text{ cm}^{-1}$ , which represent Mn–O stretching vibration of  $\text{MnO}_6$  octahedra, Mn–O stretching vibration of the basal plane of  $\text{MnO}_6$  sheets and the symmetric stretching vibration of Mn–O of the  $\text{MnO}_6$  group, respectively [18, 148]. The Raman spectrum of as–prepared  $\text{MnO}_x$  is shown in Figure 6–3. The intense peak at ca.  $658\text{ cm}^{-1}$  can be observed, which is the most notable band of  $\text{Mn}_3\text{O}_4$  [18, 164]. However, a shoulder around  $575\text{ cm}^{-1}$  can also be found, which provides further evidence that as–prepared  $\text{MnO}_x$  might not be pure hausmannite  $\text{Mn}_3\text{O}_4$ , since a minor portion of  $\text{MnO}_2$  can be found in the spectrum. Moreover, the two peaks at  $310\text{--}320$  and  $360\text{--}370\text{ cm}^{-1}$  are not able to be resolved from the background noise. The presence of (a minor portion)  $\text{MnO}_2$  in the as–

prepared  $\text{MnO}_x$  might reduce crystallinity of hausmannite  $\text{Mn}_3\text{O}_4$ , which might result in the absence of the bending mode of  $\text{Mn}_3\text{O}_4$ . The results from both Raman and XPS analyses of as-prepared  $\text{MnO}_x$  strongly indicate a minor portion of Mn (IV) is present. According to the above analyses, the as-prepared  $\text{MnO}_x$  can be considered to be hausmannite  $\text{Mn}_3\text{O}_4$  with a minor portion of Mn (IV).

### 6.3 Electrochemical Activation Process of $\text{MnO}_x$

CVs measured at a sweep rate of  $25 \text{ mV s}^{-1}$  between 0 and 1.2 V (vs. Ag/AgCl) in 0.5 M  $\text{Na}_2\text{SO}_4$  for controlled cycles are shown in Figure 6-4. For the first few cycles, the anodic peak around 1.05 V on the positive sweep can be considered to be the oxidation of  $\text{Mn}_3\text{O}_4$  to higher oxidation state. This anodic peak gradually decreased during cycling and the cathodic peak around 0.9 V on the negative sweep gradually decreased at the same time. On the other hand, the current responses of the redox peak at ca. 0.4–0.5 V gradually increased during cycling. This peak is related to partial oxidation/reduction between Mn (III) and Mn (IV) according to the Pourbaix diagram [127]. The rectangular CV profile at 500<sup>th</sup> cycle indicates that ideal capacitive performances of  $\text{MnO}_x$  can be obtained by potential cycling which has been proposed as an electrochemical activation method [21]. Note that the poor capacitive performance at first few cycles for pure  $\text{Mn}_3\text{O}_4$  (i.e., less than  $20 \text{ F g}^{-1}$ ) has been reported [17, 19]. However, the specific capacitance at 5<sup>th</sup> cycle reaches ca.  $130 \text{ F g}^{-1}$  in this work, which confirms that the as-prepared  $\text{MnO}_x$  is composed of a minor portion of  $\text{MnO}_2$  and is not pure  $\text{Mn}_3\text{O}_4$ .



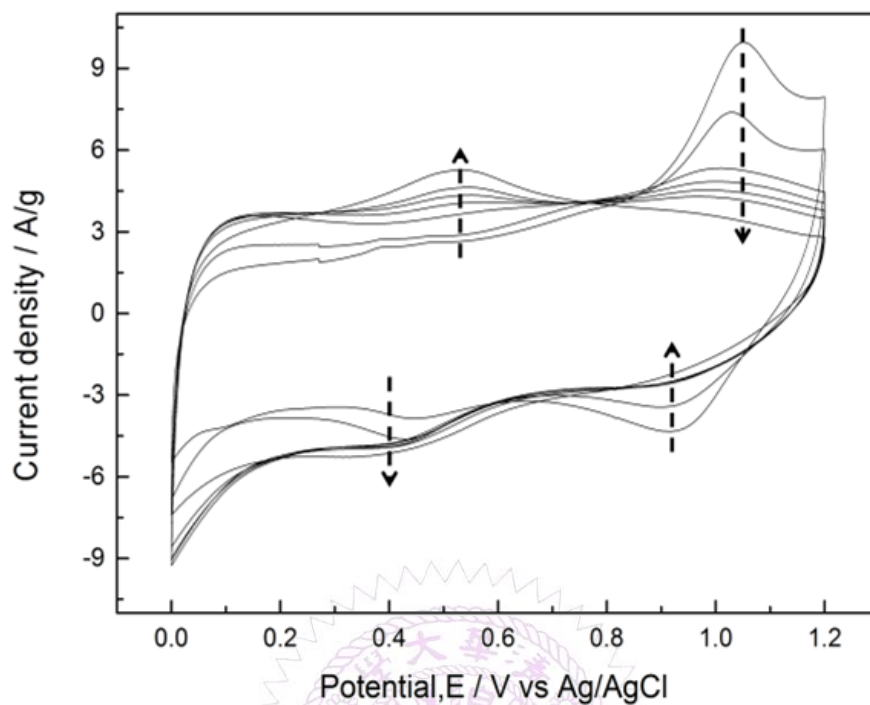


**Figure 6-4** CVs measured at a sweep rate of  $25 \text{ mV s}^{-1}$  between 0 and 1.2 V (vs. Ag/AgCl) in 0.5 M  $\text{Na}_2\text{SO}_4$  for 5, 10, 50, 100, 150, 200 and 500 cycles.

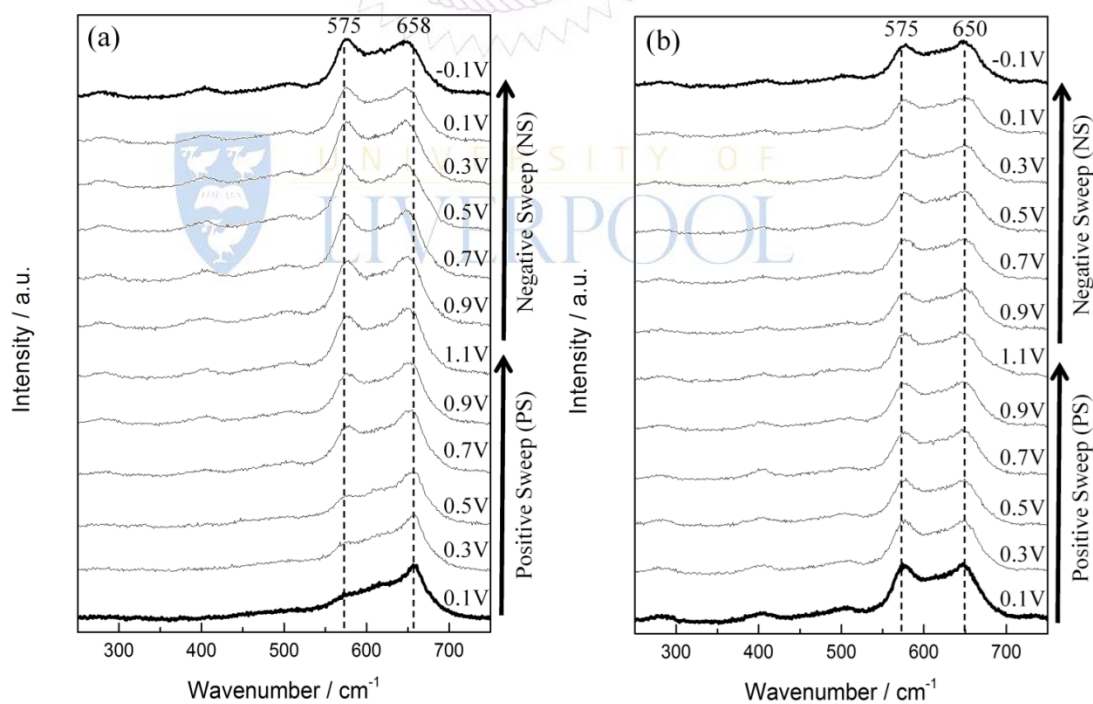


**Figure 6-5** *In situ* Raman spectra series of (a) the 1<sup>st</sup> and (b) the 2<sup>nd</sup> cycle. Each cycle started from 0.1 V (PS 0.1V) and ended at -0.1 V (NS -0.1V).

For the 1<sup>st</sup> *in situ* Raman cycle (Figure 6–5a), a strong peak located at 658 cm<sup>-1</sup> is visible from PS 0.1 V, PS 0.3 V and PS 0.5 V. This peak is characteristic of Mn<sub>3</sub>O<sub>4</sub> as described above. From PS 0.9 V to NS –0.1 V, this peak slightly shifts to a lower wavenumber (from 658 to 650 cm<sup>-1</sup>) with further applying potential. Besides, the intensity of this peak for the 12 spectra remains in the same level. On the other hand, a descending shoulder from ca. 650 to 550 cm<sup>-1</sup> is found from PS 0.1 V. The peak at 575 cm<sup>-1</sup> was gradually formed during the polarisations and this peak became significant from PS 0.7 V to NS –0.1 V. Since the peak intensity of 575 cm<sup>-1</sup> reached the same level of the peak at ca. 658 cm<sup>-1</sup>, a new MnO<sub>x</sub> species (i.e., MnO<sub>2</sub>) is believed to be formed. The spectra recorded at the 2<sup>nd</sup> cycle (Figure 6–5b) all remain the similar pattern, which indicate that the newly formed MnO<sub>2</sub> remains stable in the cycled potential window. Therefore the mean Mn oxidation state during further cycling after activation can only be accessed via other techniques such as X–ray photoelectron spectroscopy or X–ray absorption microscopy.



**Table 6–3** Peak position ( $\text{cm}^{-1}$ ) and Full Width at Half Maximum (FWHM,  $\text{cm}^{-1}$  in parenthesis) of the  $\text{Mn}_3\text{O}_4$  and  $\text{MnO}_2$  peaks by Lorentz fitting.

	$\text{Mn}_3\text{O}_4$	$\text{MnO}_2$	$\text{MnO}_2$	$\text{MnO}_2$	$\text{MnO}_2$	$\text{Mn}_3\text{O}_4$	$\text{MnO}_2$	$\text{Mn}_3\text{O}_4$	$I_{\text{MnO}_2}/I_{\text{Mn}_3\text{O}_4}$
1 <sup>st</sup> cycle PS 0.1V	658 (27)	648 (66)	618 (51)	575 (61)	506 (45)	477 (55)	408 (55)	289 (65)	0.52
1 <sup>st</sup> cycle PS 0.5V	658 (29)	648 (58)	618 (60)	575 (47)	506 (50)	477 (60)	408 (40)	284 (61)	0.65
1 <sup>st</sup> cycle PS 0.9V	658 (26)	648 (42)	618 (48)	575 (40)	506 (31)	477 (48)	408 (46)	283 (43)	1.81
2 <sup>nd</sup> cycle PS 0.1V	658 (29)	648 (37)	618 (64)	575 (33)	506 (26)	477 (48)	408 (38)	283 (33)	3.94

**Table 6–4** Peak position ( $\text{cm}^{-1}$ ) and Full Width at Half Maximum (FWHM,  $\text{cm}^{-1}$  in parenthesis) of the  $\text{Mn}_3\text{O}_4$  and  $\text{MnO}_2$  peaks by Lorentz fitting of *ex situ* Raman spectra.

	$\text{Mn}_3\text{O}_4$	$\text{MnO}_2$	$\text{MnO}_2$	$\text{MnO}_2$	$\text{MnO}_2$	$\text{Mn}_3\text{O}_4$	$\text{MnO}_2$	$\text{Mn}_3\text{O}_4$	$I_{\text{MnO}_2}/I_{\text{Mn}_3\text{O}_4}$	Cs (F/g)
as-prepared	658 (36)	648 (42)	618 (51)	575 (70)	506 (55)	477 (50)	408 (55)	289 (65)	0.42	N/a
5 <sup>th</sup> cycle	658 (36)	648 (45)	618 (45)	575 (61)	506 (55)	477 (55)	408 (55)	284 (65)	0.63	132
10 <sup>th</sup> cycle	658 (36)	648 (52)	618 (52)	575 (70)	506 (60)	477 (55)	408 (45)	285 (65)	0.89	144
50 <sup>th</sup> cycle	658 (35)	648 (46)	618 (48)	575 (55)	506 (55)	477 (40)	408 (56)	285 (65)	1.62	166
100 <sup>th</sup> cycle	658 (37)	648 (49)	618 (64)	575 (45)	506 (50)	477 (45)	408 (56)	285 (45)	2.53	169
150 <sup>th</sup> cycle	658 (33)	648 (55)	618 (50)	575 (70)	506 (55)	477 (65)	408 (55)	280 (65)	2.51	170
200 <sup>th</sup> cycle	658 (30)	648 (55)	618 (50)	575 (70)	506 (50)	477 (55)	408 (55)	284 (61)	2.45	171
500 <sup>th</sup> cycle	658 (30)	648 (53)	618 (42)	575 (53)	506 (56)	477 (55)	408 (50)	281 (60)	2.44	174

Lorentz fitting of Raman spectra is used in order to gain a further understanding of this phenomenon. The peaks at 658, 477 and 289  $\text{cm}^{-1}$  are related to hausmannite  $\text{Mn}_3\text{O}_4$  [170], while the peaks at 648, 618, 575, 506 and 408  $\text{cm}^{-1}$  are attributed to birnessite  $\text{MnO}_2$  [126]. Note that all the peak positions are fixed except for the peak at ca. 289  $\text{cm}^{-1}$  (allows from 283 to 289  $\text{cm}^{-1}$ ). The  $\text{Mn}_3\text{O}_4$  peak intensity at 658  $\text{cm}^{-1}$  gradually decreased, while peaks related to birnessite  $\text{MnO}_2$  (marked as red line in Figure 6–6) gradually enhanced during polarisations. The  $\text{Mn}_3\text{O}_4$  peak at 658  $\text{cm}^{-1}$  dominates for the 1<sup>st</sup> cycle PS 0.1 V and the 1<sup>st</sup> cycle PS 0.5 V. However, the peak at 648  $\text{cm}^{-1}$  related to birnessite  $\text{MnO}_2$  became stronger than the  $\text{Mn}_3\text{O}_4$  peak at 658  $\text{cm}^{-1}$  with the positive and negative shifts in electrode potentials. As a result, this peak shifted from 658 (1<sup>st</sup> cycle PS 0.9 V) to 650  $\text{cm}^{-1}$  (1<sup>st</sup> cycle NS –0.1 V) and further remained the same position. The peak intensity ratio of  $\text{MnO}_2$  and  $\text{Mn}_3\text{O}_4$  ( $I_{\text{MnO}_2}/I_{\text{Mn}_3\text{O}_4}$ ) is proposed to be an indicator to quantify the degree of activation from  $\text{Mn}_3\text{O}_4$  to  $\text{MnO}_2$  although the different  $\text{MnO}_x$  species show different Raman sensitivities. Here,  $I_{\text{MnO}_2}/I_{\text{Mn}_3\text{O}_4}$  is calculated on the basis of the peak intensity of 575 and 658  $\text{cm}^{-1}$  from the fitting results since these two peaks are the most distinguishable peaks for  $\text{MnO}_2$  and  $\text{Mn}_3\text{O}_4$ , respectively.  $I_{\text{MnO}_2}/I_{\text{Mn}_3\text{O}_4}$  for as-prepared  $\text{MnO}_x$  is 0.42 (Table 6–4) and the value increases gradually during the electrochemical polarisations.  $I_{\text{MnO}_2}/I_{\text{Mn}_3\text{O}_4}$  is 3.94 for the 2<sup>nd</sup> cycle PS 0.1 V, which is ca. 8 times higher than as-prepared  $\text{MnO}_x$  (Table 6–3). The mean manganese oxidation state of activated  $\text{MnO}_x$  is ca. 3.94 based on the energy separation (4.85 eV) of Mn 3s core level spectrum (Figure 3c). In comparison with the mean manganese oxidation state of as-prepared  $\text{MnO}_x$  (3.18), the results support the activation from  $\text{Mn}_3\text{O}_4$  (i.e., Mn (II) and Mn (III)) to  $\text{MnO}_2$  (Mn (IV)) during the electrochemical activation.

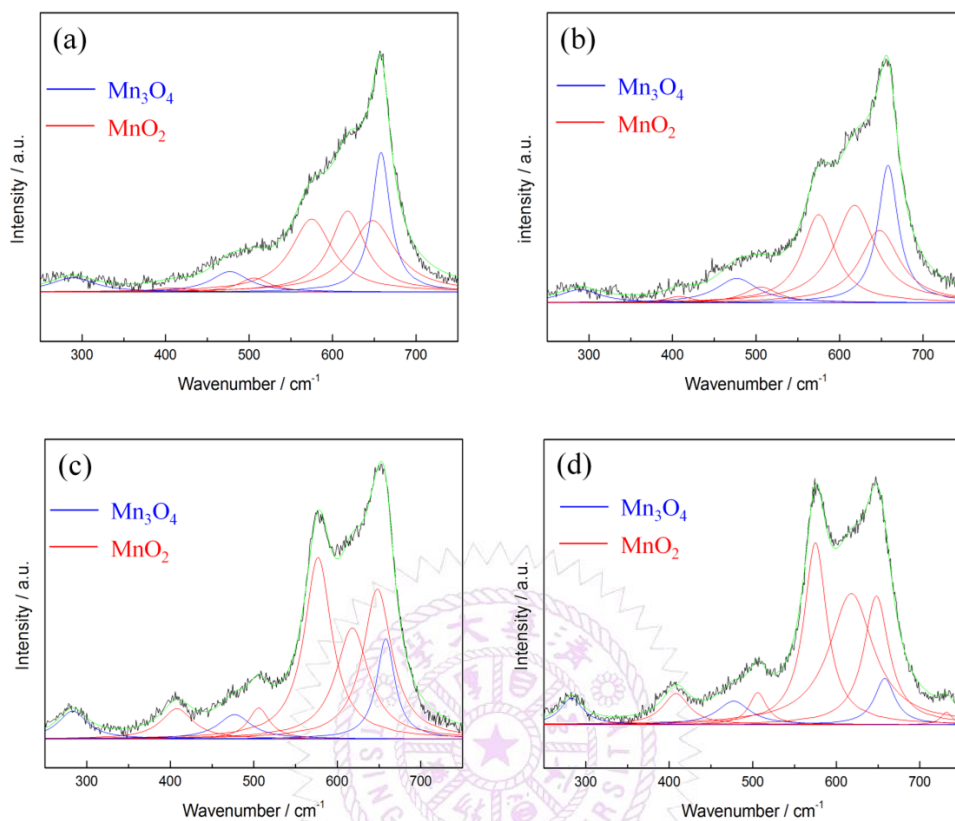


**Figure 6–6** Lorentz fitting of *in situ* Raman spectra (a) 1st cycle PS 0.1V, (b) 1st cycle PS 0.5V, (c) 1st cycle PS 0.9V and (d) 2nd cycle PS 0.1V. Green line = envelope of total of the fitted peaks.

According to the fitting results, residual  $\text{Mn}_3\text{O}_4$  can be still observed even at the 2<sup>nd</sup> *in situ* Raman cycle (Figure 6–6d). Note that the formed  $\text{MnO}_2$  is stable in the cycled potential window for the 2<sup>nd</sup> *in situ* Raman cycle (Figure 6–5b). It therefore be concluded that not all the  $\text{Mn}_3\text{O}_4$  is converted to  $\text{MnO}_2$  in the above electrochemical treatment. Due to the residual  $\text{Mn}_3\text{O}_4$ , the mean manganese oxidation state for the activated  $\text{MnO}_x$  is not exactly equal to 4.0. Hence, it can be concluded that the major portion of hausmannite  $\text{Mn}_3\text{O}_4$  can be activated to birnessite  $\text{MnO}_2$  by the electrochemical treatment. Besides, the residual  $\text{Mn}_3\text{O}_4$  in electrochemically activated birnessite  $\text{MnO}_2$  results in structure disorder of layered birnessite  $\text{MnO}_2$ , which reasonably explains why the oxide derived from  $\text{Mn}_3\text{O}_4$  showed higher cycling stability because of the coexistence of  $\text{MnO}_2$  and  $\text{Mn}_3\text{O}_4$  [21]. *Ex situ* Raman spectra

were recorded for all CV-cycled  $\text{MnO}_x$ . From Lorentz fitting results, the correlation between specific capacitance of  $\text{MnO}_x$  and CV cycle number is shown in Figure 6–7. Note that the current responses related to the activation from  $\text{Mn}_3\text{O}_4$  to  $\text{MnO}_2$  (the anodic peak around 1.05 V on the positive sweep) are evident in the first few cycles, which decreases gradually during the activation process. The ideal pseudocapacitance of  $\text{MnO}_2$  mainly contributes from the potential window between 0.2 and 0.8 V [129]. The current responses related to the oxidation of  $\text{Mn}_3\text{O}_4$  cannot be considered pseudocapacitance. Therefore, the calculation in Figure 6–7 is based on the baseline of 500<sup>th</sup> cycle (stable current responses) between 0.8 and 1.2 V. In general,  $\text{MnO}_2$  is electrochemically active and reversible for supercapacitor applications [62] comparing with  $\text{Mn}_3\text{O}_4$ , which is known as a relatively electrochemical irreversible material among  $\text{MnO}_x$  species. The specific capacitance of  $\text{MnO}_x$  rapidly increased within the initial 50 cycles, which suggests that the activation from  $\text{Mn}_3\text{O}_4$  to  $\text{MnO}_2$  is relatively fast. With further cycling, the specific capacitance of  $\text{MnO}_x$  gradually increased and reached the stable level (ca.  $170 \text{ F g}^{-1}$ ) from the 150<sup>th</sup> to the 500<sup>th</sup> cycle. Based on the Lorentz fitting of *ex situ* Raman spectra (Figure 6–8), the rapid increase of  $\text{MnO}_2$  content ( $I_{\text{MnO}_2}/I_{\text{Mn}_3\text{O}_4} = 0.63$  and  $2.53$  for 5<sup>th</sup> and 100<sup>th</sup> cycle, respectively) shows the same trend as capacitance increase. With further cycling to 500<sup>th</sup> cycle,  $I_{\text{MnO}_2}/I_{\text{Mn}_3\text{O}_4}$  remained the same level (i.e., 2.45). It should be noted that this ratio is lower than that from *in situ* measurements (3.94). Accordingly, the activation from hausmannite  $\text{Mn}_3\text{O}_4$  to birnessite  $\text{MnO}_2$  can be verified by the *in situ* and *ex situ* Raman experiments. The stable electrochemically activated birnessite  $\text{MnO}_2$  can be formed and displays promising pseudocapacitance in 0.5 M  $\text{Na}_2\text{SO}_4$ .



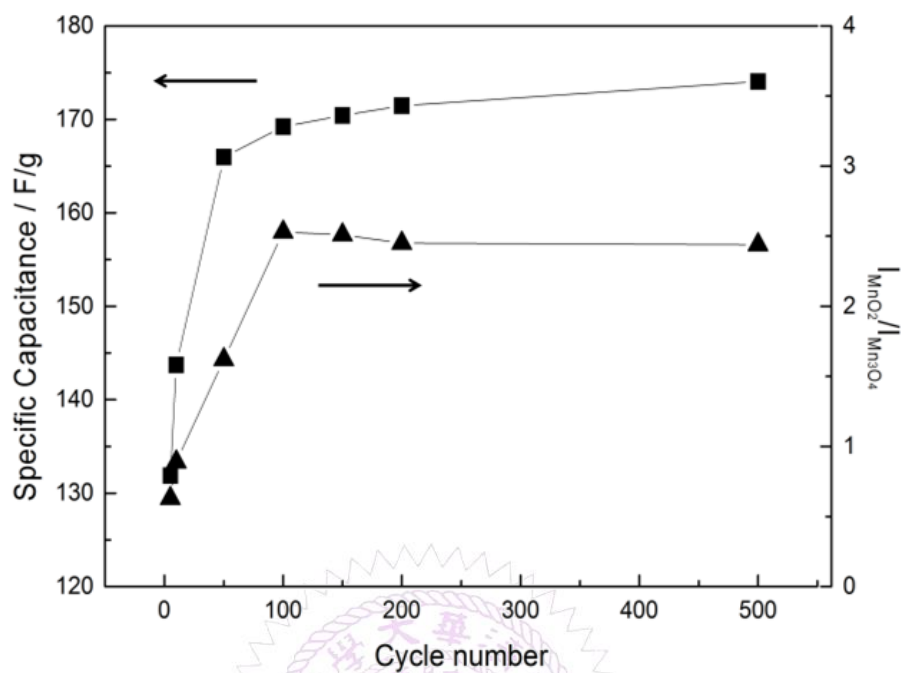


**Figure 6-7** Cycle number dependence of specific capacitance calculated by CV at  $25 \text{ mV s}^{-1}$  and intensity ratio ( $I_{\text{MnO}_2}$  of  $575 \text{ cm}^{-1} / I_{\text{Mn}_3\text{O}_4}$  of  $658 \text{ cm}^{-1}$ ) of  $\text{MnO}_x$ .

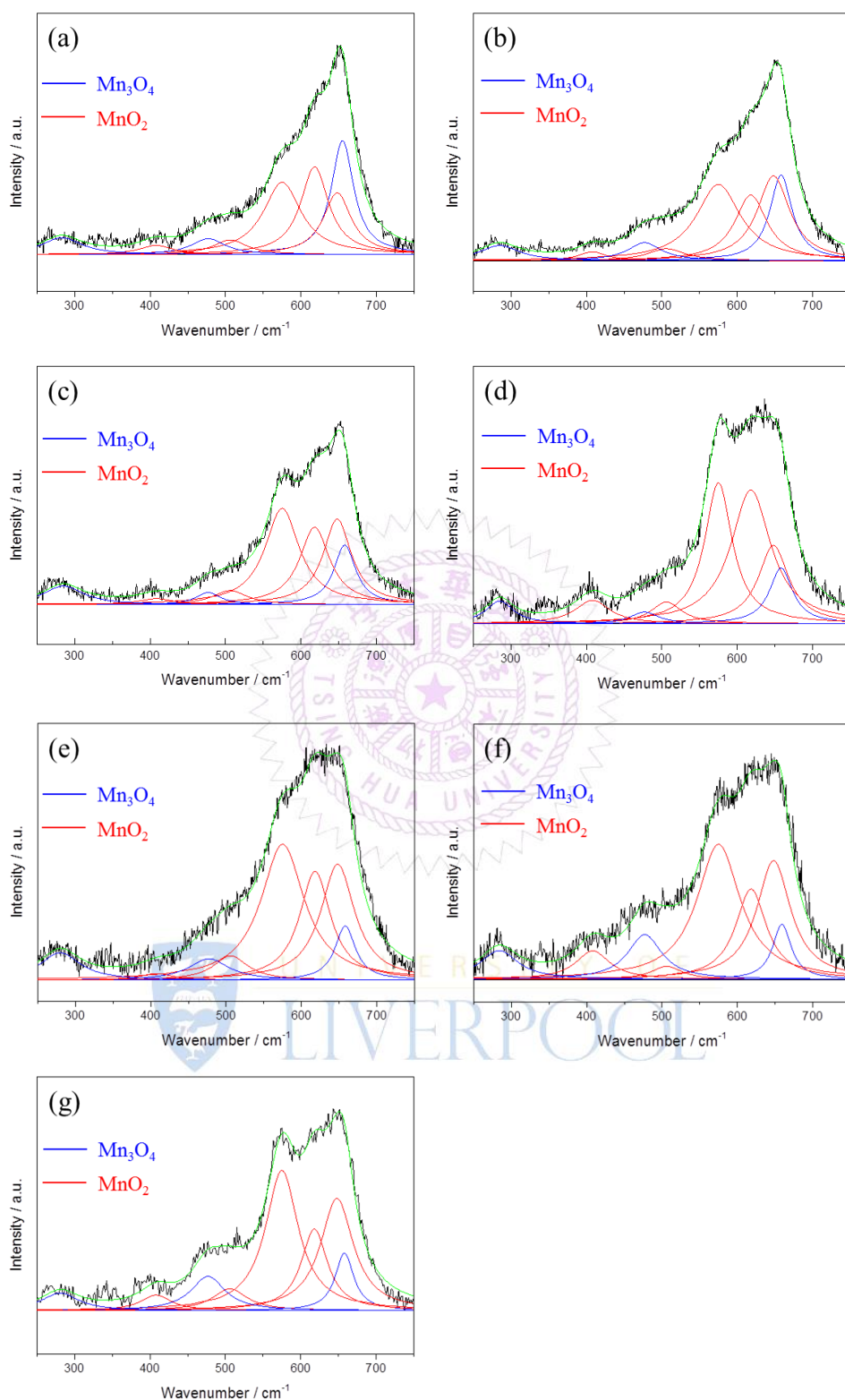


**Figure 6–8** Lorentz fitting of *ex situ* Raman spectra recorded after (a) 5<sup>th</sup>, (b) 10<sup>th</sup>, (c) 50<sup>th</sup>, (d) 100<sup>th</sup>, (e) 150<sup>th</sup>, (f) 200<sup>th</sup> and (g) 500<sup>th</sup> CV cycle. Green line = envelope of total of the fitted peaks.

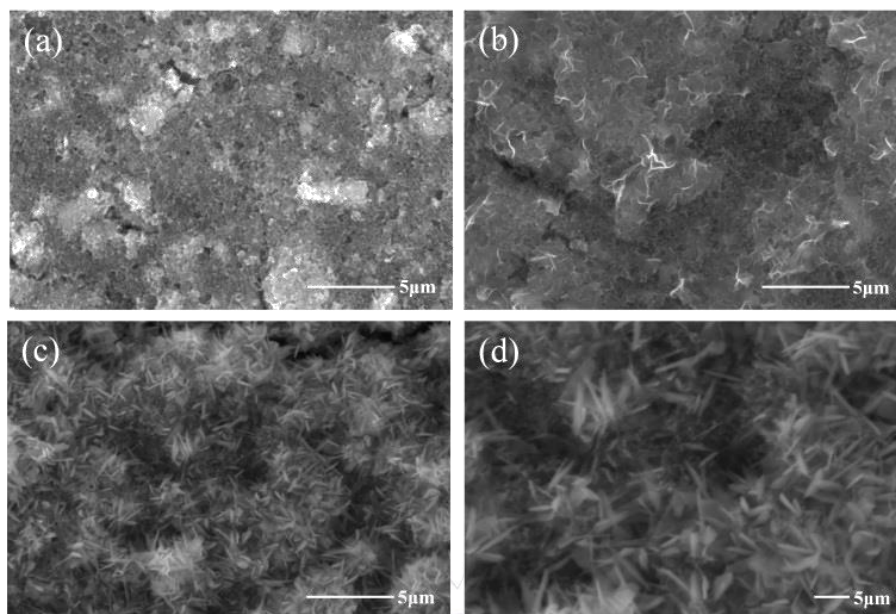


**Figure 6-9** SEM images of (a) as-prepared  $\text{MnO}_x$  and after (b) 100 (c,d) after 500 CV cycles in 0.5 M  $\text{Na}_2\text{SO}_4$ .

Figure 6-9 shows the surface morphology change  $\text{MnO}_x$  during electrochemical activation. A compact surface morphology of as-prepared  $\text{MnO}_x$  can be observed in Figure 6-9a, while it gradually changes into a porous surface after electrochemical activation (Figure 6-9b-d). It has been proposed that the porous surface layer is the re-deposition of dissolved Mn(II) (from hausmannite  $\text{Mn}_3\text{O}_4$  crystalline structure) onto the electrode surface as  $\text{MnO}_2$  during the activation process via CV cycling [20]. The proposed mechanism is reasonable since  $\text{MnO}_2$  can be successfully formed from Mn(II) precursor by potentiodynamic method [61]. Besides, the insignificant electrochemical activation of  $\text{Mn}_2\text{O}_3$  comparing with  $\text{Mn}_3\text{O}_4$  has been found [20]. Therefore, dissolution of Mn(II) from  $\text{MnO}_x$  crystalline is believed to be the key for the electrochemical activation process. In fact, from the investigation of amorphous  $\text{MnO}_2$  by electrochemical quartz crystal microbalance (EQCM), the porous surface of  $\text{MnO}_x$  (predominate  $\text{MnO}_2$ ) is not only from the re-deposition of dissolved Mn(II) during electrochemical activation process but also from the re-deposition (at ca. 0.8–0.2 V) of dissolved Mn(IV) (at ca. 0.8–1.0 V) during CV cycling [129]. The

normalised area of C 1s and Mn 3s XPS spectra of as-prepared and activated MnO<sub>x</sub> are listed in Table 6-5. In comparison with as-prepared MnO<sub>x</sub>, the normalised area ratio (C1s/Mn3s) of activated MnO<sub>x</sub> reduced from ca. 2.59 to 1.04, indicating the re-deposition of MnO<sub>2</sub> onto the electrode surface suppressing the intensity of carbon black and polymeric binder [20]. Note that the intensity (counts/second) of XPS spectra strongly depends on the distance between samples and X-ray beam source. Therefore, normalised area (by atomic sensitivity factor) instead of absolute intensity is used in this work. Moreover, from SEM images (Figure 6-9d), the porous nanostructure surface forms at the outer surface, while this structure cannot be found in some deeper regions. This suggests the electrochemical activation starts from outermost layer of Mn<sub>3</sub>O<sub>4</sub> surface and then gradually into the bulk. This finding is consistent with literature, which reported the amorphous and hydrous MnO<sub>2</sub> is formed in the outer electrode layers and proceeds to grow at the expense of the remaining bulk crystalline Mn<sub>3</sub>O<sub>4</sub> [119].

**Table 6-5** Normalised area (by atomic sensitivity factor) and area ratio calculated from XPS spectra

MnO <sub>x</sub> composite electrode	C 1s normalised area	Mn 3s normalised area	C1s/Mn3s area ratio
As-prepared MnO <sub>x</sub>	5792	3722.6	2.59
Activated MnO <sub>x</sub> (at region 1)	35096	34120	1.03
Activated MnO <sub>x</sub> (at region 2)	45909	43889	1.05

## 6.4 Charge Storage Mechanism of Electrochemically Activated MnO<sub>x</sub>

The activated MnO<sub>x</sub> was characterised by PXRD as amorphous MnO<sub>2</sub> (Figure 6–10a). The SAED pattern of activated MnO<sub>x</sub> (Figure 6–10b) suggests that the electrochemically activated MnO<sub>x</sub> within the electrode composite possess poor crystallised structure since the diffraction patterns do not have well defined rings.

Interestingly, with further analysis, both birnessite MnO<sub>2</sub> and hausmannite Mn<sub>3</sub>O<sub>4</sub> crystallites can be found in the activated MnO<sub>x</sub> (Table 6–1) although no reflections can be observed from diffraction pattern of activated MnO<sub>x</sub>. The d–spacing of 0.242 and 0.210 nm are corresponding to birnessite MnO<sub>2</sub>. Apart from these two d–spacing found in SAED pattern, others are all related to Mn<sub>3</sub>O<sub>4</sub> residual in the activated MnO<sub>x</sub>. From the TEM images of activated MnO<sub>x</sub> (Figure 6–10c), the particle–like MnO<sub>x</sub> structure can be still observed. In comparison with as–prepared MnO<sub>x</sub>, the particles and lattices of activated MnO<sub>x</sub> are not well defined. As a result, the activated MnO<sub>x</sub> is believed to have disordered layered birnessite structure; however, there is insufficient long–range order to allow for a PXRD pattern to be observed. Therefore, the structure of the electrochemically activated MnO<sub>x</sub> is determined to be composite material consisting of amorphous MnO<sub>2</sub> (with localised birnessite structure) and a minor portion of residual of hausmannite Mn<sub>3</sub>O<sub>4</sub>. Amorphous manganese oxide has been considered to be beneficial for supercapacitors since it provides large interlayer distance and surface area–to–volume ratio. The increase contact between the electrolyte and the electrode material improves the utilisation ratio of the material [203]. Besides, the significant increase of Mn–OH (hydroxide) bond in activated MnO<sub>x</sub> (Figure 6–11b and Table 6–2) indicates that the MnO<sub>x</sub> became more hydrous after electrochemical activation. As discussed above, hydrous property of MnO<sub>x</sub> facilitates ionic exchange and exhibits better capacitive

performance [95, 116].

The change of Mn oxidation state of  $\text{MnO}_x$  during activation process was estimated by the Mn K-edge XAS spectra (shown in Figure 6–12). For as-prepared sample, the Mn oxidation state is 2.88, which indicates the as-prepared material is predominant  $\text{Mn}_3\text{O}_4$  with a minor portion of  $\text{MnO}_2$ . During the activation process, the mean Mn oxidation state is found to be 3.28 and 3.41 after 100 and 500 CV cycles, respectively. This suggests the as-prepared  $\text{MnO}_x$  (mainly  $\text{Mn}_3\text{O}_4$ ) can be oxidised to a higher oxidation state ( $\text{MnO}_2$ ), where the newly formed  $\text{MnO}_2$  contributes a better capacitive performance owing to its good electrical conductivity in comparison of  $\text{Mn}_3\text{O}_4$ . Thus, this material can be ‘activated’ to better capacitive behaviour. From XPS, the oxidation state of as-prepared and activated  $\text{MnO}_x$  is 3.18 and 3.94, respectively. It is noteworthy that the change of Mn oxidation state during activation process (0.53) is not as significant as that obtained from XPS (0.76). The reason is that XPS is a surface-sensitive technique (typically in a few nanometers), while XAS is measuring bulk material by a transmission of X-ray through bulk sample pellets. The results indicate the activation process mainly occurs at surface/near-surface region of  $\text{MnO}_x$  electrode.



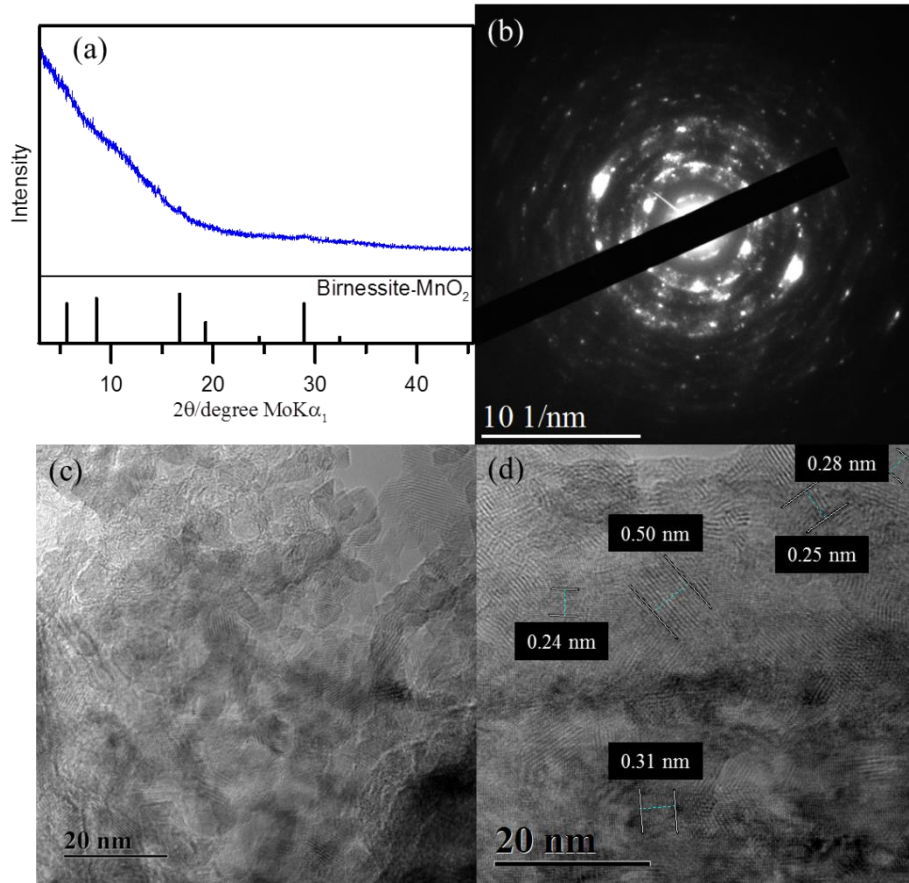


**Figure 6-10** (a) PXRD (MoK $\alpha_1$  source), (b) SAED pattern and (c,d) TEM images of activated MnO $_x$ . JCPDS CARD 18-0802 is standard birnessite MnO $_2$  from database.

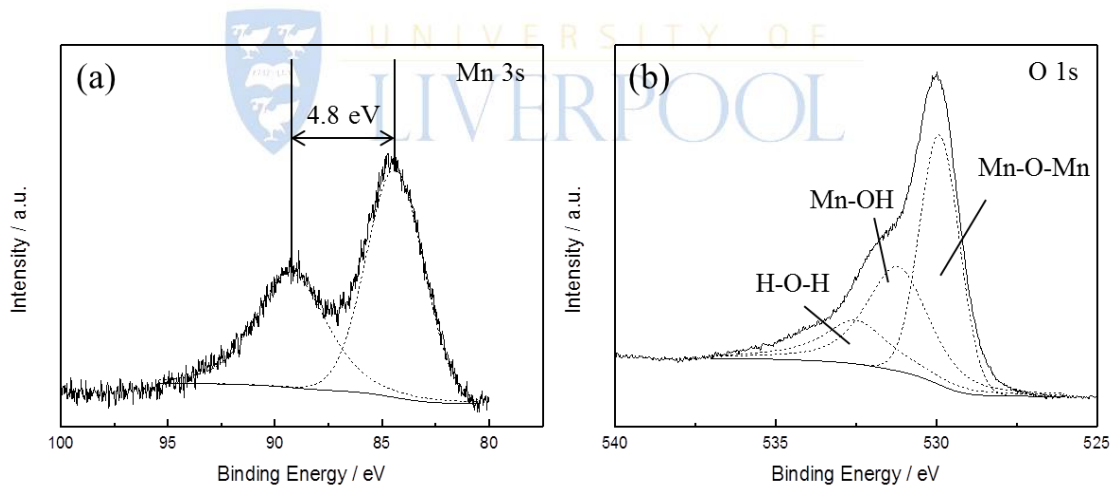


**Figure 6-11** XPS (a) Mn 3s, (b) O 1s spectra of activated MnO $_x$ .

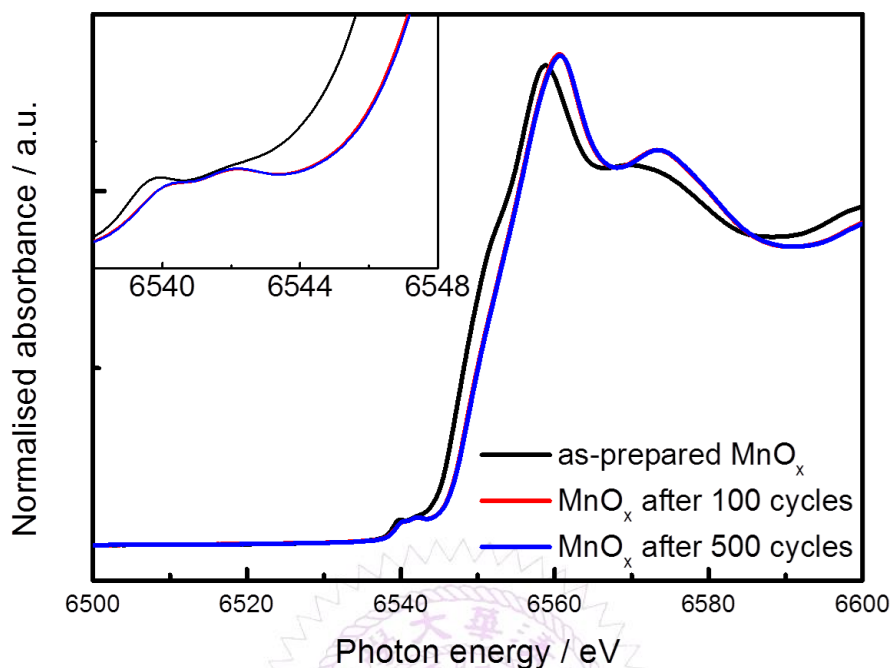


**Figure 6–12** Mn K–edge XAS spectra of as–prepared  $\text{MnO}_x$ , after 100 and 500 CV cycles in 0.5 M  $\text{Na}_2\text{SO}_4$ .

The structure transformation from hexagonal to monoclinic due to cation ( $\text{Na}^+$ ) intercalation into birnessite  $\text{MnO}_2$  has been reported [146], as well as the subtle change of Raman spectra of birnessite  $\text{MnO}_2$  with and without cation ( $\text{Li}^+$  and  $\text{Na}^+$ ) intercalated in  $\text{MnO}_2$  bilayers [148]. The intercalation of alkali–ion into birnessite  $\text{MnO}_2$  bilayers causes local lattice distortion, which results in shorter Mn–O chemical bonds (decrease of the interlayer spacing) and partial reduction of  $\text{Mn}^{4+}$  ions. As a result, the Mn–O symmetric stretching mode moves toward low wavenumber side upon alkali–ion intercalation [148]. However, this peak shift phenomenon due to cation intercalation into layers of birnessite  $\text{MnO}_2$  was not observed by *in situ* Raman during activation process in this work. The peak positions of  $\text{MnO}_2$  correspond to birnessite  $\text{MnO}_2$  rather than Na–birnessite  $\text{MnO}_2$  from literature [126, 148]. Note that the cation ( $\text{Na}^+$ ) doped birnessite  $\text{MnO}_2$  has been reported the presence of ca. 281 and 406  $\text{cm}^{-1}$  peaks, corresponding to stretching modes of  $\text{NaO}_6$  octahedron and  $\text{NaO}_4$

tetrahedron for Na–birnessite  $\text{MnO}_2$ , since Na ions occupy the trigonal prismatic sites of monoclinic  $\text{Na}_x\text{MnO}_2$  [148, 168, 169]. Moreover, the peak around  $732\text{ cm}^{-1}$ , identified as a vibrational mode for non–cation intercalated birnessite  $\text{MnO}_2$ , can be observed by the Raman spectrum of activated  $\text{MnO}_x$  (Figure 6–6d). This indicates that electrochemically activated birnessite structure might not possess a well–defined layer structure (i.e., structure disordering) to allow cation ( $\text{Na}^+$ ) intercalation into bilayers.

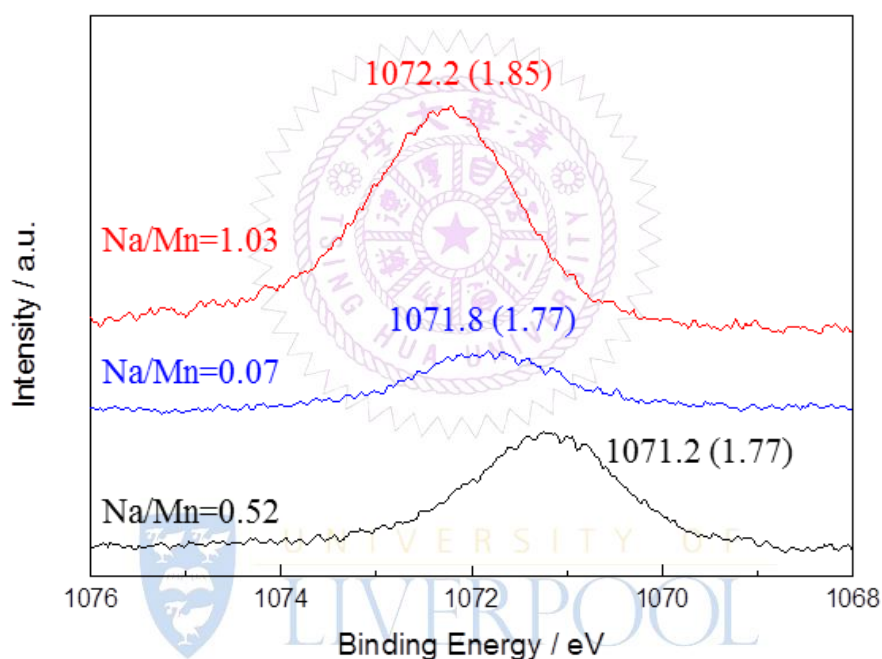


**Figure 6–13** XPS Na 1s of (blue) as–prepared, (red) activated  $\text{MnO}_x$  and (black)  $\text{Na}_{0.33}\text{MnO}_2$  sample. The denoted values are the fitted peak position (eV) and Full Width at Half Maximum (FWHM, eV in parenthesis)

The XPS Na 1s spectrum of as–prepared  $\text{MnO}_x$ , activated  $\text{MnO}_x$  and a sodium intercalated  $\text{MnO}_2$  sample ( $\text{Na}_{0.33}\text{MnO}_2$ ) are shown in Figure 6–13. The Na 1s peak was present at 1072.2 eV (FWHM=1.85) for activated  $\text{MnO}_x$  and shows ca. 1 eV shift in comparison with  $\text{Na}_{0.33}\text{MnO}_2$  at 1071.2 eV (FWHM=1.77). The binding energy at 1072–1073 eV is related to the Na–F bonding, which is attributed to the  $\text{Na}^+$  (from  $\text{Na}_2\text{SO}_4$  electrolyte) bonding with co–polymeric binder at F sites [204]. Although the

Na/Mn ratio of activated  $\text{MnO}_x$  (1.03) is higher than  $\text{Na}_{0.33}\text{MnO}_2$  (Na/Mn=0.52), the Na element contributes from the Na–F bonding rather than incorporation into the  $\text{MnO}_x$  structure after electrochemical measurements.

Based upon the *in situ* Raman and Na 1s XPS analyses, cations are believed to reach the outer surface active sites of electrochemically activated birnessite  $\text{MnO}_2$  and the capacitive behaviour is attributable to the redox reaction between Mn (III) and Mn (IV). The relatively high specific surface area of as-prepared  $\text{MnO}_x$  ( $241 \text{ m}^2 \text{ g}^{-1}$ ) can provide abundant outer surface active sites. As a result, high specific capacitance of birnessite  $\text{MnO}_2$  can be obtained (i.e., the specific capacitance measured at  $500^{\text{th}}$  is  $174 \text{ F g}^{-1}$ ) by potential cycling, which can be compared with values of similar materials in the literature (Table 6–6) [17–20]. The capacitance normalised to specific surface area ( $C_{\text{SA}}$ ) is ca.  $72.3 \mu\text{F cm}^{-2}$ , which is higher than the double layer capacitance (ca.  $10\text{--}20 \mu\text{F cm}^{-2}$ ) for high surface area (over  $1000 \text{ m}^2 \text{ g}^{-1}$ ) carbon material [3]. The real  $C_{\text{SA}}$  of electrochemically activated birnessite  $\text{MnO}_2$  should be even higher since the calculation is based on the specific surface area of as-prepared  $\text{MnO}_x$  and the material might lose some part of active surface area during electrode preparation. Based on the calculated high  $C_{\text{SA}}$ , the charge storage of electrochemically activated  $\text{MnO}_x$  is attributed to the redox reaction between Mn (III) and Mn (IV) (pseudocapacitance).

According to the discussion above, the schematic diagrams of as-prepared  $\text{MnO}_x$  activation process and the proposed charge storage mechanism of activated  $\text{MnO}_x$  are shown in Figure 6–14. For the activation process, the dissolution of Mn (II) takes place at first, followed by re-deposition of porous  $\text{MnO}_2$  onto  $\text{MnO}_x$  electrode surface during potential cycling. Therefore, the electrochemical activation starts from outermost layer of  $\text{Mn}_3\text{O}_4$  surface and then gradually into the bulk. Besides, the inner portion of  $\text{MnO}_x$  electrode remains at residual  $\text{Mn}_3\text{O}_4$ . Due to the structural

disordering of electrochemically activated  $\text{MnO}_x$ , which doesn't have well-defined layer structure to allow cation intercalation during reduction process. Moreover, the accessibility of cations to the bulk  $\text{MnO}_x$  is controlled by the solid-state diffusion, while a much faster surface redox kinetics can be obtained by the ion diffusion at the solid-liquid interface. Therefore, the charge storage of electrochemically activated  $\text{MnO}_x$  is attributable to the redox reaction between Mn (III) and Mn (IV) at outer surface active sites, rather than cations and/or protons intercalation into layer structures. Thus, the improvement of capacitive performance can be achieved by increasing specific surface area of as-prepared  $\text{Mn}_3\text{O}_4$ .

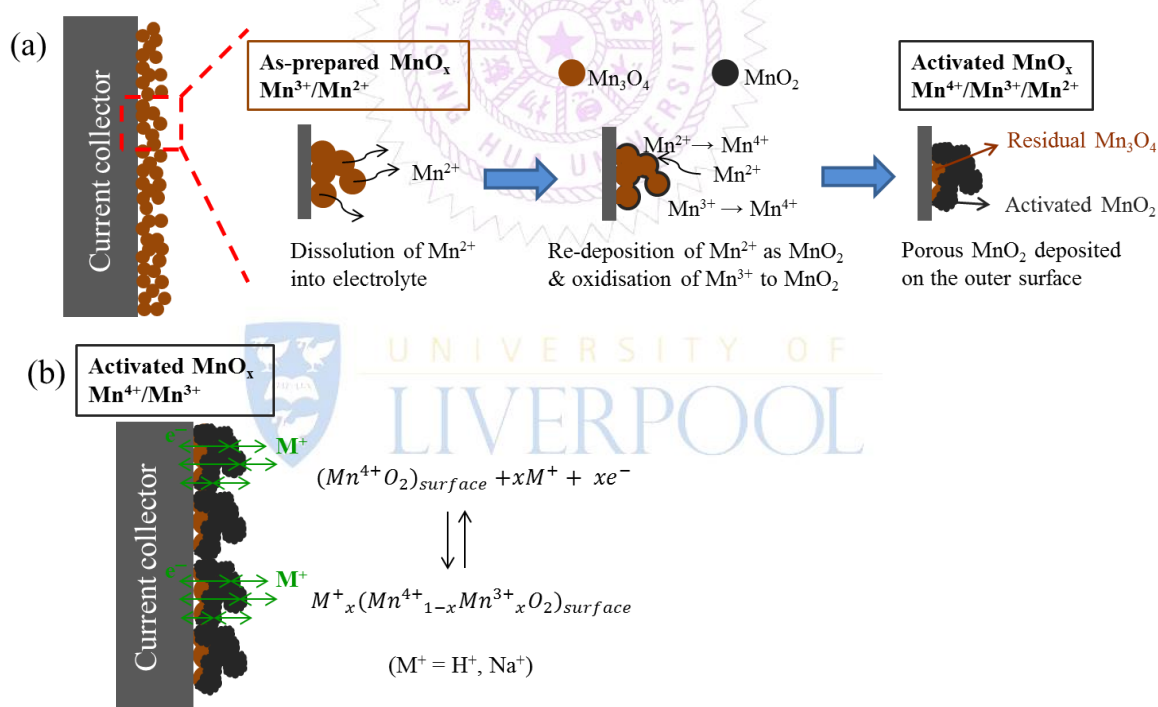


**Figure 6-14** Schematic diagrams of (a) activation process of as-prepared  $\text{MnO}_x$  under potential cycling and (b) the proposed charge storage mechanism of activated  $\text{MnO}_x$ .

The one-pot synthesised as-prepared  $\text{MnO}_x$  is characterised as hausmannite  $\text{Mn}_3\text{O}_4$  with a minor portion of  $\text{MnO}_2$ . The electrochemically activated  $\text{MnO}_x$  is characterised as a composite material consisting of localised birnessite structure

MnO<sub>2</sub> and a minor portion of hausmannite Mn<sub>3</sub>O<sub>4</sub>. The improved capacitive performance of activated MnO<sub>x</sub> is attributed to the synergistic effect of poorly crystallised MnO<sub>2</sub> and Mn<sub>3</sub>O<sub>4</sub> in the composite material and this work describes routes of generating composite materials that possess greater electrochemical performance.

**Table 6–6** Capacitive performance of electrochemically activated MnO<sub>x</sub>.

Specific capacitance (F g <sup>-1</sup> )	Potential window (V)	Electrolyte	Mass loading (mg cm <sup>-2</sup> )	references
174 at 25 mV s <sup>-1</sup>	1.2	0.5 M Na <sub>2</sub> SO <sub>4</sub>	0.71	This work
133 at 50 mV s <sup>-1</sup>	0.9	0.2 M Na <sub>2</sub> SO <sub>4</sub>	0.15 <sup>a</sup>	[17]
150 at 50 mV s <sup>-1</sup>	1.0	0.1 M Na <sub>2</sub> SO <sub>4</sub>	0.116 <sup>a</sup>	[18]
~160 at 20 mV s <sup>-1</sup>	1.0	1.0 M Na <sub>2</sub> SO <sub>4</sub>	0.72 <sup>b</sup>	[19]
~160 at 10 mV s <sup>-1</sup>	1.0	0.5 M Na <sub>2</sub> SO <sub>4</sub>	1.33 <sup>c</sup>	[20]

<sup>a</sup> The electrode is prepared by MnO<sub>x</sub> without mixing with conductive agent and binder.

<sup>b</sup> The specific capacitance is estimated from CV profile.

<sup>c</sup> The electrode consists of 80% MnO<sub>x</sub>, 10% conductive agent (carbon) and 10% poly(vinylidene fluoride) binder.



## 6.5 Conclusions

Electrochemically activated  $\text{MnO}_x$ , from one-pot synthesised hausmannite  $\text{Mn}_3\text{O}_4$ , exhibits a capacitive performance of  $174 \text{ F g}^{-1}$  (at  $25 \text{ mV s}^{-1}$ ) and  $1.2 \text{ V}$  potential window ( $0\text{--}1.2 \text{ V}$  vs.  $\text{Ag/AgCl}$ ), which is superior to reported values of comparable materials. Activation from primarily hausmannite  $\text{Mn}_3\text{O}_4$  to predominantly localised birnessite  $\text{MnO}_2$  by potential cycling is verified by both *in situ* and *ex situ* Raman microscopy, XPS and TEM analysis. Due to the structural disordering of electrochemically activated birnessite  $\text{MnO}_2$  and residual  $\text{Mn}_3\text{O}_4$ , the charge storage is attributable to the redox reaction between Mn (III) and Mn (IV) at outer surface active sites, rather than cations and/or protons intercalation into layer structures. The improved capacitive performance relates to the synergistic effect of well-dispersed  $\text{MnO}_2$  and  $\text{Mn}_3\text{O}_4$  nanoscale domains present within the activated material. Overall we show that the integrated nanoscale structuring of different phases of manganese oxides offers superior properties compared with bulk parent materials and as such offers an avenue of future supercapacitor materials development.

# Chapter 7

## A New Redox Mechanism of Ni(OH)<sub>2</sub> and Its Phase Transformation

### 7.1 Motivation

Ni(OH)<sub>2</sub> has been studied for many decades due to the versatile applications in electrochemical energy storage and conversion systems [25–30, 174–181]. For all the electrochemical applications, long-term performance retention is the jointly great concern when Ni(OH)<sub>2</sub> is utilised as an electroactive material. However, phase transformation (also called ageing process) from  $\alpha$ -Ni(OH)<sub>2</sub> to  $\beta$ -Ni(OH)<sub>2</sub> occurs spontaneously and continuously, leading to the gradual changes of both the microstructure and electrochemical performances [205, 206].

Accordingly, researchers proposed to retain the peculiar phase of Ni(OH)<sub>2</sub> by introducing ‘impurities (either cationic or anionic substitution)’ into Ni(OH)<sub>2</sub> structure [26, 190, 207, 208]. While most of them focused on the relationship between the composition or microstructure of synthesised Ni(OH)<sub>2</sub> and the performance retention, only a few studies probed the ageing process of  $\alpha$ -Ni(OH)<sub>2</sub> into  $\beta$ -Ni(OH)<sub>2</sub>. Biphasic mechanism was reported as the mechanism of  $\alpha$  phase ageing into  $\beta$  phase when  $\alpha$ -Ni(OH)<sub>2</sub> is in contact with water, suggesting that turbostratic  $\alpha$ -Ni(OH)<sub>2</sub> dissolves into water slowly and followed by nucleation and growth of  $\beta$ -Ni(OH)<sub>2</sub> from the solution [187]. The reason for the ageing process originates from the more thermodynamically stable structure of  $\beta$ -Ni(OH)<sub>2</sub> (i.e., the chemical potential is the driving force for the phase transformation). However, phase transformation of  $\alpha$ -Ni(OH)<sub>2</sub> in water solution takes a relatively long time period (ca. 43 days) [189].

With regard to the phase transformation induced by electrochemical methods in alkaline solution, the ageing process occurs much quicker in KOH (ca. few hours) [190], suggesting a different phase transformation mechanism from the proposed ‘biphasic mechanism’. The foreign cation effects on the cationic substituted Ni(OH)<sub>2</sub> (denoted as Ni<sub>1-x</sub>M<sub>x</sub>(OH)<sub>2</sub> where M could be Co, Zn, Al etc.) has been reported in literature [209, 210]. However, the foreign cation in this case is actually incorporated into the Ni(OH)<sub>2</sub> structure. To our best knowledge, the importance of electrolyte cation species to the retention issue has never been addressed.

Based on the above understanding, the effects of alkali metal cation species (LiOH, NaOH, KOH and CsOH) on the phase transformation is investigated by means of EQCM and *in situ* Raman microscopy in this work. Moreover, the computational simulation (DFT+U) based on EQCM results gives a better idea on the compositional changes in the first few potential cycles. Besides, a new redox mechanism of nickel hydroxide is proposed.

## 7.2 Electrochemical Behaviours of Ni(OH)<sub>2</sub>

According to our previous study [31], the as-deposited Ni(OH)<sub>2</sub> obtained by cathodic deposition is identified as  $\alpha$ -Ni(OH)<sub>2</sub> by X-ray diffraction. Figure 7-1 shows the CV profiles of as-deposited Ni(OH)<sub>2</sub> on EQCM gold electrodes in 1 M LiOH, NaOH, KOH, CsOH, and NH<sub>4</sub>OH. There are three features required to be further discussed.

First, the CV profiles obtained in alkaline media (curve 1-4 in Figure 7-1) exhibit the typical voltammetric behaviours of  $\gamma$ -NiOOH/ $\alpha$ -Ni(OH)<sub>2</sub> couple, i.e., a pair of redox peaks. But subtle differences between the redox peak potentials can be observed. The order of cation species with respect to the redox peak potential is: Li<sup>+</sup> >

$\text{Na}^+ \approx \text{K}^+ > \text{Cs}^+$ . In fact, the positive shift in the redox peak potentials measured in LiOH is attributable to pH effect.

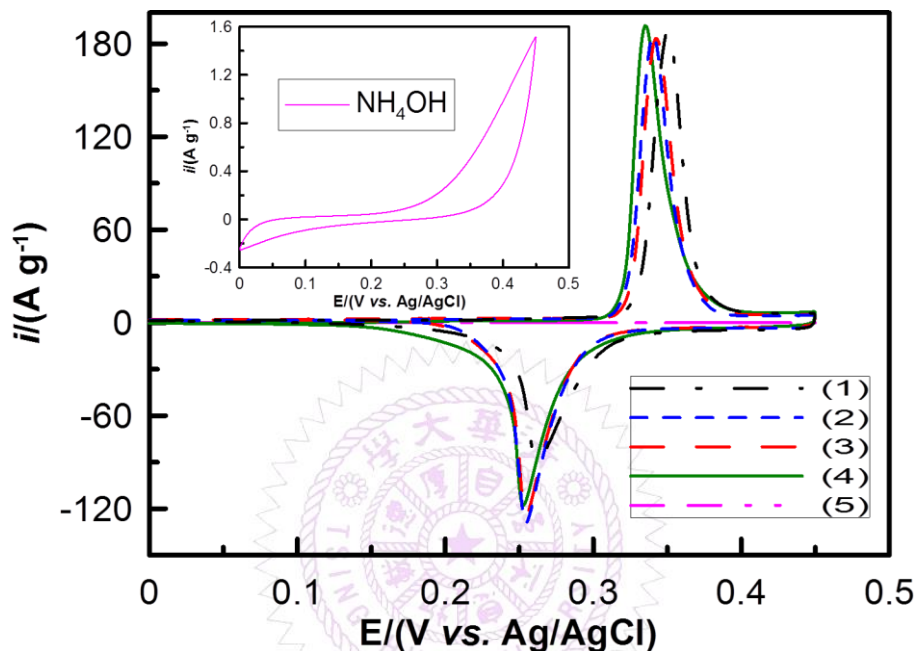


**Figure 7-1** CV curves of  $\alpha\text{-Ni(OH)}_2$  deposited on EQCM gold electrodes at  $5 \text{ mV s}^{-1}$  in 1M (1) LiOH, (2) NaOH, (3) KOH, (4) CsOH, and (5)  $\text{NH}_4\text{OH}$ .

It is noteworthy that the concentration of hydroxide ion ( $\text{OH}^-$ ) was demonstrated to play an important role on the redox behaviours of  $\gamma\text{-NiOOH}/\alpha\text{-Ni(OH)}_2$  [211]. On the basis of Nernst equation, the redox potential is pH dependent when  $\text{H}^+$  or  $\text{OH}^-$  is involved in the redox reactions. Considering base electrolytes, the concentration of  $\text{OH}^-$  is determined by base dissociation constant of supporting electrolyte. Although the concentration of supporting electrolytes is fixed as 1 M, the concentration of  $\text{OH}^-$  cannot be guaranteed to be the same for all the electrolytes. The base dissociation constants of different electrolytes are listed in Table 7-1. CsOH, KOH and NaOH are strong bases, while LiOH is the weakest base among all the alkaline solutions.

**Table 7–1** Base dissociation constant ( $K_b$ ), the onset potentials of hydrogen evolution on a Pt electrode ( $E_{HER}$ ) and the potential difference of  $\gamma$ -NiOOH/ $\alpha$ -Ni(OH)<sub>2</sub> ( $\Delta E$ ) in 1 M CsOH, KOH, NaOH, LiOH and NH<sub>4</sub>OH.

	CsOH	KOH	NaOH	LiOH	NH <sub>4</sub> OH
$K_b^a$	57.54	12.59	3.63	0.66	$1.62 \times 10^{-5}$
$E_{HER}$ (vs. Ag/AgCl) in V	-1.039	-1.024	-1.026	-1.011	-0.925
Relative pH value <sup>b</sup>	0	-0.3	-0.3	-0.5	-2.0
$\Delta E^c$ in mV	0	7	9	20	N/A

*a* The value is from ‘Das Periodensystem der Elemente online’:

<http://www.periodensystem-online.de/index.php?show=list&id=acid&prop=pKb-Werte&sel=oz&el=4>

*b* Estimated by Nernst equation (Eq 7–1) with respect to the result obtained from the 1 M CsOH electrolyte under the assumption of zero overpotential on HER.

*c* The potential difference of  $\gamma$ -NiOOH/ $\alpha$ -Ni(OH)<sub>2</sub> from CV profiles shown in Figure 7–1 with respect to the result obtained from the 1 M CsOH electrolyte.

The exact pH value of strong base is sometimes difficult to be measured properly by pH meter. Here, the onset potential of hydrogen evolution reaction ( $E_{HER}$ ) on platinum was utilised to estimate the relative pH values of electrolytes by Nernst equation (Eq 7–1) without considering overpotential on HER. The hydrogen evolution potential was defined as the reduction current density reached  $1 \text{ mA cm}^{-2}$  in LSV test at the scan rate of  $10 \text{ mV s}^{-1}$ . The relative pH values of electrolytes can be calculated via the onset potentials of hydrogen evolution on a Pt electrode.

$$E_{HER} = E_{H^+/H_2}^0 + \frac{RT}{nF} \ln \frac{[H^+]^2}{[H_2]} = -0.0591 \times pH \quad \text{Eq 7–1}$$

where R is the universal gas constant; T is the absolute temperature; n is the number of moles of electrons transferred; and F is Faraday constant. The lower pH value of

LiOH, NaOH and KOH (in comparison with CsOH) leads to the positive peak potential shift in CV profiles even though the concentration of supporting electrolytes is the same. This indicates the order of cation species with respect to the peak potential of  $\gamma$ -NiOOH/ $\alpha$ -Ni(OH)<sub>2</sub> redox is:  $\text{Li}^+ > \text{Na}^+ \approx \text{K}^+ > \text{Cs}^+$ , which is consistent with the CV profiles in Figure 7-1. Therefore, the difference of  $\gamma$ -NiOOH/ $\alpha$ -Ni(OH)<sub>2</sub> redox peak potentials in alkaline media is attributed to the OH<sup>-</sup> concentration of alkaline electrolytes.

Second, from the comparison of curves 1-4 in Figure 7-1, the CV profiles of  $\gamma$ -NiOOH/ $\alpha$ -Ni(OH)<sub>2</sub> in CsOH, KOH, NaOH and LiOH exhibit similar behaviours in the whole potential range of investigation. However, the CV curve obtained in LiOH shows smaller voltammetric current responses. This is probably caused by the formation of non-stoichiometric lithium nickelate ( $\text{Li}_{1-x}\text{Ni}_{1+x}\text{O}_2$ ) in LiOH, which possibly reduces the current responses related to  $\gamma$ -NiOOH/ $\alpha$ -Ni(OH)<sub>2</sub> redox reaction [187, 212].

Third, unlike the CV profile obtained in alkaline media, the extremely low current responses in CV is obtained in NH<sub>4</sub>OH (curve 5 in Figure 7-1). The reason is attributable to the small base dissociation constant of NH<sub>4</sub>OH. Note that the release of OH<sup>-</sup> ions is attributed to hydrolysis of ammonia rather than dissociation. Thus, NH<sub>4</sub>OH is a weak base whose base dissociation constant is 10<sup>5</sup> lower than alkaline solutions. Therefore, pH value of NH<sub>4</sub>OH is lower than that of the alkaline media at the same concentration. Such a variation in pH would only cause a positive potential shift of  $\gamma$ -NiOOH/ $\alpha$ -Ni(OH)<sub>2</sub> redox (i.e., about 100 mV in comparison with 1 M KOH), if the pH effect on redox potential shift is the only factor to be considered. However, this cannot explain the absence of redox peaks in NH<sub>4</sub>OH. According to literature [191, 192], the redox reaction of  $\gamma$ -NiOOH/ $\alpha$ -Ni(OH)<sub>2</sub> involves both cations and OH<sup>-</sup>. Thus, the insignificance of redox peaks (extremely low current



responses) is attributed to the low concentration of both  $\text{NH}_4^+$  and  $\text{OH}^-$  in 1 M  $\text{NH}_4\text{OH}$  solution due to the weak base nature of  $\text{NH}_4\text{OH}$ , which cannot provide enough ions (both cations and anions) to penetrate into  $\text{Ni}(\text{OH})_2$  structure. Therefore, the absence of the redox reaction in 1 M  $\text{NH}_4\text{OH}$  is observed.

Figure 7-2 shows the mass change profiles ( $\Delta m-E$ ) of as-deposited  $\text{Ni}(\text{OH})_2$  in various electrolytes. In  $\text{LiOH}$ ,  $\text{NaOH}$ ,  $\text{KOH}$  and  $\text{CsOH}$ , the drastic mass gain commences at ca. 0.32 V in the positive sweep, which is well known as cations insertion for the oxidation of  $\alpha\text{-Ni}(\text{OH})_2$  into  $\gamma\text{-NiOOH}$  [190, 192, 213]. In the negative sweep, mass loss occurs at ca. 0.28 V due to the extraction of cations during reduction process, revealing the typical behaviour of  $\gamma\text{-NiOOH}/\alpha\text{-Ni}(\text{OH})_2$  redox. The order of electrolytes with respect to decreasing the mass change in oxidation process is:  $\text{CsOH} > \text{KOH} > \text{NaOH} > \text{LiOH}$ , where the trend is the same as the atomic weight of cations ( $\text{Cs}^+ > \text{K}^+ > \text{Na}^+ > \text{Li}^+$ ). Accordingly, strong correspondence between insertion/removal of cations and redox reaction of  $\gamma\text{-NiOOH}/\alpha\text{-Ni}(\text{OH})_2$  is revealed. However, the mass change in  $\text{NH}_4\text{OH}$  is so trivial that it is even close to the error range of EQCM sensitivity ( $0.1 \text{ ng cm}^{-2}$ ; see the inset in Figure 7-2). The absence of redox peaks in the  $\text{NH}_4\text{OH}$  is ascribed to the low concentration of  $\text{NH}_4^+$  and  $\text{OH}^-$  in solution (i.e., small base dissociation constant). Besides, the crystallographic ionic radius of cations is 0.60, 0.95, 1.33, 1.69, and 1.48 Å for  $\text{Li}^+$ ,  $\text{Na}^+$ ,  $\text{K}^+$ ,  $\text{Cs}^+$  and  $\text{NH}_4^+$ , respectively [214]. Since the crystallographic ionic radius of  $\text{Cs}^+$  is larger than  $\text{NH}_4^+$ , the absence of redox peaks in  $\text{NH}_4\text{OH}$  would not be attributable to the steric hindrance caused by large cation size during cation insertion process. Instead, the absence of redox peak in  $\text{NH}_4\text{OH}$  is reasonably owing to the low concentration of both  $\text{NH}_4^+$  and  $\text{OH}^-$  in the solution. Accordingly, both ‘cation species’ and ‘ $\text{OH}^-$  concentration’ in the electrolytes are the key factors determining the electrochemical behaviours of  $\gamma\text{-NiOOH}/\alpha\text{-Ni}(\text{OH})_2$ .

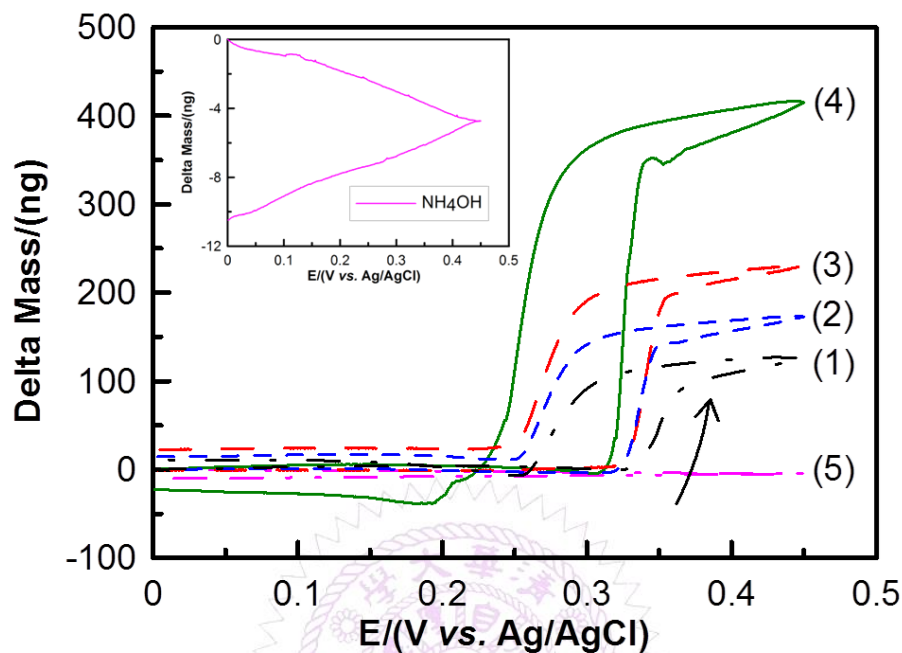


**Figure 7–2** mass change profiles of Ni(OH)<sub>2</sub> deposited on EQCM gold electrodes at 5mV s<sup>-1</sup> in 1 M (1) LiOH, (2) NaOH (3) KOH (4) CsOH and (5) NH<sub>4</sub>OH.

The effect of cation species on the ageing process is clarified by the  $\Delta m$ -E measurements through EQCM under continuous potential cycling in the above alkaline media. Figure 7–3 shows both CV and mass change profiles of NiOOH/Ni(OH)<sub>2</sub> for 10 cycles at 10 mV s<sup>-1</sup> after 10 proceeding cycles in the same potential window at 5 mV s<sup>-1</sup>. In LiOH (Figure 7–3a and 7–3e), the mass change profile remains as the typical  $\gamma$ -NiOOH/ $\alpha$ -Ni(OH)<sub>2</sub> redox behaviour, while the current response and mass change slightly decreased in the potential window. In NaOH and KOH (Figure 7–3b and 7–3c), the voltammetric currents are almost at the same level, but the mass change profiles (Figure 7–3f and 7–3g) show a minor mass loss subject to the mass gain of  $\gamma$ -NiOOH/ $\alpha$ -Ni(OH)<sub>2</sub> from 0.35 to 0.38 V on the positive sweeps. The presence of this additional mass decrease is ascribed to the oxidation of  $\beta$ -Ni(OH)<sub>2</sub> into  $\beta$ -NiOOH, where proton is removed during oxidation

process. In the following negative sweep, the reduction of  $\beta$ -NiOOH shows a minor mass gain at ca. 0.27 V due to the insertion of proton. Moreover, there is net mass gain upon potential cycling, ca. 12 and 17.5 ng per CV cycle for NaOH and KOH, respectively, which is not found in LiOH. This phenomenon indicates the inserted  $\text{Na}^+$  and  $\text{K}^+$  cannot be completely removed from the  $\text{Ni}(\text{OH})_2$  structure during reduction process, and the residual cation would remain inside the  $\text{Ni}(\text{OH})_2$  inter-slab space at the end of negative sweep. Interestingly, a different electrochemical behaviour is observable in CsOH. The voltammetric current responses decrease quickly within 10 cycles, and the oxidative peak potential gradually shifts to higher potential end (Figure 7-3d), which is well known as the ageing of  $\alpha$ - $\text{Ni}(\text{OH})_2$  to  $\beta$ - $\text{Ni}(\text{OH})_2$  in a continuous CV test [187]. With regard to mass change profile in CsOH (Figure 7-3h), features related to both  $\gamma$ -NiOOH/ $\alpha$ - $\text{Ni}(\text{OH})_2$  and  $\beta$ -NiOOH/ $\beta$ - $\text{Ni}(\text{OH})_2$  redox can be observed. In fact, the  $\beta$ -NiOOH/ $\beta$ - $\text{Ni}(\text{OH})_2$  features can be observed even in the first few cycles at  $5 \text{ mV s}^{-1}$  in Figure 7-2. Therefore, the ageing of  $\alpha$ - $\text{Ni}(\text{OH})_2$  to  $\beta$ - $\text{Ni}(\text{OH})_2$  is the most significant in CsOH in comparison with the others. Moreover, the net mass loss is drastic, suggesting the electroactive material delaminates from EQCM gold electrode (loss ca. 15% of deposited  $\text{Ni}(\text{OH})_2$  at the end of 10<sup>th</sup> cycle in Figure 7-3h). It is presumably attributed to the significant lattice expansion/contraction during oxidation/reduction process owing to insertion/removal of the large crystalline size of  $\text{Cs}^+$ , resulting in poor adhesion of  $\text{Ni}(\text{OH})_2$  in CsOH upon potential cycling.

Accordingly, the redox behaviours of NiOOH/ $\text{Ni}(\text{OH})_2$  is affected by cation species. Among the alkaline media, LiOH exhibits the best retention ability for  $\gamma$ -NiOOH/ $\alpha$ - $\text{Ni}(\text{OH})_2$  redox reaction, while CsOH shows the worst phase retention ability exhibiting the formation of  $\beta$ - $\text{Ni}(\text{OH})_2$  in a very early stage.

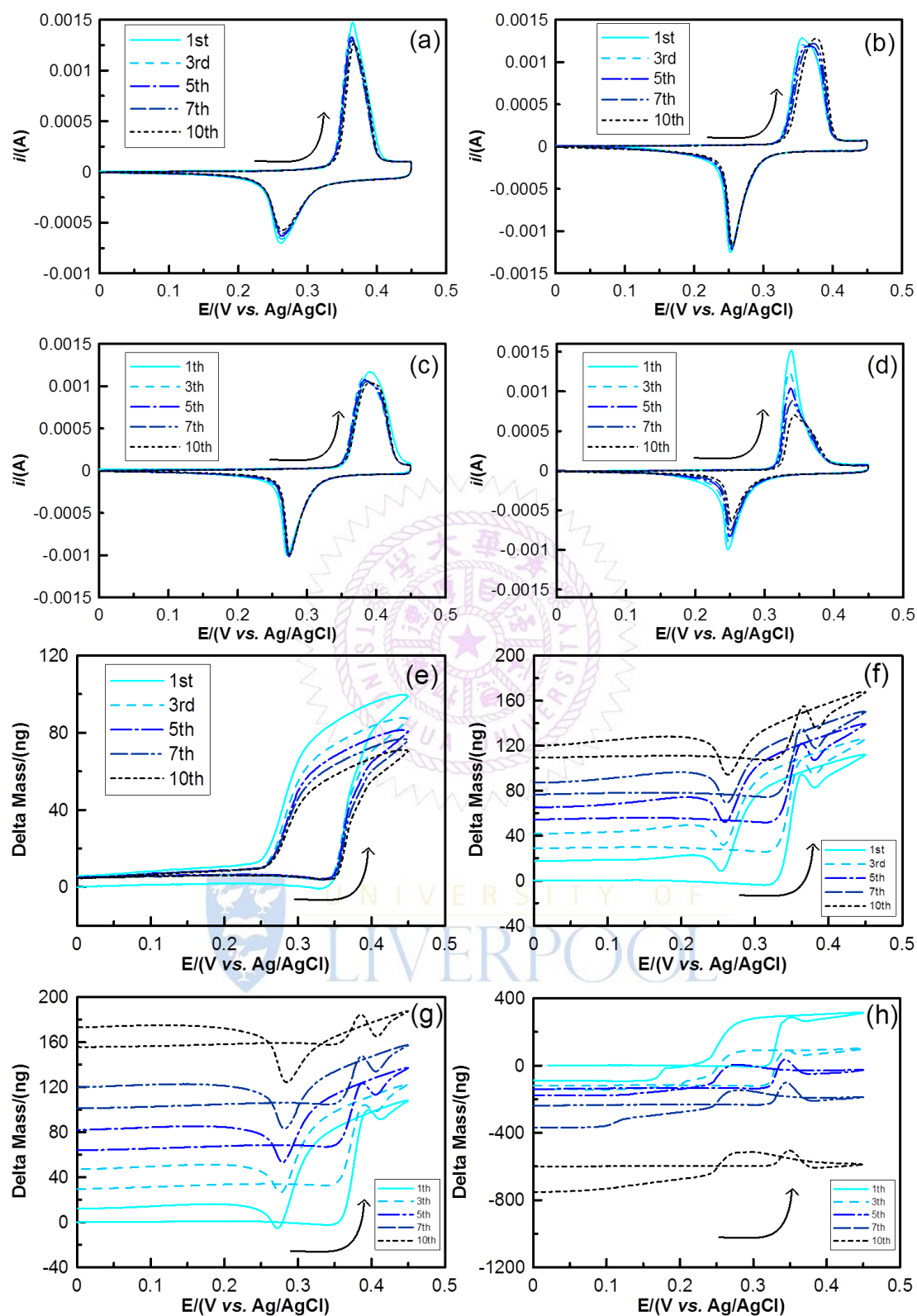


**Figure 7-3** (a–d) CV curves and (e–h) mass change curves of  $\text{Ni}(\text{OH})_2$  deposited on EQCM gold electrodes in 1 M (a, e) LiOH, (b, f) NaOH (c, g) KOH and (d, h) CsOH for 10 cycles at  $10 \text{ mV s}^{-1}$  after 10 preceding cycles in the same potential window at  $5 \text{ mV s}^{-1}$ .

The EQCM results can be also presented as massogram plots, the rate of mass change ( $d\Delta m/dt$ ) versus the electrode potential, where the current response in CV is directly proportional to mass change associated with charge transfer at the electrode surface (faradaic processes) [215, 216]. Thus, massograms are analogous to the voltammograms, and the charge transfer correlates to mass variation can be easily observed from the direct comparison of massograms and voltammograms.

Figure 7-4 shows the massograms corresponding to the EQCM results in various electrolytes (Figure 7-3). There is almost no mass flux before the redox transitions (from 0 to ca. 0.2 V), indicating that only the double layer responses occur in this potential region. On the other hand, the mass flux is proportional to the voltammetric current in the redox potential region (from 0.2 to 0.45 V), indicating that the mass change is associated with faradaic reaction of NiOOH/Ni(OH)<sub>2</sub>. In LiOH (Figure 7-4a), only a pair of mass fluxes can be observed in the first 10 cycles. This pair of mass fluxes is corresponding to  $\gamma$ -NiOOH/ $\alpha$ -Ni(OH)<sub>2</sub> redox reaction, where the slight decrease upon potential cycling is similar to the voltammetric current responses in CV (Figure 7-3a). However, a shoulder is found at ca. 0.37 V in the positive scan, indicating two mass fluxes. As discussed previously, the formation of lithium nickelate occurs by Li<sup>+</sup> exchange reaction of NiOOH once NiOOH is formed [212]. Unlike a simple insertion of Li<sup>+</sup>, the formation of lithium nickelate accompanied by ion-exchange process should take more time and thus causes the delay of mass flux. The formation of lithium nickelate also explains the smaller current responses compared to KOH and NaOH (see Figure 7-1) since the mean oxidation state of nickel in lithium nickelate is lower than that of  $\gamma$ -NiOOH [187].

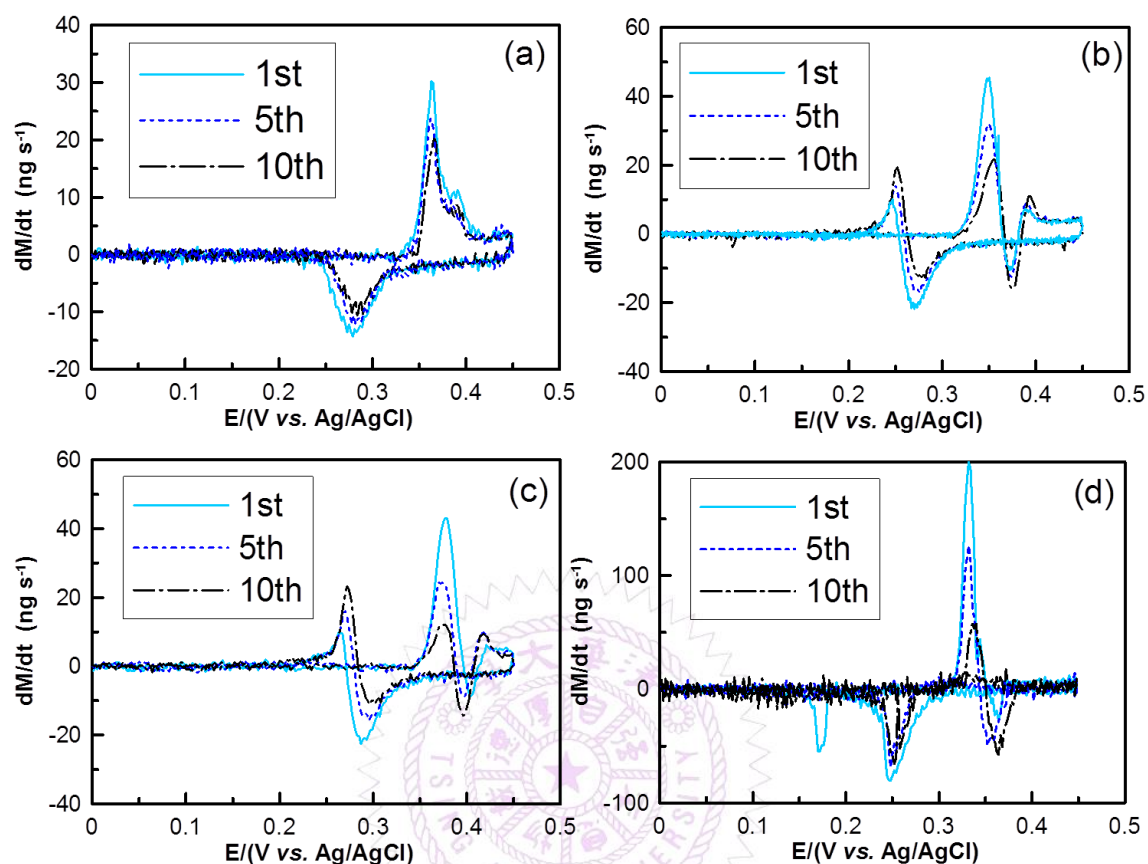


**Figure 7-4** Massograms of Ni(OH)<sub>2</sub> on EQCM gold electrodes in 1 M (a) LiOH, (b) NaOH, (c) KOH and (d) CsOH for 10 cycles at 10 mV s<sup>-1</sup> after 10 preceding cycles in the same potential window at 5 mV s<sup>-1</sup>.

The massograms of NiOOH/Ni(OH)<sub>2</sub> measured in NaOH and KOH (Figure 7-4b and 7-4c) exhibit two pairs of mass fluxes, although only one pair of redox peaks can be observed in CVs (see Figure 7-3b and 7-3c). One pair locates at ca. 0.35 (mass gain) and 0.27 V (mass loss) on positive and negative sweeps, respectively, while the other sits at ca. 0.38 (mass loss) and 0.24 V (mass gain) on positive and negative sweeps, respectively. Based on the mass change profiles, the former is reasonably attributable to  $\gamma$ -NiOOH/ $\alpha$ -Ni(OH)<sub>2</sub> redox reaction, while the latter is corresponding to  $\beta$ -NiOOH/ $\beta$ -Ni(OH)<sub>2</sub> redox reaction. Moreover, the mass fluxes of  $\gamma$ -NiOOH/ $\alpha$ -Ni(OH)<sub>2</sub> gradually decrease, while the mass fluxes of  $\beta$ -NiOOH/ $\beta$ -Ni(OH)<sub>2</sub> gradually increase. Accordingly, the ageing process takes place upon potential cycling in NaOH and KOH. Besides,  $\alpha$  and  $\beta$  phases coexist at this



stage, which supports the hypothesis of the intermediate phase [190, 217]. The intermediate phase presents a single phase, where the structural and electrochemical properties lie between  $\alpha$  and  $\beta$  phases [205]. Although the exact structure is not clear, Faure *et al.* [217] speculated a poor crystalline  $\beta$  phase; Kim *et al.* [190] proposed a microscopic mixture of  $\alpha$  and  $\beta$  phases. Here, the massograms in NaOH and KOH provide remarkably clear evidence that both phases coexist, whereas the  $\alpha$  phase was continuously converted to the  $\beta$  phase during the repeated CV cycling. Furthermore, the mass fluxes associated with the redox responses of  $\gamma$ -NiOOH/ $\alpha$ -Ni(OH)<sub>2</sub> decrease more obviously in KOH comparing with the results measured in NaOH. Accordingly, the phase transformation of  $\gamma$ -NiOOH/ $\alpha$ -Ni(OH)<sub>2</sub> to  $\beta$ -NiOOH/ $\beta$ -Ni(OH)<sub>2</sub> by means of potential cycling in KOH is severer than that in NaOH. With regard to massograms measured in CsOH (Figure 7-4d), the decrease of  $\gamma$ -NiOOH/ $\alpha$ -Ni(OH)<sub>2</sub> mass fluxes is even severer, indicating an even quicker  $\beta$  phase transition in CsOH. However, the delamination of Ni(OH)<sub>2</sub> from EQCM gold electrode occurs due to the significant lattice expansion/contraction during redox reaction in CsOH upon potential cycling. The uptake of proton involved in  $\beta$ -NiOOH/ $\beta$ -Ni(OH)<sub>2</sub> cannot be observed in CsOH.

It is noteworthy that EQCM is a very sensitive and powerful analytical tool in electrochemistry, since the  $\beta$  phase formation can be investigated in EQCM from mass change profiles and massograms but not in CV profiles. From the discussion of EQCM results, phenomenal differences in the phase retention were exactly demonstrated in electrolytes containing various alkali metal cation species (LiOH, NaOH, KOH and CsOH) under the same condition. In LiOH, the deformation of  $\gamma$ -NiOOH/ $\alpha$ -Ni(OH)<sub>2</sub> is observed with slight reduce in both the current responses and mass fluxes. The gradual transformation of  $\gamma$ -NiOOH/ $\alpha$ -Ni(OH)<sub>2</sub> to  $\beta$ -NiOOH/ $\beta$ -Ni(OH)<sub>2</sub> leads to the existence of the intermediate phase in NaOH and

KOH. On the other hand, the predominant formation of  $\beta$  phase is found in CsOH. Therefore, the order of cation species with respect to inducing the phase transformation from  $\alpha$ -Ni(OH)<sub>2</sub> into  $\beta$  phase is: Cs<sup>+</sup> > K<sup>+</sup> > Na<sup>+</sup> > Li<sup>+</sup>. The result indicates the strong influence of the 'alkali cation species' on the phase retention of  $\gamma$ -NiOOH/ $\alpha$ -Ni(OH)<sub>2</sub> redox reaction.

### 7.3 *In situ* Raman Spectroscopic Studies of Ni(OH)<sub>2</sub>

The Raman spectra of  $\alpha$  and  $\beta$ -Ni(OH)<sub>2</sub> have been widely reported in literature [189, 197, 218, 219]. In general, the signals in the region of Ni–O vibrational modes (445–465 cm<sup>-1</sup>) for  $\alpha$  and  $\beta$ -Ni(OH)<sub>2</sub> are relatively weak owing to the low Raman scattering cross-section [218]. For some cases, those peaks are not able to be observed [220, 221]. Contrarily, Raman spectra in the range of O–H vibrational region (ca. 3500–3700 cm<sup>-1</sup>) have been demonstrated as a rapid and more accessible spectral region to distinguish  $\alpha$  and  $\beta$ -Ni(OH)<sub>2</sub> [189, 219]. Moreover, the water background issue has been proposed to be able to carefully measured and removed in literature [189]. Therefore, *in situ* Raman spectra in this work were recorded in the range of 3400–3800 cm<sup>-1</sup> to understand the alkali metal cation effect on phase transformation and retention.

*In situ* Raman spectra recorded after specific CV cycles in various alkaline electrolytes were conducted to have more understanding on the cation effect on the ageing process through the observations of molecular vibrational modes changes. The Raman spectra of as-prepared  $\alpha$ -Ni(OH)<sub>2</sub> on Ni electrode surface in LiOH are shown in Figure 7–5. In general,  $\alpha$ -Ni(OH)<sub>2</sub> exhibits a weak peak at ca. 460 cm<sup>-1</sup> and a merged wide-broad peak roughly between 3550–3680 cm<sup>-1</sup> [189, 197, 218, 219]. These two peaks are assigned as lattice mode and vibration of lattice hydroxyl groups,

respectively [219]. For  $\beta$ -Ni(OH)<sub>2</sub>, two weak peaks locate at ca. 315 and 450 cm<sup>-1</sup>, which are identified as E<sub>g</sub> and A<sub>1g</sub> lattice mode, respectively [197, 219]. A sharp and strong peak at ca. 3580 cm<sup>-1</sup> is the signature of  $\beta$ -Ni(OH)<sub>2</sub>, which is A<sub>1g</sub> O-H stretching mode [197, 219]. The peak at ca. 3601 cm<sup>-1</sup> is corresponding to O-H stretching in disordered  $\beta$ -Ni(OH)<sub>2</sub> [205, 219], which is commonly found in electrochemical induced  $\beta$ -Ni(OH)<sub>2</sub> from repeated CV cycling of  $\alpha$ -Ni(OH)<sub>2</sub> presumably owing to the residual cations and water molecules inside the structure.

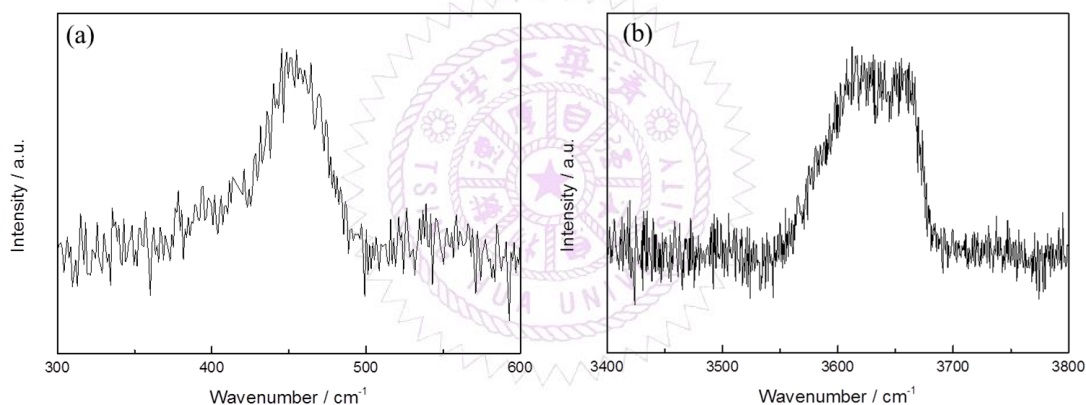


**Figure 7-5** Raman spectra at (a) 300–600 and (b) 3400–3800 cm<sup>-1</sup> of as-prepared  $\alpha$ -Ni(OH)<sub>2</sub> on Ni electrode surface recorded in 1M LiOH.

As discussed previously, *in situ* Raman spectra were recorded in the range of O-H vibrational region (ca. 3500–3700 cm<sup>-1</sup>) due to the low Raman scattering cross-section of Ni–O vibrational modes (445–465 cm<sup>-1</sup>) for  $\alpha$  and  $\beta$ -Ni(OH)<sub>2</sub> [218]. In order to remove water background of *in situ* Raman spectra, Raman spectra of Ni(OH)<sub>2</sub> with wider window were recorded in Figure 7-6. The water background signals were recorded on the bare gold electrode surface in alkaline electrolytes in order to avoid the simultaneous formation of  $\alpha$ -Ni(OH)<sub>2</sub> on the Ni electrode surface [221]. Generally, the water background arises in the range of 3000–3700 cm<sup>-1</sup> (in Figure 7-6a), which is partially superimposed with the signals from O-H stretching

mode of  $\text{Ni(OH)}_2$ . In this work, the water background issue has been carefully removed by Renishaw WiRE 4.0 software.

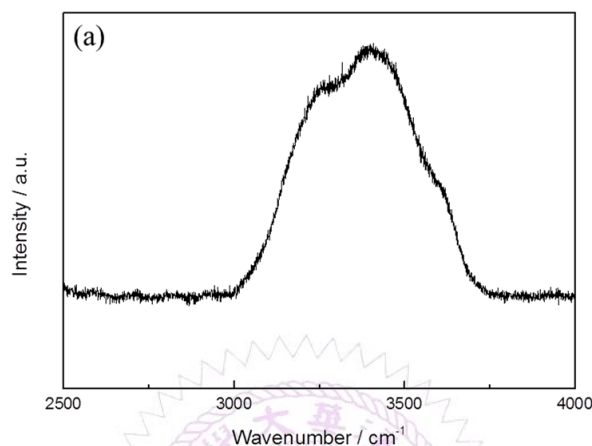


**Figure 7–6** Raman spectra of bare gold electrode surface in 1M LiOH.

*In situ* Raman spectra recorded at rest potential after CV cycling separately in LiOH, NaOH, KOH and CsOH are shown in Figure 7–7. After 10 CV cycles (Figure 7–7a), the spectra in all the alkaline media are similar, which all the spectra exhibit a broad and wide peak related to lattice O–H vibrational mode of  $\alpha\text{-Ni(OH)}_2$ . The Raman spectrum in LiOH exhibits a smooth increase of intensity in the range of  $3550\text{--}3600\text{ cm}^{-1}$ , which is identical to the spectrum of  $\alpha\text{-Ni(OH)}_2$  (Figure 7–6b). However, instead of this smooth increase of intensity, a nascent peak locates at  $3580\text{ cm}^{-1}$  related to the O–H stretching vibrational mode of  $\beta\text{-Ni(OH)}_2$  appeared in NaOH, KOH and CsOH. With further cycling to 30 cycles (Figure 7–7b), a subtle change of  $\text{Ni(OH)}_2$  in LiOH can be observed, in which the  $3580\text{ cm}^{-1}$  peak starts to appear. On the other hand, two significant peaks at  $3580$  and  $3601\text{ cm}^{-1}$  can be clearly found in KOH and CsOH. These two peaks can be observed in NaOH after 150 cycles (Figure 7–7c). The spectrum in LiOH at 150 cycles is similar to 30 cycles, while these two  $\beta\text{-Ni(OH)}_2$  peaks are much sharper and predominant in KOH and CsOH. When  $\text{Ni(OH)}_2$  cycled to 200 cycles (Figure 7–7d), the predominant  $\beta\text{-Ni(OH)}_2$  peaks can

be observed in NaOH, KOH and CsOH. However, the  $3580\text{ cm}^{-1}$   $\beta$ -Ni(OH)<sub>2</sub> peak intensity is much lower in LiOH comparing with others. Most importantly, the  $3601\text{ cm}^{-1}$  peak related to disordered  $\beta$ -Ni(OH)<sub>2</sub> do not appear in LiOH. The results indicate LiOH possess the best ability to keep at  $\gamma$ -NiOOH/ $\alpha$ -Ni(OH)<sub>2</sub> redox reaction in comparison with NaOH, KOH and CsOH.

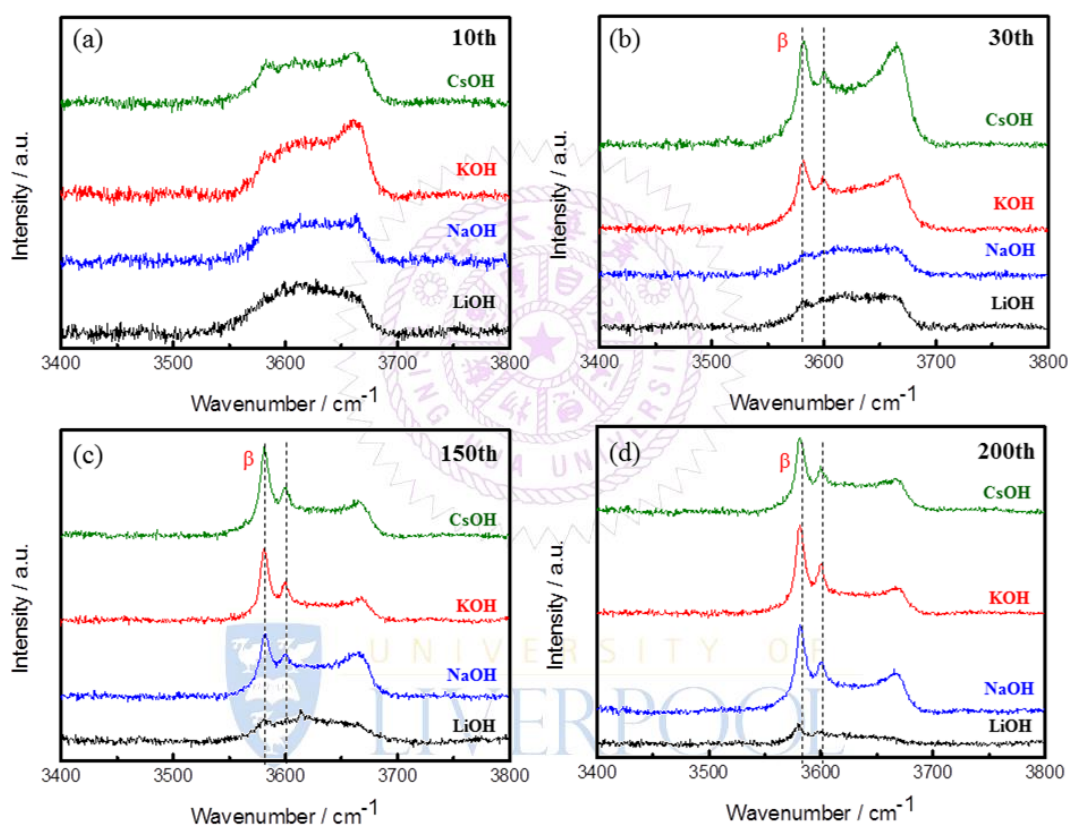


**Figure 7-7** *In situ* Raman spectra of Ni(OH)<sub>2</sub> recorded after (a) 10, (b) 30, (c) 150, and (d) 200 CV cycles at  $10\text{ mV s}^{-1}$  in 1 M LiOH, NaOH, KOH and CsOH.

From direct comparison between the ‘CV curves’ (Figure 7-8) and ‘*in situ* Raman spectra sequences’ (Figure 7-9), the *in situ* Raman results confirm the observations from EQCM, which demonstrates the order of cation species with respect to inducing the phase transformation from  $\gamma$ -NiOOH/ $\alpha$ -Ni(OH)<sub>2</sub> into  $\beta$ -NiOOH/ $\beta$ -Ni(OH)<sub>2</sub> is:  $\text{Cs}^+ > \text{K}^+ > \text{Na}^+ > \text{Li}^+$ . Furthermore, both of  $\alpha$  and  $\beta$ -Ni(OH)<sub>2</sub> vibrational peaks coexisted during the phase transformation process.

Therefore, the results also support the viewpoint of microscopic mixture of  $\alpha$  and  $\beta$  phases coexisted in the intermediate phase proposed in literature [190, 222]. However, the reasons of alkali cation effect on the phase transformation and redox retention of  $\alpha$ -Ni(OH)<sub>2</sub> requires further discussion.

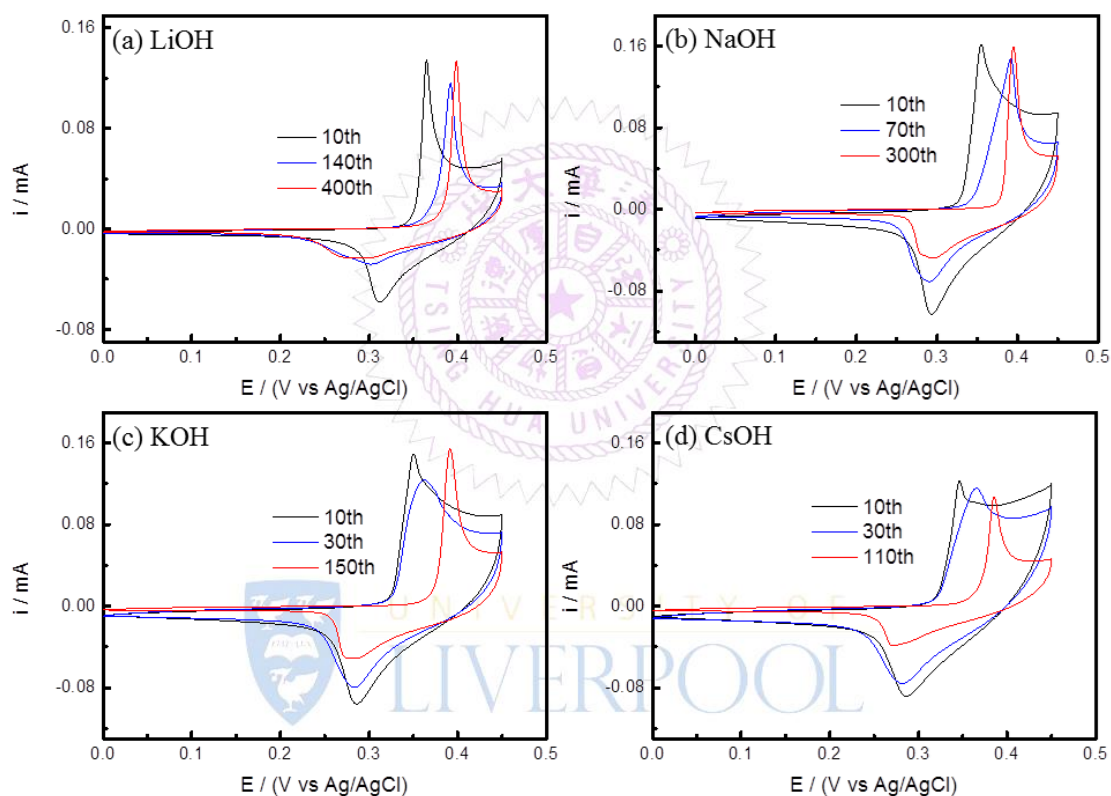


**Figure 7-8** CV curves of Ni(OH)<sub>2</sub> deposited on gold electrodes measured at 10 mV s<sup>-1</sup> in 1M (a) LiOH, (b) NaOH, (c) KOH, (d) CsOH.



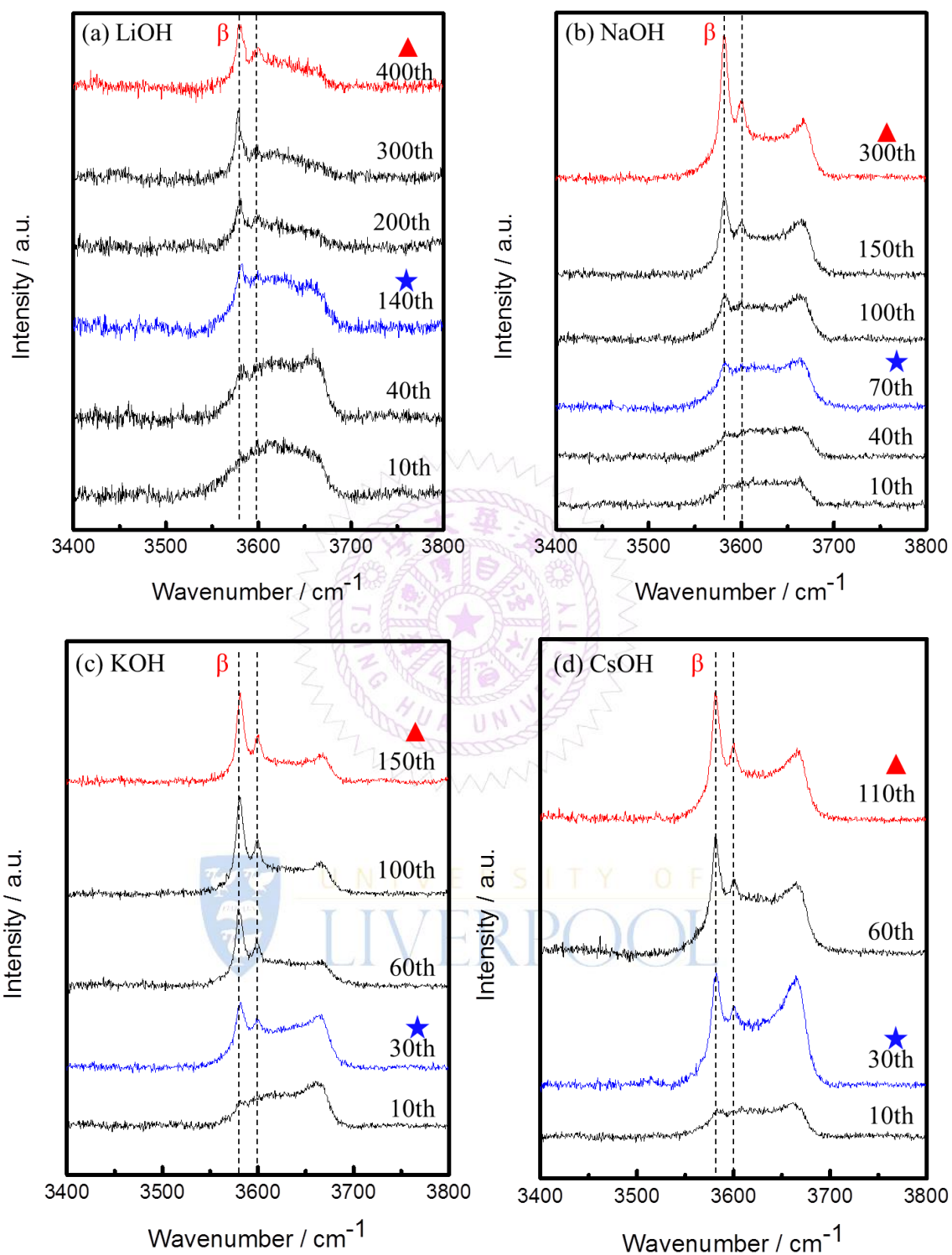
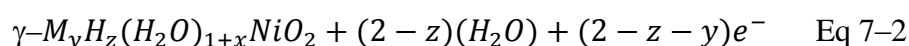
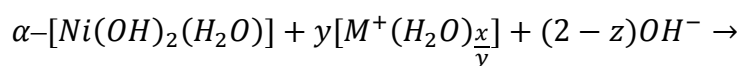


**Figure 7-9** The corresponding *in situ* Raman spectra recorded after specific CV cycles at  $10 \text{ mV s}^{-1}$  in 1M (a) LiOH, (b) NaOH, (c) KOH and (d) CsOH.

## 7.4 The Proposed New Redox Mechanism of Ni(OH)<sub>2</sub>

Generally,  $\alpha$ -Ni(OH)<sub>2</sub> has a larger inter-slab distance due to the trigonal symmetry consisting of planes of  $\beta$ -Ni(OH)<sub>2</sub> intercalated with water molecules. The nature of phase transformation from  $\alpha$ -Ni(OH)<sub>2</sub> to  $\beta$ -Ni(OH)<sub>2</sub> is attributed to the more thermodynamically stable phase of  $\beta$ -Ni(OH)<sub>2</sub>. Therefore, phase transformation would gradually occur once  $\alpha$ -Ni(OH)<sub>2</sub> contacts with aqueous solution. The  $\beta$ -Ni(OH)<sub>2</sub> can be obtained non-electrochemically by immersing  $\alpha$ -Ni(OH)<sub>2</sub> into water or KOH solutions [189, 205, 219]. The phase transformation can also be achieved electrochemically by repeated CV cycling in alkaline solutions (such as NaOH and KOH) [218, 221, 223], where  $\beta$ -Ni(OH)<sub>2</sub> is generally formed much faster than non-electrochemical methods. This indicates the electrochemical redox reaction in NaOH and KOH medium induces this phase transformation. Based on the consistent results from EQCM and *in situ* Raman, the order of cation species with respect to inducing the phase transformation from  $\gamma$ -NiOOH/ $\alpha$ -Ni(OH)<sub>2</sub> into  $\beta$ -NiOOH/ $\beta$ -Ni(OH)<sub>2</sub> is: Cs<sup>+</sup> > K<sup>+</sup> > Na<sup>+</sup> > Li<sup>+</sup>.

In order to further discuss this cation effect, density functional theory (DFT+U) simulations were used to investigate the reasons why KOH and NaOH promote the phase transformation from  $\gamma$ -NiOOH/ $\alpha$ -Ni(OH)<sub>2</sub> into  $\beta$ -NiOOH/ $\beta$ -Ni(OH)<sub>2</sub>. According to Cordoba-Torresi *et al.* [192], a modified model for the oxidation of  $\alpha$ -Ni(OH)<sub>2</sub> is proposed as following:



where M<sup>+</sup> = Li<sup>+</sup>, Na<sup>+</sup>, K<sup>+</sup>. The stoichiometric numbers  $x$ ,  $y$  and  $z$  are related through mass and charge balance equations (refer to Eq 2-21 and Eq 2-22). The term  $x/y$  in Eq 7-2 stands for the water to cation ratio involved in the process. According to the

DFT computational results from our collaborate colleagues (please refer to Appendix [224]), the energetically most favourable  $\gamma$  structure for  $\text{Li}^+$  is obtained when  $x/y = 0$ , while it is given as  $x/y = -0.6$  and  $-1.34$  for  $\text{Na}^+$  and  $\text{K}^+$ , respectively. Note that a negative value for water/cation ( $x/y$ ) indicates that a 'x' amount of water molecules in  $\alpha\text{-Ni(OH)}_2(\text{H}_2\text{O})$  structure is substituted by the 'y' amount of inserted cations. This means the insertion of hydrated cations during oxidation process would not take place. Instead, the water molecules in  $\alpha\text{-Ni(OH)}_2(\text{H}_2\text{O})$  would be removed from host structure by the insertion of cations during oxidation process. It's noteworthy that the water/cation ( $x/y$ ) value has always been considered to be positive values in literature [183, 192]. However, the simulation results clearly demonstrate that the inclusion of solvated cations ( $x/y \geq 0$ ) is energetically unfavourable. Based on the above results, a new mechanism of oxidation from  $\alpha$  to  $\gamma$  phase is proposed. The solvated cations are driven to the electrode surface under the applied potential. Due to the abundant water content inside  $\alpha\text{-Ni(OH)}_2(\text{H}_2\text{O})$  inter-slab space, it is reasonably believed that the hydration sphere of water molecules around the alkali metal cation is essentially stripped away before inserting into  $\alpha\text{-Ni(OH)}_2(\text{H}_2\text{O})$  structure. Once cations inserted into the structure, they would bond with the water molecules those already existed inside the inter-slab space of  $\alpha\text{-Ni(OH)}_2(\text{H}_2\text{O})$  during the oxidation process. Therefore, the inserted cations can be considered to be bare ions moving rapidly into the structure. There is a significant removal of water molecules (largest for  $\text{K}^+$ ) upon insertion of  $\text{Na}^+$  and  $\text{K}^+$ , while  $\text{Li}^+$  insertion remains the water content inside the host structure unchanged. Moreover, it is energetically more favourable that all protons are removed to form water leaving the host structure.

In order to investigate how the stoichiometry change in  $\text{LiOH}$ ,  $\text{NaOH}$  and  $\text{KOH}$  media upon CV cycling, the computational studies were carried out to the first few cycles recorded under the scan rate of  $5 \text{ mV s}^{-1}$  in EQCM. At discharged state, the

amount of water in the host structure remains practically the same for LiOH, however, a drastic reduction of water content in  $\gamma$  phase can be clearly observed in NaOH and KOH. This reduction of water content is the most significant for  $K^+$ . Moreover, the accumulation of residual mass at the end of reduction process was found for NaOH and KOH cases in EQCM, which is attributed to the residual cations in the structure that could not be reversibly removed from the structure. This means that the charge-discharge process in NaOH and KOH is not entirely reversible. Based on these results, the mechanism for reduction process is proposed to take place through the removal of the cation from the host structure followed by the re-insertion of the corresponding amount of water (in  $x/y$  ratio) back into  $Ni(OH)_2$  structure. This process also complies with the mass and charge balance equations.

Based on the experimental results and the computational evidence, it can be concluded that the capability to retain water molecules inside the nickel structure is crucial for the stability of  $\gamma$ -NiOOH/ $\alpha$ -Ni(OH)<sub>2</sub> redox reaction. The intercalated water molecules can act as ‘amorphous glue’ holding the randomly stacking structure of  $\alpha$ -Ni(OH)<sub>2</sub> [184]. Therefore, the loss of water molecules in Ni(OH)<sub>2</sub> structure during charge-discharge process is the key for phase transform (ageing) to  $\beta$ -Ni(OH)<sub>2</sub>. In fact, since the insertion/removal of  $Li^+$  does not alter the content of water inside the structure,  $\gamma$ -NiOOH/ $\alpha$ -Ni(OH)<sub>2</sub> redox reaction in LiOH medium is the most stable. Contrarily, the insertion of  $Na^+$  and  $K^+$  leads to a significant removal of water, which in turn introduces structural instabilities. On the other hand, the reduction process will be conducted by cation removal prior to the re-insertion of water molecules from the electrolyte. However, if water molecules do not immediately re-insert back into the nickel structure once the cations are removed, the structure would be prone to collapse, leading to the formation of  $\beta$  phase. Therefore, gradual loss of water molecules in Ni(OH)<sub>2</sub> structure is the intrinsic reason for the formation of  $\beta$  phase upon charge-

discharge process.

As mentioned previously, the stacking of Ni(OH)<sub>2</sub> layers is in a random manner for α-Ni(OH)<sub>2</sub>, which is subject to the accommodated water molecules and/or anions inside the inter-slab space [187, 208]. On the other hand, the crystal structure of γ phase has been reported to be significantly ordered comparing with α phase [187]. Therefore, it is energetic unfavourable to obtain a well crystallised γ phase from electrochemical oxidation of an amorphous α phase. This means the redox reaction between a well crystallised γ phase and an amorphous α phase is unlikely to occur during a relatively fast electrochemical reaction (much faster than chemical synthesis process). Based on this argument, the optimised supercell for the α-Ni(OH)<sub>2</sub>(H<sub>2</sub>O) was used to build various simulation models for the γ phase with different values of stoichiometric factors for Ni(OH)<sub>2</sub> cycling in LiOH, NaOH and KOH media. Nevertheless, the well crystallised γ phase can be achieved by overcharging of β-NiOOH or chemical synthesis routes [183, 187, 225]. Accordingly, the proposed new redox mechanism of Ni(OH)<sub>2</sub> is shown in Figure 7-10.



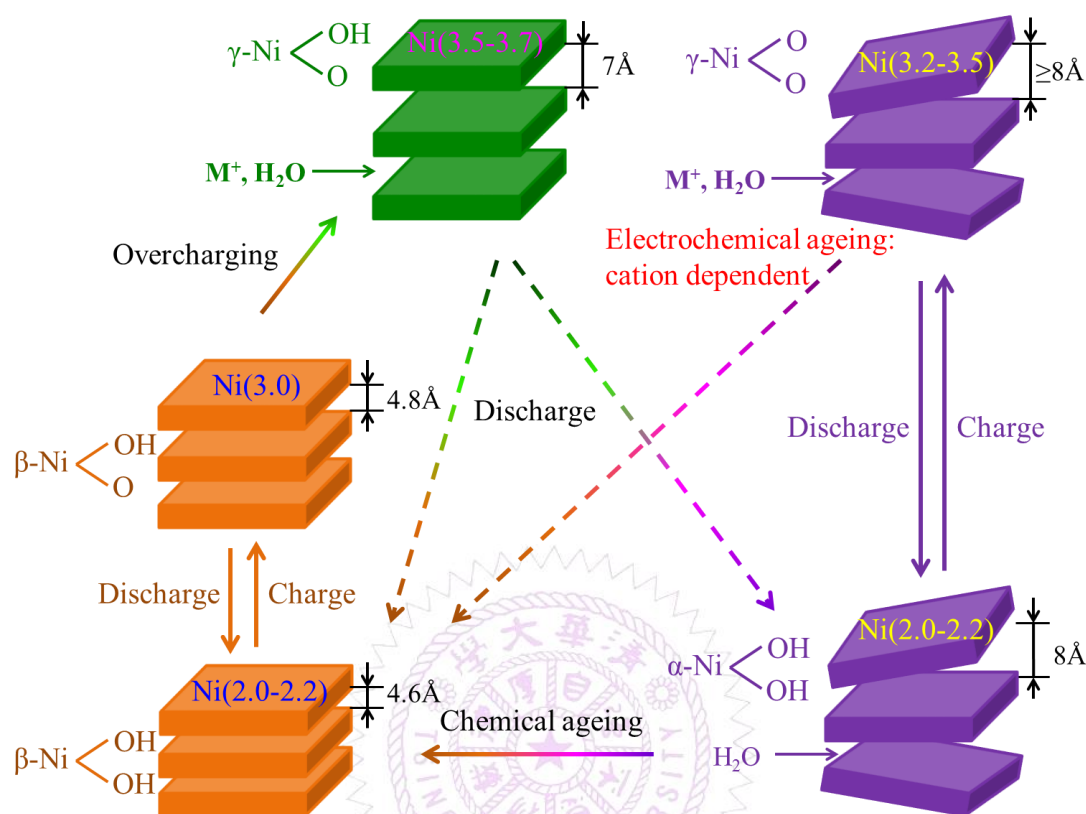


**Figure 7–10** The proposed new redox mechanism of nickel hydroxide.

## 7.5 Conclusions

The redox behaviours of  $\gamma$ -NiOOH/ $\alpha$ -Ni(OH)<sub>2</sub> in various electrolytes are discussed in this work. The necessity of both cations and OH<sup>-</sup> is clarified from the absence of the redox peaks in NH<sub>4</sub>OH. By utilising EQCM technique, both mass change profiles and massograms reveal distinctive behaviours in alkaline media, which cannot be observed from CV profiles. From EQCM and *in situ* Raman results, the order of cation species with respect to inducing the phase transformation from  $\gamma$ -NiOOH/ $\alpha$ -Ni(OH)<sub>2</sub> into  $\beta$ -NiOOH/ $\beta$ -Ni(OH)<sub>2</sub> is: Cs<sup>+</sup> > K<sup>+</sup> > Na<sup>+</sup> > Li<sup>+</sup>. The result indicates that cation species plays a critical role in redox reaction and phase transformation. Based on the computational evidence, it can be concluded that the capability to retain water molecules inside the Ni(OH)<sub>2</sub> is crucial for the stability of



$\gamma$ -NiOOH/ $\alpha$ -Ni(OH)<sub>2</sub> redox reaction. Therefore, the loss of water molecules in Ni(OH)<sub>2</sub> structure during charge–discharge process is the key for phase transform (ageing) to  $\beta$ -Ni(OH)<sub>2</sub>. The insertion/removal of Li<sup>+</sup> does not alter the content of water inside the structure, while the insertion of Na<sup>+</sup> and K<sup>+</sup> leads to a significant removal of water. The removed water molecules cannot be reversibly re–inserted back into the nickel structure in NaOH and KOH, leading to structure collapse. Eventually,  $\beta$  phase is formed upon repeated charge–discharge process. Accordingly, a new redox mechanism of Ni(OH)<sub>2</sub> is proposed in this work.



UNIVERSITY OF  
LIVERPOOL

# Chapter 8

## Summary and Future Works

This study successfully demonstrates how to evaluate the highest acceptable cell voltage and optimise cell voltage of aqueous symmetric (Chapter 4) and asymmetric ECs (Chapter 5) by means of various electrochemical techniques. From an engineering viewpoint, it is advantageous to optimise cell voltage (and hence improve energy storage) of ECs by tuning the cell parameters without changing electroactive materials and electrolytes. The important parameters affecting the cell voltage of aqueous symmetric ECs were discussed in Chapter 4, and the necessity of charge-balanced condition between positive and negative electrodes within their electrochemically stable potential windows was demonstrated to optimise the cell voltage of aqueous symmetric ECs. In Chapter 5, the evaluation methods for appointing the highest acceptable cell voltage of asymmetric ECs were proposed on the basis of two typical asymmetric ECs (RGO//MnO<sub>x</sub> and RGO//RuO<sub>2</sub>). From a series of electrochemical analyses, the most important criterion was proposed as the phase angle of resultant cell capacitance in EIS spectra while energy efficiency is an approximate indicator of capacitor or non-capacitor like behaviour.

Further fundamental study of activated MnO<sub>x</sub> (Chapter 6) and Ni(OH)<sub>2</sub> (Chapter 7) was done by *in situ* Raman microscopy coupled with other material characterisation techniques. From a scientific viewpoint, it is necessary to fully understand the charge storage mechanism of transition metal oxides and hydroxides in order to further improve their electrochemical performance in various electrochemical applications. In Chapter 6, the primarily hausmannite Mn<sub>3</sub>O<sub>4</sub> can be activated by potential cycling, leading to a predominantly localised birnessite MnO<sub>2</sub>. The

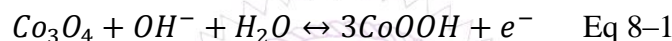
activation process and charge storage mechanism of activated  $\text{MnO}_x$  were both proposed in this work. Unlike well crystallised birnessite  $\text{MnO}_2$ , the charge storage mechanism of electrochemically activated  $\text{MnO}_x$  is attributable to the redox reaction between Mn (III) and Mn (IV) at outer surface active sites due to the structural disordering of the activated  $\text{MnO}_x$ . In Chapter 7, a new redox mechanism of  $\text{Ni(OH)}_2$  was proposed based on experimental results (EQCM and *in situ* Raman) and computational analyses (DFT+U). The loss of water molecules in  $\text{Ni(OH)}_2$  structure during charge–discharge process is the key for phase transform (ageing) to  $\beta\text{-Ni(OH)}_2$ , which is strongly dependent on alkali metal cation species.

### **Possible Future works**

It was reported the electrolyte additives ( $\text{Na}_2\text{HPO}_4$  or  $\text{NaHCO}_3$ ) not can only improve the capacitance of  $\text{MnO}_x$  pseudocapacitors, but also they can effectively suppress the manganese dissolution into electrolyte [131]. Although it was analysed by EQCM in the previous work [129], the effects of electrolyte additives on suppressing manganese dissolution are still not fully understood. It would be definitely interesting to study the mechanism of electrolyte additives for  $\text{MnO}_x$  pseudocapacitors. It was firstly tried by *in situ* Raman techniques; however, the additives signals were extremely weak due to low concentration of additives in electrolyte. On the other hand, laser power is needed to be controlled in a certain level in order to avoid  $\text{MnO}_x$  structural change inducing by laser heating. One way to enhance additives Raman signals is using surface–enhancement Raman spectroscopy (SERS). The additives Raman signals might be able to be observed by using silver or gold substrate. These two metals are typical for SERS experiments, since their plasmon resonance frequencies fall within the wavelength ranges of visible and near–infrared radiation, providing maximal enhancement. Thus, weak signals and subtle changes might be

able to be detected by using SERS. Another way is using *ex situ* FTIR to analyse the functional groups on MnO<sub>x</sub> electrode surface after cycling in additive-containing electrolytes. However, *ex situ* techniques would not have concrete evidence as *in situ* one.

The redox mechanism of cobalt oxide (Co<sub>3</sub>O<sub>4</sub>) and hydroxide (Co(OH)<sub>2</sub>) in alkaline media has been reported in literature. Two pairs of redox reactions are proposed to be involved in the redox mechanism of Co<sub>3</sub>O<sub>4</sub> (Eq 8–1 and 8–3) and Co(OH)<sub>2</sub> (Eq 8–2 and 8–3) [226–232].



In our preliminary tests, we purchased commercial Co<sub>3</sub>O<sub>4</sub> and Co(OH)<sub>2</sub> powders for electrochemical analyses. The preliminary results demonstrate only one redox peak observable in CV the curve of Co<sub>3</sub>O<sub>4</sub> electrode (shown in Figure 8–1a), while two pairs of humps can be found in the CV curve of Co(OH)<sub>2</sub> electrode (shown in Figure 8–1b). Besides, the effect of alkali metal cation species on the redox peak potential is also examined. For Co<sub>3</sub>O<sub>4</sub>, it seems only Co(III) is active because of the absence of CoOOH/Co<sub>3</sub>O<sub>4</sub> redox peak in the CV profiles. Moreover, the Co(IV)/Co(III) redox is not cation species dependent, since the peak potential difference obtained in LiOH, NaOH and KOH is attributable to the subtle difference of pH values of electrolytes. On the other hand, both Co(III)/Co(II) and Co(IV)/Co(III) redox peaks are observable for Co(OH)<sub>2</sub>. The former is found to be cation species dependent, while the latter is not. Accordingly, the results evoke the further study on the charge storage mechanism of Co<sub>3</sub>O<sub>4</sub> and Co(OH)<sub>2</sub>. EQCM is useful to measure the mass-to-charge ratio (MCR) if cations are involved in the redox mechanism. *In situ* Raman spectroscopy can give us a better idea on the structural change during charge-discharge process. X-ray

absorption spectroscopy can provide the information of the mean nickel oxidation state during charge–discharge process.

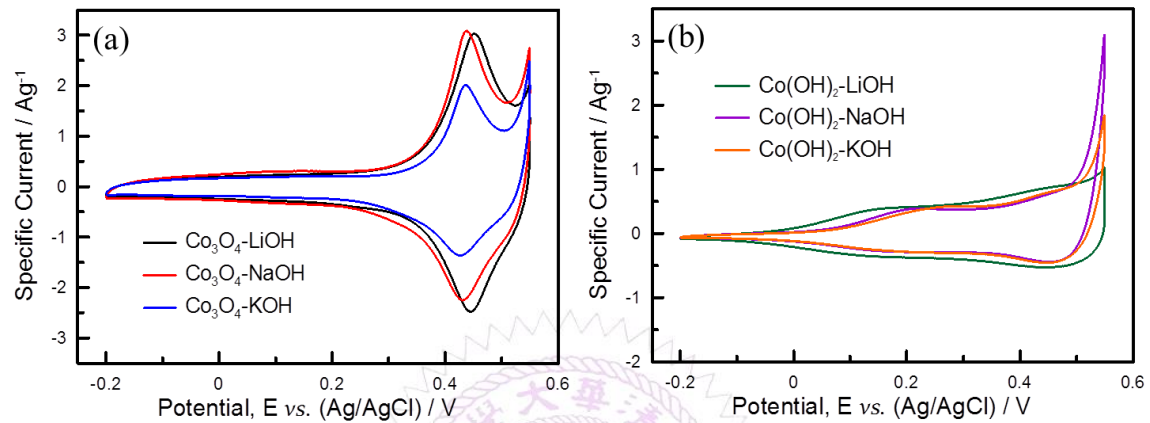


**Figure 8–1** CV curves of (a)  $\text{Co}_3\text{O}_4$  and (b)  $\text{Co(OH)}_2$  in 1 M LiOH, NaOH and KOH.



UNIVERSITY OF  
LIVERPOOL

## References

1. P. Simon, Y. Gogotsi and B. Dunn, *Science*, **343**, 1210 (2014).
2. Y. Gogotsi and P. Simon, *Science*, **334**, 917 (2011).
3. R. Kötz and M. Carlen, *Electrochimica Acta* **45**, 2483 (2000).
4. A. Burke, *Journal of Power Sources*, **91**, 37 (2000).
5. M. Winter and R. J. Brodd, *Chemical Reviews*, **104**, 4245 (2004).
6. J. M. Miller and A. F. Burke, *Electrochemical Society Interface*, **17**, 53 (2008).
7. J. H. Chae and G. Z. Chen, *Electrochimica Acta*, **86**, 248 (2012).
8. B. E. Conway, *Electrochemical Supercapacitors: Scientific Fundamentals and Technological Applications*, Kluwer–Plenum Pub. Co., New York (1999).
9. C. C. Hu, K. H. Chang, M. C. Lin and Y. T. Wu, *Nano letters*, **6**, 2690 (2006).
10. Z. Fan, J. Yan, T. Wei, L. Zhi, G. Ning, T. Li and F. Wei, *Advanced Functional Materials*, **21**, 2366 (2011).
11. C. Peng, S. Zhang, X. Zhou and G. Z. Chen, *Energy & Environmental Science*, **3**, 1499 (2010).
12. K. H. Chang, C. C. Hu, C. M. Huang, Y. L. Liu and C. I. Chang, *Journal of Power Sources*, **196**, 2387 (2011).
13. C. C. Hu, J. C. Chen and K. H. Chang, *Journal of Power Sources*, **221**, 128 (2013).
14. T. Cottineau, M. Toupin, T. Delahaye, T. Brousse and D. Bélanger, *Applied Physics A*, **82**, 599 (2005).
15. D. Cericola and R. Kötz, *Electrochimica Acta*, **72**, 1 (2012).
16. V. Khomenko, E. Raymundo–Piñero and F. Béguin, *Journal of Power Sources*, **153**, 183 (2006).
17. Y. Dai, K. Wang and J. Xie, *Applied Physics Letters*, **90**, 104102 (2007).
18. K. W. Nam and K. B. Kim, *Journal of The Electrochemical Society*, **153**, A81 (2006).
19. D. P. Dubal, D. S. Dhawale, R. R. Salunkhe and C. D. Lokhande, *Journal of Alloys and Compounds*, **496**, 370 (2010).
20. S. Komaba, T. Tsuchikawa, A. Ogata, N. Yabuuchi, D. Nakagawa and M. Tomita, *Electrochimica Acta*, **59**, 455 (2012).
21. C. C. Hu, C. Y. Hung, K. H. Chang and Y. L. Yang, *Journal of Power Sources*, **196**, 847 (2011).
22. C. C. Hu, Y. T. Wu and K. H. Chang, *Chemistry of Materials*, **20**, 2890 (2008).
23. C. Chen, Y. Lyu, C. Su, H. Lin and C. Lin, *Surface and Coatings Technology*, **202**, 1277 (2007).
24. T. H. Wu, Y. H. Chu, C. C. Hu and L. J. Hardwick, *Electrochemistry*



- Communications*, **27**, 81 (2013).
25. P. V. Kamath, M. Dixit, L. Indira, A. K. Shukla, V. G. Kumar and N. Munichandraiah, *Journal of The Electrochemical Society*, **141**, 2956 (1994).
  26. H. Chen, J. M. Wang, T. Pan, Y. L. Zhao, J. Q. Zhang and C. N. Cao, *Journal of Power Sources*, **143**, 243 (2005).
  27. B. Li, H. Cao, J. Shao, H. Zheng, Y. Lu, J. Yin and M. Qu, *Chemical Communications*, **47**, 3159 (2011).
  28. C. C. Hu and C. Y. Cheng, *Electrochemical and Solid–State Letters*, **5**, A43 (2002).
  29. Z. Tang, C. H. Tang and H. Gong, *Advanced Functional Materials*, **22**, 1272 (2012).
  30. H. Wang, H. S. Casalongue, Y. Liang and H. Dai, *Journal of the American Chemical Society*, **132**, 7472 (2010).
  31. J. C. Chen and C. C. Hu, *Thesis* (2013).
  32. Y. H. Lee, K. H. Chang and C. C. Hu, *Journal of Power Sources*, **227**, 300 (2013).
  33. S. Stankovich, D. A. Dikin, R. D. Piner, K. A. Kohlhaas, A. Kleinhammes, Y. Jia, Y. Wu, S. T. Nguyen and R. S. Ruoff, *Carbon*, **45**, 1558 (2007).
  34. H. J. Shin, K. K. Kim, A. Benayad, S. M. Yoon, H. K. Park, I. S. Jung, M. H. Jin, H. K. Jeong, J. M. Kim, J. Y. Choi and Y. H. Lee, *Advanced Functional Materials*, **19**, 1987 (2009).
  35. M. J. Fernández–Merino, L. Guardia, J. I. Paredes, S. Villar–Rodil, P. Solís–Fernández, A. Martínez–Alonso and J. M. D. Tascón, *The Journal of Physical Chemistry C*, **114**, 6426 (2010).
  36. H. A. Becerril, J. Mao, Z. Liu, R. M. Stoltenberg, Z. Bao and Y. Chen, *ACS Nano*, **2**, 463 (2008).
  37. W. Chen, L. Yan and P. R. Bangal, *Carbon*, **48**, 1146 (2010).
  38. M. D. Stoller, S. Park, Y. Zhu, J. An and R. S. Ruoff, *Nano letters*, **8**, 3498 (2008).
  39. Y. Wang, Z. Shi, Y. Huang, Y. Ma, C. Wang, M. Chen and Y. Chen, *The Journal of Physical Chemistry C*, **113**, 13103 (2009).
  40. J. R. Miller, R. A. Outlaw and B. C. Holloway, *Electrochimica Acta*, **56**, 10443 (2011).
  41. S. Y. Yang, K. H. Chang, H. W. Tien, Y. F. Lee, S. M. Li, Y. S. Wang, J. Y. Wang, C. C. M. Ma and C. C. Hu, *Journal of Materials Chemistry*, **21**, 2374 (2011).
  42. Y. Zhu, S. Murali, M. D. Stoller, K. J. Ganesh, W. Cai, P. J. Ferreira, A. Pirkle, R. M. Wallace, K. A. Cychosz, M. Thommes, D. Su, E. A. Stach and R. S. Ruoff, *Science*, **332**, 1537 (2011).

43. C. Bouchelta, M. S. Medjram, O. Bertrand and J.-P. Bellat, *Journal of Analytical and Applied Pyrolysis*, **82**, 70 (2008).
44. K. Fic, G. Lota, M. Meller and E. Frackowiak, *Energy & Environmental Science*, **5**, 5842 (2012).
45. F. C. Wu, R. L. Tseng, C. C. Hu and C. C. Wang, *Journal of Power Sources*, **138**, 351 (2004).
46. E. Frackowiak, *Physical Chemistry Chemical Physics*, **9**, 1774 (2007).
47. E. Frackowiak and F. Béguin, *Carbon*, **39**, 937 (2001).
48. J. Lee, J. Kim and T. Hyeon, *Advanced Materials*, **18**, 2073 (2006).
49. K. Jurewicz, C. Vix-Guterl, E. Frackowiak, S. Saadallah, M. Reda, J. Parmentier, J. Patarin and F. Béguin, *Journal of Physics and Chemistry of Solids*, **65**, 287 (2004).
50. A. B. Fuertes, G. Lota, T. A. Centeno and E. Frackowiak, *Electrochimica Acta*, **50**, 2799 (2005).
51. J. Li, X. Wang, Q. Huang, S. Gamboa and P. J. Sebastian, *Journal of Power Sources*, **158**, 784 (2006).
52. W. Li, G. Reichenauer and J. Fricke, *Carbon*, **40**, 2955 (2002).
53. C. Merlet, B. Rotenberg, P. A. Madden, P. L. Taberna, P. Simon, Y. Gogotsi and M. Salanne, *Nature materials*, **11**, 306 (2012).
54. Y. Gogotsi, A. Nikitin, H. Ye, W. Zhou, J. E. Fischer, B. Yi, H. C. Foley and M. W. Barsoum, *Nature materials*, **2**, 591 (2003).
55. J. Chmiola, G. Yushin, Y. Gogotsi, C. Portet, P. Simon and P. L. Taberna, *Science*, **313**, 1760 (2006).
56. D. Qu and H. Shi, *Journal of Power Sources*, **74**, 99 (1998).
57. C. Vix-Guterl, E. Frackowiak, K. Jurewicz, M. Friebe, J. Parmentier and F. Béguin, *Carbon*, **43**, 1293 (2005).
58. X. Yang, Y. S. He, G. Jiang, X. Z. Liao and Z. F. Ma, *Electrochemistry Communications*, **13**, 1166 (2011).
59. D. Qu, *Journal of Power Sources*, **109**, 403 (2002).
60. C. C. Hu and Y. H. Huang, *Journal of The Electrochemical Society*, **146**, 2465 (1999).
61. C. C. Hu and C. C. Wang, *Journal of The Electrochemical Society*, **150**, A1079 (2003).
62. H. Y. Lee and J. B. Goodenough, *Journal of Solid State Chemistry*, **144**, 220 (1999).
63. S. C. Pang, M. A. Anderson and T. W. Chapman, *Journal of The Electrochemical Society*, **147**, 444 (2000).
64. H. Jiang, T. Zhao, C. Li and J. Ma, *Journal of Materials Chemistry*, **21**, 3818 (2011).

65. S. K. Meher, P. Justin and G. R. Rao, *ACS applied materials & interfaces*, **3**, 2063 (2011).
66. V. Gupta, T. Kusahara, H. Toyama, S. Gupta and N. Miura, *Electrochemistry Communications*, **9**, 2315 (2007).
67. L. Cao, F. Xu, Y. Y. Liang and H. L. Li, *Advanced Materials*, **16**, 1853 (2004).
68. T. Y. Wei, C. H. Chen, H. C. Chien, S. Y. Lu and C. C. Hu, *Advanced Materials*, **22**, 347 (2010).
69. C. T. Hsu and C. C. Hu, *Journal of Power Sources*, **242**, 662 (2013).
70. C. Yuan, J. Li, L. Hou, X. Zhang, L. Shen and X. W. D. Lou, *Advanced Functional Materials*, **22**, 4592 (2012).
71. J. M. Li, K. H. Chang, T. H. Wu and C. C. Hu, *Journal of Power Sources*, **224**, 59 (2013).
72. Z. Chen, Y. Qin, D. Weng, Q. Xiao, Y. Peng, X. Wang, H. Li, F. Wei and Y. Lu, *Advanced Functional Materials*, **19**, 3420 (2009).
73. H. Y. Lee and J. B. Goodenough, *Journal of Solid State Chemistry*, **148**, 81 (1999).
74. W. Shi, J. Zhu, D. H. Sim, Y. Y. Tay, Z. Lu, X. Zhang, Y. Sharma, M. Srinivasan, H. Zhang, H. H. Hng and Q. Yan, *Journal of Materials Chemistry*, **21**, 3422 (2011).
75. Q. Qu, S. Yang and X. Feng, *Advanced Materials*, **23**, 5574 (2011).
76. B. Li, H. Cao, J. Shao, M. Qu and J. H. Warner, *Journal of Materials Chemistry*, **21**, 5069 (2011).
77. C. C. Hu, E. Chen and J. Y. Lin, *Electrochimica Acta*, **47**, 2741 (2002).
78. A. Rudge, I. Raistrick, S. Gottesfeld and J. P. Ferraris, *Electrochimica Acta*, **39**, 273 (1994).
79. L. Athouël, F. Moser, R. Dugas, O. Crosnier, D. Bélanger and T. Brousse, *The Journal of Physical Chemistry C*, **112**, 7270 (2008).
80. T. Brousse, P.-L. Taberna, O. Crosnier, R. Dugas, P. Guillemet, Y. Scudeller, Y. Zhou, F. Favier, D. Bélanger and P. Simon, *Journal of Power Sources*, **173**, 633 (2007).
81. T. Brousse, M. Toupin and D. Bélanger, *Journal of The Electrochemical Society*, **151**, A614 (2004).
82. C. C. Hu and T. W. Tsou, *Electrochemistry Communications*, **4**, 105 (2002).
83. M. Toupin, T. Brousse and D. Bélanger, *Chemistry of Materials*, **14**, 3946 (2002).
84. H. Xia, W. Xiao, M. O. Lai and L. Lu, *Nanoscale research letters*, **4**, 1035 (2009).
85. S. W. Zhang and G. Z. Chen, *Energy Materials*, **3**, 186 (2008).
86. M. Toupin, T. Brousse and D. Belanger, *Chemistry of Materials*, **16**, 3184

- (2004).
87. Y. S. Chen, C. C. Hu and Y. T. Wu, *Journal of Solid State Electrochemistry*, **8**, 467 (2004).
  88. E. Narita and T. Okabe, *Bulletin of the Chemical Society of Japan*, **53**, 525 (1980).
  89. H. Unuma, T. Kanehama, K. Yamamoto, K. Watanabe, T. Ogata and M. Sugawara, *Journal of Materials Science*, **38**, 255 (2003).
  90. H. P. Stadniychuk, M. A. Anderson and T. W. Chapman, *Journal of The Electrochemical Society*, **143**, 1629 (1996).
  91. H. Y. Lee, S. W. Kim and H. Y. Lee, *Electrochemical and Solid–State Letters*, **4**, A19 (2001).
  92. M. S. Wu, *Applied Physics Letters*, **87**, 153102 (2005).
  93. C. C. Hu and T. W. Tsou, *Journal of Power Sources*, **115**, 179 (2003).
  94. C. C. Hu, K. H. Chang, Y. T. Wu, C. Y. Hung, C. C. Lin and Y. T. Tsai, *Electrochemistry Communications*, **10**, 1792 (2008).
  95. C. C. Hu and T. W. Tsou, *Electrochimica Acta*, **47**, 3523 (2002).
  96. O. Ghodbane, F. Ataherian, N. L. Wu and F. Favier, *Journal of Power Sources*, **206**, 454 (2012).
  97. T. Brousse, M. Toupin, R. Dugas, L. Athouël, O. Crosnier and D. Bélanger, *Journal of The Electrochemical Society*, **153**, A2171 (2006).
  98. A. Boisset, L. Athouël, J. Jacquemin, P. Porion, T. Brousse and M. Anouti, *The Journal of Physical Chemistry C*, **117**, 7408 (2013).
  99. R. N. Reddy and R. G. Reddy, *Journal of Power Sources*, **124**, 330 (2003).
  100. M. S. Wu and P. C. Julia Chiang, *Electrochemical and Solid–State Letters*, **7**, A123 (2004).
  101. J. Y. Luo and Y. Y. Xia, *Journal of The Electrochemical Society*, **154**, A987 (2007).
  102. J. N. Broughton and M. J. Brett, *Electrochimica Acta*, **49**, 4439 (2004).
  103. J. W. Long, D. Bélanger, T. Brousse, W. Sugimoto, M. B. Sassin and O. Crosnier, *MRS BULLETIN*, **36**, 513 (2011).
  104. P. Staiti and F. Lufrano, *Journal of Power Sources*, **187**, 284 (2009).
  105. P. C. Gao, A. H. Lu and W. C. Li, *Journal of Power Sources*, **196**, 4095 (2011).
  106. X. D. Dong, W. Shen, J. Gu, L. Xiong, Y. Zhu, H. Li and J. Shi, *Journal of Physical Chemistry B*, **110**, 6015 (2006).
  107. W. Qian, Z. Chen, S. Cottingham, W. A. Merrill, N. A. Swartz, A. M. Goforth, T. L. Clare and J. Jiao, *Green Chemistry*, **14**, 371 (2012).
  108. X. Jin, W. Zhou, S. Zhang and G. Z. Chen, *Small*, **3**, 1513 (2007).
  109. S. M. Li, Y. S. Wang, S. Y. Yang, C. H. Liu, K. H. Chang, H. W. Tien, N. T. Wen,

- C. C. M. Ma and C. C. Hu, *Journal of Power Sources*, **225**, 347 (2013).
110. J. Li, X. Wang, Q. Huang, S. Gamboa and P. J. Sebastian, *Journal of Power Sources*, **160**, 1501 (2006).
111. M. Wu, G. A. Snook, G. Z. Chen and D. J. Fray, *Electrochemistry Communications*, **6**, 499 (2004).
112. C. Wan, K. Azumi and H. Konno, *Electrochimica Acta*, **52**, 3061 (2007).
113. S. B. Ma, Y. H. Lee, K. Y. Ahn, C. M. Kim, K. H. Oh and K. B. Kim, *Journal of The Electrochemical Society*, **153**, C27 (2006).
114. P. Simon and Y. Gogotsi, *Nature material*, **7**, 845 (2008).
115. D. Bélanger, T. Brousse and J. W. Long, *The Electrochemical Society Interface*, **17**, 49 (2008).
116. C. H. Liang and C. S. Hwang, *Japanese Journal of Applied Physics*, **47**, 1662 (2008).
117. S. Devaraj and N. Munichandraiah, *Journal of The Electrochemical Society*, **154**, A80 (2007).
118. M. Chigane and M. Ishikawa, *Journal of Electroanalytical Society*, **147**, 2246 (2000).
119. B. Djurfors, J. N. Broughton, M. J. Brett and D. G. Ivey, *Acta Materialia*, **53**, 957 (2005).
120. J. K. Chang, Y. L. Chen and W. T. Tsai, *Journal of Power Sources*, **135**, 344 (2004).
121. J. K. Chang and W. T. Tsai, *Journal of The Electrochemical Society*, **152**, A2063 (2005).
122. B. Liu, P. S. Thomas, A. S. Ray, R. P. Williams and S. W. Donne, *Journal of Thermal Analysis and Calorimetry*, **88**, 177 (2007).
123. R. Ma, Y. Bando, L. Zhang and T. Sasaki, *Advanced Materials*, **16**, 918 (2004).
124. F. Buciuman, F. Patcas, R. Craciun and D. R. T. Zahn, *Physical Chemistry Chemical Physics*, **1**, 185 (1999).
125. M. C. Bernard, A. H. L. Goff and B. V. Thi, *Journal of The Electrochemical Society*, **140**, 3065 (1993).
126. C. Julien and M. Massot, *Physical Chemistry Chemical Physics*, **4**, 4226 (2002).
127. M. Pourbaix, *Atlas of Electrochemical Equilibria in Aqueous Solutions*, National Association of Corrosion Engineers, Houston, TX (1996).
128. W. Wei, X. Cui, W. Chen and D. G. Ivey, *Journal of Power Sources*, **186**, 543 (2009).
129. Y. H. Chu, C. C. Hu and K. H. Chang, *Electrochimica Acta*, **61**, 124 (2012).
130. Y. C. Hsieh, K. T. Lee, Y. P. Lin, N. L. Wu and S. W. Donne, *Journal of Power Sources*, **177**, 660 (2008).



131. S. Komaba, A. Ogata and T. Tsuchikawa, *Electrochemistry Communications*, **10**, 1435 (2008).
132. M. S. Hong, S. H. Lee and S. W. Kim, *Electrochemical and Solid–State Letters*, **5**, A227 (2002).
133. Q. Qu, P. Zhang, B. Wang, Y. Chen, S. Tian, Y. Wu and R. Holze, *The Journal of Physical Chemistry C*, **113**, 14020 (2009).
134. Z. S. Wu, W. Ren, D. W. Wang, B. Li and H. M. Cheng, *ACS Nano*, **4**, 5835 (2010).
135. Q. Qu, L. Li, S. Tian, W. Guo, Y. Wu and R. Holze, *Journal of Power Sources*, **195**, 2789 (2010).
136. Q. T. Qu, Y. Shi, S. Tian, Y. H. Chen, Y. P. Wu and R. Holze, *Journal of Power Sources*, **194**, 1222 (2009).
137. L. Deng, G. Zhu, J. Wang, L. Kang, Z.–H. Liu, Z. Yang and Z. Wang, *Journal of Power Sources*, **196**, 10782 (2011).
138. C. Xu, H. Du, B. Li, F. Kang and Y. Zeng, *Journal of The Electrochemical Society*, **156**, A435 (2009).
139. A. Sumboja, C. Y. Foo, X. Wang and P. S. Lee, *Advanced Materials*, **25**, 2809 (2013).
140. Y. Jin, H. Chen, M. Chen, N. Liu and Q. Li, *ACS applied materials & interfaces*, **5**, 3408 (2013).
141. P. C. Chen, G. S. Shen, Yi, H. Chen and C. Zhou, *ACS Nano*, **4**, 4403 (2010).
142. S. F. Chin, S. C. Pang and M. A. Anderson, *Journal of The Electrochemical Society*, **149**, A379 (2002).
143. S. L. Kuo and N. L. Wu, *Journal of The Electrochemical Society*, **153**, A1317 (2006).
144. K. W. Kim, M. G. Kim and K. B. Kim, *Journal of Physical Chemistry C*, **111**, 749 (2007).
145. J. K. Chang, M. T. Lee and W. T. Tsai, *Journal of Power Sources*, **166**, 590 (2007).
146. Y. K. Hsu, Y. C. Chen, Y. G. Lin, L. C. Chen and K. H. Chen, *Chemical Communications*, **47**, 1252 (2011).
147. D. Chen, D. Ding, X. Li, G. H. Waller, X. Xiong, M. A. El–Sayed and M. Liu, *Chemistry of Materials*, **27**, 6608 (2015).
148. C. Julien, *Solid State Ionics*, **159**, 345 (2003).
149. L. J. Hardwick, P. W. Ruch, M. Hahn, W. Scheifele, R. Kötz and P. Novák, *Journal of Physics and Chemistry of Solids*, **69**, 1232 (2008).
150. L. J. Hardwick, M. Hahn, P. Ruch, M. Holzapfel, W. Scheifele, H. Buqa, F. Krumeich, P. Novák and R. Kötz, *Electrochimica Acta*, **52**, 675 (2006).



151. L. Hardwick, H. Buqa and P. Novak, *Solid State Ionics*, **177**, 2801 (2006).
152. S. Osswald, G. Yushin, V. Mochalin, S. O. Kucheyev and Y. Gogotsi, *Journal of the American Chemical Society*, **128**, 11635 (2006).
153. G. K. Ramesh and S. Sampath, *The Journal of Physical Chemistry C*, **113**, 7985 (2009).
154. A. Das, S. Pisana, B. Chakraborty, S. Piscanec, S. K. Saha, U. V. Waghmare, K. S. Novoselov, H. R. Krishnamurthy, A. K. Geim, A. C. Ferrari and A. K. Sood, *Nature nanotechnology*, **3**, 210 (2008).
155. E. Pollak, B. Geng, K. J. Jeon, I. T. Lucas, T. J. Richardson, F. Wang and R. Kostecki, *Nano letters*, **10**, 3386 (2010).
156. M. Kalbac, H. Farhat, J. Kong, P. Janda, L. Kavan and M. S. Dresselhaus, *Nano letters*, **11**, 1957 (2011).
157. M. Frumar, Z. Polak and Z. Cernosek, *Journal of Non-Crystalline Solids*, **256&257**, 105 (1999).
158. G. Mestl, *Journal of Molecular Catalysis A*, **158**, 45 (2000).
159. M. A. Vuurman and I. E. Wachs, *Journal of Physical Chemistry*, **96**, 5008 (1992).
160. X. Gao, S. R. Bare, B. M. Weckhuysen and I. E. Wachs, *Journal of physical Chemistry B*, **102**, 10842 (1998).
161. G. J. Hutchings, A. Desmartin-Chomel, R. Olier and J. C. Volta, *Nature*, **368**, 41 (1994).
162. J. M. Jehng and I. E. Wachs, *Chemistry of Materials*, **3**, 100 (1991).
163. M. Sun, B. Lan, T. Lin, G. Cheng, F. Ye, L. Yu, X. Cheng and X. Zheng, *CrystEngComm*, **15**, 7010 (2013).
164. C. M. Julien, M. Massot and C. Poinsignon, *Spectrochimica Acta Part A: Molecular and Biomolecular Spectroscopy*, **60**, 689 (2004).
165. Y. Li, J. Wang, Y. Zhang, M. N. Banis, J. Liu, D. Geng, R. Li and X. Sun, *Journal of colloid and interface science*, **369**, 123 (2012).
166. E. Widjaja and J. T. Sampanthar, *Analytica chimica acta*, **585**, 241 (2007).
167. A. Iyer, J. Del-Pilar, C. K. King'ondou, E. Kissel, H. F. Garces, H. Huang, A. M. El-Sawy, P. K. Dutta and S. L. Suib, *The Journal of Physical Chemistry C*, **116**, 6474 (2012).
168. A. Dias, R. G. Sá, M. C. Spitale, M. Athayde and V. S. T. Ciminelli, *Materials Research Bulletin*, **43**, 1528 (2008).
169. J. Zhou, L. Yu, M. Sun, S. Yang, F. Ye, J. He and Z. Hao, *Industrial & Engineering Chemistry Research*, **52**, 9586 (2013).
170. M. Richter, A. Trunschke, U. Bentrup, K. W. Brzezinka, E. Schreier, M. Schneider, M. M. Pohl and R. Fricke, *Journal of Catalysis*, **206**, 98 (2002).

171. G. C. Silva, F. S. Almeida, A. M. Ferreira and V. S. T. Ciminelli, *Materials Research*, **15**, 403 (2012).
172. P. L. Goff, N. Baffier, S. Bach and J. P. Pereira–Ramos, *Journal of Materials Chemistry*, **4**, 875 (1994).
173. B. Djurfors, J. N. Broughton, M. J. Brett and D. G. Ivey, *Journal of The Electrochemical Society*, **153**, A64 (2006).
174. K. E. Toghill, L. Xiao, M. A. Phillips and R. G. Compton, *Sensors and Actuators B: Chemical*, **147**, 642 (2010).
175. K. E. Toghill and R. G. Compton, *International Journal of Electrochemical Science*, **5**, 1246 (2010).
176. G. A. Niklasson and C. G. Granqvist, *Journal of Materials Chemistry*, **17**, 127 (2007).
177. A. I. Inamdar, A. C. Sonavane, S. M. Pawar, Y. Kim, J. H. Kim, P. S. Patil, W. Jung, H. Im, D.–Y. Kim and H. Kim, *Applied Surface Science*, **257**, 9606 (2011).
178. D. Wei, M. R. Scherer, C. Bower, P. Andrew, T. Ryhanen and U. Steiner, *Nano letters*, **12**, 1857 (2012).
179. Q. Wu, L. Jiang, Q. Tang, J. Liu, S. Wang and G. Sun, *Electrochimica Acta*, **91**, 314 (2013).
180. J. Ponce, J. L. Rehspringer, G. Poillerat and J. L. Gautier, *Electrochimica Acta*, **46**, 3373 (2001).
181. V. Rashkova, S. Kitova, I. Konstantinov and T. Vitanov, *Electrochimica Acta*, **47**, 1555 (2002).
182. H. Bode, K. Dehmelt and J. Witte, *Electrochimica Acta*, **11**, 1079 (1966).
183. M. Wehrens–Dijksma and P. H. L. Notten, *Electrochimica Acta*, **51**, 3609 (2006).
184. R. S. McEwen, *The Journal of Physical Chemistry*, **75**, 1782 (1971).
185. D. A. Corrigan and S. L. Knight, *Journal of The Electrochemical Society*, **136**, 613 (1989).
186. R. Barnard, C. F. Randell and F. L. Tye, *Journal of Applied Electrochemistry*, **10**, 109 (1980).
187. P. Oliva, J. Leonardi and J. F. Laurent, *Journal of Power Sources*, **8**, 229 (1982).
188. A. Van der Ven, D. Morgan, Y. S. Meng and G. Ceder, *Journal of The Electrochemical Society*, **153**, A210 (2006).
189. D. S. Hall, D. J. Lockwood, S. Poirier, C. Bock and B. R. MacDougall, *ACS applied materials & interfaces*, **6**, 3141 (2014).
190. M. S. Kim and K. B. Kim, *Journal of The Electrochemical Society*, **145**, 507 (1998).
191. G. T. Cheek and W. E. O'Grady, *Journal of Electroanalytical Chemistry*, **421**, 173 (1997).

192. S. I. Cordoba-Torresi, C. Gabrielli, A. Hugot-Le Goff and R. Torresi, *Journal of The Electrochemical Society*, **138**, 1548 (1991).
193. S. Ardizzone, G. Fregonara and S. Trasatti, *Electrochimica Acta*, **35**, 263 (1990).
194. C. C. Hu and C. H. Chu, *Journal of Electroanalytical Chemistry*, **503**, 105 (2001).
195. P. J. Hung, K. H. Chang, Y. F. Lee, C. C. Hu and K. M. Lin, *Electrochimica Acta*, **55**, 6015 (2010).
196. P. W. Ruch, D. Cericola, M. Hahn, R. Kötz and A. Wokaun, *Journal of Electroanalytical Chemistry*, **636**, 128 (2009).
197. D. Yang, R. Wang, M. He, J. Zhang and Z. Liu, *The Journal of Physical Chemistry B*, **109**, 7654 (2005).
198. J. N. Barisci, G. G. Wallace and R. H. Baughman, *Journal of Electroanalytical Chemistry*, **488**, 92 (2000).
199. Q. Gao, L. Demarconnay, E. Raymundo-Piñero and F. Béguin, *Energy & Environmental Science*, **5**, 9611 (2012).
200. Q. Wang, J. Yan, Y. Wang, G. Ning, Z. Fan, T. Wei, J. Cheng, M. Zhang and X. Jing, *Carbon*, **52**, 209 (2013).
201. I. Stepniak and A. Ciszewski, *Electrochimica Acta*, **56**, 2477 (2011).
202. C. T. Hsu, C. C. Hu, T. H. Wu, J. C. Chen and M. Rajkumar, *Electrochimica Acta*, **146**, 759 (2014).
203. C. H. Wang, S. C. Hsu and J. H. Hu, *Journal of Power Sources*, **249**, 1 (2014).
204. M. Kalapsazova, R. Stoyanova, E. Zhecheva, G. Tyuliev and D. Nihtianova, *Journal of Materials Chemistry A*, **2**, 19383 (2014).
205. M. C. Bernard, P. Bernard, M. Keddam, S. Senyariçh and H. Takenouti, *Electrochimica acta*, **41**, 91 (1996).
206. A. Delahaye-Vidal, N. Sac-Epée, K. Tekaia-Elhsissen, A. Audemer and M. Figlarz, *Solid State Ionics*, **84**, 239 (1996).
207. Y. L. Lo, S. C. Chou and B. J. Hwang, *JOURNAL OF APPLIED ELECTROCHEMISTRY*, **26**, 733 (1996).
208. J. W. Lee, J. M. Ko and J.-D. Kim, *The Journal of Physical Chemistry C*, **115**, 19445 (2011).
209. R. S. Jayashree and P. V. Kamath, *Journal of Applied Electrochemistry*, **31**, 1315 (2001).
210. M. E. Uñates, M. E. Folquer, J. R. Vilche and A. J. Arvia, *Journal of The Electrochemical Society*, **139**, 2697 (1992).
211. C. C. Hu, K. H. Chang and T. Y. Hsu, *Journal of The Electrochemical Society*, **155**, F196 (2008).
212. J. Maruta, H. Yasuda and M. Yamachi, *Journal of Power Sources*, **90**, 89 (2000).

213. M. S. Kim, T. S. Hwang and K. B. Kim, *Journal of The Electrochemical Society*, **144**, 1537 (1997).
214. E. R. Nightingale Jr., *Journal of Physical Chemistry*, **63**, 1381 (1959).
215. G. A. Snook, A. M. Bond and S. Fletcher, *Journal of Electroanalytical Chemistry*, **526**, 1 (2002).
216. A. Méndez, P. Díaz-Arista, L. Salgado, Y. Meas and G. Trejo, *International Journal of Electrochemical Science*, **3**, 918 (2008).
217. C. Faure, C. Delmas and M. Fouassier, *Journal of Power Sources*, **35**, 279 (1991).
218. R. Kostecki and F. McLarnon, *Journal of The Electrochemical Society*, **144**, 485 (1997).
219. D. S. Hall, D. J. Lockwood, S. Poirier, C. Bock and B. R. MacDougall, *The Journal of Physical Chemistry A*, **116**, 6771 (2012).
220. M. Merrill, M. Worsley, A. Wittstock, J. Biener and M. Stadermann, *Journal of Electroanalytical Chemistry*, **717–718**, 177 (2014).
221. B. S. Yeo and A. T. Bell, *The Journal of Physical Chemistry C*, **116**, 8394 (2012).
222. C. Delmas, *Materials Science Forum*, **152–153**, 131 (1994).
223. M. W. Louie and A. T. Bell, *Journal of the American Chemical Society*, **135**, 12329 (2013).
224. T. H. Wu, I. Scivetti, J. C. Chen, C. T. Hsu, T. Gilberto, C. C. Hu and L. J. Hardwick, *under preparation* (2016).
225. C. Delmas, Y. Borthomieu and C. Faure, *Solid State Ionics*, **32/33**, 104 (1989).
226. J. A. Koza, C. M. Hull, Y.-C. Liu and J. A. Switzer, *Chemistry of Materials*, **25**, 1922 (2013).
227. E. Scavetta, B. Ballarin, C. Corticelli, I. Gualandi, D. Tonelli, V. Prevot, C. Forano and C. Mousty, *Journal of Power Sources*, **201**, 360 (2012).
228. Y. C. Liu, J. A. Koza and J. A. Switzer, *Electrochimica Acta*, **140**, 359 (2014).
229. J. K. Chang, C. M. Wu and I. W. Sun, *Journal of Materials Chemistry*, **20**, 3729 (2010).
230. K. Nakaoka, M. Nakayama and K. Ogura, *Journal of The Electrochemical Society*, **149**, C159 (2002).
231. D. Ghosh, S. Giri and C. K. Das, *Environmental Progress & Sustainable Energy*, **33**, 1059 (2014).
232. Y. F. Yuan, X. H. Xia, J. B. Wu, X. H. Huang, Y. B. Pei, J. L. Yang and S. Y. Guo, *Electrochemistry Communications*, **13**, 1123 (2011).
233. M. Aghazadeh, M. Ghaemi, B. Sabour and S. Dalvand, *Journal of Solid State Electrochemistry*, **18**, 1569 (2014).
234. D. S. Hall, D. J. Lockwood, C. Bock and B. R. MacDougall, *Proceedings*.

*Mathematical, physical, and engineering sciences / the Royal Society*, **471**, 20140792 (2015).





## Appendix

In order to further discuss the cation effect on  $\text{Ni(OH)}_2$  in Chapter 7, we cooperated with Dr Gilberto Teobaldi and Dr Ivan Scivetti for density functional theory (DFT) simulations to investigate the reasons why KOH and NaOH promote the phase transformation from  $\gamma/\alpha$  phases into  $\beta/\beta$  phases. The results in this section were kindly provided by our collaborative colleagues.

First of all, the simulation has to start with the construction of the structure of  $\alpha\text{-Ni(OH)}_2$ .  $\alpha\text{-Ni(OH)}_2$  actually possesses intercalated water molecules in the inter-slab space. It was reported the water content in  $\alpha\text{-Ni(OH)}_2$  generally ranges from 0.3 to 0.8 [233, 234], subjected to the preparation methods and experimental conditions. The intrinsically hydrated  $\text{Ni(OH)}_2$  is considered with the formula presenting as  $\alpha\text{-Ni(OH)}_2(\text{H}_2\text{O})_\delta$ , where  $\delta$  is the degree of hydration in the pristine structure. The observed randomness in the orientation of  $\text{Ni(OH)}_2$  layers is believed to be a consequence of the amorphous pattern of the intercalated water molecules [184, 234]. In addition, structural disorders (such as stacking faults, ionic substitutions, crystalline defects, grain boundaries, etc.) have shown to play a decisive role in the phase structure. From the modelling viewpoint, the inclusion of all these possible sources of amorphicity is obviously unfeasible. In order to make the simulation executable, we assumed that, whereas the whole structure of  $\alpha\text{-Ni(OH)}_2$  is amorphous, there will be domains of local order (relatively small in size) where one can use the approximation of crystal periodicity.

Figure A-1 shows the computed formation energy of  $\alpha\text{-Ni(OH)}_2(\text{H}_2\text{O})_\delta$  as a function of the degree of hydration,  $\delta$ . Interestingly, there are two minima were observed, one at  $\delta=0$  and another at  $\delta\approx 1$ . In addition, the zero-point-energy (ZPE)



effects has been corrected by including the vibrational contributions of water and the H atoms of the Ni(OH)<sub>2</sub> host. The results exhibit the similar trend to that without considering ZPE. This indicates that ZPE effects do not play a significant role for this system. Therefore, ZPE effects have been neglected in the following calculations. Note that the computed Ni–Ni distance for the pristine  $\alpha$ -Ni(OH)<sub>2</sub>(H<sub>2</sub>O) is 7.88 Å, which is in agreement with the reported value of 8 Å [183]. The amount of intercalated water can be determined experimentally by TGA analyses. According to weight loss profile shown in Figure A–2, three distinguishable regions can be found by two observable plateaus. The regions <150 °C and 150–270 °C correspond to the weight loss of physisorbed H<sub>2</sub>O and intercalated H<sub>2</sub>O, respectively, while the region 270–600 °C represents the dehydroxylation of Ni(OH)<sub>2</sub> into NiO [187, 233]. Thus, the composition of as-deposited  $\alpha$ -Ni(OH)<sub>2</sub> can be determined by the weight loss of these three regions (Table A–1). The intercalated water content is 0.97 for the as-deposited  $\alpha$ -Ni(OH)<sub>2</sub> prepared by cathodic deposition, which is in good agreement with the computational findings (i.e.,  $\delta \approx 1$ ).

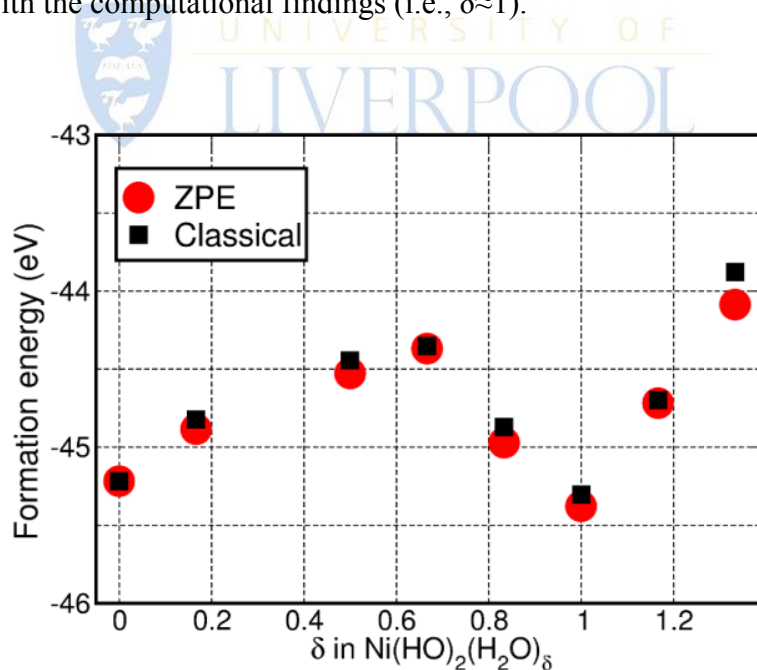


**Figure A–1** Computed formation energy of  $\alpha$ -Ni(OH)<sub>2</sub>(H<sub>2</sub>O) <sub>$\delta$</sub>  as a function of the amount of hydration  $\delta$ .

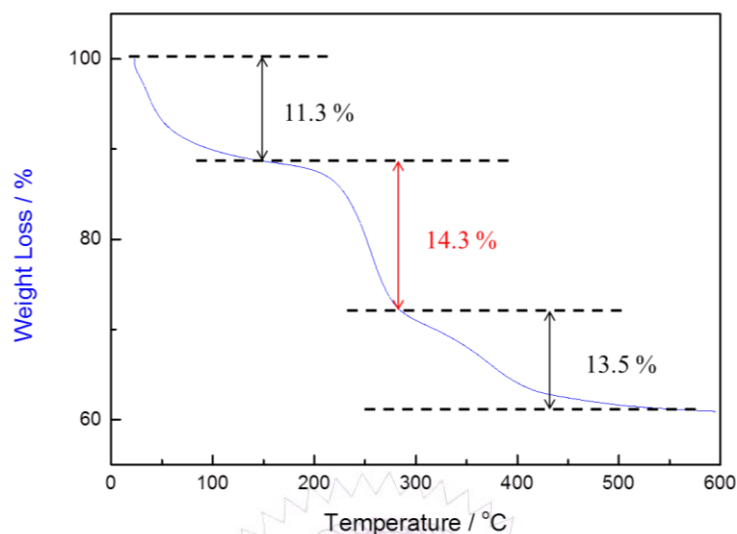


**Figure A-2** TGA curve of as-deposited  $\alpha$ -Ni(OH)<sub>2</sub>.

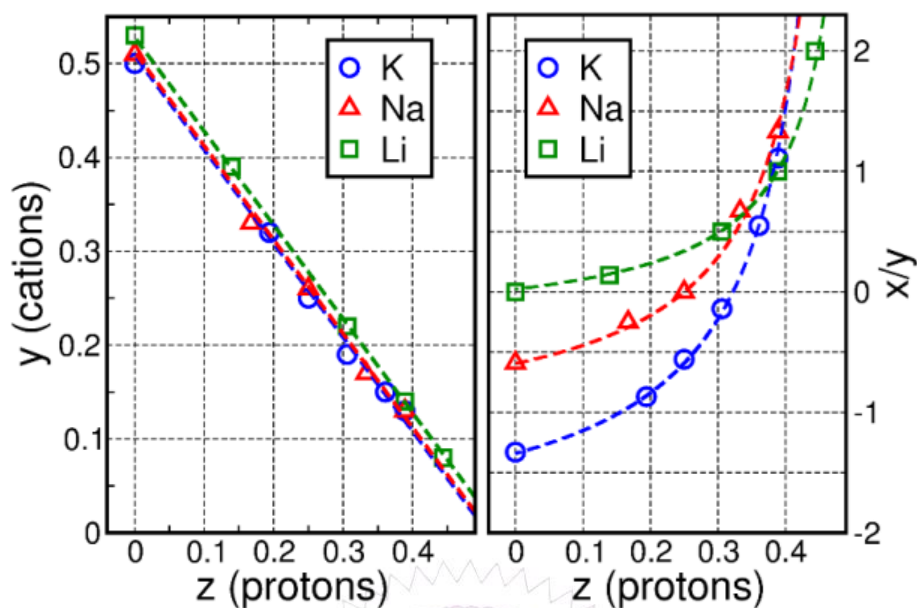
**Table A-1** The composition of as-deposited  $\alpha$ -Ni(OH)<sub>2</sub> calculated from TGA analysis in Figure A-2.

Temperature range (°C)	Weight (%)	Mole (%)	Composition	Reaction
25-150	11.3	0.63	0.77	Physical adsorbed H <sub>2</sub> O
150-270	14.3	0.79	0.97	Intercalated H <sub>2</sub> O
At 600	60.9	0.82	1	Remaining NiO

According to Cordoba-Torresi *et al.* work [192], a modified model for the oxidation of  $\alpha$ -Ni(OH)<sub>2</sub> is proposed in Eq 7-2. The stoichiometric numbers  $x$ ,  $y$  and  $z$  are related through mass and charge balance equations (refer to Eq 2-21 and Eq 2-22). Note that two parameters, the mole number of Ni(OH)<sub>2</sub> ( $n$ ) and the total charge in the oxidation process ( $q$ ), have to be carefully determined from EQCM experiments. Here, one further assumption was made that the precipitated  $\alpha$ -Ni(OH)<sub>2</sub>(H<sub>2</sub>O) films on the gold electrode for EQCM are sufficiently thin that all the precipitates can undergo

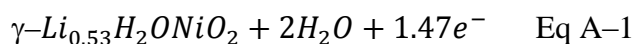
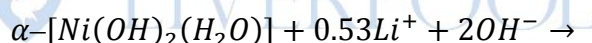
reaction. In the case, the mole number of  $\text{Ni(OH)}_2$  ( $n$ ) can be easily calculated from the recorded mass difference during cathodic deposition of  $\alpha\text{-Ni(OH)}_2(\text{H}_2\text{O})$ . Thus, omission of hydrated water in  $\alpha\text{-Ni(OH)}_2$  structure overestimates the mole number of  $\text{Ni(OH)}_2$  ( $n$ ). This could lead to an incorrect description of the electrochemical reaction.

The term  $x/y$  in Eq 7-2 stands for the water to cation ratio involved in the process. From the experimental values for mass change ( $\Delta m$ ) and the total charge ( $q$ ) at the end of the first oxidation process, the dependence of cation ( $y$ ) and water/cation ( $x/y$ ) with respect to proton ( $z$ ) can be obtained based on mass and charge balance equations (as shown in Figure A-3). Interestingly, negative values of water/cation ( $x/y$ ) are also possible solutions of the mass and charge balance equations when using either  $\text{Na}^+$  or  $\text{K}^+$  as cation species. Note that a negative value for water/cation ( $x/y$ ) indicates that a 'x' amount of water molecules in  $\alpha\text{-Ni(OH)}_2(\text{H}_2\text{O})$  structure is substituted by the 'y' amount of inserted cations. This means the insertion of hydrated cations during oxidation process would not take place. Instead, the water molecules in  $\alpha\text{-Ni(OH)}_2(\text{H}_2\text{O})$  would be removed from host structure by the insertion of cations during oxidation process.



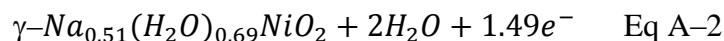
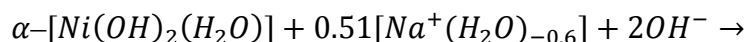
**Figure A-3** proton ( $z$ ) dependence of cation ( $y$ ) and water/cation ( $x/y$ ) at the charged state in the first cycle. Symbols indicate the selected stoichiometry the computation of various structural models.

Figure A-4 shows the computed formation energy as a function of water/cation ( $x/y$ ) for  $\text{Li}^+$ ,  $\text{Na}^+$  and  $\text{K}^+$  at the charged state in the first cycle. The energetically most favourable  $\gamma$  structure for Li is obtained for  $x/y = 0$  ( $z = 0$  and  $y = 0.53$ ). The formula of the first cycle oxidation in LiOH can be presented as following:



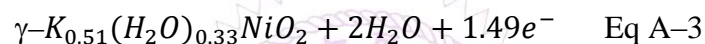
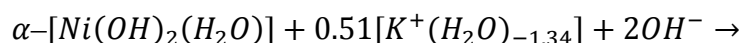
This indicates that all protons are removed by forming  $\text{H}_2\text{O}$  (combination of  $\text{H}^+$  and inserted  $\text{OH}^-$ ) when  $\text{Li}^+$  is inserted in the structure. And the content of water within the host structure remains unchanged. It is noteworthy that the water/cation ( $x/y$ ) value have always been considered to be positive values in literature [183, 192]. However, the simulation results clearly demonstrate that the inclusion of solvated cations ( $x/y \geq 0$ ) is energetically unfavourable. With regard to the first cycle oxidation in NaOH, the energetically most favourable configuration is given as  $x/y = -0.6$  ( $z = 0$

and  $y = 0.51$ ):



indicating that the insertion of  $\text{Na}^+$  entails the removal of 0.6 water molecule per  $\text{Na}^+$ .

The effect of water molecules removal is even more severe for  $\text{K}^+$  where the computed optimum for  $x/y$  is equal to  $-1.34$  ( $z = 0$  and  $y = 0.51$ ):



leading to the significant reduction of 78% water molecules inside the host structure.

Based on the above results, a new mechanism of oxidation from  $\alpha$  to  $\gamma$  phase is proposed. The solvated cations are driven to the electrode surface under the applied potential. Due to the abundant water content inside  $\alpha\text{-Ni}(\text{OH})_2$  inter-slab space, it is reasonably believed that the hydration sphere of water molecules around the alkali metal cation is essentially stripped away prior to insertion into  $\alpha\text{-Ni}(\text{OH})_2$  structure and bond with the water molecules those already inside the inter-slab space during the oxidation process.. Therefore, the inserted cations can be considered bare ions moving rapidly inside the structure. There is a significant removal of water molecules (largest for  $\text{K}^+$ ) upon insertion of  $\text{Na}^+$  and  $\text{K}^+$ , while  $\text{Li}^+$  insertion remains the content of water inside the host structure unchanged. Moreover, it is energetically more favourable that all protons are removed to form water leaving the host structure.

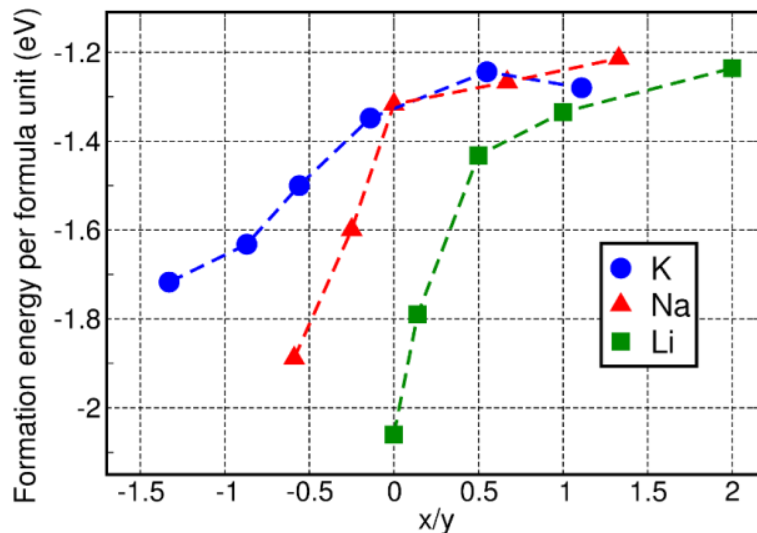


**Figure A-4** Computed formation energies per formula unit for the insertion of Li, Na and K cations as a function of water/cation ( $x/y$ ) at the charged state in the first cycle. Values for the selected stoichiometry of proton ( $z$ ) and cation ( $y$ ) in the simulations are reported in Figure A-3.

Similarly, the DFT+U computations were conducted based on experimental data for reduction process in order to compute the energetically most favourable stoichiometry of the host cell in LiOH, NaOH and KOH media. To this purpose, further assumptions were made that the computed magnitude of water/cation ( $x/y$ ) during the previous oxidation is the same as for reduction and the accumulated charge involved in reduction process is the same as during discharge (no current leakage). Based on these approximations, the energetically most favourable stoichiometries for the first cycle in LiOH, NaOH and KOH media were demonstrated in Figure A-5.



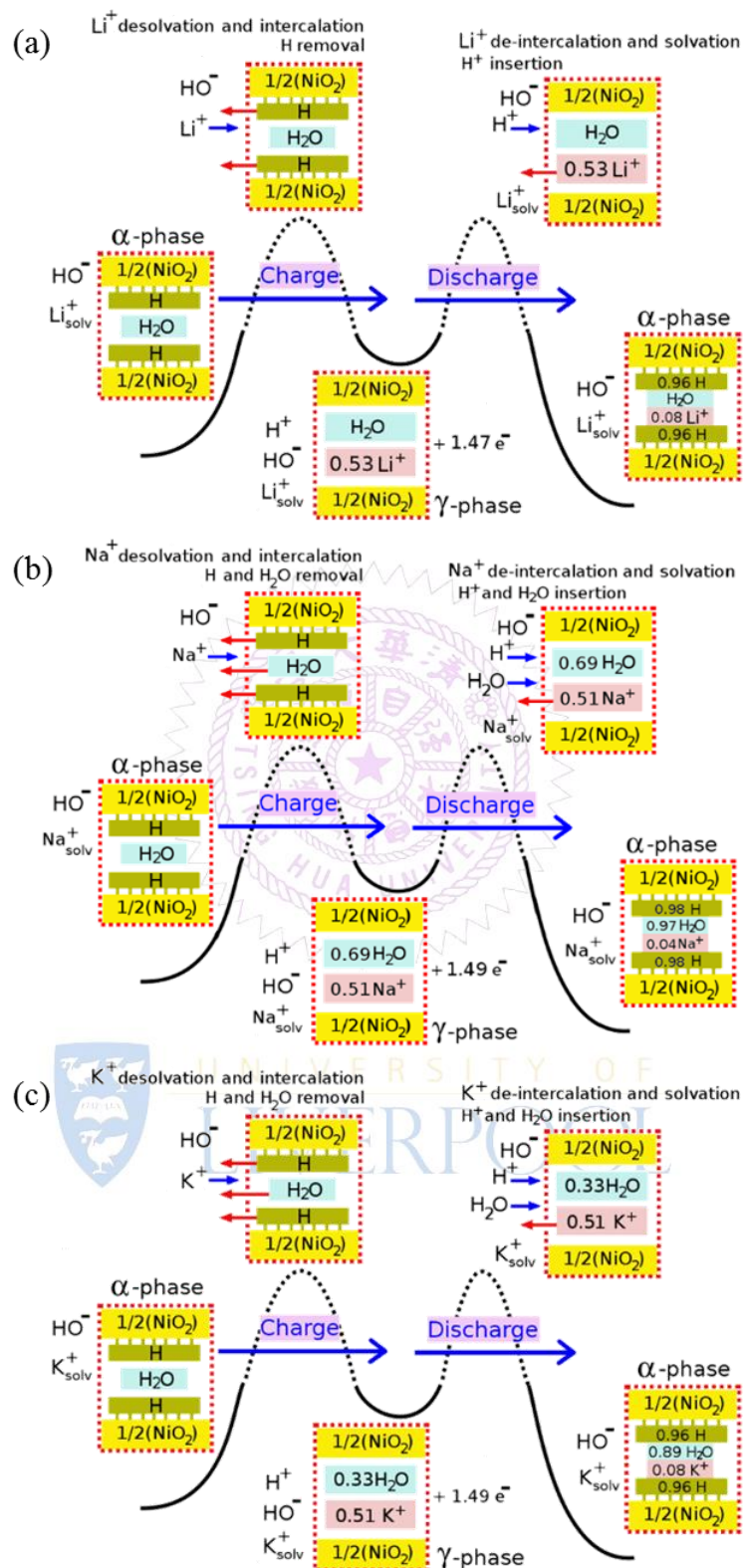


**Figure A-5** Schematic diagrams the first cycle in (a) LiOH, (b) NaOH and (c) KOH media.

In order to investigate how the stoichiometry change in LiOH, NaOH and KOH media upon cycling, the computational studies were carried out to the first six cycles

recorded under the scan rate of  $5\text{mV s}^{-1}$  in EQCM. For NaOH and KOH, the  $\beta$  phase behaviour was found since the seventh cycle in EQCM. Thus, in order to ensure  $\gamma/\alpha$  is the only redox reaction involved, we have restricted our computational study only to the first six cycles. Figure A-6 shows the calculated stoichiometry of the energetically most favourable  $\gamma$  phase (at charged state) for the first six cycles. Based on the findings from Figure A-4, it is reasonable to assume that there is absence of proton ( $z=0$ ) at charged state. Although the amount of intercalated  $\text{Li}^+$  increases with cycle number, the amount of water remains practically the same. On the other hand, the content of  $\text{Na}^+$  and  $\text{K}^+$  also increases, while a drastic reduction of water content in  $\gamma$  phase can be clearly observed. This reduction of water content is the most significant for  $\text{K}^+$ .

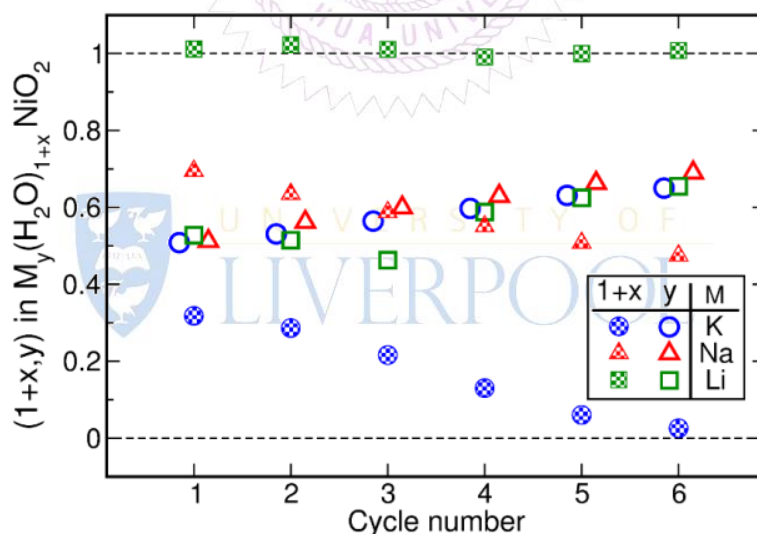


**Figure A-6** Most favourable stoichiometry for water ( $1+x$ ) and cations ( $y$ ) in  $\gamma\text{-M}_y(\text{H}_2\text{O})_{1+x}\text{NiO}_2$  ( $M = \text{Li}^+$ ,  $\text{Na}^+$  and  $\text{K}^+$ ) at charged state during the first six cycles.

Figure A-7 (a) shows magnitude of the water to cation ratio  $|x/y|$  with cycle number. The results are similar to the findings from Figure A-4 that insertion of  $\text{Na}^+$  and  $\text{K}^+$  is achieved through removal of water molecules inside the  $\alpha\text{-Ni}(\text{OH})_2$  structure. From the computed stoichiometry at charged state, the average oxidation

state of nickel can be estimated at each cycle, as shown in Figure A-7 (b). The noticeable drop after six cycles was found, indicating the nickel oxidation state of  $\gamma$  phase obtained from electrochemical oxidation of  $\alpha$ -Ni(OH)<sub>2</sub> decreases significantly in the first six charge-discharge cycles. Note that the nickel oxidation state of  $\gamma$  phase (i.e., 3.5~3.7) is in good agreement with those reported (i.e., 3.3~3.75) in literature [183, 187].

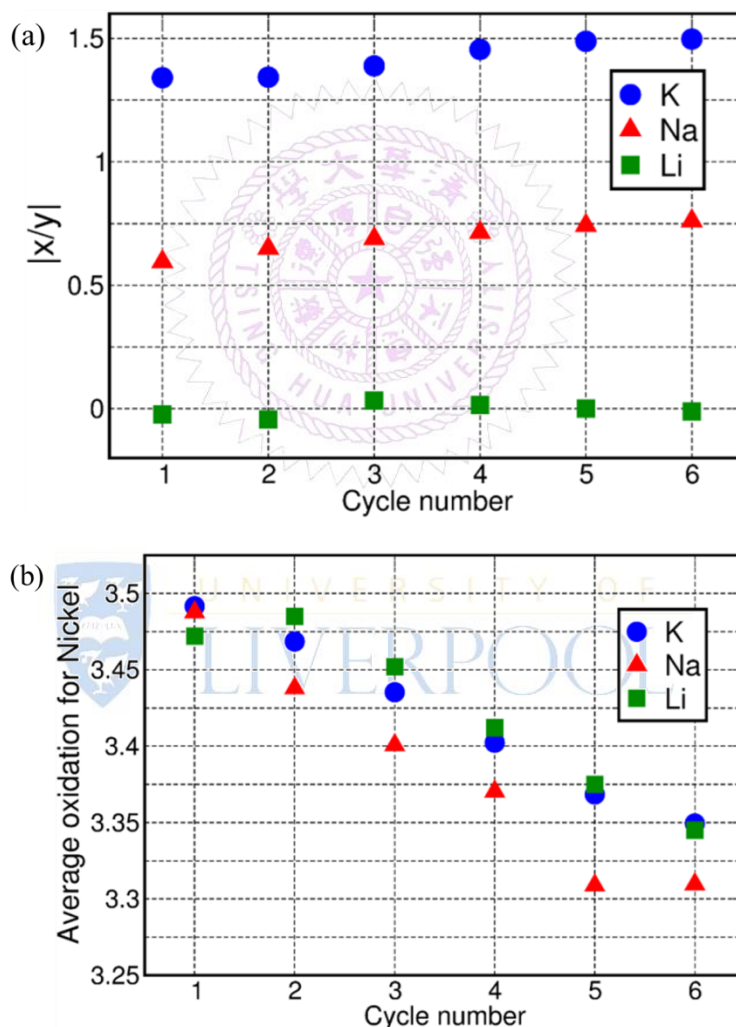


**Figure A-7** (a) calculated magnitude of the water to cation ratio  $|x/y|$  during the first six charge-discharge cycles. (b), the calculated average oxidation state of nickel at charged state as a function of cycle number.

Figure A-8 shows the evolution of the predicted most favourable stoichiometry for water, cations and protons in  $\alpha$  phase (at discharged state). The amount of cations

increases with the cycle number, and this leads to a reduction in the amount of protons. At discharged state, the amount of water remains the same for  $\text{Li}^+$ , while it decreases for  $\text{Na}^+$  and  $\text{K}^+$ . Moreover, the accumulation of residual mass at the end of reduction process was found for NaOH and KOH cases in EQCM, which is attributed to the residual cations in the structure that could not be reversibly removed from the structure. The amount of protons reduces accordingly to the increase of residual cations in the structure to keep the average nickel oxidation state equal to two. This means that the charge–discharge process in NaOH and KOH is not entirely reversible. Based on these results, the mechanism for reduction process is proposed to take place through the removal of the cation from the host structure followed by the re–insertion of the corresponding amount of water (in  $x/y$  ratio) back into  $\text{Ni}(\text{OH})_2$  structure. This process also complies with the mass and charge balance equations.

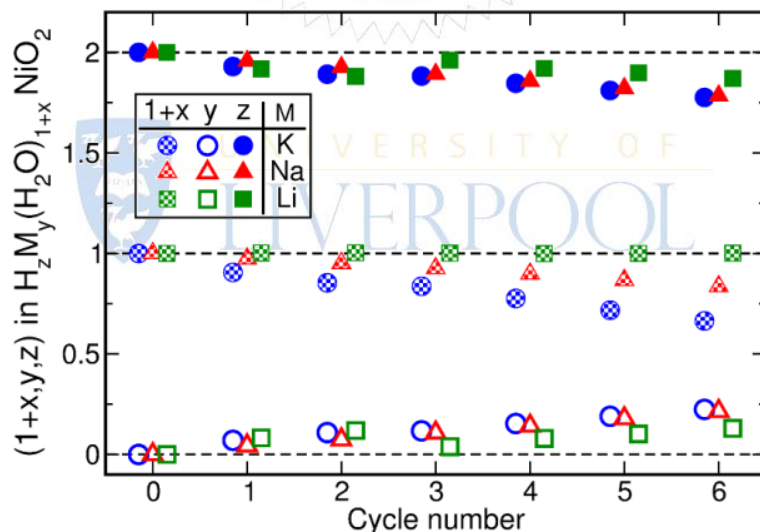


**Figure A–8** Most favourable stoichiometry for water ( $1+x$ ), cations ( $y$ ) and protons ( $z$ ) in  $\alpha\text{-H}_z\text{M}_y(\text{H}_2\text{O})_{1+x}\text{NiO}_2$  ( $\text{M} = \text{Li}^+, \text{Na}^+$  and  $\text{K}^+$ ) at discharged state during the first six cycles. Here, cycle zero corresponds to the pristine  $\alpha\text{-Ni}(\text{OH})_2(\text{H}_2\text{O})$ .

The computed the formation energy per formula unit for the first, third and sixth cycle are shown in Figure A–9. Numerical labels for each value indicate the stoichiometry of water in the structure. In addition, the formation energy of the

pristine  $\alpha$ -Ni(OH)<sub>2</sub>(H<sub>2</sub>O) (labeled as magenta diamond) and  $\beta$ -Ni(OH)<sub>2</sub> (labeled as dashed orange line) are shown in Figure A-9. At charged state in the first cycle, computed values demonstrate that the insertion of Li<sup>+</sup> exhibits the lowest formation energy, followed by Na<sup>+</sup> and K<sup>+</sup> (the same as Figure A-4). This trend for the formation energy of the charged  $\gamma$  phase can still be observed in the following cycles. In addition, the increase of residual cation content with the cycle number leads formation energies to decrease. At discharged state, the formation energy of the structure containing Li<sup>+</sup> remains practically constant due to the similar content of residual Li<sup>+</sup> in the first six charge-discharge cycles. And the formation energy of the structure containing Li<sup>+</sup> is relatively close to the corresponding value of  $\beta$ -Ni(OH)<sub>2</sub> (dashed orange line). On the other hand, the formation energy decreases gradually with the cycle number for Na<sup>+</sup> and K<sup>+</sup> at discharged state due to the increase of residual cation in the structure.

Based on the experimental results and the computational evidence, it can be concluded that the capability to retain water inside the nickel structure is crucial for the stability of  $\gamma/\alpha$  redox reaction. The intercalated water molecules can act as an ‘amorphous glue’ keeping the randomly stacking structure of  $\alpha$ -Ni(OH)<sub>2</sub> [184]. Therefore, the loss of water molecules in Ni(OH)<sub>2</sub> structure during charge-discharge process is the key for phase transform (ageing) to  $\beta$ -Ni(OH)<sub>2</sub>. In fact, since the insertion/removal of L<sup>+</sup> does not alter the content of water inside the structure,  $\gamma/\alpha$  redox reaction in LiOH medium is stable. Contrarily, the insertion of Na<sup>+</sup> and K<sup>+</sup> leads to a significant removal of water, which in turn introduces structural instabilities. At the charged state in the sixth cycle, the amount of water in the structure was reduced to 0.47 for Na<sup>+</sup>, while there is almost no water for K<sup>+</sup> (i.e., 0.03). On the other hand, the reduction process will be conducted by cation removal prior to the re-insertion of water molecules from the electrolyte. However, if water molecules do

not immediately re-insert back into the nickel structure once the cations are removed, the structure will be prone to collapse, leading to the formation of  $\beta$ -phase. Therefore, gradual loss of water molecules in  $\text{Ni}(\text{OH})_2$  structure is the intrinsic reason for the formation of  $\beta$  phase upon charge-discharge process. The proposed diagrams for  $\beta$  phase formation during 6<sup>th</sup> cycle discharge in NaOH and KOH are shown in Figure A-10.

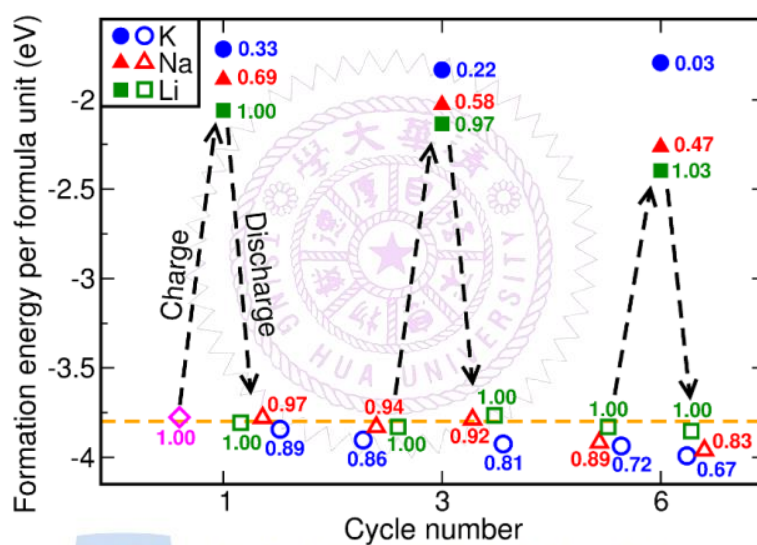


**Figure A-9** Computed formation energy per formula unit after charge (filled) and discharge (empty) for the first, third and sixth cycle. Numerical labels indicate the predicted amount of water '1+x' (Fig. FIGST4 and FIGST6). The magenta diamond and the dashed orange line correspond to the formation energy of the pristine  $\alpha$ - $\text{Ni}(\text{OH})_2$  ( $\text{H}_2\text{O}$ ) and  $\beta$ - $\text{Ni}(\text{OH})_2$ , respectively.



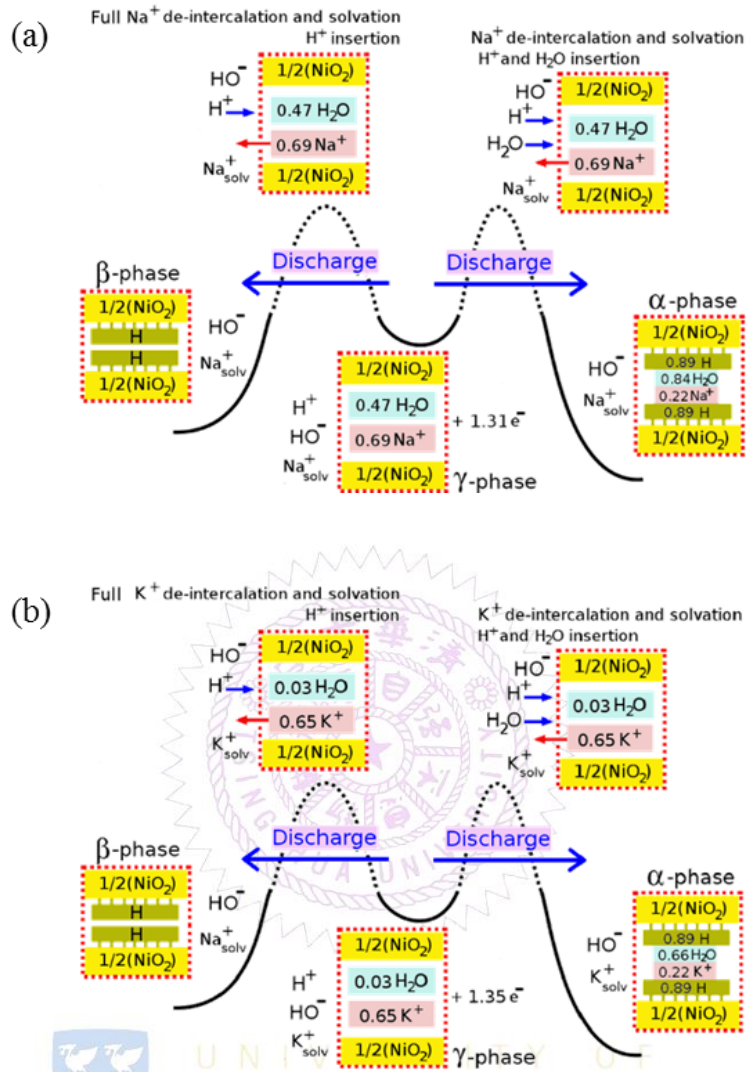


**Figure A-10** The proposed diagrams for  $\beta$  phase formation during 6<sup>th</sup> cycle discharge for (a) NaOH and (b) KOH.

## Acronyms

Activated carbon	AC
Brunauer, Emmett and Teller	BET
Carbide-derived carbon	CDC
Charge-coupled device	CCD
Chronopotentiometry	CP
Cobalt hydroxide	Co(OH) <sub>2</sub>
Cobalt oxide	Co <sub>3</sub> O <sub>4</sub>
Columbic efficiency	CE
Cyclic voltammetry	CV
Electric double-layer capacitors	EDLCs
Electrochemical capacitors	ECs
Electrochemical Impedance Spectroscopy	EIS
Electrochemical Quartz Crystal Microbalance	EQCM
Electrolytic manganese dioxide	EMD
Electron spectroscopy for chemical analysis	ESCA
Energy-dispersive X-ray spectroscopy	EDS
Energy efficiency	EE
Full width at half maximum	FWHM
Generalised gradient approximation	GGA
Graphene oxide	GO
Hydrogen evolving reaction	HER
Inductance-capacitance-resistance meter	LCR meter
Manganese oxide	MnO <sub>x</sub>

Nickel hydroxide	Ni(OH) <sub>2</sub>
Oxygen evolving reaction	OER
Powder X-ray diffraction	PXRD
Quasi-reference electrode	QRE
Reduced graphene oxide	RGO
Ruthenium dioxide	RuO <sub>2</sub>
Scanning Electron Microscopy	SEM
Single wall carbon nanotubes	SWNT
State of discharge	SOD
Surface-enhancement Raman spectroscopy	SERS
Transmission Electron Microscopy	TEM
X-ray absorption near-edge structure	XANES
X-ray absorption spectroscopy	XAS
X-ray photoelectron spectroscopy	XPS



UNIVERSITY OF  
**Symbols**  
LIVERPOOL

Capacitance normalized to SSA	C <sub>SA</sub>
Cell voltage	V
Charge-transfer resistance	R <sub>ct</sub>
Constant phase element	CPE
Double-layer capacitance	C <sub>dl</sub>
Effective cell capacitance	C <sub>cell</sub>
Electrical resistance of bulk porous electrode	R <sub>s</sub>
Faradaic pseudocapacitance	C <sub>f</sub>
Finite diffusion impedance	W <sub>f</sub>
Ionic resistance with porous electrode	R <sub>p</sub>

Lorentz fitted Raman peak intensity ratio of MnO <sub>2</sub> at 575 cm <sup>-1</sup> and Mn <sub>3</sub> O <sub>4</sub> at 658 cm <sup>-1</sup>	$I_{\text{MnO}_2}/I_{\text{Mn}_3\text{O}_4}$
Open-circuit potential	$E_{\text{cop}}$
Relative permittivity	$\epsilon_r$
Solution resistance	$R_s$
Specific capacitance of ECs	$C_s$
Specific energy stored in ECs	$E$
Specific surface area	$\text{SSA}$
Vacuum permittivity	$\epsilon_0$



# Curriculum Vitae

吳子和 Tzu-Ho Wu

Permanent address: 4F., No.39, Ln. 106, Sanzhuazikeng Rd., Ruifang Dist., New Taipei City 22442, Taiwan (R.O.C.)

E-mail: [tzuhowu@gmail.com](mailto:tzuhowu@gmail.com); [henry\\_20040102@hotmail.com](mailto:henry_20040102@hotmail.com)

## PROFILE

---

I am an academic researcher with great interests in ‘electrochemical energy storage and conversion’. I have been working on both carbon-based (such as activated carbon and graphenic carbon) and transition metal oxide-based (such as manganese and ruthenium oxides; nickel and cobalt hydroxides) supercapacitors since my master degree. I am familiar with plenty of analytical techniques.

## EDUCATION & QUALIFICATIONS

---

07/2011~07/2016: dual PhD programme between ‘National Tsing Hua University, Taiwan’ and ‘The University of Liverpool, UK’.

**Master and dual PhD**, Chemical Engineering and Chemistry

Research topic: *Optimising cell voltage and understanding charge storage mechanism of transition metal oxides and hydroxides for aqueous supercapacitors*

Supervisors: Prof. Chi-Chang Hu and Dr. Laurence J. Hardwick

09/2007~06/2011: National Tsing Hua University, Taiwan

**Bachelor of Science**, Chemical Engineering

## INTERESTS

---

- Football: runners-up in ‘2014 Five-A-Side Tournament’, The University of Liverpool, UK.
- Football: runners-up in 2014 summer five-a-side ‘World-Cup Tournament’, The University of Liverpool, UK.

## PERSONAL AWARDS

---

- The Second Place of Oral Paper Presentation, Graduate Students of Chemical Engineering Department, National Tsing Hua University, April, 2016.
- ‘National Tsing Hua University Presidential Scholarship’, 2012–2013.
- ‘Daxin Materials Corp. Scholarship’, 2015–2016.

## RESEARCH & SKILLS

---

- Electrochemical analyses, such as analytical cyclic voltammetry, electrochemical impedance spectroscopy and electrochemical quartz crystal microbalance.
- *In situ* electrochemical Raman microscopic studies of transition metal oxides and hydroxides.
- Conducting XRD, SEM, TGA, Raman, FTIR, gas absorption/desorption experiments.
- Familiar with analytic techniques, such as TEM, XPS, XAS...etc.
- Synthesis of transition metal oxides and hydroxides, such as electrochemical deposition and hydrothermal synthesis.
- Synthesis of graphene oxide and reduced graphene oxide (through microwave-assisted hydrothermal or thermal reduction).
- Synthesis of mesoporous silica materials, such as SBA-15 and MCM-41.

## TEACHING EXPERIENCES

---

- 09/2015--01/2016: teaching assistant of module 'Chemical Reaction Engineering'.
- 01/2013~06/2013: teaching assistant of module 'Unit Operation Laboratory'.
- 09/2012~08/2013: lab demonstration 'application of transition metal oxides for aqueous oxygen reduction reaction' for undergraduate project students.

## PUBLICATIONS

---

I have started scientific research on electrochemical energy storage and conversion since 2011. I have 11 peer reviewed published papers in which 8 of them focus on transition metal oxides for supercapacitors and 1 of them on electrochemical catalysis. Another 3 manuscripts about supercapacitors are presently under preparation and will be submitted shortly.

1. Chien, H.C., **Wu, T.H.**, Rajkumar, M., Hu, C.C., "Effects of buffer agents on hydrogen adsorption and desorption at/within activated carbon for the negative electrode of aqueous asymmetric supercapacitors", *Electrochim. Acta*, 205 (2016), 1-7. [\[Link\]](#)
2. Lee, J.S.M., **Wu, T.H.**, Alston, B.M., Briggs, M.E., Hasell, T., Hu, C.C., Cooper, A.I., "Porosity-Engineered Carbons for Supercapacitive Energy Storage Using Conjugated Microporous Polymer Precursors", *J. Mater. Chem. A*, (2016), DOI: 10.1039/C6TA02319C. [\[Link\]](#)
3. Rajkumar, M., Hsu, C.T., **Wu, T.H.**, Chen, M.G., Hu, C.C., "Advanced materials for aqueous supercapacitors in the asymmetric design", *Prog. Nat. Sci.*, 25 (2015), 527-544. [\[Link\]](#)



4. **Wu, T.H.**, Hesp, D., Dhanak, V.R., Collins, C., Braga, F., Hardwick, L.J., Hu, C.C., “Charge storage mechanism of activated manganese oxide composites for pseudocapacitors”, *J. Mater. Chem. A*, 3 (2015), 12786–12795. [\[Link\]](#)
5. Peng, Y.J., **Wu, T.H.**, Hsu, C.T., Li, S.M., Chen, M.G., Hu, C.C., “Electrochemical characteristics of the reduced graphene oxide/carbon nanotube/polypyrrole composites for aqueous asymmetric supercapacitors”, *J. Power Sources*, 272 (2014), 970–978. [\[Link\]](#)
6. Hsu, C.T., Hu, C.C., **Wu, T.H.**, Chen, J.C., Rajkumar, M., “How the electrochemical reversibility of a battery–type material affects the charge balance and performances of asymmetric supercapacitors”, *Electrochim. Acta*, 146 (2014), 759–768. [\[Link\]](#)
7. Liu, C.L., Hu, C.C., Wu, S.H., **Wu, T.H.**, “Electron Transfer Number Control of the Oxygen Reduction Reaction on Nitrogen–Doped Reduced Graphene Oxides Using Experimental Design Strategies”, *J. Electrochem. Soc.*, 160 (2013), H547–H552. [\[Link\]](#)
8. **Wu, T.H.**, Hsu, C.T., Hu, C.C., Hardwick, L.J., “Important parameters affecting the cell voltage of aqueous electrical double–layer capacitors”, *J. Power Sources*, 242 (2013), 289–298. [\[Link\]](#)
9. **Wu, T.H.**, Chu, Y.H., Hu, C.C., Hardwick, L.J., “Criteria appointing the highest acceptable cell voltage of asymmetric supercapacitors”, *Electrochem. Commun.*, 27 (2013), 81–84. [\[Link\]](#)
10. Li, J.M., Chang, K.H., **Wu, T.H.**, Hu, C.C., “Microwave–assisted hydrothermal synthesis of vanadium oxides for Li–ion supercapacitors: The influences of Li–ion doping and crystallinity on the capacitive performances”, *J. Power Sources*, 224 (2013), 59–65. [\[Link\]](#)
11. Hu, C.C., Wang, C.W., **Wu, T.H.**, Chang, K.H., “Anodic composite deposition of hydrous RuO<sub>2</sub>–TiO<sub>2</sub> nanocomposites for electrochemical capacitors”, *Electrochim. Acta*, 85 (2012), 90–98. [\[Link\]](#)

#### CONFERENCE PRESENTATIONS

---

1. Poster Presentation: 5<sup>th</sup> International Conference on Advanced Capacitors, Otsu, Japan, May 23–27, 2016.
2. Poster Presentation: The 66th Annual Meeting of the International Society of Electrochemistry, Taipei, Taiwan, October 4–9, 2015.
3. Oral Presentation: 4<sup>th</sup> International Symposium on Enhanced Electrochemical Capacitors, Montpellier, France, June 8–12, 2015.
4. Poster Presentation: Electrochem North–West, Manchester, UK, May 23, 2015.
5. Oral Presentation: Latest Developments in Electrochemical Capacitors, Poznan,

- Poland, January 29–31, 2015.
6. Poster Presentation: Carbon in Electrochemistry, Faraday Discussion 172, Sheffield, UK, July 28–30, 2014.
  7. Poster Presentation: Electrochem North–West, Liverpool, UK, June 23, 2014.
  8. Poster Presentation: International Conference on Advanced Capacitors, Osaka, Japan, May 27–30, 2013.

#### CONFERENCE AWARDS

---

1. Student Poster Award, 5<sup>th</sup> International Conference on Advanced Capacitors, Otsu, Japan, May 23–27, 2016. [\[Link\]](#)
2. Hot Presentation, 5<sup>th</sup> International Conference on Advanced Capacitors, Otsu, Japan, May 23–27, 2016. [\[Link\]](#)
3. Best Poster Award, The 66th Annual Meeting of the International Society of Electrochemistry, Taipei, Taiwan, October 4–9, 2015. [\[Link\]](#)
4. Best Poster Award, Electrochem North–West, Manchester, UK, May 23, 2015. [\[Link\]](#)
5. Student Poster Award: International Conference on Advanced Capacitors, Osaka, Japan, May 27–30, 2013. [\[Link\]](#)

#### REFERENCES

---

Dr. Chi–Chang Hu

Professor

Address: Department of Chemical Engineering, National Tsing Hua University, Hsin–Chu 30013, Taiwan

Email: [cchu@che.nthu.edu.tw](mailto:cchu@che.nthu.edu.tw)

Dr. Laurence J. Hardwick

Reader in Chemistry

Address: Stephenson Institute for Renewable Energy, Department of Chemistry, The University of Liverpool, Chadwick Building, Peach Street, Liverpool, L69 7ZF, UK

Email: [hardwick@liverpool.ac.uk](mailto:hardwick@liverpool.ac.uk)

Dr. Rong–Ming Ho

Professor

Address: Department of Chemical Engineering, National Tsing Hua University, Hsin–Chu 30013, Taiwan

Email: [rmho@mx.nthu.edu.tw](mailto:rmho@mx.nthu.edu.tw)